Universidade de Aveiro
2013
Departamento de Engenharia de Materiais e Cerâmica

Arivumani Ravanan

Processamento e tenacificação de compósitos de fase metálica e carbonetos duais

Processing and Toughening of Dual-Metallic Phase Dual-Carbide Composites

Universidade de Aveiro
2013
Departamento de Engenharia de Materiais e Cerâmica

Arivumani Ravanan

Processamento e tenacificação de compósitos de fase metálica e carbonetos duais

Processing and Toughening of Dual-Metallic Phase Dual-Carbide Composites

Dissertação apresentada à Universidade de Aveiro para cumprimento dos requisitos necessários à obtenção do grau de Mestre do mestrado europeu EMMS - Mestrado Europeu em Ciência dos Materiais, realizada sob a orientação científica do Doutor Joaquim Manuel Vieira Professor Catedrático do Departamento de Engenharia de Materiais e Cerâmica da Universidade de Aveiro.

Dissertation presented to University of Aveiro for the requirement of partial fulfillment of the Masters of Science degree European EMMS Masters - Joint European Master in Materials Science under supervision of Doctor Joaquim Manuel Vieira, Full Professor in the Department of Materials and Ceramic Engineering of the University of Aveiro.

o júri

Presidente	Professora. Drª. Maria Margarida Tavares Lopes de Almeida, Professora Auxiliar da Universidade de Aveiro
Arguente	Professor Dr. Manuel Fernando Gonçalves Vieira, Professor Associado da Universidade do Porto - Faculdade de Engenharia
Vogal	Doutor Filipe José Alves de Oliveira, Equiparado a Investigador Auxiliar da Universidade de Aveiro
Orientador	Professor Dr. Joaquim Manuel Vieira, Professor Catedrático da Universidade de Aveiro

acknowlegments

I am thankful to my supervisor Professor Dr. Joaquim M. Vieira for the guidance in the work as in the philosophy of science which enabled me to develop and conclude this dissertation. I also would like to extend my gratitude to my co-supervisor Professor Dr. Patrick Huber of Technical University Hamburg-Harburg for his time in reviewing the thesis under the Erasmus Mundus in Materials Science program.

I am also very thankful to Professor Dr. Augusto Luís Barros Lopes for his useful advice and Dr. Filipe J. Oliveira for his support during mechanical experiments. I am also very grateful to Professor Dr. Joachim Albrecht for his valuable guidance in TUHH and also to Dr. Karl-Heinz Schwalbe and Dr.Prof. Jörg Müller in TUHH.

And I convey my hearty thanks to my program co-ordinators and teachers Professors Dr. Vitor S. Amaral and Dr. Florinda M. Costa of UA for their support for completing this course. I oblige my deepest thanks to my scientific co-ordinators Professors Drª Margarida M. Almeida and Dr. Hans Wittich of UA and TUHH, respectively, for their guidance during my initial period of these studies.

I wish to share my thanks to all the members of Department of Materials and Ceramic Engineering especially Ms.Célia Cristina Miranda, Ms. Alexandra Vale Martins, Ms. Maria João Bastos, Mr. Octavio Santos Contente, and also thanking the PhD. scholars MSc Diogo Mata, Muhammad Asif Rafiq and Devaraj Ramasamy Nadar and pos-doctoral fellows Dr. Flávia Aparecida de Almeida and Dr. Miguel Neto

My hearty regards to all my friends, family and other officials of UA and TUHH who supported me by all the ways and they are many, however a few to mention here are Drª. Lúcia Avelar, Dr. Niall Power, Mr.Sivakumar Rajendiran, Ms.Vijayalakshmi Srikanth, Ms.Harini Sampathkumar and Maha Meru Mandali.

And my sincere thanks to another hand of this experimental work MSc Bruno Almeida, for his supporting during all experiments and electron microscopy, useful comments and helpful suggestions in this work.

And my obedient gratitude to the almighty of God and the Master who has been educating me as well.

I would like to thank the EMMS consortium for the program and the European Commission for the scholarship.

I also acknowledge RNME – Pole University of Aveiro (FCT Project RED/1509/RME/2005) for grating the use of the Hitachi SU-70 SE-SEM with the Bruker QUANTAX 400 high yield EDS system and for scientific and technical assistance.

palavras-chave

Liga de Al-Si, carboneto de boro, carboneto de silício, infiltração reactiva, compósitos, dureza, tenacidade, diagramas de fases.

resumo

Este trabalho incide sobre o processamento e estudo da tenacificação dos compósitos de fase metálica dual e dupla fase de carbonetos, com B_4C e SiC, e utiliza a técnica infiltração reactiva da liga fundida para preparar amostras quase totalmente densas dos compósitos.

Lotes de ligas hipereutécticas de Al-Si fundidas uma e duas vezes foram produzidas a partir de pós de alumínio e de silício, na proporção de 25% em peso e 35% em peso de Si e tendo-se feito a fusão a 1000 ºC durante 60 minutos em atmosfera de argon. Utilizou-se um pó de carboneto de boro de 10 um de tamanho médio de partícula, com carbono livre, principalmente grafite, para preparar provetes cilíndricos, de 7,5 mm de altura e densidade relativa nominal de 50%, por prensagem uniaxial seguida de prensagem isostática a frio. O fundido reactivo da liga de Al-Si infiltra espontaneamente as preformas de B_4C às temperaturas de 1200 ºC e 1300 ºC, em 5 minutos, tendo-se utilizando um forno de resistência de grafite com uma atmosfera inerte de árgon. No estudo descrevem-se os defeitos relacionados com a infiltração e são discutidas as condições experimentais e da contaminação em oxigénio da atmosfera do forno e da liga que poderiam ter causado a infiltração parcial ou a ausência de infiltração das preformas de B_4C. Obteve-se um conjunto de amostras dos compósitos totalmente infiltradas representando diferentes proporções de Si no infiltrado e as duas temperaturas em que a infiltração se tornou exequível dentro do intervalo de condições experimentais deste estudo. Seções polidas longitudinais dos provetes foram investigadas através de métodos quantitativos de DRX com padrões para a determinação das fracções volúmicas das principais fases cristalinas, Al, Si, B_4C e SiC e a microscopia electrónica de varrimento com análise de energia dispersiva sem padrão SEM/EDS para distribuição dos elementos na composição das fases. Os percursos de reacção no interior dos compósitos tendo em conta as alterações na fracção volúmica das fases entre a face superior, a face infiltração do fundido, e a face inferior dos provetes fundo foram representados na secção isotérmica do diagrama de fases Al-Si-B_4C. As correspondentes representações da composição química elementar média dos compósitos nos diagramas de fases de Al-Si-C e Al-Si-B-C põem em evidência o elevado teor de Al nos compósitos, principalmente Al metálico, o que explica os valores de dureza comparativamente baixos. Um efeito do tamanho de indentação é observado na dureza Vickers para as cargas de indentação de 9,8 N, 98 N e 294 N, estando a dureza aos 98 N correlacionada com a concentração de Si no infiltrado de Al-Si. Apesar da dispersão de valores da tenacidade à fractura de indentação determinada a 98 N, a valores altos da tenacidade dos compósitos deste estudo estão correlacionados com os valores relativamente baixos de dureza da mesma maneira como se encontrou nos resultados recentemente publicados de um estudo semelhante de infiltração reactiva de

compósitos B_4C com ligas Al-Si com teor de Si mais elevado. Procurou-se discutir ainda a forma como o mecanismo de tenacificação poderá depender das distribuições das fases frágeis e da fase dúctil de Al e bem como do desligamento do Al nas interfaces com as fases cerâmicas.

keywords

Al-Si alloy, boron carbide, silicon carbide, reactive melt infiltration, composites, hardness, toughness, phase diagrams

abstract

This work on the processing and study of the indentation fracture composites of dual-metallic phase of Al-Si and dual carbide phase of B_4C and SiC uses the reactive melt infiltration method to prepare nearly fully dense samples.
Batches of single and twice smelted Al-Si alloys of hypereutectic composition were produced by mixing aluminium and silicon powders in the proportion of 25 wt% and 35 wt% Si and melting at 1000 ºC for 60 minutes in argon atmosphere. Boron carbide powder of 10 µm average particle size, containing free carbon, mostly graphite, was used to prepare nominally 50% dense cylindrical pellets of 7.5 mm of height by uniaxial pressing followed by cold isostatic pressing. B_4C preforms become spontaneously infiltrated by the reactive melt of the Al-Si alloy at 1200 °C and 1300 °C in 5 minutes using a resistive heated graphite furnace with inert argon atmosphere. Defects related to infiltration are described in the study, the conditions and contamination in oxygen of the alloy and furnace atmosphere that could have caused partial or absence of infiltration of the B_4C preforms are discussed.
A set of fully infiltrated samples of the composites was obtained representing different Si proportions in the infiltrate and two temperatures where infiltration became feasible within the range of experimental conditions of this study. Polished longitudinal sections of the pellets were further investigated by using quantitative XRD methods with standards for the volume fractions of the main crystalline phases, Al, Si, B_4C and SiC and scanning electron microscopy with standard-less energy dispersive analysis SEM/EDS for the element distribution in the phases. The reaction path accounting for changes in the volume fraction of the phases from top, the melt infiltration face, to the bottom areas were represented in isothermal section of the Al-Si-B_4C phase diagram. The corresponding representations of the average elemental composition of the composites in the Al-Si-C and Al-Si-B-C phase diagrams expose a large content of Al, mostly Al metal in the composites which explains the comparatively low values of hardness. An indentation size effect of the Vickers hardness is observed for indentation loads of 9.8 N, 98 N and 294 N, the hardness of the composites determined at 98 N being correlated to the Si concentration of the Al-Si infiltrate. In spite of the scatter of indentation fracture toughness determined at 98 N, the high values toughness of the composites in this study are correlated to the comparatively low values of hardness in the same way as recently published in a similar study of reactive melt infiltration of B_4C composites with Al-Si alloys of high Si content. The way the toughening mechanism may depend on the distribution of the brittle phases and ductile Al and interphase de-bonding is further discussed.

TABLE OF CONTENTS

LIST OF FIGURES

LIST OF TABLES

SYMBOLS AND ABBREVIATIONS

A_B , A_C - undeterminable unknowns, the XRD absorption coefficients for the given peaks of the B_4C and graphite phases respectively,

c - Length of radial crack taken from the center of the indenter impression to the crack tip

d_{Al} - Density of aluminium

d_{gb} - Apparent density of the green body

d_{H2O} - Density of water

d_m - Density of liquid metal,

d_s - Density of the solid (as B_4C)

D_s - Equivalent spherical diameter of the loose particles in the porous bed.

d_{Si} - Density of silicon,

E - Young modulus,

f_I - Buoyancy force

g - Acceleration of gravity

H - Hardness

Hv - Vickers Hardness / HV_1, HV_{10} and HV_{30} -Vickers hardness (Suffix 1, 10, 30 indicates the load applied in Kgs.)

K - Calibration constant of the method

K - Symmetric tensor of permeability of the porous medium, or

K_{IC} - Fracture toughness

L_{Cap} - Capillary length

m - Mass,

P - Applied load,

P - Porosity fraction of the porous bed/Permeability coefficient of Darcy´s equation

R_1, R_2 - Principal radii of curvature of the curved interface

r_p - Average pore radius/ equivalent cylindrical pore radius of the open porosity

S_o - Specific surface area per unit of volume of the solids

S_w - Mass specific surface area of the powder.

V_s - Solid volume fraction or relative density (ρ) of the preform

v_s - Volume of the solid phase

X_C	-	Corresponding weight fraction of the C phase (graphite) in the sample
σ_a	-	Tensile stress
∇p	-	Gradient of pressure acting on the fluid
μ	-	Viscosity
2θ	-	Diffraction angles (where, θ - Bragg angle)
at%	-	Atomic percentage
m_{Al}	-	Mass of aluminium
m_{Si}	-	Mass of silicon
υ_{Al}	-	Volume of aluminium,
υ_c	-	Volume of composite,
υ_o	-	Superficial velocity of the fluid (the infiltrate, liquid metal),
υ_p	-	Volume of pores
υ_{Si}	-	Volume of silicon
wt%	-	Weight percentage
γ_{lv}	-	Specific surface energy of liquid-vapour interface
γ_{sl}	-	Specific surface energy of solid-liquid interface
γ_{sv}	-	Specific surface energy of solid-vapour interface
Δp	-	Pressure difference across the curved liquid-vapour interface
θ	-	Contact angle (Wetting Phenomena)
ρ	-	Relative density
4-D	-	Four Dimensional (phase diagram)
CIP	-	Cold Isostatic Pressing
DTA	-	Differential Thermal Analysis
EDS	-	Energy Dispersive X-ray Spectroscopy
FCC	-	Face Centred Cubic;
LPCVD	-	Low Pressure Chemical Vapor Deposition
LPS	-	Liquid Phased Sintered
MRI	-	Melt Reactive Infiltration
SEM	-	Scanning Electron Microscope
TG	-	Thermo Gravimetric Analysis (TGA)
XRD/ DRX	-	X-Ray Diffraction

1.0 INTRODUCTION

On account of the greater benefits of excellent combinations of properties of a few metal ceramic composites which play a significant role in the modern industry, there is the need to identify more economic and effective processing methods and to incorporate them in the industrial practice. The subject of the experimental work as given by the titled of the dissertation deals with *processing and toughening of dual metallic phase dual carbide composites* where the processing and resulting properties of new combinations of metal Al-Si alloys infiltrate into the low density B_4C carbide matrix is explored to formulate metal reinforced ceramic matrix composites of wide potential of use. Development of such composites is dictated by the need of reduction in absolute weight ratio, increase in strength to weight ratio, better toughness in combination with high neutron absorption of boron containing materials. Also relevant for nuclear and non-nuclear use as advanced composites are the expected high wear resistance, lower density and potentially high impact resistance that gives them ballistic features. As such, this study in line with other results of the research group[1] is an attempt to improve the understanding of these new composites and gather data that may contributed to improved economic design procedures and processing methodologies for achieving the best combination of attributes of the metals and ceramics in light weight composites of better reliability.

The processing procedure was designed in the view of obtaining a good fracture toughness preserving the hardness property through the use of a dual metallic phase that reacts with the starting carbide in the matrix to produce dual carbide phases in the finished composite. This research was undertaken and started with the following objectives: (i) processing of metal ceramic composites (ii) studying their composition in phases, microstructure, hardness and indentation fracture toughness, (iii) investigating the conditions of the liquid metallic phases and carbide phases of the composites and quantification of the dual metallic and dual carbide phases using reference standards (iv) characterizing the mechanical behavior of the composites.

The key materials of this work are aluminium, silicon and boron carbide powders in the pure form. The inherent quality and characteristics of these materials in various combinations and processing methods provide the required tailor made composites. When alloying the aluminium with silicon a material of even lower density which also increases

the fluidity of the melt a reduction of the melting temperature is anticipated and a decrease in the shrinkage and residual porosity related with solidification is expected. On account of the least solubility of silicon in aluminium, phases separate and virtually pure silicon forms hard precipitates which generally improves the abrasion resistance.

Boron carbide is an important ceramic material by itself with outstanding hardness, excellent mechanical and thermal properties. The attribute of a large cross section for thermal neutrons makes it an attractive candidate for absorption or retardation of neutron radiation in power plants and as well as in first-wall coating in fusion reactors. It has found applications in the fields of micro-electronics, nuclear, military, space and medical technologies. It has a low density (2.52g/cm^3) comparable to the density of silicon (2.34 g/cm^3) or the aluminium (2.70 g/cm^3). A few expected qualities of B_4C composites object of this experimental work, the better toughness in combination with the mentioned above high neutron absorption have activated the interest in lower weight and high strength aluminium-boron carbide composites. Moreover, the study of the phase equilibrium of combinations of these two materials (B_4C and Al) set the standing conditions for adequate processing; especially of the temperatures which promote the wetting to high level, yield better control of reactions and properly designed microstructures. The presence of the silicon improves the wetting and accelerates the penetration of the molten alloy into the porous medium. Indeed, a good wetting between ceramic and metal phases is needed in order to accomplish fully infiltrated composites.

In this work, a method seen as economic, the reactive infiltration is used for bonding B_4C into a ceramic structure apart from the other two conventional processes such as hot pressing and pressure-less sintering with solid or liquid phase sintering aids. Conventional hot-pressing methods need extra pressure with high fabrication temperature (>1800 °C) and high sintering temperature (2000 °C – 2400 °C) is required for pressure-less sintering process and both are more expensive methods [2]. At the same time, reaction bonding method is a spontaneous infiltration process where a molten metal can penetrate into the pore channels of a powder, fiber or pre-sintered preform by capillary pressure of the liquid that wets the solid. Spontaneous infiltration demands good wetting between two main phases of the process. For a solid liquid phase system with suitable surface free energy, infiltration can be used to achieve full density, preserve dimensions with precision, save

the geometry of the pieces and assure good bonding of the composites. And in such process no external pressure has to be applied by any mode [1].

In the present process, initially uni- axially pressed and iso-static compacted porous B_4C preforms were been prepared to achieve 50% of nominal porosity. In a resistance heated graphite furnace, the Al-Si alloy (range of 25 wt% Si to 35 wt% Si) was fused by twice smelting, cut into bits and compacted by pressing. By the effect capillary pressure the prepared uni-axially pressed Al-Si alloy in a protective atmosphere of argon gas infiltrates into the porous B_4C pre-forms in the temperature range of 1200 °C or 1300 °C after a five minute duration of time at the maximum infiltration temperature. The successful infiltration provided the dual metallic phase dual carbide composites of various grades due to various combinations of alloys and parameters used.

As the chemical interaction between the molten Si and B_4C is strong, the carbon of boron carbide can dissolve into to the metallic phase to form SiC in a significant level. Apart from formation of aluminum- silicon phases the newly fabricated dual carbide phases such as silicon carbide and boron sub-carbides took a significant role in the investigation. The major goal of this research work is producing a tough, reliable ceramic composite.

The experimental work was planned under the assumption that in order to obtain a tougher composite the metallic Si content in the reactive melt infiltration composite should be kept to a minimum favouring the maximum volume fraction of the tough metallic Al phase [2], provided that the Si content would be maintained above a threshold of Si in the Al-Si alloy that inhibits the formation of Al_4C_3 carbide [1]. These kind of metal ceramic composites have previously recorded values of the fracture toughness of less than 4 $MPa.m^{1/2}$ [1]whereas in this experimental work, the processes, procedure, and combination of materials are newly designed to the anticipated toughness limit of nearly 9 $MPa.m^{1/2}$.

In the structure of this dissertation, the state of art of this work has been prepared by studying the history of the related materials, their properties, processes and applications. It was then drafted with necessary things in brief form. The chapter on the experimental procedure comprises the preparation of the ceramic powder, smelting of alloys and infiltration processes along with sort description of main equipments, techniques and methods of this study. It also deals with the methodologies such as sample preparation and

characterization by XRD, SEM/EDS and indentation hardness and fracture toughness mechanical tests.

The characterisation of as supplied B_4C powder was done by analysing the constituents and contribution of in free carbon by XRD tests and thermal analysis (DTA/TG). The pressing efficiency of the B_4C materials used for the preform was determined too. The influence of the various compositions of the Al-Si alloy and the characterisation results were described. The Al-Si reactive melt infiltrations of B_4C, the consequences of failure of the melt infiltration process, partially and fully infiltrated composites were reported with the support of images. These elements are presented and discussed in the first three sections of the chapter on results and discussion.

Three successfully impregnated composites which were prepared from various compositions and processing parameters were separated and used for further investigation of properties such as the structural evolution, physical, chemical and mechanical characterization. Based on the appearance, performance during sample preparation the results of XRD and SEM/EDS analysis were used to characterised the composites and do the representation of their composition in Al-Si-B_4C ternary diagrams. With the aid of standards related to this experimental work, the quantification of individual phases of the composites was done and the volumetric phase distribution of each composite was determined. The comparisons of the composites were conducted based on the SEM/EDS analysis and volumetric phase distribution of composites. The characterisations and the comparisons among the composites were supported by the graphical and pictorial representations. For this investigation on the distribution of phases each composite was divided in three zones top, middle and bottom with respect to the infiltration direction hence details of the changes occurring inside each region were obtained.

By applying the elemental fraction method and the phase quantification by quantitative XRD methods with standards the amounts of individual elements and of each crystalline phases in the composition of the composites were determined. The identification and location of carbides of each composite were done by preparing isothermal section Al-Si-C ternary phase diagram. For the in depth investigation of the process a related isothermal section of Al - Si - B -C quaternary phase diagram was composed where the composition of the each composite as derived is plotted and further discussed in the text.

The mechanical behaviours of the composites were evaluated by the results of microhardness and marcohardness test conducted at the loads of 9.8 N, 98 N and 294 N. The discussion of the elastic modulus, fracture toughness and the toughening mechanism of the composites were further done. Some supplementary images and tables are given in annexes.

2.0 STATE OF ART

The objective of the Masters work is the study of *´Processing and toughening of dual metallic phase dual carbide composites´*. In relation to this theme a bibliographic review of different types of sources, research articles, book chapters, conference proceedings and doctoral thesis works was done and is succinctly presented in this chapter of the dissertation. The past background on the materials, methods and processes involved in this research are handled at the beginning. The up-date of the state of art on the processing and properties of such composites with most recent publications, such as the group publication Wu H et al (2012) that inspired this work was determinant for this study[1]. Details of the methods and specific equipment used to prepare or study the composites are left for the following chapter on the experimental lay-out and techniques. This chapter briefly deals with the overall reviewing of necessary parts of the literature to support the work to be done.

The raw materials of the experimental tasks of the study were taken in the form of powders: boron carbide, aluminium and silicon. Composites made of four solid phases, B_4C, SiC, metallic Al and Si are the major output of this work and form a dual metallic, dual carbide system. As schematically represented in figure 2.01 various properties of the individual elements and compounds are interconnected and involved in the design and processing of such metal matrix composites.

The structure of B_4C, SiC, Al and Si solid alloy are described in the first section of this chapter which also includes the a selection of representative binary phase diagrams such as the B-C, Si-C, Al-Si systems.

The reactions and representation of changes in composition of multi-element systems are better followed on phase diagrams and there are many combinations of the elements of the system that lead to relevant binary and ternary phase diagrams as indicated in figure 2.02. In this connection, the ternary systems including boron carbide are outlined in the final part of this chapter where the isothermal sections of ternary phase diagrams of Al-B-C and Si-B-C systems are added and discussed.

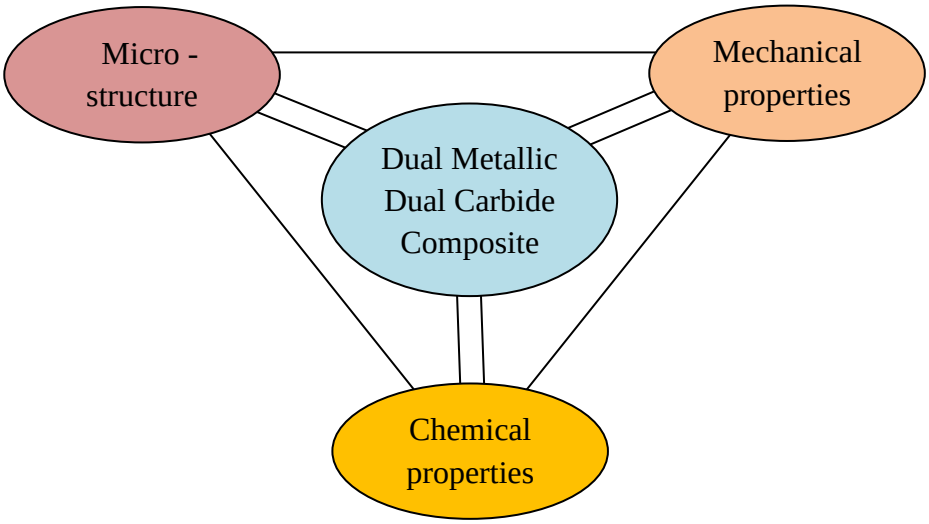

Figure 2.0 1: Interdependence of microstructural, physical, mechanical and chemical properties in designing a metal matrix composite

Furthermore, physical, mechanical and chemical properties of these phases are assessed in a short way. It is of this experimental work the reactive infiltration, which is reviewed in the following section along with major phenomena that control pressure-less, spontaneous infiltration, the wetting and the action of capillary forces, wetting of graphite surfaces by Al melts and wetting on ceramic phases by molten metal, namely by those of the Al-Si system.

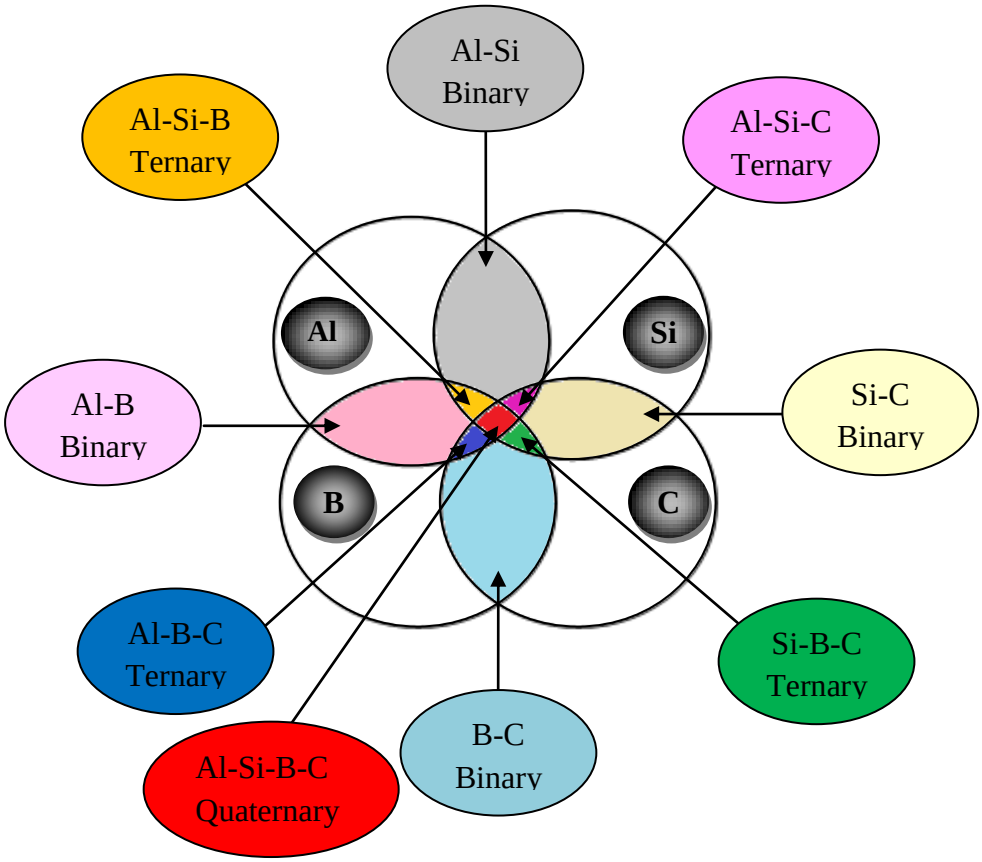

Figure 2.02: Combination of the four elements relevant for the present study and the complete set of possible binary, ternary and the one quaternary phase diagrams involved in the results of the experimental work.

2.1 Boron carbide

Easy to be synthesized, boron carbide (B_4C) is also the hardest material next to diamond and cubic boron nitride. The applications of B_4C are wide. Some of its distinctive properties are the low density (2.52 g/cm^3), chemical inertness and refractoriness thus sustaining the mechanical strength at elevated temperatures. B_4C raw materials often contain graphite as second phase which influences the strength of the material. In general the B_4C material is identified by the ratio of boron to carbon. The rhombohedral crystalline structure is observed when the stoichiometry of boron and carbon is close to 4:1 and beyond this value. As B and C atoms have similar cross sections for elastic scattering, it is

difficult to locate them in the crystalline them by neutron or X-ray diffraction techniques [3]. The location of C in the crystalline structure is best established by using spectroscopic methods.

The figure 2.03 displays the rhombohedral crystal structure of B_4C, the cell being filled in by 15 atoms corresponding to the $B_{13}C_2$ chemical formula of the B_4C solid solution, a crystalline phase of wide solid solution limits [4]. The changes of stoichiometry inside the crystalline structure of B_4C place a significant role in its mechanical properties. The space group of B_4C rhombohedral crystal structure is is D_{3d}^{3}- $R\bar{3}m$, a primitive cubic lattice distorted in the direction of the cell diagonal with almost regular icosahedra at the corners, figure 2.03.

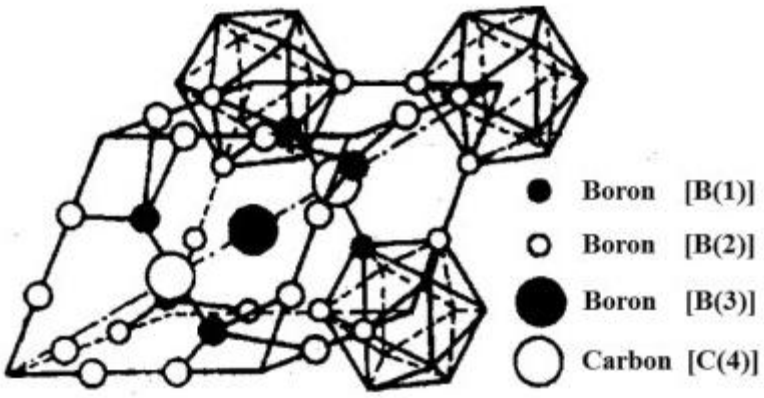

Figure 2.03: Rhombohedral crystalline structure of B_4C [4].

Parallel to the cell main diagonal, which becomes the c-axis of the hexagonal crystalline structure, a linear chain consisting of three atoms (two carbons [C(4)] and one boron [B(3)] interconnects adjacent icosahedra built of B atoms at the corners. In such complex unit cell there are 15 atoms corresponding to the model stoichiometry of ($B_{13}C_2$) of B_4C or ($B_{12}C_3$) when reported to the filled crystalline unit cell. Among the 15 atoms, 12 atoms are needed to form the icosahedron structures at the corners of the crystalline cell the remaining three constitute the C-B-C chains. C-B-C links build the rhombohedral structure. Zoning of the B_4C solid solution with fluctuations of B/C ratio often yields $B_{13}C_2$ domains formed between B_4C zones of composition close to the $B_{12}C_3$ stoichiometry, the average size $B_{13}C_2$ domains being smaller than those of B_4C.

2.1.1 B-C phase diagram

Two versions of the B-C binary phase diagram are given in figure 2.04, calculated (a)[5] and prepared after the experimental study (b) with microprobe analysis of *Schwetz and Karduc [6]* where a maximum C content of only 19.2 at% was found in the B_4C phase in equilibrium with graphite at the eutectic point (2380 ºC), and concentration of 18.5 at% C at 1000 ºC the late value corresponding to $B_{4.3}C$. In the calculated binary phase diagram given on figure 2.04 (a) the eutectic temperature appears at 2375 ± 5ºC, with the maximum C content of the B_4C solid solution 19.3–20.0 at% for an eutectic composition around 29-31 at%.

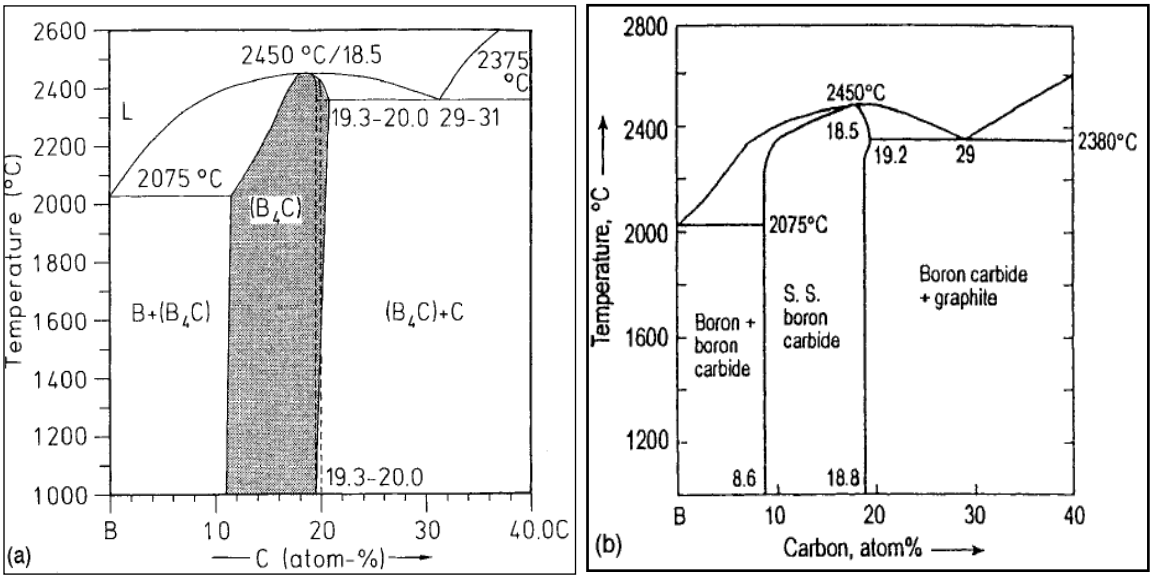

Figure 2.04: The B-C binary phase diagram: (a) calculated [5], (b) from experimental results [6].

Depending on the temperature, $B_{13}C_2$, the only crystalline structure of the binary phase accepted at the present among several phases of B_4C, has a broad range of homogeneity which ranges from 8.8 at% C at the low solid solution limit to the 20 at% C discussed above. This phase at the composition of 18.5 at% C melts congruently with the maximum melting point of 2450 ºC [7].

2.1.2 Mechanical behavior

Large refractoriness and covalent bonding of B_4C leads to poor sinterability requesting additives to promote grain boundary diffusion and often the use of sintering temperatures above 2000 ºC and applied pressure to achieve full densification of the ceramic part[1, 8]. The variations in modulus of elasticity, hardness, mechanical strength and fracture toughness of B_4C ceramics are explained by the sintering temperature, content of graphite and particle size. The Young modulus is an intrinsic property of a material dominated by the intensity of the chemical bond between atoms. The modulus of elasticity of B_4C is about 474 GPa and 480 GPa for $B_{13}C_2$ [9] . Due to such high elasticity modulus it is being selected material in several high technology fields such as ballistic armour applications[9]. Figure 2.05 gives the dependence of Young modulus of high B B-C coatings on the concentration of the carbon in of LPCVD (Low Pressure Chemical Vapour Deposited) coating.

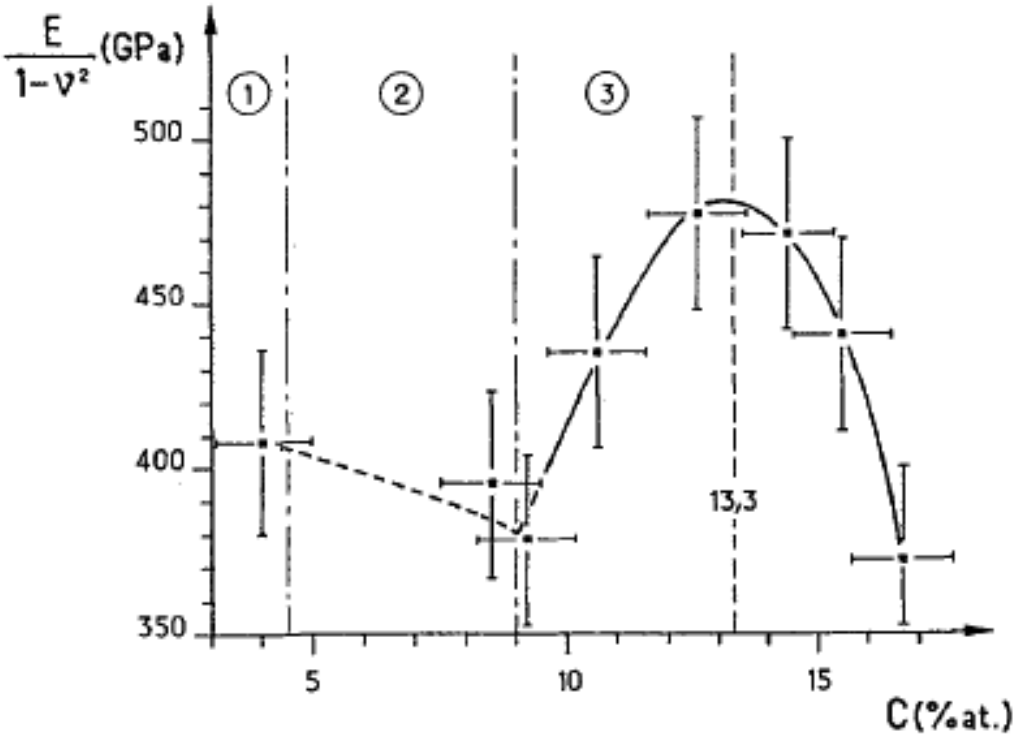

Figure 2.05 : Variation of $E/(1 - \upsilon^2)$ ratio versus the carbon concentration LPCVD coatings deposited at 1020 ºC in which (1) $B_{50}C_2$, (2) $B_{50}C_2$+$B_{13}C_2$, (3) $B_{13}C_2$ [10], ($\nu \approx 0.2$ is the Poisson ratio).

These coatings show the strong influence of composition on the elastic modulus where the maximum value of 475 GPa is obtained for the $B_{13}C_2$ stoichiometry. *Bouchacourt* reported an (ISE) indentation size effect in the hardness values of B_4C displaying exponentially rise with decreasing loads [11]. At very low loads (around 0.25 N), hardness values up to 58 GPa have been measured in B_4C with large standard deviation[11]. In general, approximately constant hardness values of B_4C materials are measured at loads above 20 N in which the large area of the indentations incorporates the details of the microstructure to return microstructure averaged values of hardness in the range 26-35 GPa [1]. At the same time, residual porosity, flaws, the presence of free carbon, namely as graphite in the B_4C samples and the loads of indentation testing explane the scatter of hardness values of B_4C reported in the bibliography. When comparing the hardness of diamond, c-BN and B_4C, the last compound displays the lowest hardness of the three at room temperature, at 500-600 ºC the structure of diamond transforms to graphite of much lower hardness, whereas above 1100 ºC in non-oxidizing atmosphere B_4C becomes the hardest material in this set [12]. Hence it has been used in high temperature technologies, in wear-resistant parts and inserts for mortars and ball mills, wear resistant nozzles, dressing tools in grinding application, lightweight armor plates for helicopters, tanks, and in fiber reinforced plastics (as bullet-proof protection) [12].

Large effort has been done to toughen the brittle ceramics and increase the fracture energy. Successful results were obtained by using short fibre and whisker reinforcements as well as by inclusion transformation toughening, even though the effectiveness of such toughening mechanisms and the improved performance of the ceramics matrix composites under the elevated temperatures is often subtle[13]. In general toughening mechanisms can be classified as intrinsic and extrinsic. The intrinsic mechanisms act ahead of the crack tip in which the original microstructure of the system loses stability and is modify by the stress field of the coming crack tip. In the general case, the plasticity can blunt crack tips by motion of dislocations in the process zone ahead of the crack. Crack tip blunting may equally come from viscous deformation of amorphous phases softened by heating. By increasing the precipitate particle spacing, as in the case of metallic alloys, the ductility and plasticity of the materials are changed which results in improvements of fracture

toughness. There are two different principles that explain the extrinsic mechanism of toughening, zone shielding and crack shielding which act behind the crack tip during crack propagation and decrease the stress intensity factor of the applied stress at the location of the crack front. Crack deflection toughening, micro-crack toughening, macro-crack bridging are few of the toughening mechanisms operating in the single phase polycrystalline ceramics. Transformation toughening is one of the methods in which the constituents of the second phase (or partially stabilized particles of the same phase) experience a stress induced martensitic phase transformation that absorbs the elastic energy and positively contributes to toughen the structural ceramics [13]. In a different way, toughening by soft metal inclusions is an alternative method to toughen ceramics in a compromise with the hardness and temperature of use of the finished composites.

Processed as ceramics, B_4C materials display high hardness but with moderate mechanical bending strength in the 270-420 MPa range. Hot isostatic pressing of high grade B_4C eliminated the residual porosity and improved the (1600-1800 ºC) hot strength to 500-700 MPa, a remarkable value among high technology structural materials[14]. But the true limitation of the B_4C ceramics for engineering applications is the low fracture toughness limited to values in the 1.3-3.7 $MPa.m^{1/2}$ range[8] . The room temperature strength of B_4C composites prepared by reactive melt infiltration with the Al-Si alloy are comparable to the bending strength of hot pressed B_4C ceramics, the dual phase composites of B_4C displaying higher fracture toughness and being much less demanding in temperatures for processing[1].

The low density of B_4C coupled to the high hardness and availability of raw materials makes this material either as dense ceramic plates or as mosaics of dual phase B_4C composites a candidate for the design of ballistic protection armour in the combination with other materials. The ballistic response of hard materials like B_4C is dependent on microstructure, especially trough the hardness. Density and elastic modulus are deciding factors that set mechanical impedance and determine shock behavior. Light weight and at the same time stiffer ceramics are considered as effective armor modulus. Materials that combine high hardness, high elastic modulus and low density have exceptionally high specific stopping power to defeat high velocity projectiles[15, 16]. Deflection of the projectile, erosion of projectile and target shattering, propagation and reflection of

shockwaves, crack initiation and coalescence and are the usual failure modes of the protection and are affected by the inertia and rigidity of the armor module [15, 16]. While all these mechanisms have a part in deciding for the minimum least weight armor protection, the potential role of B_4C materials for such applications is appreciable.

2.1.3 Chemical behaviour and oxidation of B_4C

Oxidation of B_4C in air and other oxygen containing atmospheres is one of the chemical properties of B_4C that limits its use as structural material. B_4C strongly reacts in oxidizing environment. The second limitation of B_4C for wider application at high temperature is its instability when in contact with most metals. The formation of borides and carbides are determined by the affinity of metal to boron or carbon[17] . When there are no stable metal carbides in the system the reaction of B_4C with the metals leads to formation of free carbon. When oxides contacting the B_4C are reduced borides and CO are formed. In spite that a few borides can be formed when the reaction occurs in air, it is mostly the metal borates that are generated by the reaction of B_4C and metals in air. In gaseous hydrogen B_4C reacts slowly with this element above 1200°C to form borane and methane, the vapor phase transport inhibits sintering of B_4C in hydrogen atmosphere[12].

B_4C powders begin to oxidize in detectable way at 250 ºC in the presence of H_2O vapor and at 450 ºC in dry air [18], the oxidation by dry air being slower than in H_2O vapour for temperatures up to approximately 700 ºC [18]. As it oxidizes in air B_4C is immediately coated by a passivation B_2O_3 layer, while in presence of water a hydroboric acid (H_2BO_3) layer forms within a few moments[19, 20]. Oxidation initiated at 500-600 ºC accelerates significantly above 800-1000 ºC, depending on the humidity in the atmosphere. In the work of *Matje et al[19]*, B_4C powders were surface cleaned, Si-sputtered and (1 ppm O_2 and 1 ppm H_2O impurity) Ar^+ ion implanted or left untreated and the weight gain at 20°C in air was monitored. The Si-sputtered and Ar-implanted powder showed a strong and immediate weight gain, it was substantially higher for the treated powder compared to the untreated one. While the Si-sputtered material remained stable after 20 hours, the Ar-implanted powder exhibited a continuous weight gain with increasing final oxygen content 4 wt%. Ar-implanting of the Si-sputtered B_4C powder lead to the enlarged surface area

besides formation of structural defects which facilitated oxygen diffusion and oxidation at room temperature[19]. These studies also indicated similar weight-gains in the dry and humid air atmospheres, a parabolic weight-gain and an increase in weight linear dependent on time at 52% humidity and 92% humidity, respectively.

Following *Telle et al* the large cross section of 4000 barn for thermal neutrons of the ^{10}B isotope that exists at concentration of 19.9% in natural boron makes B_4C ceramics special for absorption or retardation of neutron radiation. It is widely used in nuclear fission power plants and may become the first-wall coating in fusion reactors where it also guarantees stability to ionizing radiation and most chemicals[12].

2.2 Silicon carbide

Silicon carbide the compound with Si and C covalently bonded in tetrahedral coordination has over 180 polymorphic forms. SiC is a prominent representative of polytypic compounds [21]. Noteworthy properties of SiC materials are the low density (3.21 g/cm^3), high elastic modulus and hardness, superior chemical inertness and excellent thermal shock resistance. In recent times improved grades of SiC emerged as high quality technical ceramics with improved mechanical properties. It is used in abrasives, refractories and other high-tech applications. Structural and wear applications of SiC are constantly developing. It is extensively employed as an electrical semiconductor for resistance heating applications, flame igniters and electronic components[22].

Si and C layers are alternatively stacked in the crystalline structure of SiC due to its binary, tetragonal structure half the tetragonal voids between consecutive closed packed Si layers are occupied by a C layer, as shown in figure 2.06 a). The two identical closed-packings (Si and C) interpenetrate each other and form the structure where one packing is displaced relative to the other along c- axis with the layer spacing of 1/4. There are only four possible space groups for SiC as the tetragonal arrangement of atoms in SiC does not permit either a centre of symmetry or a plane of symmetry perpendicular to [001]. There are only three possible positions for atom centers - A, B and C - given in figure 2.06 a) [23]. The most frequently occurring stack sequences in the crystalline structure of SiC correspond to the

6H, 4H, 15R and 3C polytypes. Three of these stacks, the close packed hexagonal stacks 4H and 6H and the close packed cubic 3C stacks are displayed in figure 2.06 (b). It is the next nearest occupied positions filled by neighbor atoms that vary in the different crystalline lattices available for SiC. It is in 3C-SiC and 2H-SiC alone that all atom positions are equivalent and correspond to cubic or hexagonal sites of the crystal lattice, respectively.

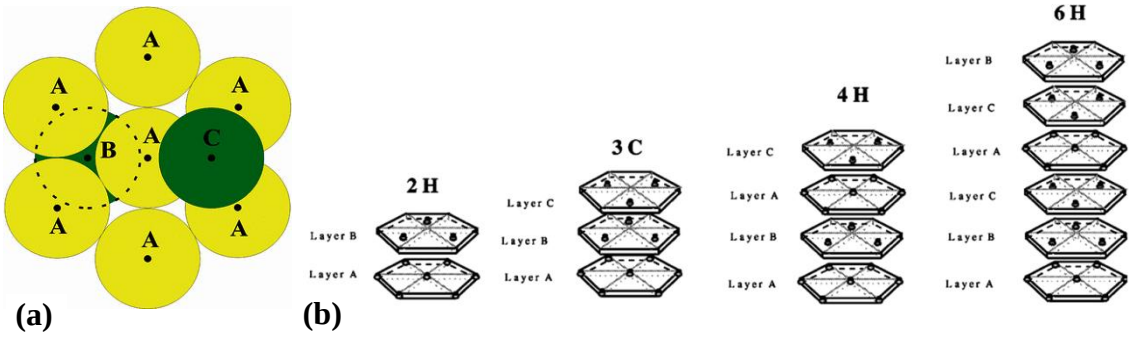

Figure 2.06: (a) Schematic positions of atom centers for a close spherical packing [23]. (b) Stacking of successive layers of Si and C in polytypes of SiC[24].

In the stacking sequence of 4H there is one cubic and one hexagonal arrangement of layers while the 6H polymorph is built as one hexagonal stack sequence of two cubic stacks combined in symmetrical way [25]. Figure 2.07 (a) shows four samples of SiC single crystals of the most used SiC polytypes. Figure 2.07 (b) describes the structure of the most common high temperature α-SiC modification with 6H packing and figure 2.07(c) the low temperature cubic β-SiC phase of 3C packing. SiC polytypes 2H and 4H are applied in electronics. The 6H polytype is in use in optoelectronics as monocrystalline SiC or thin films. The cubic 3C polytype forming polycrystalline ceramic materials is commonly found in refractories for high temperature applications.

The α-SiC is the stable phase of SiC above 2000 ºC, the 6H,15R and 4H polytypes being the most common modifications in the hexagonal phase. The stacking sequences of the 4H and 6H lattices are displayed in figure 2.06 (b), the sequence of 15 stacked atomic layers of the 15R polytype being -ABCBACABACBCACB. Along with these basic structures of SiC many other polytypes with in a wide range of stacking successions are known, such as

the remarkably long 51R SiC often detected in reaction-bonded SiC ceramic matrix composites[26].

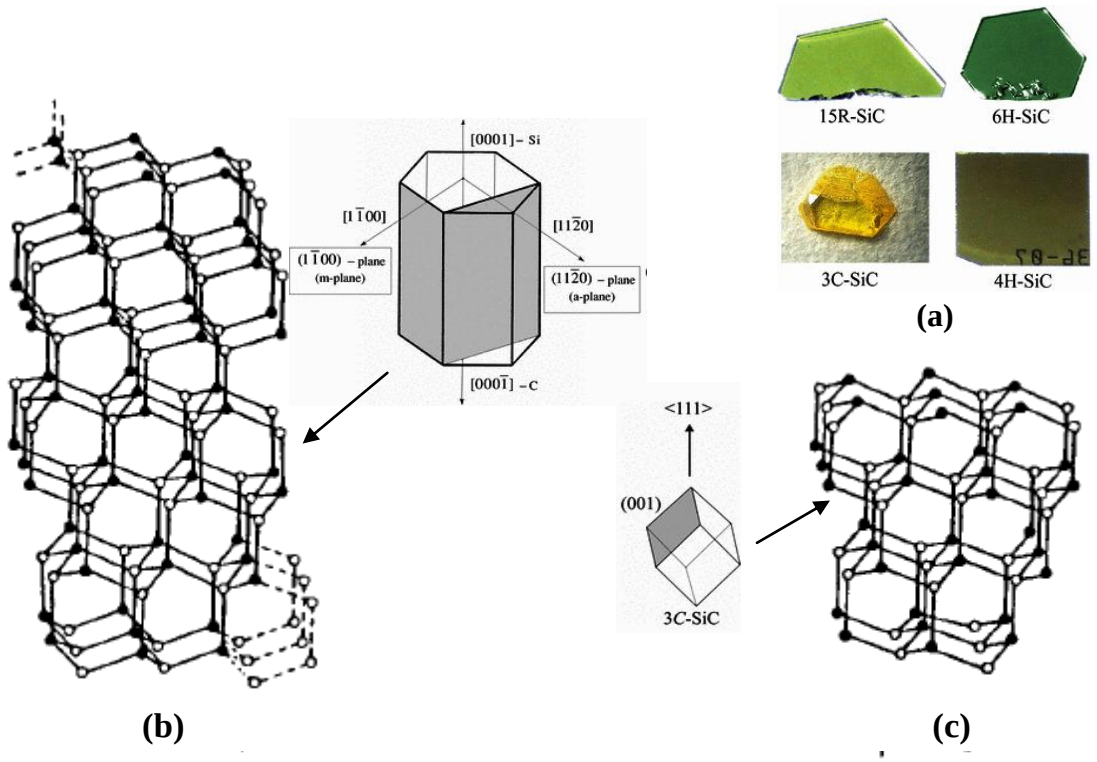

Figure 2.07: SiC polytypes with images of the atom arrangement of the crystalline lattices, (a) Single crystals of SiC polytypes[26] (b) Hexagonal crystal lattice of α-SiC (6H-polytype)[21, 27] and, (c) Cubic crystal lattices of β-SiC (3C-polytype)[21, 27]

The cubic β-SiC (3C) is stable below 1800 ºC and transforms into the stable, high temperature hexagonal α-SiC (6H) phase above this temperature [28, 29]. Metastable modifications of SiC may undergo solid-state transformation to the 3C and 6H structures at temperatures above 1400 ºC [29]. *Inomata et al* determined the following ranges of stability for some of SiC polytypes: the 2H is stable below 1400 ºC, 3C between 1400 ºC and 1600 ºC, 4H between 1600 ºC and 2100 ºC, 6H above 2100 ºC and 15R above 2200 ºC [30]. The impurities play a role in developing of different SiC polytypes. In short, 4H is crystallised by additions of Al, pure α-SiC mainly appears as 6H and Al in small amounts promoted the formation of 15R SiC.

2.2.1 Si-C Phase diagram

Figure 2.08 gives the Si-C binary phase diagram at the total pressure of 0.1 MPa (1 atm) which has SiC as the only binary compound (at 70 wt% Si). By introducing a transition metal the solubility of C in Si melt may be increased[31]. SiC does not have a congruent melting point. In an open system SiC start to compose at 2300 ºC with the formation of gaseous Si and graphite as a residue whereas in a closed system in equilibrium conditions the decomposition of SiC occurs at 2830 ºC,

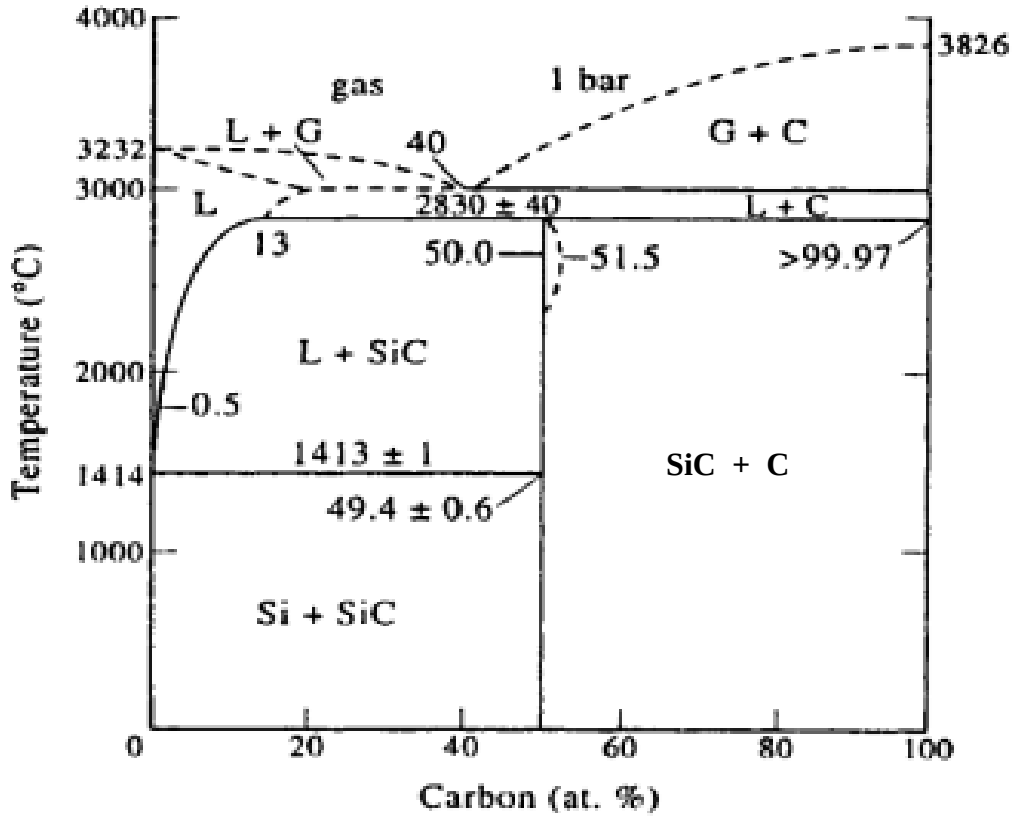

Figure 2.08: The binary phase diagram of the Si-C system [32]

the highest temperature at which crystallization of SiC may be observed during solidification of the Si-C melts. Conversely this is the temperature at which SiC breaks down into graphite and a Si rich melt at total pressure of 0.1 MPa. At the peritectic temperature, 2830 ºC, the solubility of C in liquid Si is 13 at% C. The solubility of C in crystalline Si in very low, SiC and Si forming a degenerate eutectic at 1413 ºC and 0.02 at% C, as given in figure 2.08 [32].

2.2.2 Chemical stability of SiC

Despite the high affinity of silicon for oxygen, SiC materials have the prominent property of high chemical resistance. Oxidation of pure SiC at around 600 ºC forms a passivation SiO_2 coating that prevents further oxidation and allows the use of SiC refractories and heating elements in air atmosphere to temperatures in excess of 1500 ºC. If this passivation layer is removed as in atmospheres of high H_2O partial pressure at high temperature, the oxidizing agents will attack and decompose SiC and enable the corrosion reactions to go on[33]. The behaviour of SiC in contact molten metal is manifold. Zinc and zinc vapour do not attack SiC, whereas Al attacks SiC in a slow way forming the aluminium carbide and silicon as reaction products, but as Si concentration in the liquid increases the reaction finally ceases because the equilibrium conditions are reached[34].

2.2.3 Mechanical behaviour of SiC

SiC is noted for the outermost hardness H of about 9.50-9.75 Mohs scale, SiC being an abrasive of widespread industrial use, the SiC ceramics exhibiting high abrasion resistance. It equally has high rigidity, the Young modulus E being close to 450 GPa. Both the high values of E and H explain the brittleness of SiC. High grade SiC materials retain the hot strength till temperatures above 1500 ºC[14]. SiC materials made by various methods are available as (solid state) sintered silicon carbide (SSiC), chemical vapour deposited silicon carbide (CVD SiC) and reaction bonded silicon carbide (RBSC), or as a composite of SiC and Si_3N_4 in the nitride bonded silicon carbide (NBSC)[27]. The differences of residual porosity, particle size and chemical composition of SiC materials impose changes in the microstructure and a wide span of values of the mechanical properties. Though there are some general limitations in the mechanical strength of SiC due to the brittleness, recrystallized SiC is much stronger than ceramic (phase) bonded SiC. Reaction-sintered SiC is still stronger but only up to 1400ºC, whereas the best strength values are provided by the hot pressed materials and sinter-HIPed ones. Liquid phased sintered SiC (LPS-SiC) has improved fracture toughness, this property imparts resistance against mechanical chipping, hence the application of LPS-SiC is wider in grinding works, components for equipment in transportation sectors, tooling industries than that of SSiC[27, 35]. The mechanical

strength and fracture energy of SiC can be improved when SiC fibers are embedded in the SiC ceramic matrix forming composites. Mechanical properties of ceramic composites can be tailor made by controlling the parameters of the SiC fibers and fiber/matrix interface[36].

2.3 Aluminium-Silicon alloys

Important technological properties of aluminium are low density, high specific strength, superior malleability, ability to be machined, excellent corrosion resistance and good thermal and electrical conductivity. Silicon is able to reduce the density, the coefficient of thermal expansion and improve the hardness of the Al alloys hence Si has been added to Al at various proportions. Though several additives are used to modify the industrial Al alloys, hypereutectic Al-Si alloys got much attention recently[37, 38]. Along with the above features silicon improved room temperature mechanical properties such as elastic modulus and strength, thermal stability and wear resistance of aluminum. Hypereutectic Al-Si alloys caused considerable interest leading to research of new members of the Al–Si alloys with potentially new applications in several fields of technology[37]. Recent research was focussed on unmodified cast alloys, especially with hypereutectic Al–Si alloys. The structure and mechanical properties of hypereutectic unmodified cast alloys have been studied mainly in relation to the increasing in Si content up to a concentration 19 at% Si.

The α-Al solid solution, the matrix phase of cast aluminum-silicon forms the non-faceted dendrites. The α-Al phase has the face centered cubic (fcc) lattice, shown in figure 2.09 (a), with Al in coordination 12 and 4 Al atoms in each fcc crystalline cell, the corresponding cell filling factor being 0.74 [39].

Silicon crystal lattice is A4, cubic, of diamond type where each atom is connected with four others with covalent bonds and forming a tetrahedron. Eight tetrahedrons form one elementary cell of the face centered A4 lattice, with four additional atoms from the center of each tetrahedron[40]. When comparing to A1 lattice this structure is lesser close packed with the filling factor of 0.34. Si has very low solubility in aluminium as shown in the Al-

Si binary phase diagram in figure 2.10. Therefore Si precipitates as virtually pure silicon which is hard and improves the abrasion resistance of the Al-Si alloys.

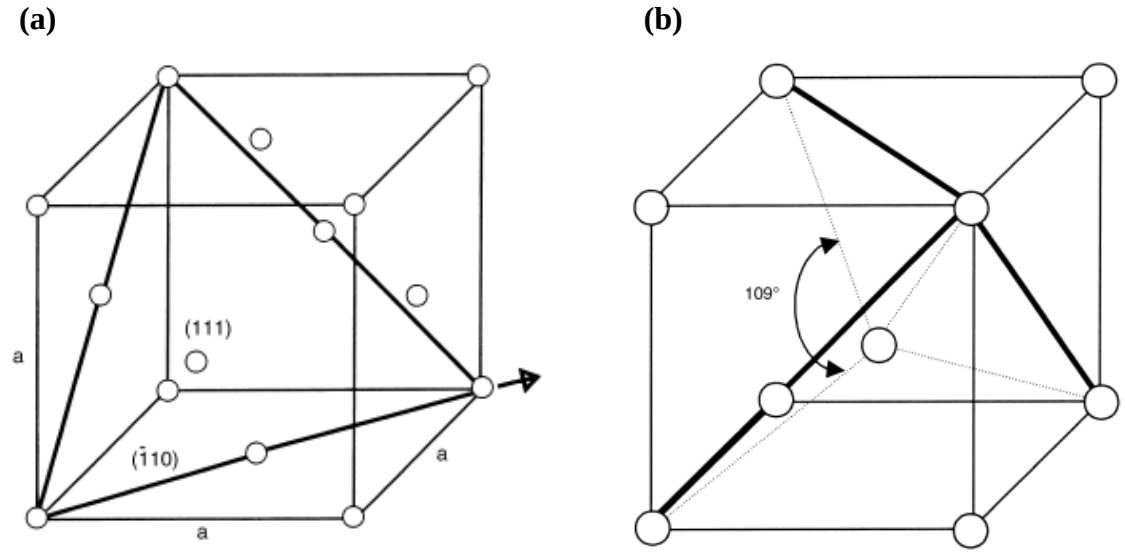

Figure 2.09: Crystal structure of aluminum and silicon[41] (a) Crystalline cell of the Al cubic lattice, (b) Elementary cell of Si the crystalline lattice [40].

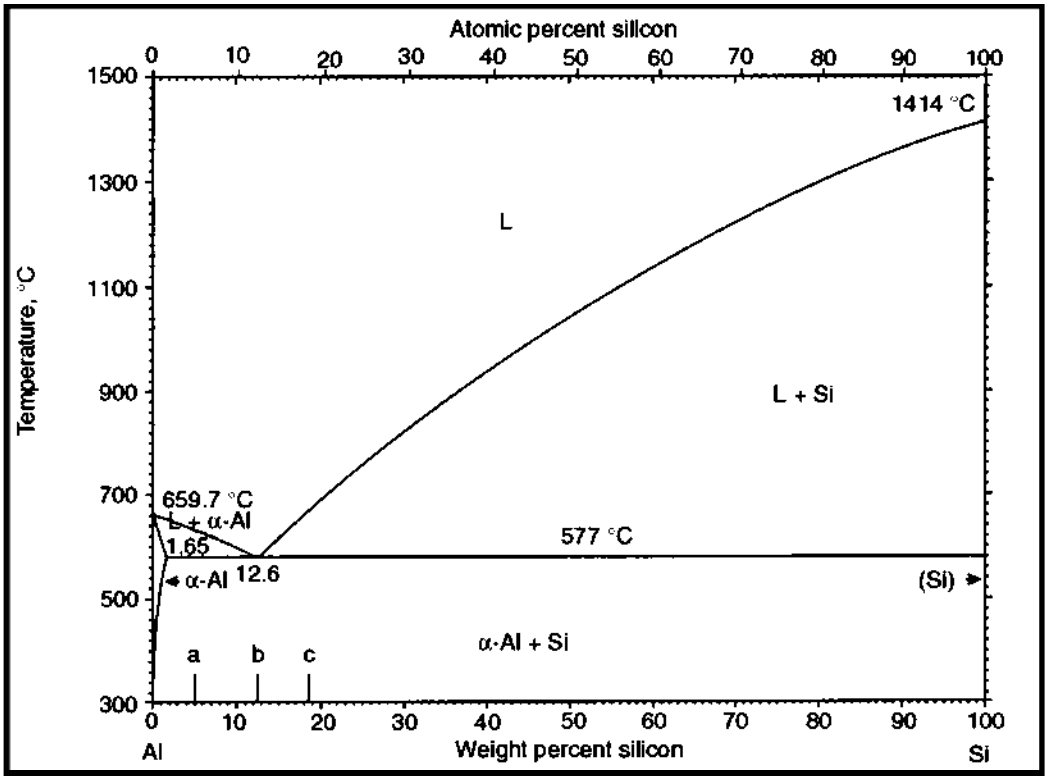

Figure 2.10: Al-Si equilibrium binary phase diagram [40].

The Al-Si alloys have composition close to the Al-Si eutectic point. The eutectic composition is 12.2±0.1 at% Si. The eutectic Al-Si alloys exhibit low melting point (577°C), below the melting point of pure Al, 660°C. The molten alloy exhibits properties such as high fluidity and rapid solidification.

2.3.1 Properties of Aluminium-Silicon alloys

The combination of silicon with aluminium makes the alloys heat treatable. Si increases the fluidity of the melt, reduces the melting temperature, decreases the shrinkage associated with solidification and casting porosity, besides being a low cost a raw material. Al-Si castings exhibit weldability and good resistance to corrosion. The overall weight of the cast component is reduced by the silicon due its low density (2.34 gcm^{-3}). The Si inclusions of the Al-Si alloys can have different morphologies like primary, compact, massive precipitates in hypereutectic alloys or the branched plates of the aluminum-silicon eutectic [42, 43]. In a simple model the microstructure of Al-Si alloys can be presented in the form of a soft continuous matrix (α-Al solid solution) and hard precipitates of silicon of different morphology as shown on the figure 2.11. The microstructure can be refined by rapidly cooling the alloy to increase the strength and ductility.

Several factors control solidification and determine the structural and mechanical properties of the alloys. Among those factors, the composition of the melt, temperature gradient at the liquid–solid interface and solidification velocity are of most importance. As shown in figure 2.12 the decrease in density of Al-Si alloys is almost linearly with respect to Si concentration, the dependence of other properties on solidification conditions being more complex [38].

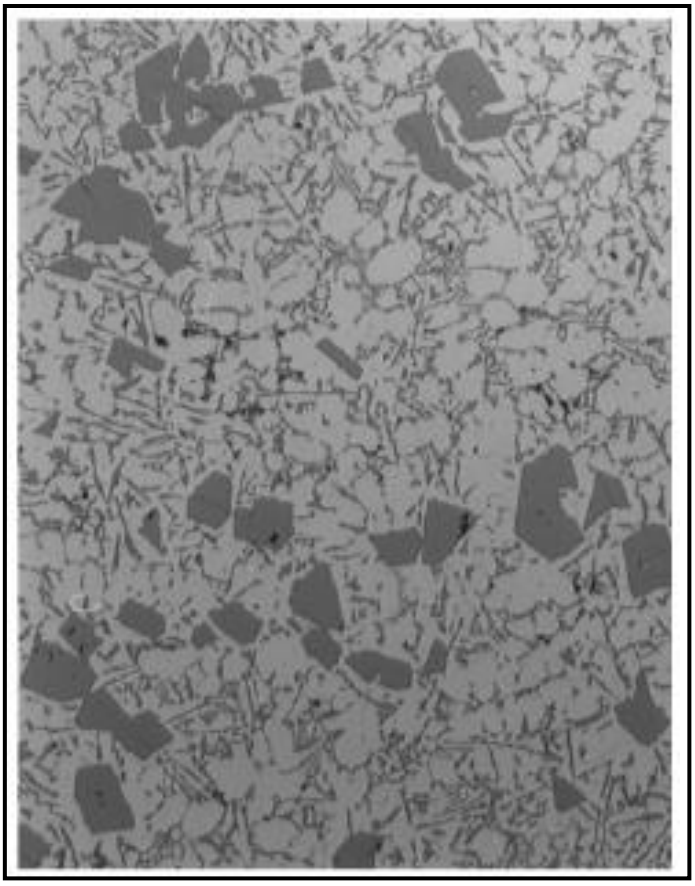

Figure 2.11: Microstructure of a hypereutectic Al-Si alloy [40]

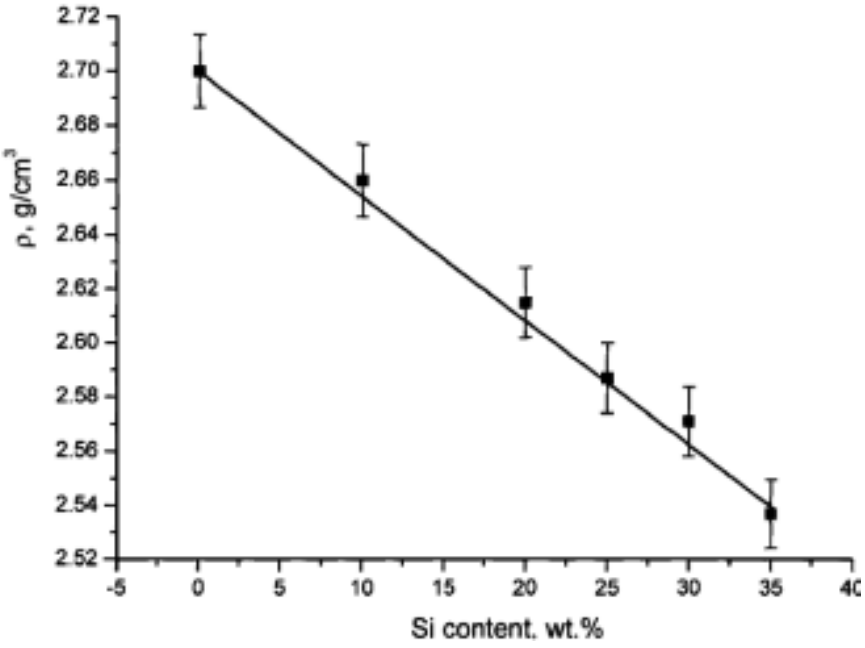

Figure 2.12: Density of Al-Si alloy as a function of Si content in wt% [38]

2.3.2 Mechanical properties of the Al-Si alloys

As for the density, the increase of the Young modulus E of the Al-Si alloy in figure 2.13 is almost linear with respect to the Si content [38]. The increase in Si content may decrease the temperature coefficient of Young modulus because Si raises the covalent contribution to atomic bonding.

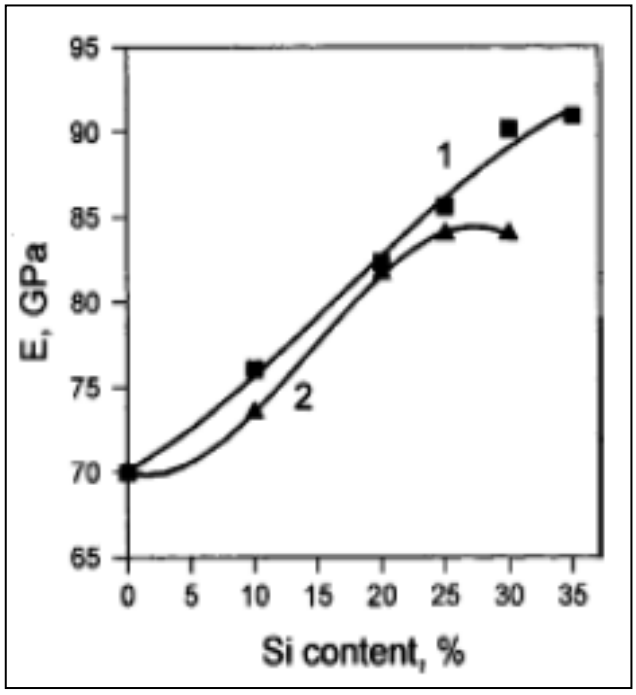

Figure 2.13: Dependence of Young modulus of Al–Si alloys on Si content (1) results of levitated melt [38] and (2) results of conventional casting in mould [44].

In the work of *Nikanorov et al* on the structure and mechanical properties of Al–Si alloys [38] impurities were prevented from contaminating the crucible and the environment, constant superheating and effective mixing of the molten alloy were maintained and solidification occurred with constant and rather high cooling rate. As shown in figure 2.14, uniform heating of the Al-Si alloy to the temperature of 500 ºC and uniform cooling to room temperature, resulted in increments of the Young modulus that are centred at 20 wt% Si composition compared to the values of E of the as cast alloys; the changes of E being attributed to modifications of the microstructure during heating in the heat treatment.

Results reported in the bibliography are not in complete agreement about the effect of Si on $\sigma_{0.2}$ yield stress of the Al-Si alloys[38]. It was observed that the increase in Si content may result in increase in strength of hypoeutectic alloys with the opposite effect on the strength of the hypereutectic alloys. Assuming an important simplification, the average strength of the alloys would be a linear function of the volume fraction of Si in proportion with the increase of density of Si inclusions. In correspondence with changes documented in figure 2.14, the applied load corresponding to the yield point of the Al-Si alloys of the

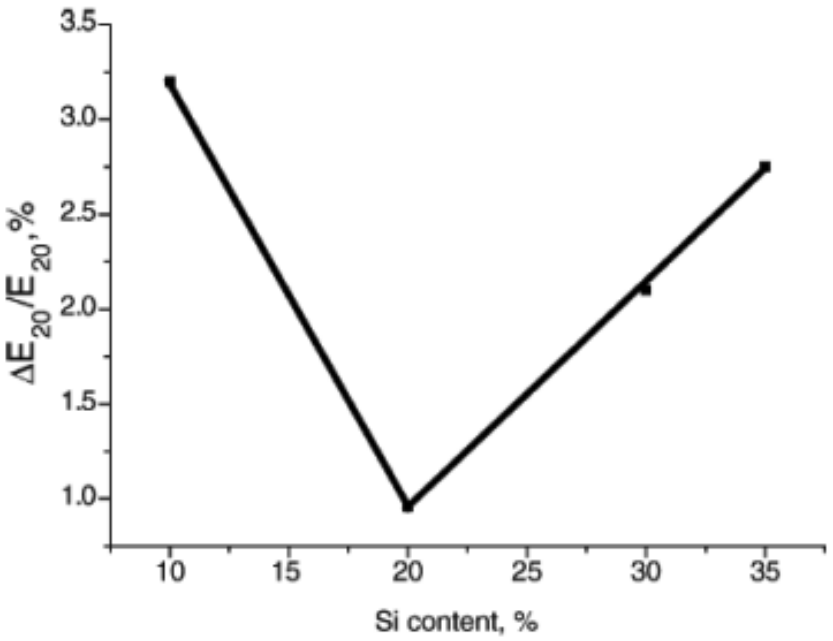

Figure 2.14: Correlations of the change of Young modulus with Si content after heat treatment of the Al-Si alloys to 500 ºC [38].

same study exhibited a maximum at about 20 wt% Si, such maximum value of the yield stress being concentration of Si above that of the eutectic point (11.7 wt% Si). In the cited work the decrease of yield point as the Si content diminishes towards the solid solution limit of α-Al is attributed to decreasing size of the Si inclusions in the eutectic structure balanced by the growing number of plastically deforming dendrites of the α-Al solid solution; while the decreasing of the same property in the hypereutectic alloys above 20 wt% Si is explained by spreading of the interfacial area between primary Si crystals and eutectic structure [38].

2.4 Reactive melt infiltration

Melt infiltration was early proposed as an alternative route to prepare dense ceramic-matrix composites and ceramic-metal composites [45-47]. The possibility that the driving pressure for melt infiltration derived from the capillary forces developed by the wetting liquid in the open pores of the fine grain ceramic matrix may easy overcome the forces of gravity on the melt is a relevant technological advantage[48]. In the absence of reactions between the melt and the porous matrix the rate of melt infiltration is determined by viscous flow dependent on viscosity of the melt, wetting angle and the porosity and morphology of the porous bed, namely the hydraulic pore radius[45]. More often, reactions occur either at the melt-ceramic-gas triple line setting the wetting and fixing the velocity of spreading of the liquid in the pores or they develop afterwards in the spaces filled by the melt with changes in volume fraction and composition of the solid skeleton, alteration of the composition of the melt and modification of the permeability of the bed faced by the advancing reactive melt[1, 49, 50]. By the process of reactive melt infiltration (RMI) near-net shape manufacturing, quick processing times and at low cost can be achieved. The reactants and reaction products are usually of varying density and the overall conservation of mass imposes straining forces related to chemical conversion which can directly influence the infiltration behaviour. As a result the advancing of the infiltration front is affected by fluctuations of the driving pressure coupled to competing driving forces coming from chemical conversion of phases.

In (RMI), the desired shape is first formed by the production of a porous preform of the piece. As a driving force of spontaneous RMI, gravity and capillary forces are used in wetting systems like Si and C. In the non-wetting systems (such aluminium-alumina) applied pressure is needed to force the infiltrate liquid into the porous preform. The commercial production of reinforced Al, Zn, Cu based alloys and Mg is usually done by pressure assisted melt infiltration [51]. Near net shape processing of materials that have little or no machinability, conservation of integrity of the preforms in non-reacting systems, efficiency in time and lower material costs are the major advantages of the several variant methods melt infiltration. The need of post-process machining is limited in RMI making this process particularly attractive for the manufacturing of brittle and hard ceramic-matrix composites[27, 37].

2.4.1 Melt infiltration controlled by viscous flow

Infiltration processes governed by viscous flow are generally ruled by Darcy´s law [52] that gives the velocity of the permeating incompressible fluid (liquid metal, water) per unit area, or the volumetric flux, as

$$v_o = -\frac{K}{\mu}(\nabla p - d_m\, g) \qquad \text{Eq. (2.01)}$$

where υ_o is the superficial velocity of the fluid (the infiltrate, liquid metal), μ its viscosity, d_m its density, K the symmetric tensor of permeability of the porous medium, ∇p the gradient of pressure acting on the fluid, g the acceleration of gravity. Neglecting the effect of gravity compared to the driving pressure from the curvature of the meniscus of the wetting fluid inside open pores with diameters of few microns or even smaller and invoking continuity, the pore velocity or velocity that the fluid presents inside pores is faster than υ_o and it is given as:

$$v = \frac{-K\,\nabla p}{\mu\,(1-V_s)} \qquad \text{……Eq. (2.02)}$$

where V_s is the solid volume fraction or relative density (ρ) of the preform, and 1 - V_s = P is the porosity fraction of the porous bed.

Several models and correlations were made available to set the relationship between the permeability coefficient of Darcy´s equation, K, and particle size and morphology of the porous bed. The Blake-Kozeny equation is one of the simplest and most widely used approaches for the permeability of an isotropic porous medium:

$$K = \frac{(1-V_s)^3}{4.2\,S_0^2\,V_s^2} \qquad \text{……Eq. (2.03)}$$

where the factor 4.2 accounts for the tortuosity of the open porosity and S_o is the specific surface area per unit of volume of the solids which is related to equivalent spherical diameter of the loose particles in the porous bed, D_s, as,

$$S_w\, d_s = S_0 = \frac{6}{D_s} \qquad \text{……..Eq. (2.04)}$$

S_w being the mass specific surface area of the powder.

The powder bed is not a regular system of capillaries of equal radius. Out of several methods proposed to define the average pore radius r_p or equivalent cylindrical pore radius of the open porosity in the porous bed of loose particles, the following equation of r_p due to Carman is in frequent use [53]:

$$r_p \approx \frac{(1 - V_s)}{S_w d_s V_s} \qquad \text{.....Eq. (2.05)}$$

where V_s, d_s and S_w were defined above.

For nonreactive wetting, the contact angle of the infiltrate on the preform must remain constant thus fixing the value of the capillary forces. Capillary forces drive the whole process of spontaneous, pressure-less infiltration. The overall infiltration kinetics is calculated by using slug-flow assumption. When the pressure gradient in Eqs. (2.01 and 2.02) is approximated by the difference of pressure at the advancing interface of the fluid and the pressure at the entrance divided by the length of the infiltrated layer, the squared length becomes proportional to the time of infiltration.

The permeability, K, in Darcy´s law, equations (2.01 and 2.02), is a complex function of time and position in reactive systems such as the RMI systems, because the pore space filled in by the melt changes size, shape and volume fraction when reactions occur. The sum of the applied pressure, of the internal pressure of entrapped gas phases and the integral of the capillary pressure in the system yields the effective pressure noted as p in the Darcy´s law.

Brusque changes in the flow of the infiltrate due to constrictions in pore geometry or roughness of pore surfaces are known as Haines jumps. Due to Haines jumps hysteresis is observed between the imbibition and drainage of a porous medium, a difference of energy being involved in an irreversible way [54]. Even if there are no chemical reactions between infiltrate and preform, Haines jumps would disturb the local velocity of the infiltrate and lead to a rough melt-gas interface at the forefront of the advancing melt inside the porous preform which may cause isolation of volumes missing the infiltration process. If the

isolated volumes become close they will retain gas from the furnace atmosphere. The internal pressure of the entrapped gases in the closed volume will resist filling by the melt under the driving pressure of capillary forces.

This kind of process will also complicate the chemical interactions between the liquid and solid phases when active as in the RMI. The spontaneous infiltration of the Al-Si alloy in B_4C preforms is like a wicking action; hence it is relatively important to address the subjects of wetting and capillary phenomenon which is the objective of the following two subsections.

2.4.2 Wetting Phenomena

Wettability describes ability of a liquid to spread on a solid surface. This usually represents the extent of intimate contact between a liquid and a solid. Al alloys exhibit poor wettability of ceramics. This is due to the presence of contamination, moisture or a adsorbed gas layer covering the ceramic surface, or the Al_2O_3 layer that coats liquid Al and/or to the native SiO_2 layer that ordinarily covers SiC particles[55].

The infiltration of the liquid into the porous bed depends on the degree at which the liquid wets the solid. Most often as given in literature sources wettability is determined by using the sessile drop method. In this method a droplet of liquid, said probe liquid with a known specific surface energy is placed on the surface of a solid and the contact angle of the drop is measured, the specific surface energy of the solid being determined from the values of the contact angle and liquid specific surface energy of a set of several probe liquids. The results are given in terms of the contact angle θ shown in figure 2.15**,** where if $\theta < 90°$ the liquid wets the solid. The surface tension or specific surface energies γof the three interfaces are related to the contact angle through Young's equation [56]:

$$\gamma_{sv} = \gamma_{sl} + \gamma_{lv}\, cos\theta \qquad \text{.....Eq. (2.06)}$$

where θ is the contact angle and the subscripts in the specific surface energy γ_{lv}, γ_{sv}, and γ_{sl} refer to the liquid-vapour, solid-vapour, and solid-liquid interface, respectively.

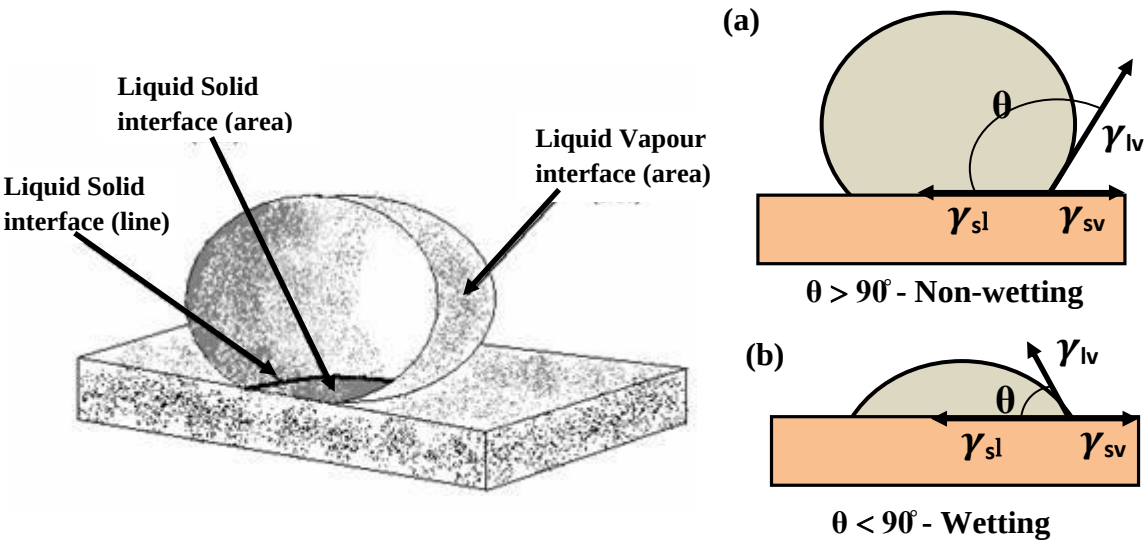

Figure 2.15: The dependence of the shapes of partially wetting liquid droplets on the equilibrium of surface tension in accordance with Young's equation[57]: (a) Poor wetting, and (b) Wetting.

Figure 2.15 describes the force balance derived from the Eq 2.06 omitting the force of gravity which was later derived from Gibbs energy balance [58]. A necessary assumption was made that in both wetting and non-wetting the three phases (solid, liquid and vapour) are in chemical equilibrium. To determine the length scale at which the force of gravity can be neglected, the magnitude of the gravitational and the liquid-vapour interfacial energies can be equated to define the capillary length, L_{Cap} [59].

$$L_{\text{Cap}} = \sqrt{\frac{2\gamma_{\text{lv}}}{d_m\, g}} \qquad \text{.....Eq. (2.07)}$$

where γ_{lv}, d_m and g were defined above.

2.4.3 Capillary Phenomena

Accordingly to the Young-Laplace the γ_{lv} surface tension yields a pressure difference across the curved liquid-vapour interface given as[60]**:**

$$\Delta p = \gamma_{lv} \left[\frac{1}{R_1} + \frac{1}{R_2}\right] \quad \text{Eq (2.08)}$$

where R_1, and R_2 are the principal radii of curvature of the curved interface as shown in figure 2.16.

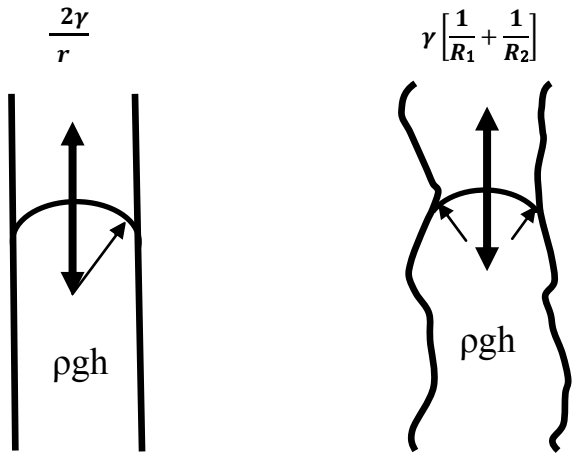

Figure 2.16: Capillary pressure across a curved interface with surface tension γ [59, 61].

Meniscus effects are considered important in the systems of capillary flow into packed beds. From the Young-Laplace equation 2.08 it is clearly shown that the smaller the radius of the capillary higher the capillary pressure driving the infiltration (in wetting systems). But, for a distribution of capillary radii the driving pressure on the fluid will be higher in smaller capillaries. Moreover, when analysing the meniscus curvature, differences also arise from the irregularity of the capillary shapes. Wherever the particles developed these small angularities in their rough surfaces, a large rise of curvature occurs shown by the edges of meniscus, which is called as meniscus effect, explained by equation 2.08, in terms of the pressure increase due to the increased curvature of the interface, as indicated. Hence, as the difference in pressure is higher there is a larger driving force for capillary flow resulting in these narrower regions being filled faster (in a wetting system).

2.4.4 Reactive infiltration of intermetallics and composites

The techniques used and the major problems in wetting of graphite surface and the ceramic surfaces during the reactive infiltration processes are discussed in this section with the aid of some experimental works related to Al, Si and B_4C. In order to produce stainless steel fibre reinforced aluminium matrix composites, *Colin et al* used the squeeze casting technique. However, they have found that the complex interactions and reactions during solidification cause significant problems in achieving non-reacted samples [62].

Production of titanium aluminide composites in situ by infiltrating titanium oxide preforms with aluminium was done by squeeze casting by *Fukunaga et al.* Alumino thermal reduction occurred in parallel with infiltration. The flow of the liquid aluminium is restricted by the formation of the solid reaction layer that constricted the channels for advancing of the liquid metal. The effect is named as reaction choking, which is also observed for capillary driven reactive infiltration of carbon by silicon [63].

When considering the potential chemical reactions between the Si and Al elements and the B_4C powder of the preforms there are four reactions that can yield the SiC phase, alone or in combination with ternary carbides and boron-carbides. The direct reaction of liquid Si with C (mostly graphite in B_4C powders):

$$Si + C \rightarrow SiC \qquad \text{.....Eq. (2.09)}$$

at melt infiltration temperatures yields the rhombohedral 15R SiC phase[27].The simultaneous reaction of B_4C with the Al and Si also produces SiC as given by the following reactions:

$$12B_4C + 10Si + 3Al \rightarrow Al_3B_{48}C_2 + 10SiC \qquad \text{.....Eq. (2.10)}$$

$$3B_4C + Si + 3Al \rightarrow Al_3B_{12}C_2 + SiC \qquad \text{.....Eq. (2.11)}$$

Besides the reactions 2.09 to 2.12 above, the reaction Si of with B_4C may also deliver the siliconised $B_{12.97}Si_{0.03}C_2$ phase, equation 2.12, whereas B_4C may decompose into the high B and low B sub-carbides, equation 2.13 [12]:

$$4B_4C + 1.03Si \rightarrow B_{12.97}Si_{0.03}C_2 + SiC + B_3C \quad \text{.....Eq. (2.12)}$$

$$4B_4C \rightarrow B_{13}C_2 + B_3C_2 \quad \text{.....Eq. (2.13)}$$

The temperature dependence of the wetting angles of aluminium and its alloys on graphite substrates determined by the sessile drop method was investigated by *Pastukhov et al* [64], the results for the Al-Si alloy being given in figure 2.17. They found that formation of aluminium carbide took place after heating the aluminium drop at 1200 ºC which spreads on the graphite with a wetting angle 38º after 13 minutes. Between 1100 ºC and 1200 ºC the adhesion of Al to graphite increases from 0.15 J/m^2 up to 1.52 J/m^2. In their experiments the wetting angles of Al on graphite reduced to 85º after 5 minutes at 1200 ºC. Foaming of the metal drop begins resulting in an increase in volume due to carbide formation, where the drop moves from the liquid state to a mixed liquid/solid state [64].

Increased temperature above 1200 ºC resulted in greater distortion of the drop, leading to spread of the liquid aluminium with the formation of a thin coating on the graphite substrate surface and inflows on the metallic surface of the drop. The drop presented the Al_4C_3 phase. Two carbon modifications and one unidentified phase were determined by the x-ray diffraction.

Better understanding of the wetting properties was gained from the study of wetting and adhesion of several non-reactive silicon-ceramic systems. It was shown that when band energy of the solid decreases, the work of adhesion increases and the contact angle decreases. The existence of these relationships strongly suggests that silicon-ceramic interface is formed which is associated with the creation of chemical bonds at the interface, caused by the charge transfer between silicon and the ceramic[65].

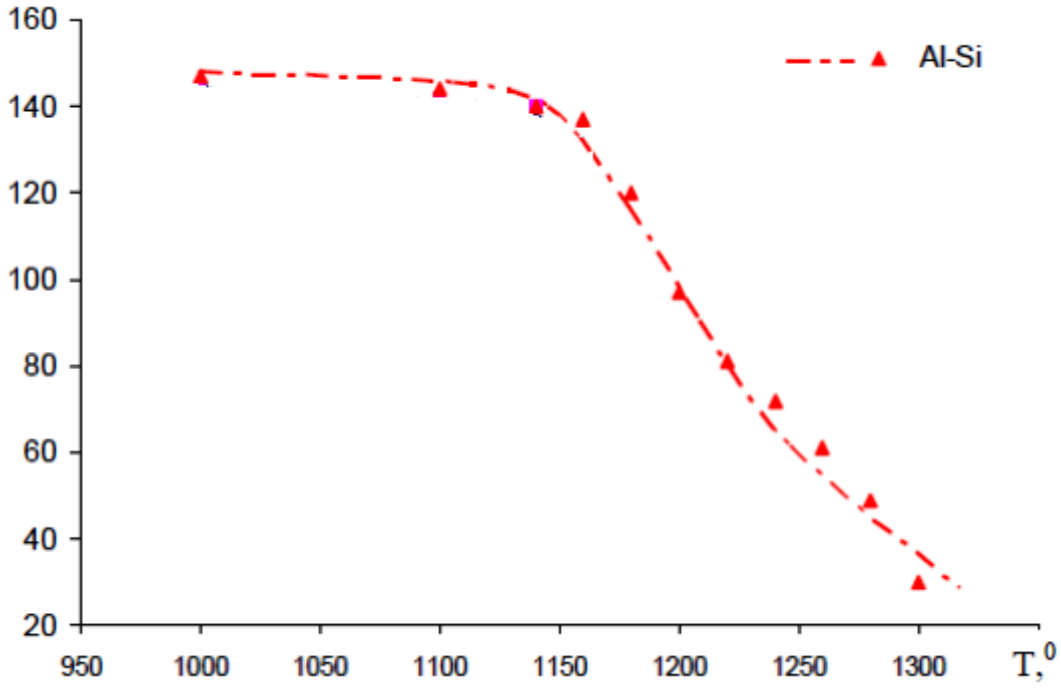

Figure 2.17: Dependence of the wetting angle on temperature in graphite wetting by the Al-Si melts [64]

The wetting of ceramic materials by liquid silicon, aluminium and metallic melts was reviewed by *Jian-Guo Li* and he concluded that wetting in metal/ceramic systems is complex and depends strongly on the development of chemical reactions at the metal-ceramic interfaces[55]. In the few of experimental results related to reactive infiltration processes of B_4C by Al, Si in the study of *Hayun et al* the presence of Al in the B_4C–Si system significantly enhances the transformation of the initial B_4C particles into a newly formed quaternary carbide phase and the kinetics of the rim-region growth. This work was conducted in the presence of alumina parts inside the graphite furnace. It was the source of Al in the composites fabricated by infiltration of porous boron carbide preforms with liquid Si at 1753K under vacuum condition [49].

Toptan et al reported poor wetting of B_4C particles by liquid aluminium. The effective bonding could not be formed at the matrix/reinforcement interface in Al-B_4C composites produced at the relatively lower temperature of 850°C. The poor wetting issue was effectively solved by allowing for the formation of 80-180 nm thin reaction layers of TiB2 and TiC by adding the K_2TiF_6 flux [50]. *Wu et al* [1] stated that during the preparation of

multi-carbides/(Al, Si) composites by infiltrating porous B_4C and B_4C/C preforms with several hypereutectic Al–Si alloys in the temperature range of 1200 ºC – 1400 ºC under vacuum, the dense composites showed besides B_4C, SiC, Al and Si the presence of the ternary carbides $AlB_{12}C_2$, $Al_3B_{48}C_2$. It was also reported that the added C remained partially unreacted in the composites and lowered the flexural strength. Ductile tearing of the Al phase and partial de-bonding of Al/carbide interfaces favoured the fracture toughness of the composites [1].

2.5. Ternary phase diagrams with boron carbide

Three dimensional representations of the equilibrium relations between three components of a ternary system are known as ternary phase diagrams in which the composition of phases is considered along the sides of the basal triangle and temperature is plotted along the vertically axis. Surfaces delimit volumes of coexistence of phases in equilibrium in accordance with the Gibbs phase rule. Contours representing lines of constant temperature on surfaces are known as isotherms. The boundary curves of the ternary phase diagrams, drawn as lines in ternary systems are the homologous of eutectic points of the binary systems and any composition on one of these curves will crystallize the two phases of the solidification fields on either side of the curve[66].

Borides keep an important place in many ternary, quaternary and higher order systems [12]. Of high melting point and stiff, boron itself has a significant role in technology as a single component material. Its flexibility to enter in the preparation of tailor made solid solutions and composites provide room for attaining optimised properties of the materials. Boron is also useful as a sintering aid of covalent bonded compounds of high melting point. A number of systematic studies and investigations on the characteristics of chemical bonding in multi-component phases and ternary diagrams have been stated in the recent times[12]. When elemental boron and carbon are combined with aluminium they become the appropriate sintering aids to attain high densification of the B_4C and SiC ceramics. The phase relationships pointed out by the B-C-Al-Si quaternary system lead to the appropriate procedures to identify the composition of transient liquid phases that improved transient

liquid sintering of the refractory solids. Moreover, molten Al wets and spreads on B_4C surfaces and may be used to infiltrate the B_4C porous bodies and acting as a reinforcing phase [8, 12].

2.5.1 Al-B-C ternary system

The volume of experimental data on the Al-B-C ternary equilibrium system is limited[67]. Six ternary phases, $B_{40}A1C_4$, $B_{48}Al_{12}C$, $B_{51}A1_2C$, orthorhombic $B_{48}Al_3C_8$, hexagonal BAl_3C_3 (also labelled as $B_4Al_8C_7$) and the orthorhombic B_4A1_8C may be found in this system however their ranges of temperature stability are generally unknown. The range of solubility of the ternary solid solution $B_{12}(B,C,Al)_3$ was determined by *Lukas* et al who

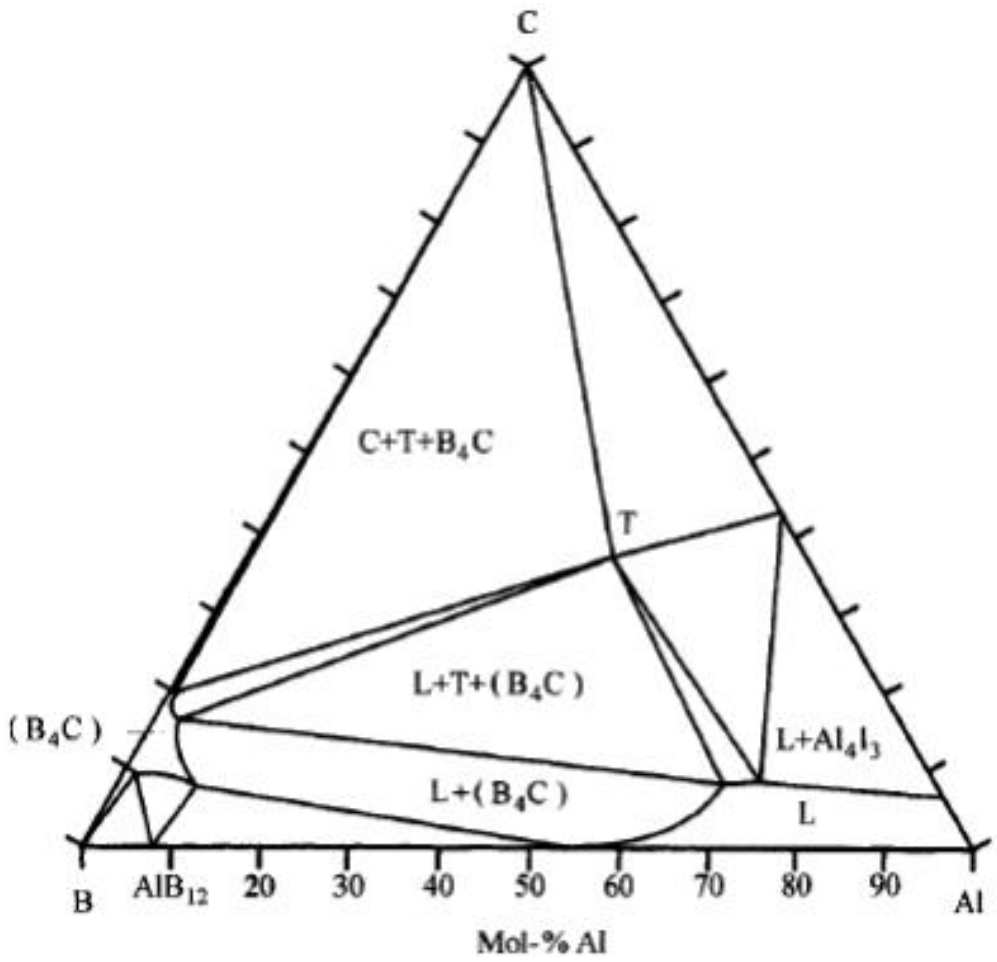

Figure 2.18: B - Al - C ternary phase diagram at 1400 ºC [5]

have calculated an isothermal section of the ternary system with the $B_{12}(B,C,Al)_3$ in equilibrium with a boron-rich Al melt at above 1000°C, by omitting all boron-rich ternary phases except the T ($B_4Al_8C_7$) phase given on figure 2.18 [5, 67].

2.5.2 B-C-Si ternary system

The isothermal section at 1727℃ of the Si - B - C ternary phase diagram is shown in figure 2.19 [68]. *Kieffer et al* did the initial experimental study of the B-C-Si ternary phase diagram and reported the equilibrium between B_4C, SiB_6 and SiC phases up to temperatures exceeding 1900 °C [69]. The thermodynamic calculations of *Telle* confirmed the existence of a binary phase equilibrium between B_4C, Si and the Si and B containing melt above 1560 °C; the study also rendered in detail the extension of the homogeneity field of B_4C towards the Si-rich corner of the system B-C-Si [17]. Deviations on the B-Si system in the view of past and more recent experiments and theoretical calculations arose especially from the less reliable data on equilibrium at the Si rich corner. The problems with the experiments in the ternary phase diagram are related with the high Si vapour pressure above 1400 °C. In a latter study the stability of $B_{12}(B,C,Si)_3$ solid solution of B-C-Si system was found to have the upper limit of 2.5 at% Si [70] which is in equilibrium with a boron-saturated silicon melt [17]. Above 1380 ºC, the formation of the solid solution of $B_{12}(B,C,Si)_3$ is corroborated by the β-SiC precipitates which melts eutectically with SiB_6

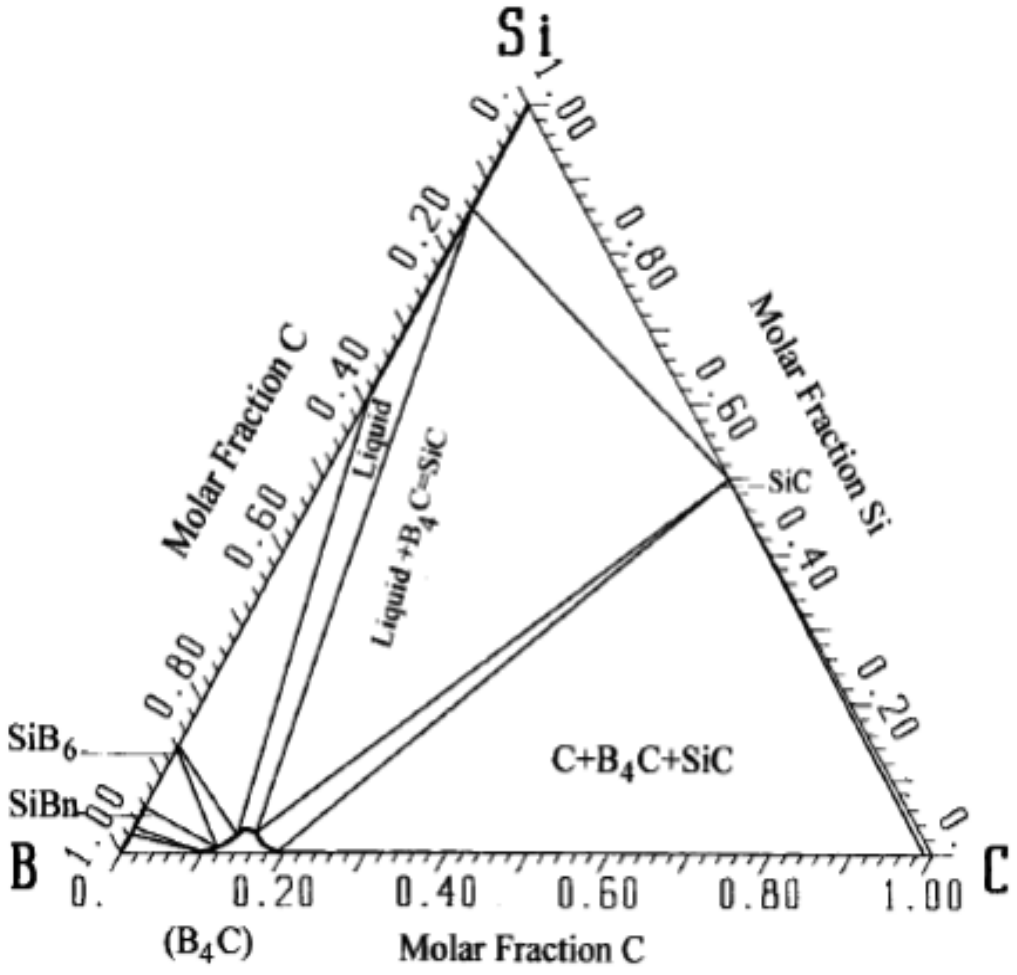

Figure 2.19 Isothermal section at 1727 ºC of the Si - B - C ternary phase diagram [68].

and residual solid Si. It has always been observed either the releasing of C or simultaneous developing of SiC when Si incorporated into the boron provided the Si in excess; this process can be defined as C in $B_{12}(B,C,Si)_3$ being replaced by Si presuming that there is no content of C on interstitial sites of the boron carbide. *Telle et al* confirmed that previous studies provided complete, coherent and reliable data about the maximum solid solubility of B_4C and the peritectic decomposition of the particular silicon borides [12].

3.0 EXPERIMENTAL PROCEDURE

3.1 Preparation of B_4C preforms

3.1.1 B_4C powders

Boron carbide (B_4C) powder with 10 µm average particle size and density of 2.52 g/cm^3 (Electron Microscopy sciences EMS#50510-10, lot #BC80A22#36) was used for preparing the porous preforms. In order to determine the graphite content of this power by X-ray diffraction methods (DRX) a second batch of B_4C powder, with very low free carbon in its composition (Electron Microscopy sciences, EMS#50510-18, lot #BC50A25#08) with 18 µm average particle size was utilized. The two as supplied B_4C powders and mixtures of both in the proportions (25 %, 50 %, 75 %) by weight were prepared and submitted to X-ray diffraction. The mass of 29.2 g of the 10 µm B_4C powder was used in simultaneous thermogravimetric analysis (TG) and differential thermal analysis (DTA) conducted at temperatures up 800 ºC in the air to derive the thermal behavior of the powder, namely the weight loss by combustion of free carbon.

3.1.2 B_4C preform preparation process

The process flow diagram for preparation of B_4C preform is given in figure 3.01. By estimating the relative density of the preform after pressing to be about 50 % [1] it was planned to press the B_4C into cylindrical pellets of 2 cm diameter and 0.75 cm height. The (1 wt% PVA + water) 1 wt% soluble dilute polyvinyl alcohol (PVA) solution in amounts 4.0 wt% to 4.5 wt% of PVA was added to the dry B_4C powder as pressing aid. For the intended porosity of 50 % 2.9673 g of B_4C powder and 0.1187 g of PVA (4 wt%) were taken for each pellet, as per the calculation given in the following.

$$\text{Porosity, } P = 1 - \frac{d_{gb}}{d_s} \qquad \text{…….. Eq. (3.01)}$$

$$m = d_s \times v_s \qquad \text{..... Eq. (3.02)}$$

= 1.26 g/cm^3 (50% dense B_4C) x 2.355 cm^3 (for 2 cm diameter and 0.75 cm height)

where m is mass, v_s the volume of the solid phase, d_s the density of the solid (as B_4C), d_{gb} the apparent density of the green body.

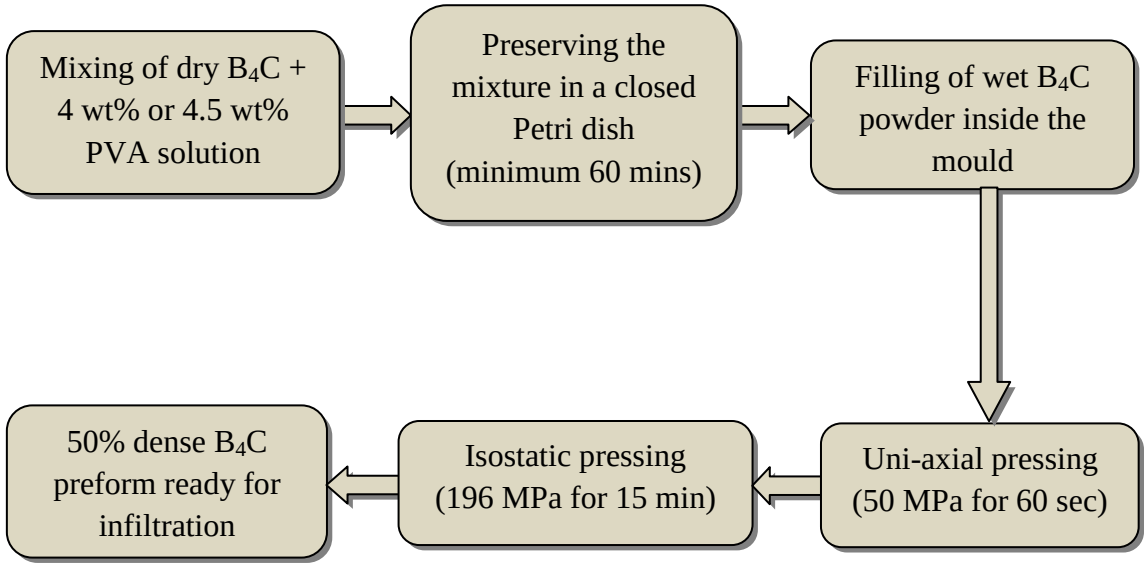

Figure 3.01: Flow diagram of B_4C preform preparation process

Table 3.01: Mass calculation for the preparation of a 50% porous green pellet, of the Al-Si alloy and mass of alloy needed for melt infiltration.

NOMINAL MASS CALCULATION								
Mass of the greenbody (B_4C+PVA)			**Mass of the elements required for fusion of Al-Si**			**Mass of the alloy required for infiltration**		
Diluted PVA solution (1% solubility)	PVA solution g	Nominal mass = B_4C +PVA solution g		Al g	Si g	Theoritical density of alloy g/cm^3	102% Volume of the alloy cm^3	Nominal mass of the alloy g
4 wt% PVA	0.119	3.086	Al-25 wt% Si	9.000	3.000	2.597	2.452	6.366
5 wt% PVA	0.148	3.116	Al-35 wt% Si	7.800	4.200	2.557	2.452	6.270

Note : Mass of 50% dense B_4Cgreen body = 2.9673g (for a 2cm diameter and 0.75cm height sample)

The dry B_4C powder was added to polyvinyl alcohol (PVA) about 4.0% to 4.5 wt.% of the B_4C. The 1% concentrated PVA solution was mixed well with the fine particles of the B_4C powder. Shaking of this mixture with a spatula provided good blending of the loose particles. They became clustered together and spontaneously granulated into of approximately spherical shapes of sizes,

Figure 3.02: Granulated mixture of B_4C powder and PVA solution

ranging from 0.1 mm to 10 mm, shown in figure 3.02. The soft granulates were collected and preserved in closed Petri dishes from one to several hours; this length of time improved the distribution of humidity inside the agglomerates and the bonding of the particles.

On the completion of this stage, granulates of B_4C were crushed by gentle hand pressing using a rubber bob and weighted with a balance. The correct weighted amount of the material was filled into the steel mould for uniaxial pressing as shown in the figure 3.03. A uniaxial load of 50 MPa was applied (Carver Laboratory Press, uniaxial pressing with the capacity of 5 tons) for the duration of 1 minute in order to achieve the high densification without delamination of the pressed pellets. The bulk density of the as-pressed cylindrical pellets of B_4C was determined by the measurements of pellet volume and mass, the pressed samples being preserved in closed Petri dishes.

In the next step the isostatic pressing was conducted without delay in order to avoid breaking the prepared pellets due to drying. The B_4C pellets were put inside elastic rubber sleeves. The sleeves were evacuated and sealed with a knot. These B_4C pellets protected by liquid tight sleeves were inserted in the chamber of the cold isostatic press, (Autoclave Engineers, Penna USA) and a pressure of 2000 kgf/cm^2 was applied for 15 minutes at room temperature.

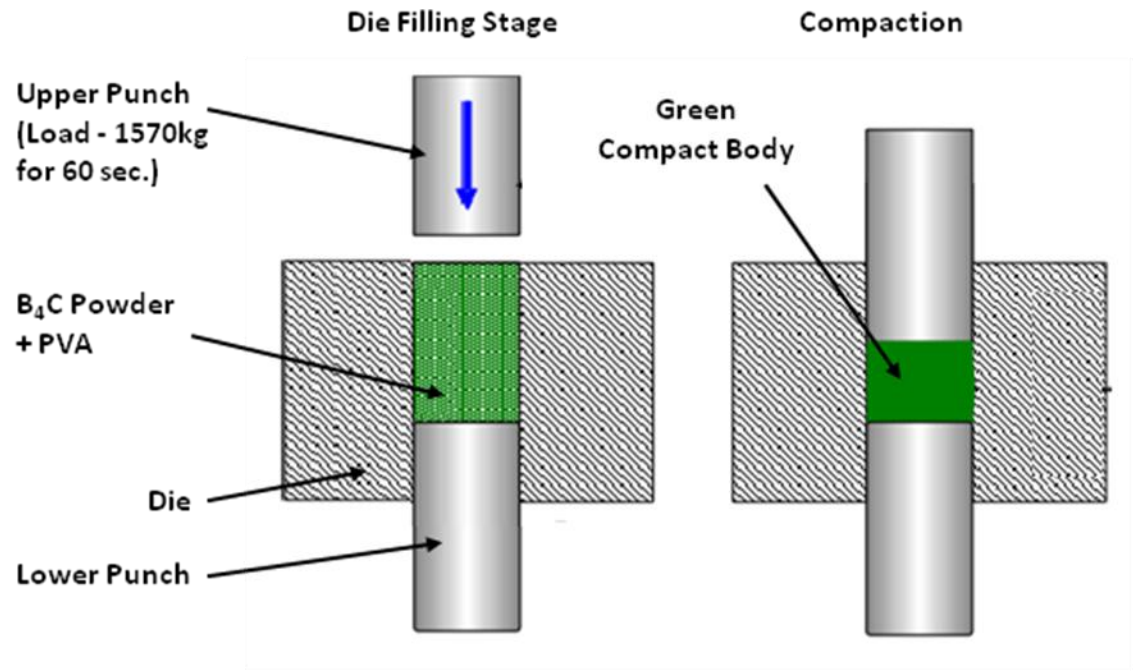

Figure 3.03: Uniaxial pressing of as prepared the B_4C powder with addition of PVA.

Those isostatically pressed B_4C preforms were taken out of the rubber sleeves and their density determined again from measurements of their mass and volume. A desiccator was used to store the B_4C preforms.

3.2. Preparation and melting of the Aluminium-Silicon alloys

Powders of aluminium (2.7 g/cm^3), atomic weight 26.98 g/mol, with 99.7% of purity (ABCR GmpH & Co., CAS# 7429-90-5, lot# 143946-11), and of silicon (2.329 g/cm^3) atomic weight 28.09 g/mol, 99% pure (Emerk, Germany - 12497.0250, 201N628697) were used for preparing the Al-Si alloys, as represented in the process flow diagram given in figure 3.04.

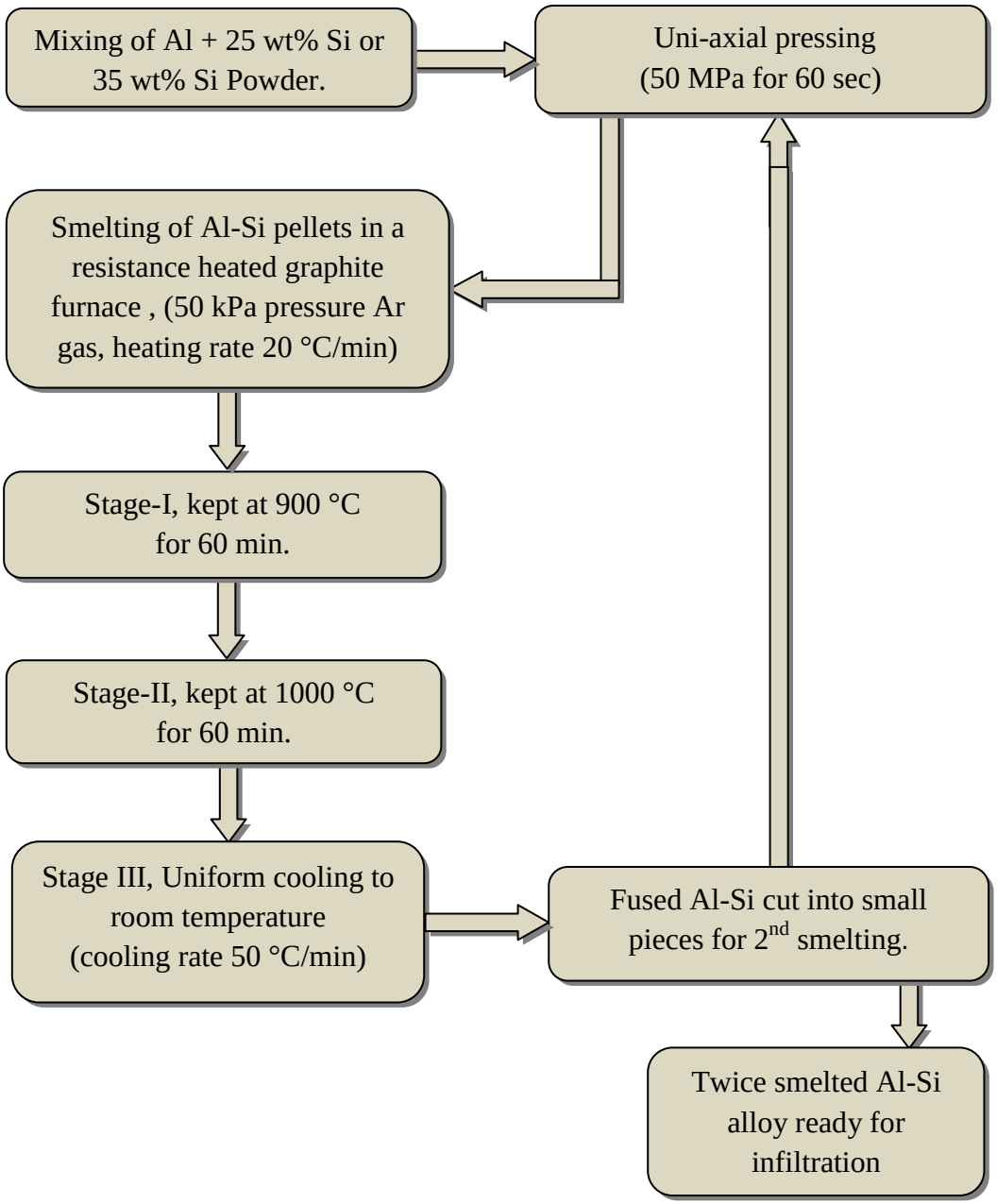

Figure 3.04: Process flow diagram of fusion Al-Si alloys

Silicon in weighted amounts of 25 wt% or 35 wt% of total and was added to the aluminum powder. The calculation of the mass of the elements was given in table 3.01, above. The mixture of the powders was shaken inside a closed container for improved homogeneity. Cylindrical pellets of the due Al-Si composition with diameter 2 cm x 2.2 cm height (approximately 12 g) were uniaxially pressed under the pressure of 50 MPa for 60 seconds. A total of five smelting batches were prepared, one with Al-35 wt% Si proportion and the remaining ones in the Al-25 wt% Si proportion. The first three fusion batches were single smelted and the last two batches were smelted twice for achieving improved homogeneity of the alloy. Three or four cylindrical pellets (each 12 g) were picked for each fused batch of the Al-Si alloy. Smelting was accomplished in a resistance heated graphite furnace (Thermal Technology Inc.,) the hot chamber being constructed from a graphite crucible. The cylindrical pellets were placed inside an alumina crucible, covered on top by an alumina cap as shown in figure 3.05. The loaded crucible was positioned in the hot zone of the graphite furnace on a graphite base.

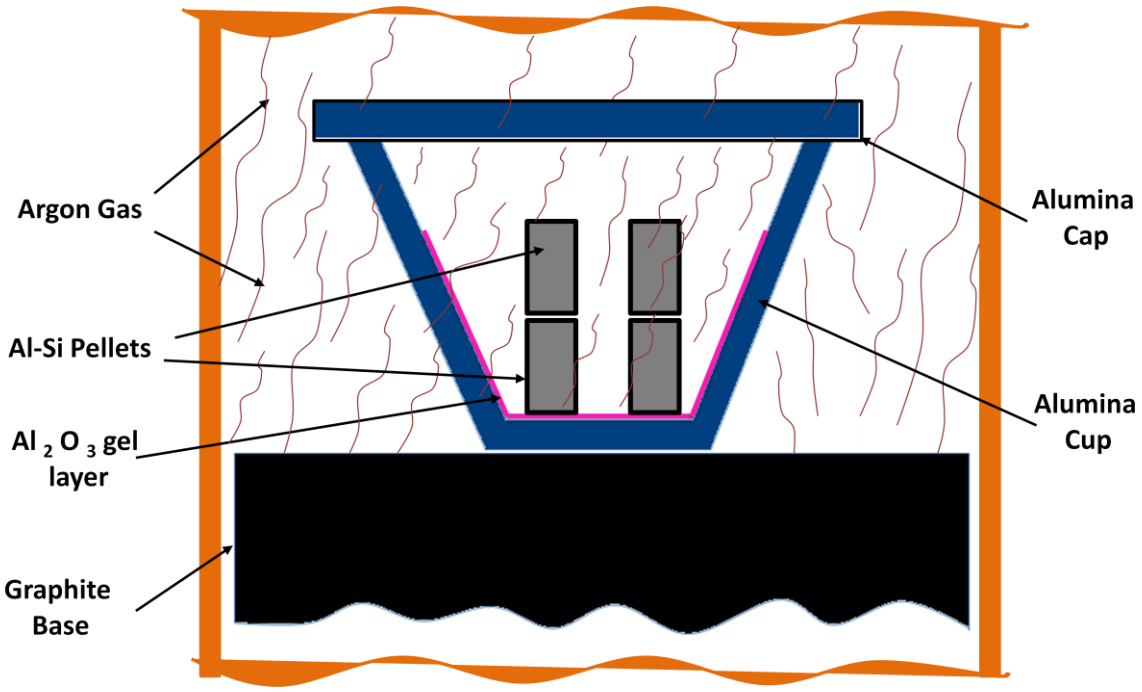

Figure 3.05: Apparatus inside the resistance furnace chamber for fusion of Al-Si alloys

The furnace chamber was flushed with argon gas after evacuation using a rotary pump, the cycle being successively reaped three times. The furnace chamber was then filled with flowing Ar gas (with an overpressure of 50 kPa pressure above atmospheric pressure). The inert atmosphere must protect the metallic melts from oxidation.

The heating cycle, temperature holdings and cooling cycle in the fusion process of the Al-Si alloys are represented in figure 3.06. On stage I, the furnace is started and the temperature risen at 20 °C/min heating rate to 900 °C with an hold of 60 minutes for premixing of the smelted alloy. On stage II, the temperature was further increased to 1000 °C with the same heating rate with a final temperature hold of 60 minutes for better homogeneity of the melt. Controlled cooling of the melt in the furnace, stage III is done with a constant cooling rate of 50 °C/min.

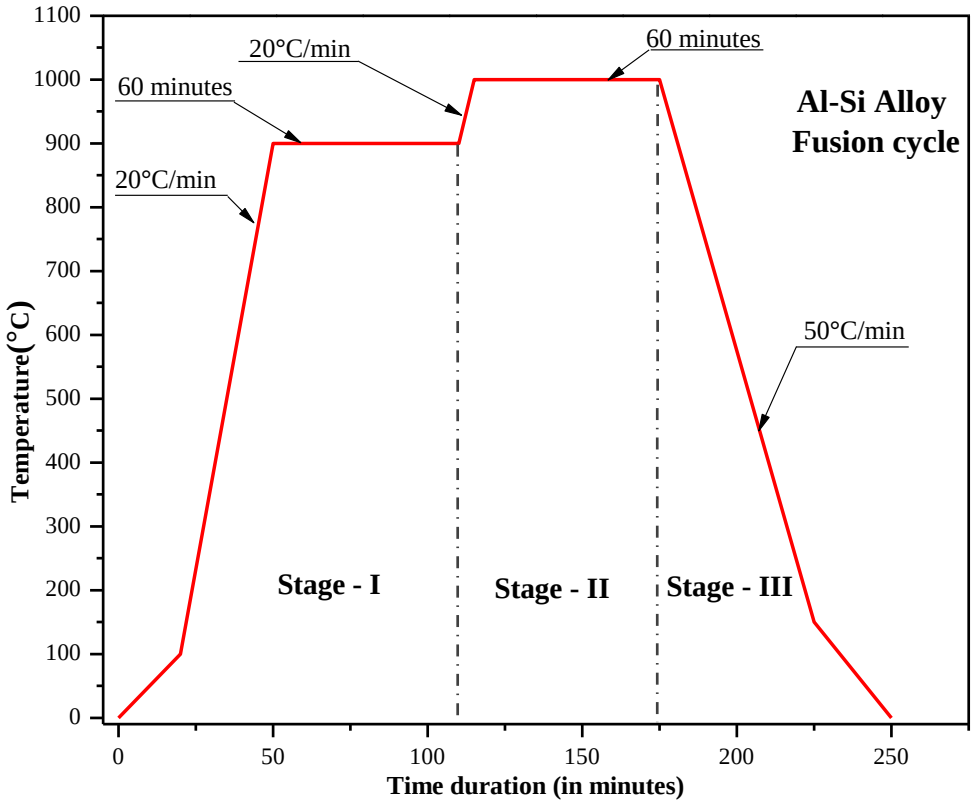

Figure 3.06: Heating cycle, temperature holdings and cooling cycle in the fusion of Al-Si alloys.

After removal of the fused product out from the furnace, the alloy was cleaned, cut into small pieces by using a cutting machine or a hand hacksaw. For the twice smelted Al-Si alloy, the cut bits were put together inside the alumina crucible, the crucible loaded into the graphite furnace for the second smelting run under identical conditions as already described for the first smelting run.

3.3. Melt infiltration process

After the smelting, the prepared Al-Si alloy was cleaned and sliced into very small pieces, and collected in a cylindrical mold for making as cylindrical pellets by applying the uniform uniaxial load about 50 MPa for 60 seconds. Flow diagram of the complete melt infiltration process is given in figure 3.07.

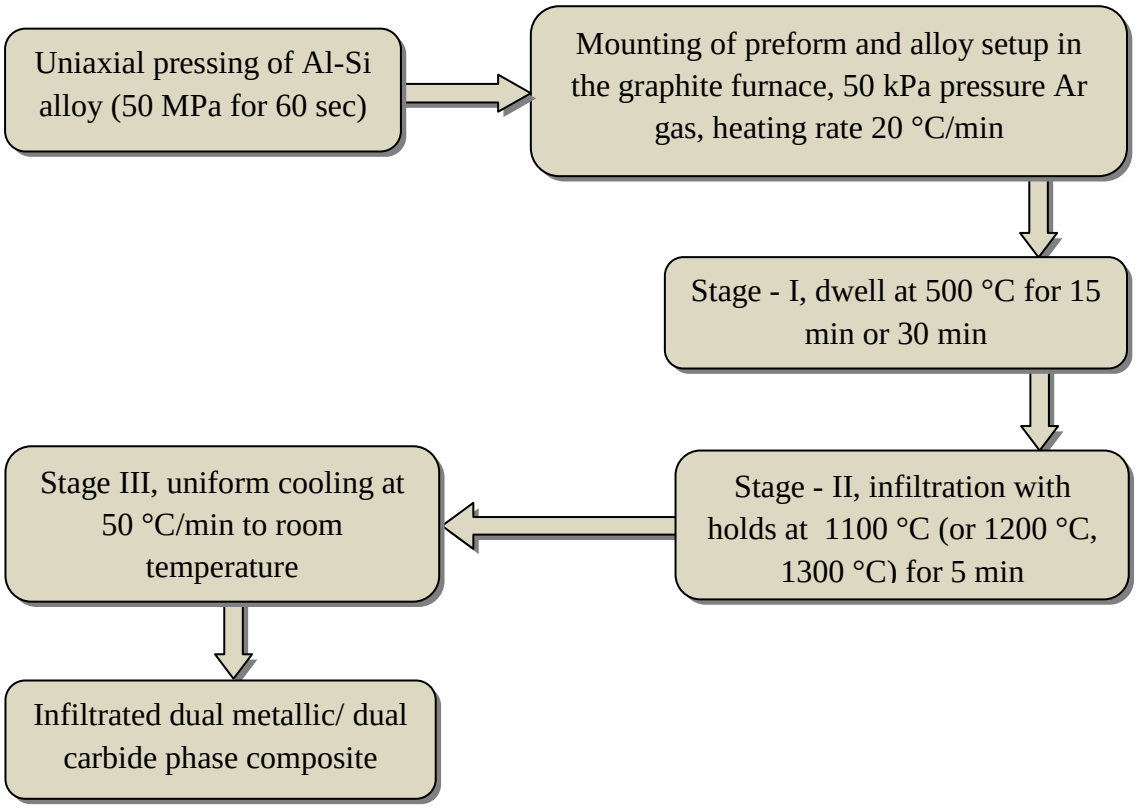

Figure 3.07: Flow diagram of the melt infiltration process

Minimum of 102% to 110% in excess of the pore volume of the preform was used to infiltrate the 50% porous B_4C preform. The model mass calculation is given in table 3.01, accordingly to the following equations, for a 25 wt% Si alloy:

$$d_{75\%Al-25\%Si} = \frac{d_{Al} \text{ x } d_{Si}}{75\%\, d_{Si} + 25\%\, d_{Al}} \quad \text{..... Eq. (3.03)}$$

$$v_{Al-Si} = 102\% \text{ x } v_p \quad \text{..... Eq. (3.04)}$$

$$m_{Al-Si} = d_{Al-si} \text{ x } v_{Al-Si} \quad \text{..... Eq. (3.05)}$$

where d_{Al} is density of aluminium, d_{Si} density of silicon, υ_{Al} volume of aluminium, υ_{Si} volume of silicon, υ_p volume of pores and m_{Al} mass of aluminium and m_{Si} mass of silicon.

Round plates of alumina of ~25 mm diameter were coated with a thin layer of an alumina slurry and used as bases for the pressed B_4C pellets, as shown in figure 3.08. The pellets of the Al-Si alloy were placed on top of the B_4C preforms. This setup was mounted on the graphite base of the chamber of the graphite furnace and covered with an alumina crucible in order to maintain uniform temperature.

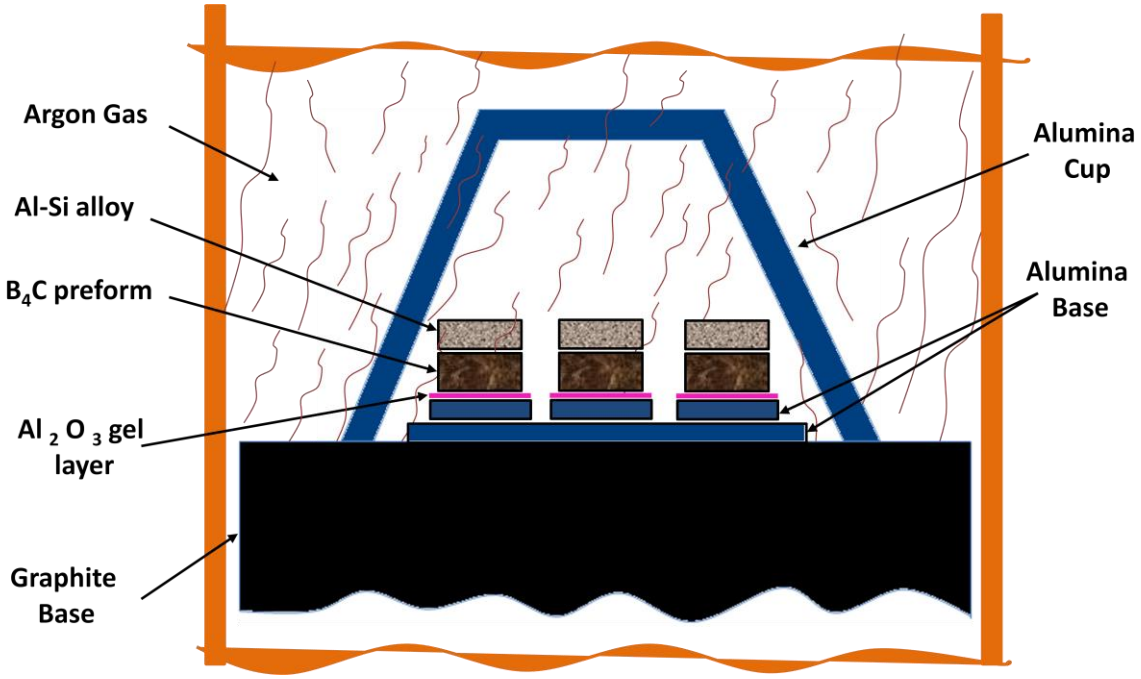

Figure 3.08: Assembly of samples inside the furnace chamber for melt infiltration

The chamber of the resistance heated graphite furnace was flushed three times with Ar gas as described above in section 3.2 and filled with flowing inert Ar gas kept at a pressure of 50 kPa above atmospheric pressure. Time-temperature cycles of the different melt infiltration runs are plotted in figure 3.09. On stage I, the furnace temperature is raised to 500 °C with constant heating rate of 20 °C/min and hold for 15-30 minutes at this temperature to decompose the organic binders in the B_4C preform.

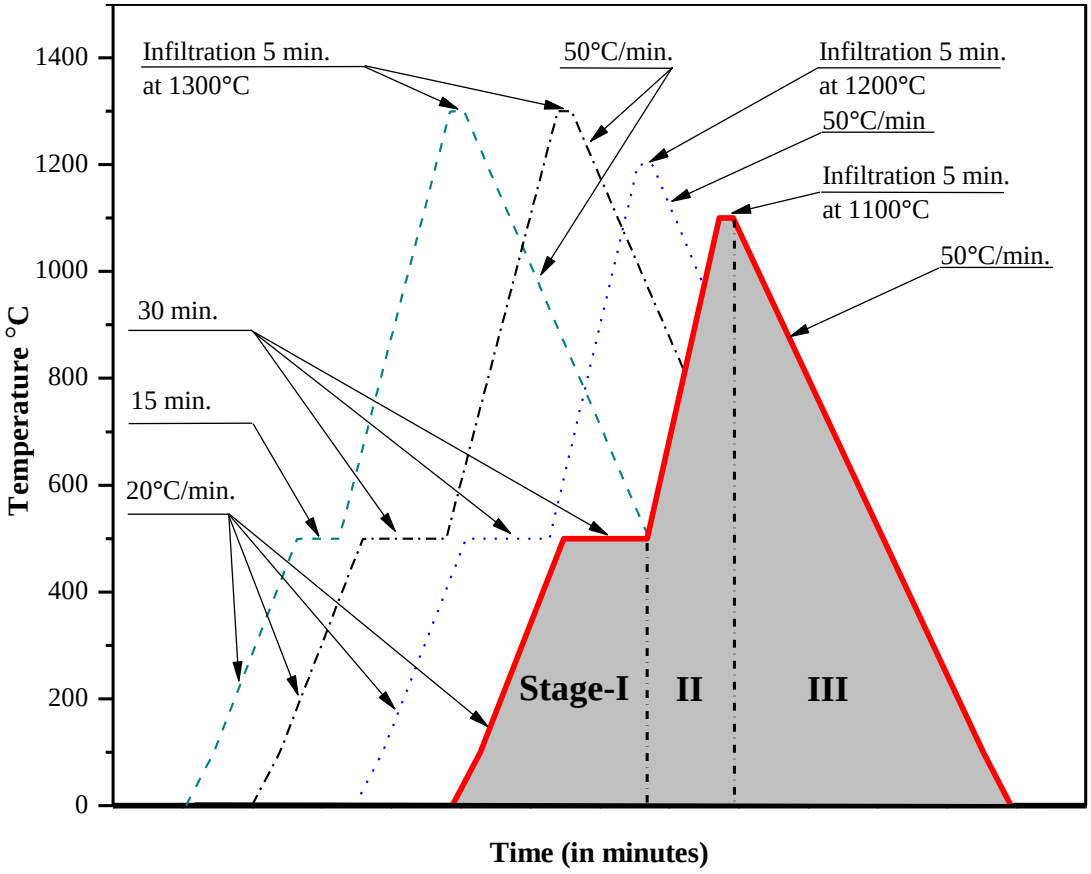

Figure 3.09: Time-temperature cycles of different melt infiltration runs.

On stage II, the temperature was further increased at the same heating rate to the final melt infiltration temperature (1300 °C for infiltration runs 01 to 08, 1200 °C for infiltration runs 09 to 11, or 1100 ºC trial infiltration runs which failed infiltration) and hold there for 5 minutes. On stage III, controlled cooling is done at the cooling rate of 50 °C/min.

The products of melt infiltration were cleaned and their dimensions measured in order to find dimensional changes and to determine the density after infiltration. Density of the composites was also established by the Archimedes method too. The composite was immersed in the water. The buoyancy force f_I equal to the weight of displaced water was determined by using a balance, f_I been calculated as the difference of weight of the sample in air and its apparent weight when immersed. By assuming that the melt infiltrate composite has no open porosity and approaching the specific mass of water to 1 g/cm^3 at room temperature, the volume of the composite sample v_c is calculated as the volume of displaced water:

$$v_c = \frac{f_I}{d_{H2O}} \qquad \text{..... Eq. (3.06)}$$

where υ_c is the volume of composite, f_I the buoyancy force and d_{H2O} the density of water.

3.4 Sample preparation and characterization by XRD and SEM/EDS

The composite was cut into two pieces to expose the cross section by using a water lubricated diamond saw (Struers – section 10 M/C) of 12.5 cm diameter at the speed of 3000 rpm and 0.005 mm/s feed rate. The two halves were committed for SEM/EDS, XRD analysis and for the indentation hardness and toughness tests, respectively**.** The composite half reserved for hardness and toughness tests was small and difficult to held stable during harness and toughness tests; hence hot mounting in transparent acrylic resin (Charofast labopress, Struers) was done.

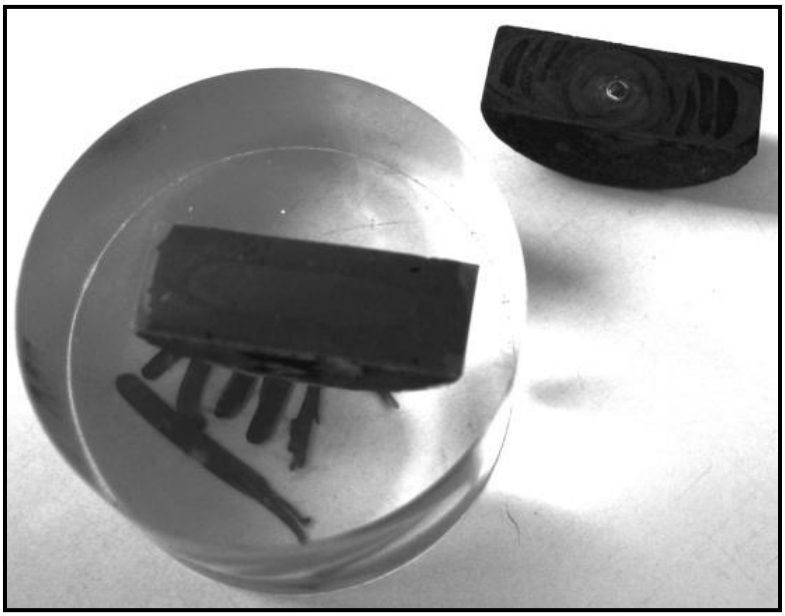

Figure 3.10: Cross sectioned composites (one half is acrylic mounted)

For this mounting, the flat side of the cut done in the composite sample was placed on the polished surface of the machine base (inside the small chamber of the equipment), the methyl methacrylate powder was used to cover the other sides of the composite sample. The chamber is closed and heated. When temperature reaches 180 ºC, a 25 kN load is applied for five minutes followed by the cooling in six minutes. For the second half of the composite piece used for XRD, SEM/EDS analysis, resin mounting prior to grinding and polishing was not necessary ant it was not done.

Grinding to create flat surfaces in both halves of the composite was done with the aid of a semi automatic polishing machine (Struers grinder-polisher M/C), where successive grades of silicon carbide abrasive paper (from 180, 400, 800, 1000 to 1200 grit sizes) were utilized. Polishing of the ground surfaces of the composite was done by using polishing cloth loaded with diamond pastes of 15 µm, 9 µm, 6 µm, 3 µm and 1 µm particle sizes, respectively. The flatness and quality of finishing of the surface was repeatedly checked with the optical microscope (Nikon Microport) during polishing. Ultrasonic cleaning of the samples between grinding and polishing steps was done in the ultrasonic bath (Peralab

Equipment Industries de Laboratories) for six minutes with the specimen immersed in ethanol.

The half of the specimen reserved for XRD and SEM/EDS characterization was further sliced into two parts along the direction of the pellet diameter for adequate fixing in the sample holder of the X-Ray diffractometer (Rigaku Model - Geigorflux). For the purpose of XRD analysis, three zones were defined on the cross section area along the infiltration direction as corresponding to the top, middle and bottom (final of infiltration) zones, respectively. Examination by XRD was done in the range $2\theta = 10^{o}$- 80^{o} at 3 °/min, θ being the Bragg angle. DRX spectra were repeated three times on each area of observation for the purpose of quantifying the phases with the aid of XRD standards.

The same specimens of the DRX characterization were also used for SEM/EDS observation and analysis in the scanning electron microscopes Hitachi S-4100 CFE-SEM with a Rontec EDS spectrometer and Hitachi SU-70 SE-SEM with the Bruker QUANTAX 400 high yield EDS system (facility of RNME-UA, the National Network of Electron Microscopy, Pole University of Aveiro; FCT Project REDE/1509/RME/2005). To eliminate electrical charging of the ceramic phases in the composites, the SEM specimen after properly glued onto the aluminum stubs were C coated by uisng the carbon coating unit (EMITECH K950).

Homogenous mixtures of Si, Al, B_4C, SiC powders with pre-set weight fractions representing the Al-Si and B_4C-SiC systems and combinations of the two binary systems were prepared and the corresponding XRD spectra used as standards for the quantitative analysis of the phases present in Al-Si smelted alloys and in given zones of the cross-sections of the melt infiltrated composites, Annex A. After analysis of overlapping of XRD peaks of the different crystalline phases relevant for this study, the intensity of major XRD peaks of Al, Si, SiC and B_4C phases corresponding to the diffraction angles 2θ between 38.50° - 39.50°, 28° - 29°, 36° and 38°, respectively, were selected as base for the XRD quantitative method with standards. For the selected DRX peaks given above polynomial functions of the relative intensity of the peaks as a function of the weight fractions of the phases in the mixtures were calculated by least-square methods. Polynomial interpolation

using the calculated correlation functions was applied to find the weight fraction of each phase from the corresponding ratio of measured XRD peak heights.

Although the free C (graphite) content in the as supplied 10 μm B_4C powder could be roughly estimated from the value of the intensity ratio C/B_4C of the main XRD peaks of each crystalline phase. Such quantification does not account for the difference of mass absorption coefficients of the X-rays in the two phases. By using the almost pure 18 μm B_4C powder as internal standard for the quantitative XRD method added with increasing x weight fractions in the total mixture, the weight fraction of B_4C, $X_{B,}$ in the binary system of crystalline phases of the 10 μm B_4C can be determined as the quotient of the constant to the slope of the linear dependence of the measured peak intensity ratio on the quantity [x/(1-x)]:

$$\frac{I_{B_4C}}{I_C}(x) = \frac{A_B}{X_C A_C}\frac{x}{1-x} + \frac{X_B A_B}{X_C A_C} \; ;$$

$$X_B + X_C = 1$$

$$K = \frac{A_B}{A_C} \qquad \text{…….. Eq. (3.07)}$$

where X_C is the corresponding weight fraction of the C phase (graphite) in the sample and A_B and A_C are undeterminable unknowns, the XRD absorption coefficients for the given peaks of the B_4C and graphite phases respectively, that set the value of the calibration constant of the method, K.

3.5 Indentation hardness and fracture toughness mechanical tests

Vickers indentation hardness was determined on the polished surface of acrylic mounted specimens. For the Vickers microhardness the testing machine (Shimadzu Data Letty 150) with a pyramidal diamond indenter and applied load of 1 kgf (9.8 N) was used. The dimensions of the impression of the indenter were measured with the measuring scale of the optical microscope of the microhardness equipment.

The Vickerss hardness (H_V) was computed by the formula [71]:

$$H_V = 2\,sin\left(\frac{136^o}{2}\right)\frac{P}{a^2} \quad \text{..... Eq. (3.08)}$$

where P is the applied load, (P = 1, 10 and 30 kgf , 9.8, 98 and 294 N, in the present study) and a is the average length of the diagonal of the indenter impression. In the standardize Vickers test method of hardness the load is given in kgf and the indentation diagonal in mm, hence the Vickers hardness number xxxHVyy/zz specifies the hardness xxx in kgf/mm^2 and it must include the indication of the applied load yy in kgf (and often the loading time zz in s); in present study it would be HV_1, HV_{10} and HV_{30}. HV_1 micro hardness values were calculated by the software of the microhardness equipment from dial readings of the diagonal a in the optical microscope. The dimensions of the indenter impression were also cross checked with images taken with a second optical microscope.

For evaluation of Vickers macrohardness at 98N and 294N loads the macrohardness tester (Zwick/Roell ZHU) was used. Figure 3.11 indicates the points of the cross section (top, middle and bottom) where HV_{10} macrohardness of the composite was measured. The dimensions of the indenter impression were determined with the optical microscope. Images were also taken with a second optical microscope and used for measuring the size of the diamond indenter impression and the length of indentation fracture cracks propagated from the indentation corners as elements for the determination of indentation fracture toughness, K_{IC}. In the process of determining K_{IC}, SEM microscopy was also used to establish in accurate way the position of indentation corners and extent of indentation crack propagation.

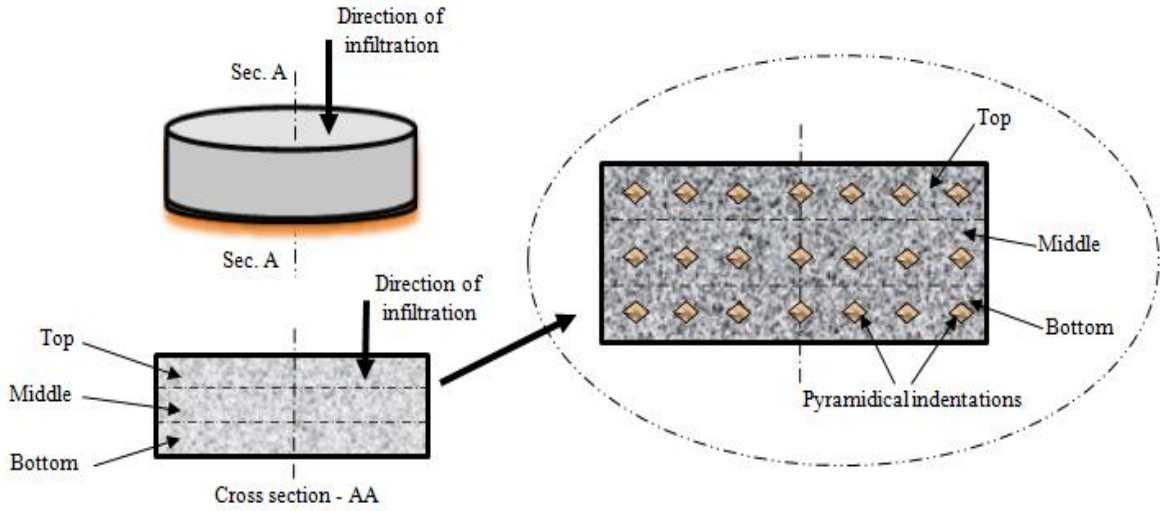

Figure 3.11: Indication of points on the cross-section of the composite (top, middle and bottom) selected for Hv_{10} macrohardness testing.

By applying the simplified fracture mechanics method of *Anstis et al* the indentation facture toughness [72] is determined as:

$$K_{IC} = 0.016 \left(\frac{E}{H}\right)^{\frac{1}{2}} \frac{P}{c^{3/2}} \qquad \text{..... Eq. (3.09)}$$

where, E is the Young modulus, P the applied load, H the hardness, c the length of the radial crack taken from the center of the indenter impression to the crack tip, as shown in the schematic diagram of Vickers-produced radial/median crack system, figure 3.12 (a), where σ_a is the tensile stress from the deformation field left by the applied P.

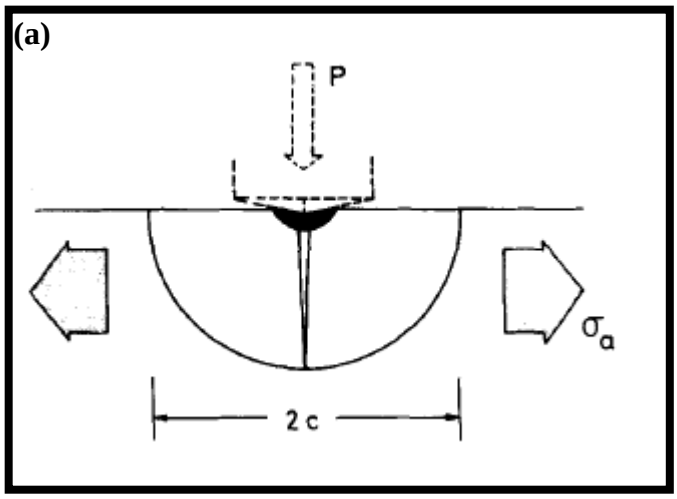

(b)

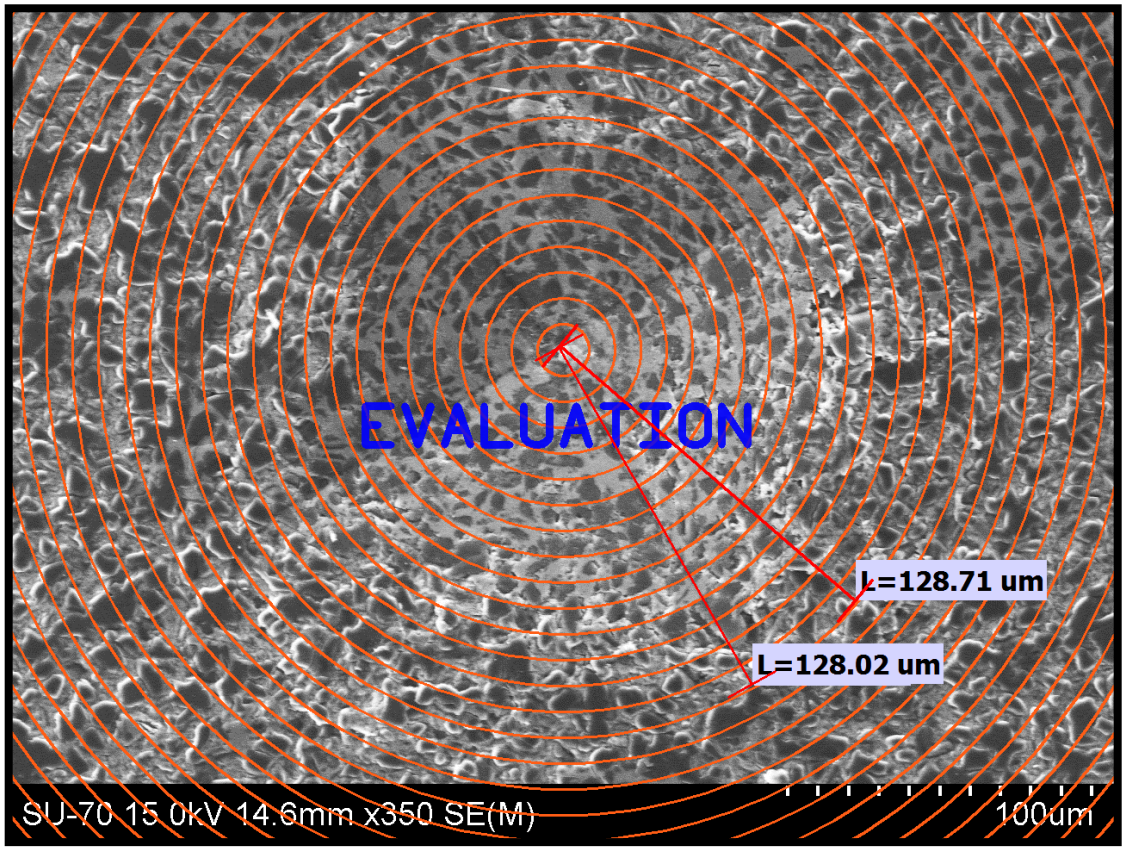

Figure 3.12: Indentation fracture. (a) Scheme of Vickers indentation radial/median crack system, (b) Measurement of the radial crack length, c, on a SEM image for determining the indentation fracture toughness K_{IC}.

4.0 RESULTS AND DISCUSSION

The properties and composition of the B_4C powders, degree of compaction of the B_4C preforms, the melting and quality of the Al-Si alloy are presented and discussed in the first two sections of this chapter. The third section of this chapter gives the results of reactive melt infiltration of the B_4C preforms and discusses the effects of the infiltration processes along with their causes. Out of the produced composites some show non-infiltration, poor infiltration or partial infiltration which is discussed with the support of images and interpreting schemes.

Successfully infiltrated composites prepared in limited numbers from different compositions and conditions were separated for continuation of the analysis, the corresponding results were tabulated and are discussed in last two sections of this chapter. The evolution of microstructure, distribution of phases and phase formation mechanism of the three composites are dealt with in section 4.4 supported by XRD, SEM/EDS techniques, quantitative analysis and representation of the composition of the composites in ternary and quaternary phase diagrams. The mechanical behaviour of the selected three composites is discussed in the last section of this chapter 4.5 on the bases of microhardness, macrohardness and indentation fracture toughness results followed by the tentative description of the mechanism of the fracture.

4.1 Characterization of B_4C powder and green density of the preforms

The ceramic raw material of this study, the B_4C powder of 10µm average grain size was selected by considering the fine grain size and size distribution as well deagglomeration as relevant properties for pressing packing efficiency, the velocity of reactive melt infiltration and mechanical properties of the composites. B_4C powders of about 10 µm mean grain size with minimum of 5wt.% free carbon may yield enhanced fracture toughness of the melt infiltrated composites[73]. A coarser B_4C powder almost C free, with 18µm average grain size was used as internal standard in XRD. Characterisation of the 10µm B_4C powder to determine the amount free C from weight loss by combustion of carbon in air was also

done. The values of green density of the pressed B_4C preforms are presented in this section too.

4.1.1 Free carbon content of the B_4C powder

Due to the low atomic numbers of the elements carbon and boron, conducting the chemical analysis to establish the free C content of B_4C powder through EDS spectrometry with the SEM electron microscope would provide an unreliable result. B would hardly be detected by SEM/EDS. Free carbon, as graphite is detected by XRD in the as received 10µm B_4C powder, figure 4.01.

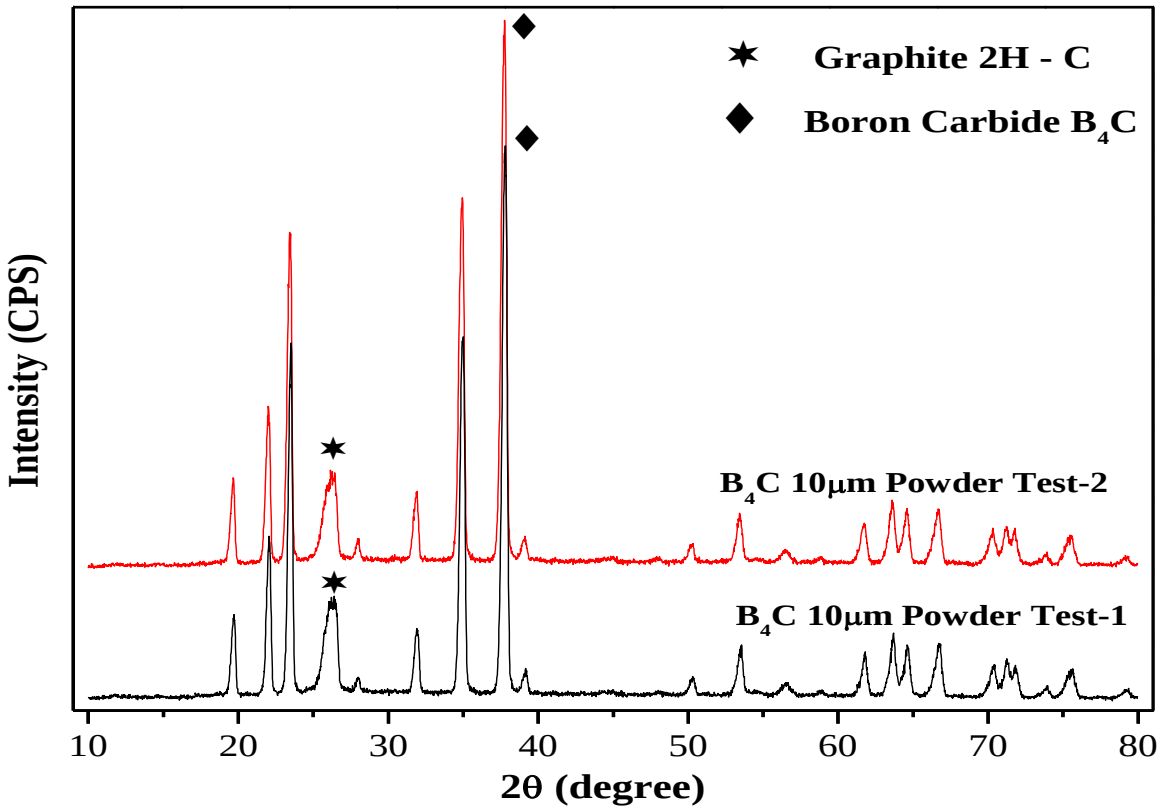

Figure 4.01: Crystalline phases of the 10µm B_4C powder as detected in two separated XRD tests

The content of free C, determined as crystalline graphite was established by comparing the intensity ratio of the main XRD peaks of graphite and B_4C phases. The XRD spectra of each of the B_4C powders of particle sized 10µm and 18µm, respectively and of the mixtures of 10µm powder to which 25 wt.%, 50 wt.% and 75 wt.% of 18µm B_4C powder was added are shown in figure 4.02. XRD results of the as supplied and 10 µm and 18 µm B_4C powders show very similar XRD spectra with the primary peak of B_4C registered in

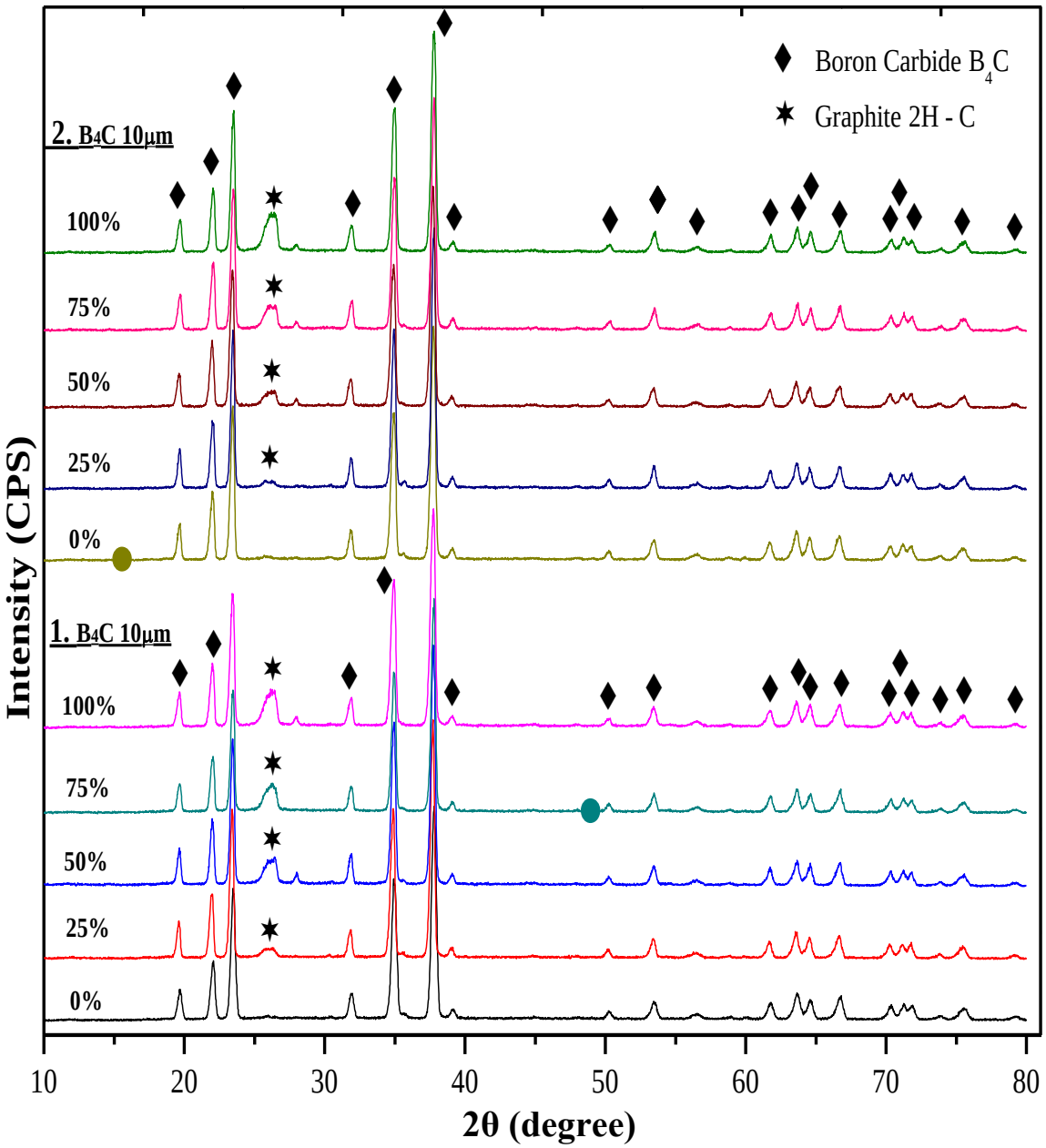

Figure 4.02: X-ray diffraction spectra of the as supplied 10µm and 18µm B_4C powders and their mixtures; results of two independent tests.

38º (2θ angle), the only noticed difference being the presence 2H graphite peaks at 2θ – 26-27º of the 10 µm B_4C powder. The corresponding values of intensity ratio of the 2H graphite 2θ - 26° XRD peak as the percentage of the intensity of the 2θ - 26° XRD main peak of the B_4C phase for the as supplied B_4C powders and mixtures of them in the given weight fractions are given in table 4.01.

Table 4.01: Relative intensity of the 2H graphite 2θ - 26° XRD peak as percentage of the intensity of the 2θ - 38° XRD main peak of the B_4C phase for the as supplied powders and mixtures of them in the given weight fractions.

No. of Tests	100wt.% of B_4C 10µm %	75wt.% of B_4C 10µm %	50wt.% of B_4C 10µm %	25wt.% of B_4C 10µm %	100wt.% of B_4C 18µm
1	15.5	12.8	11.4	5.4	No peaks identified
2	16.3	10.9	8.3	4.2	

Due to the mixing of two different grit sizes of the B_4C powders, a small variation is found in the intensity ratio C/B_4C of the main XRD peaks. An estimate of the free C content as about 16 % is obtained as the value of the intensity ratio C/B_4C of the main XRD peaks of the 10 µm B_4C powder in table 4.01. Such quantification does not account for the difference of mass absorption coefficients of the X-rays in the two phases.

A more reliable quantification of the graphite (C) content in 10 µm B_4C powder is obtained by applying the quantitative XRD method established in section 3.4 to determine the fraction of the B_4C phase in the as received powder as quotient of the constant to the slope of the linear dependence of the measured XRD peak intensity ratio given by the relationship in equation 3.07. The average values of each two peak intensity ratio were calculated for each composition in table 4.01. The C/B_4C peak intensity ratio for the 25 wt% of B4C 10 µm mixture of powders is of low accuracy and has a large relative error. This value was not included in the following calculations of the quantitative XRD method. The ratio of the calculated values of the constant and slope of the correlation as given by Eq. 3.07 yields the values of result as $X_B = 0.93$ and $X_B = 0.92$ from the values on each

row in table 4.01. The corresponding value free C content in the 10 μm B_4C will be very close $X_C \approx 8$ wt%.

4.1.2 Thermal analysis of the B_4C powders

The simultaneous thermogravimetric (TG) and differential thermal analysis (DTA) for both the 10μm and 18μm B_4C powders were done in air for heating temperatures up to at 800 ºC, figure 4.03. The onset of oxidation of B_4C in air yielding B_2O_3 occurs below 800 ºC [18-20, 74]. As the temperatures for graphite combustion and for oxidation of the B_4C particles neatly overlap the weight loss due to combustion of free carbon alone could not be clearly determined. The strong exothermic peak at temperatures close to 680 ºC of the 10 μm B_4C powder in figure 4.03 (a) and the decrease of weight of the TG plot can be attributed to combustion of free carbon with a growing contribution of oxidation of B_4C. The overlap of the two reactions would be accentuated if the free C is made of graphite inclusions kept inside the B_4C grains or in the dense agglomerates of the grains.

The corresponding exothermic peak of the 18 μm B_4C powder in figure 4.03 (b) moves to temperatures above 700 ºC and the observed weight loss is lower in correspondence with the low the C content and the coarser sizes of the B_4C particles. B_4C powders revealed net oxidation in air at 800 ºC [18-20, 74]. The early starting of the exothermic reaction of oxidation Figure 4.03 (a) for the 10 μm B_4C powder compared to the reaction in figure 4.03 (b) for the 18μm B_4C powder gives evidence of graphite presence and of finer particle size of the B_4C corresponding to the figure 4.03 (a).

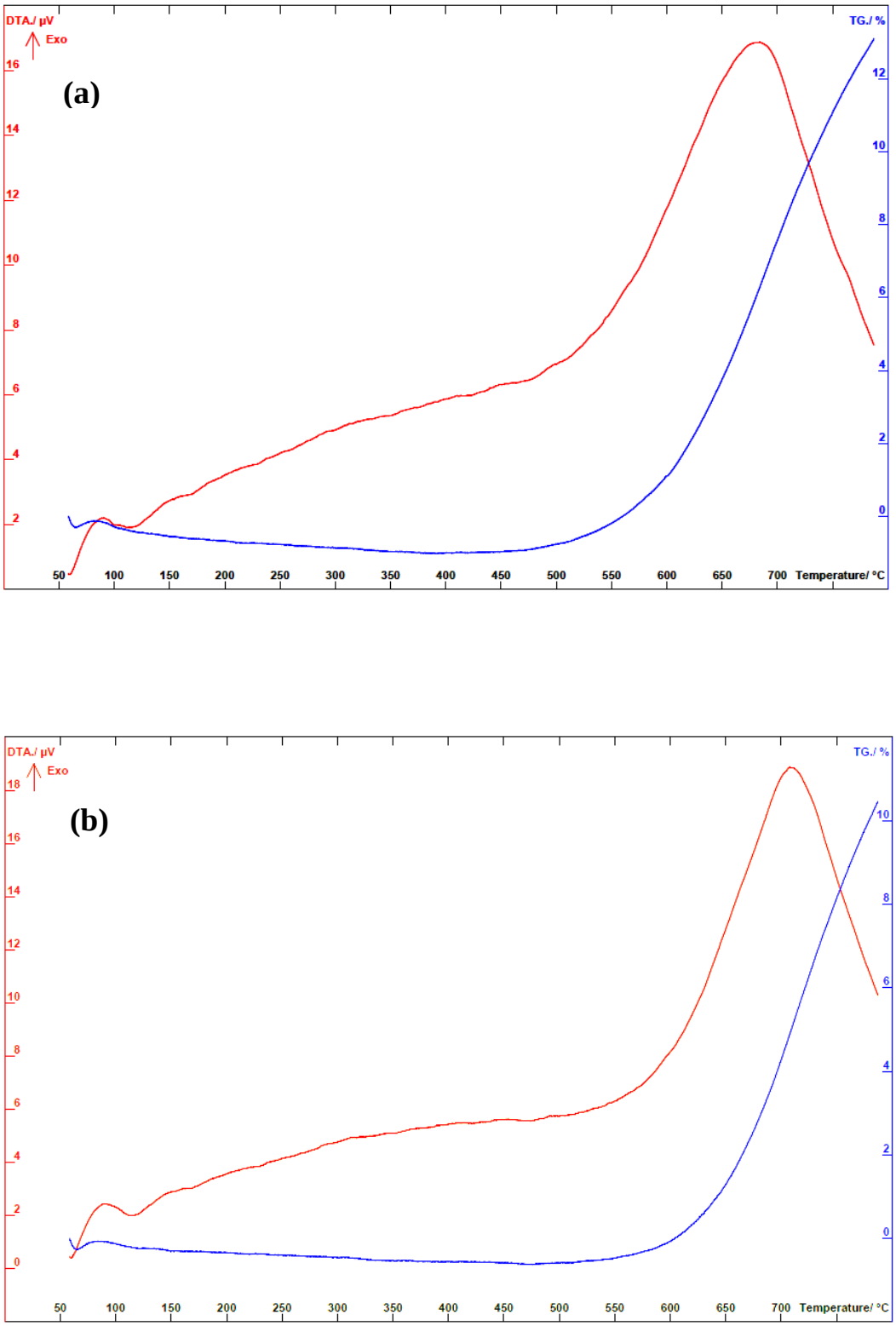

Figure 4.03: Simultaneous DTA/TG analysis in air: (a) 10 µm B_4C powder, (b) 18 µm B_4C powder.

4.1.3 Pressing efficiency of the B_4C powder

Uniaxial pressing followed by cold isostatic pressing (CIP) was done as described in section 3.1.2 to attain the estimated 50% of relative density of the green body where 4 wt.% of PVA solution was added as binder. The values of green density in table 4.02 of 24 compacted preforms measured for control of the process range from 1.25g/cm^3 to 1.46 g/cm^3. The wt % of the added PVA solution is also given in this table along with measured values of density of the preforms. The relative density values of the prepared preforms in table 4.02 were calculated by excluding the water content of the PVA solution and its actual corrected values were given as "corrected" green density in table 4.02. The corresponding values of relative density are plotted in figure 4.04.

Table 4.02: Samples of isostatic pressed B_4C preform with its corrected green density, relative density and the PVA solution added for binding.

Samples		1	2	3	4	5	6	7	8	9	10	11	12
Corrected green density	(g/cm^3)	1.31	1.31	1.33	1.30	1.30	1.31	1.30	1.33	1.30	1.32	1.31	1.33
Relative density	%	51.9	51.9	52.9	51.7	51.7	51.8	51.7	52.8	51.8	52.5	51.9	52.7
PVA solution added	wt%	3		4.5								3.5	4.5

Samples		13	14	15	16	17	18	19	20	21	22	23	24
Corrected green density	(g/cm^3)	1.33	1.33	1.30	1.37	1.37	1.38	1.39	1.36	1.38	1.34	1.33	1.35
Relative density	%	52.9	51.7	54.4	54.3	54.8	55.0	54.1	54.8	53.0	52.7	53.6	52.8
PVA solution added	wt%	4.5		5							4	4.5	4

The green density of preforms compacted by isostatic pressing was improved about 6% compared to the corresponding values of the density after the first step of uniaxial pressing. They also maintain the uniform shape in isostatic pressing. Good binding of the B_4C powder was achieved by the initial addition of the PVA solution; however the water in the binder was completed evaporated during the early heating stages of the infiltration process.

The gray-green shaded performs in table 4.02 were selected to be processed as melt infiltrated composites and further studied, as described in the following of this chapter.

The average value of density of the isostatic pressed preforms is 1.33±0.03 g/cm^3 which corresponds to the porosity fraction of 47.2 % ± 1%, reported to the density of pure B_4C, 2.52 g/cm^3 as given in section 3.1.1. The measured relative density of the green preforms is slightly above the pre-set value of 50% densification.

Experimental factors such as content of added binder (PVA) and retained humidity, regularity of distribution of the binder and degassing before the final step of CIP may have contributed for the scatter of values of green density of the preforms around the average value. All preforms were prepared as batches with various combinations of PVA solution for ensuring good compacting performance. In the figure 4.04 two sets of values of the relative density of the preforms are found. The preforms of those values encircled by X were prepared with 4 wt% to 4.5 wt% of the PVA solution while the preforms of those values marked with Y were prepared with 5 wt% of the PVA solution.

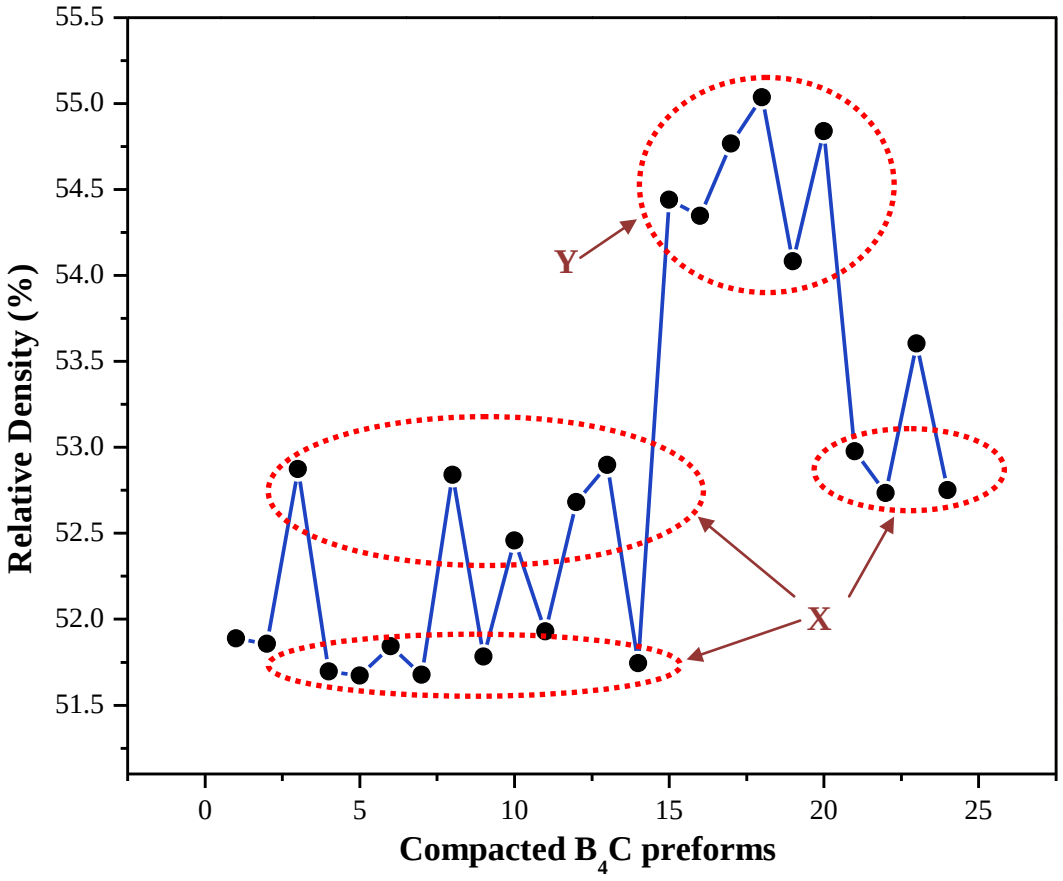

Figure 4.04: Values of the corrected relative density of isostatic pressed B_4C preforms determined for control of the process, X and Y in the text.

4.2. Characterisation of the Al-Si alloy

The elemental composition, phase structure and mechanical properties of alloys depend on several factors related to the solidification process. *Burminskaya et al* reported that strength and hardness of the binary alloys with mutually insoluble phases increase by augmenting the amount of the harder phase in the alloys[75]. Moreover the chemical composition of the alloy also controls the wetting and reaction with the B_4C particles even at the lower temperatures. The smelting process of the Al-Si batches was done in an argon atmosphere as described in section 3.2, ending with a final isothermal dwell at 1000 ºC for 60 minutes. In the XRD results of four fusion batches given in figure 4.06, Al and Si are the main phases.

The weight fractions of Al and Si of the batches of Al-Si alloy were determined from quantitative measurements of the phase main peaks in DRX, $2\theta = 38.5^{o}$ for Al and $2\theta = 28.5^{o}$ for the Si, by comparison with values of corresponding peak intensity ratio of the mixtures of Al and Si powders used as standards. The values of the metal weight fractions in the alloys, the corresponding values of density of the alloy calculated from the nominal composition and from the weight fractions determined by XRD are given in table 4.02. The calculated density was determined according to equation 3.03. The maximum solubility of the Si in Al is 1.65±0.1 at% at the eutectic temperature of 577 ºC. The density of pure Al (d_{Al} = 2.702 g/cm^3) and Si (d_{Si} = 2.329 g/cm^3) metals were taken for calculating the density of the alloy.

Table 4.03: Composition of the Al-Si alloy batches after melting determined from quantitative DRX measurements and calculated values of density.

No. of Batches	Al-Si Mixture	Composition Measured				Density		Indication of Prepared Composites
	Nominal	XRD		EDS		Nominal	Calculated	
		Al	Si	Al	Si			
	(in wt.%)	(wt %)	(wt %)	(wt %)	(wt %)	(g/cm^3)	(g/cm^3)	
1	Al-25 wt% Si	76.2	23.8	62.4	37.6	2.60	2.60	I, **II(A),** III
2	Al-35 wt% Si	70.0	30.0	52.0	48.0	2.56	2.58	**IV(B),** V
3	Al-25 wt% Si (twice smelted)	83.0	17.0	71.0	29.0	2.60	2.63	VI, VII, **VIII(C)**
4	Al-25 wt% Si (twice smelted)	78.0	22.0	73.1	26.9	2.60	2.61	--

The four batches of Al-Si were melted with little modifications in composition of the alloys and number of smelting times as given in section 3.2 and table 4.03. The composition of fusion batch (1) after the smelting was the closest to the corresponding nominal composition. Batches (3) and (4) were prepared by twice smelting for expectedly better quality of the alloy. Specimens of the smelted Si-Al batches were also analysed by SEM/EDS to check the distribution of Al and Si phases in the microstructure and the

elemental chemical composition. The results of SEM/EDS analysis on Al and Si concentration of the same batches of the Al-Si alloy are also given in table 4.03.

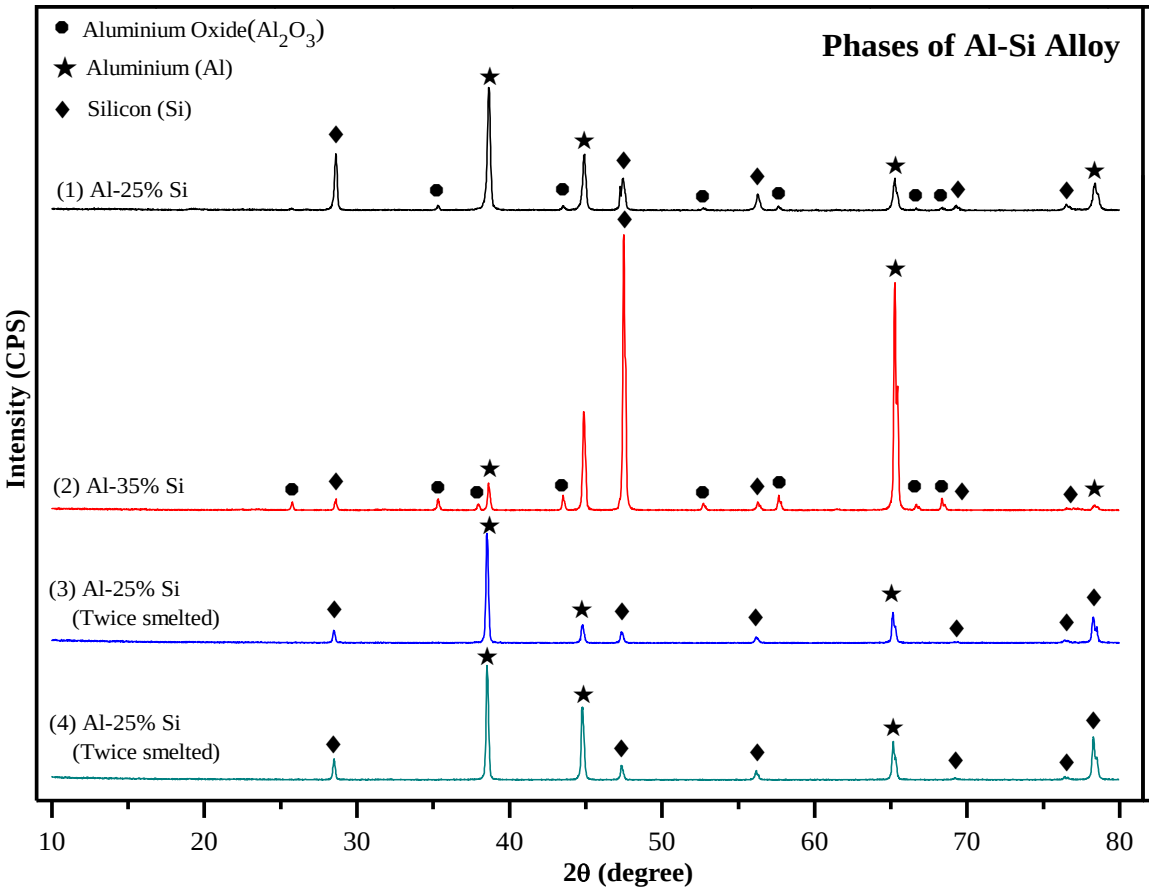

Figure 4.05: XRD result of Al-Si alloys of fusion batches (1) to (4).

Due to difficulties in cleaning the furnace atmosphere, the residual oxygen inside the furnace reacted with Al and formed a minute quantity of Al_2O_3 phase in the first and second fusion batches. Increased vacuum in the furnace chamber preceding the argon gas flushing and repeating the argon gas flushing three times eliminated this problem.

Nominal composition of fusion batch (1) in table 4.03 has 25 wt% of Si while the XRD analysis yield the value 23.8 wt% of Si and EDS a content of 37.6 wt% Si. The SEM/EDS results provide the mean value of 48 wt% Si in the alloy of fusion batch (2), 29 wt% Si and 26.9 wt% Si as the Si content of the molten alloys of the 3rd and 4th fusion batches (3) and

(4). For confirming the composition, batches (3) and (4) have been tested twice by XRD. Batch (3) of the twice smelted alloy gave similar alloy proportions in the XRD results both analysis, but for batch (4) the results varied slightly. The Al-Si ratio values from the EDS analysis corroborate the main trends of the XRD results, but EDS seemingly overestimated the Si content of the Al-Si alloys of this study.

The SEM images in figures 4.06 and 4.07 are from specimens of fusion batches (2) and (1), respectively. The elemental composition of each fusion batch was also determined by EDS by applying an area box to a few regions of the specimen surface being analysed by SEM, as schematically represented by rectangular areas in figure 4.06.

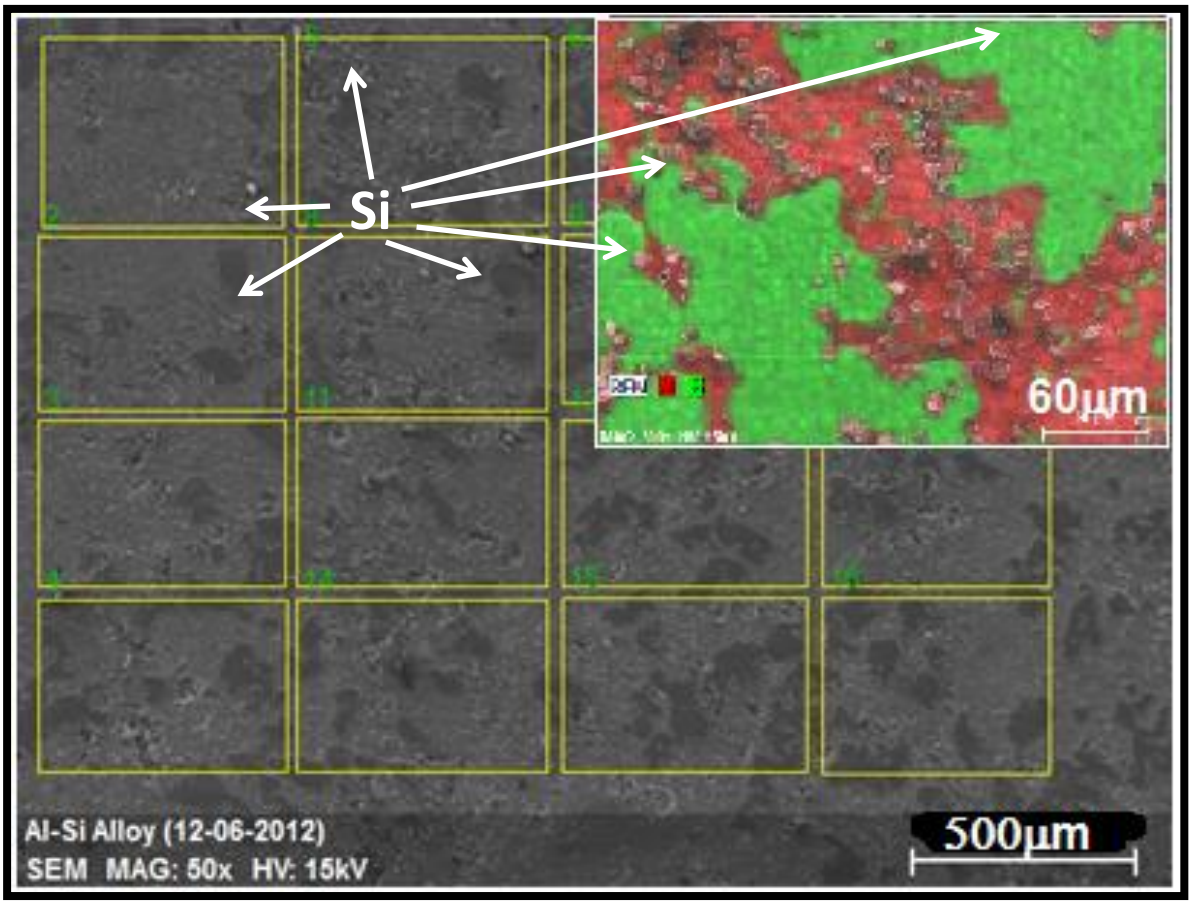

Figure 4.06: Dendrite formation in star like agglomerates of Si in the Al-35 wt.% Si alloy

The work of *Nikanorov et al* on fast cooled Al-Si alloys [38] describes the precipitation of the Si in a Al-30 wt% Si alloy with dendrite growth forming star like aggregates of Si,

whereas the figure 4.06 indicates in detail widespread formation of the primary dendrites of the Si, mainly due to higher value of Si concentration and a solidification rate under more conventional cooling of the present study, section 3.2. The figure 4.07 shows the alloy of 23.8 wt% Si content of batch (1), in which the growth of particles do not show any star or needle like dendrites.

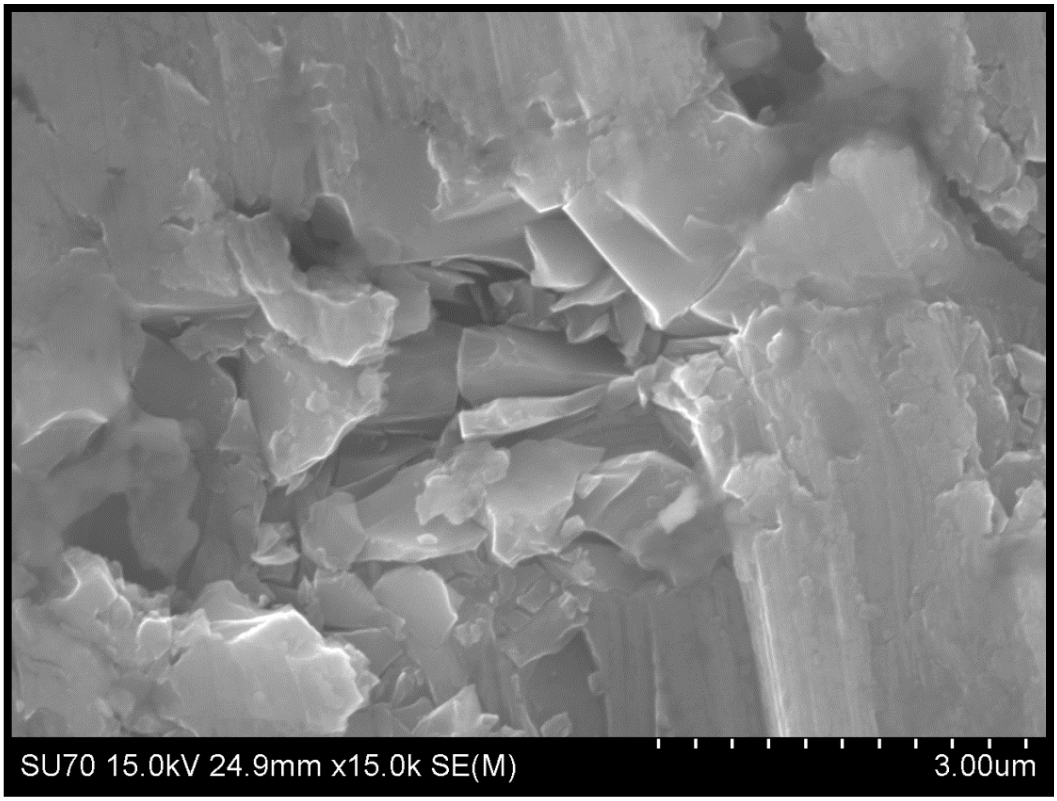

Figure 4.07: Bulky dendrite formation in Al-25 wt.% Si alloy of fusion batch (1).

For the range of composition of the present study the decrease of density of Al-Si alloy with the Si content is almost linear [38]. In the hypoeutectic Al-Si alloy, increasing of Si content improves the hardness of the alloy, whereas in the hypereutectic alloy (> 12.7 wt% Si) there is the opposite trend [38]. The Al-Si alloys of the present study are hypereutectic. As Si is taken out of the alloy during reactive melt infiltration of the B_4C ceramic preforms the composition of the metallic phase moves towards the eutectic composition and the yield stress and hardness of the metallic phase in the composite may increase. The composition of the melt, the temperature gradient at the solid-liquid interface and

crystallization rate are major factors in solidification. The simultaneous changes of these factors may lead to conflicting effects on the formation of the microstructure of the solidified alloy and its mechanical behaviour.

4.3. Al-Si reactive melt infiltration of B_4C

The prepared Al-Si alloys were pressed as discs and put on the top of the porous B_4C preforms. The process of spontaneous melt infiltration at the elevated temperature was conducted as described in section 3.3. During the infiltration and solidification stages the infiltrated Al-Si alloy reacted with elements of B_4C and formed new carbide or boron carbide phases.

One of the important parameters was the infiltration time as it is intended the time to be enough for the metal go through the total thickness of the porous samples at the lowest temperatures that make infiltration feasible and stay short to decrease the extent of reactions and preserve the Si content in the alloy above the threshold concentration of 12-13 wt% Si for formation of brittle Al_4C [76].The spontaneous infiltration of porous B_4C preforms with Al-Si alloys by the effect of capillary forces of surface tension had been described in previous works[1, 76] but not at such short duration of infiltration time as planned for this study. A tentative explanation for the actions occurring inside the pellet during the infiltration process can be worked out from the early study on the kinetics of the reaction of B_4C with liquid Al, Si and other metals [77], the study of metal spreading having been done on the polished surfaces of dense sintered B_4C ceramic specimen. Liquid Al may disperse free on a B_4C flat surface at a rate of $1x10^{-4}$ m/sec to $8x10^{-4}$ m/sec at temperatures around 1200 ^oC. If during the melt infiltration processes the hypereutectic Al-Si alloy also advances at such speed, the time for infiltration of a 15 mm thick pellet would be less than 3 minutes. The same study also showed that the speed of Al spreading was non constant and came down rapidly as the driving force for flowing of liquid Al on B_4C becomes almost nil in about 4 to 5 minutes due to the formation of new phases in the contact from reactions of the liquid with the solid phase. At the same time, after 3 minutes the contact angle of the molten Al had decreased from the initial value of about 92° to 28°

and slowed the movement of the Al by viscous flow. The same study of *Panasyuk et al.* also indicates that the spreading velocity of molten Si on the B_4C surface would also be high of $8x10^{-4}$ to $1.3x10^{-3}$ m/sec at the beginning with a rapid non-linear decrease with time, becoming constant and close to zero after the first 3 minutes [77]. The melt infiltration of the porous B_4C preform may either be controlled by rate of the reactions or by the permeation rate regulated by the dynamical viscosity of the liquid alloy and the curvature pressure of the concave meniscus formed by the liquid inside the pore channels.

The track of the advancing molten Al-Si alloy along a thin flaw of the pellet as the liquid moved from top of the preform (right) towards to bottom (left) during the infiltration process of B_4C is shown in figure 4.08. The composite matrix around the flaw also went complete infiltration at the same time as the flaw became filled in.

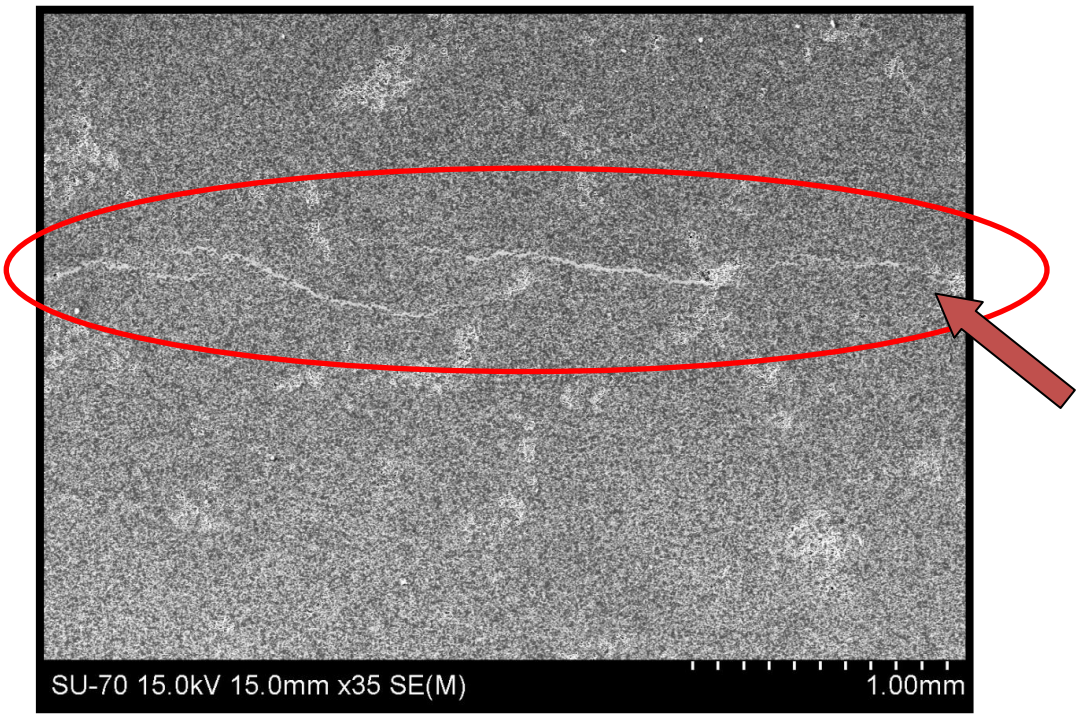

Figure 4.08: Cross sectioned view of a melt infiltrated B_4C composite - spreading of the alloy along a thin flaw of the porous medium, (arrow mark indicates the direction of infiltration from the top side)

The conditions set for the preparation of the composites and the final values of density and relative density of the B_4C melt infiltrated composites are given in table 4.04. The table shows the corrected relative density (densification) of the preforms also presented in table 4.02 as gray/green shaded cells. The densification of the green bodies exceeded by 1.7% to 4.8% the target value of 50 % relative density. But, reducing the amount of the PVA solution from 4.5wt% even to 3 wt% was not feasible as the green body was spoiled during handling especially at the time of cold isostatic pressing.

Table 4.04: Conditions selected for the preparation and melt infiltration of the B_4C composites and final values of density and relative density of the composites.

Composites	Densification	Nominal Si Content	Densities of the Composites			Infiltration Parameters
			Theoritical	Measured	Relative	
	(%)	(%)	(g/cm^3)	(g/cm^3)	(%)	
II / (A)	52.9	25	2.57	2.55	99.51	1300°C for 5min.
III	51.7			2.44	95.00	
IV / (B)	52.9	35	2.55	2.53	99.07	
V	51.7			2.50	98.02	
VI	54.3	25 (twice smetled)	2.58	2.51	97.51	
VII	54.8			2.51	97.47	
VIII / (C)	54.1			2.55	98.72	1200°C for 5min.

Table 4.04 gives the nominal weight fraction of Si in the Al-Si alloy used for infiltration, while in determining the theoretical density of the composite the actual density of the Al-Si alloy given on table 4.03 was considered. The values of the density of the composite measured by the Archimedes method (section 3.3) range from 2.44 g/cm^3 to 2.55 g/cm^3 (Annex C). Though the composites II, IV and VIII, also referenced with big capital letters A, B and C in table 4.04, have been produced from different combinations of the Al-Si alloy and different smelting processes and infiltration conditions they possessed the measured density of 2.53 g/cm^3, or superior, and the relative density close to 99%; hence

they were selected for further investigation of the structure and mechanical properties of the composites in the following sections 4.4 and 4.5. The lower values of relative density of the remaining composites in table 4.04 are explained by the presence of defects of reactive infiltration of insufficient time for the complete infiltration of their volumes, as follows.

4.3.1 Failure of the melt infiltration process

During the infiltration processes, a few preforms did not infiltrate due to poor wetting or oxidation problems. The causes behind those difficulties are analysed here. Figure 4.09 shows three pellets of one same infiltration run at 1300 ºC in which one non-infiltrated perform was found just aside two other pellets that were both fully infiltrated under same conditions. In initial infiltration trials the preforms were directly located over the small alumina plates. Due to brazing at the end of the infiltration cycle, it was difficult to remove the composite from the plate after processing. A slurry of alumina was painted on the face of the alumina plates in the following experiments. The thin coating of the alumina fine powder (C), figure 4.09, may turn into a source of oxidative gases (CO/CO_2) when it becomes reduced in contact with C in the pellet or with the B_4C itself. Observation of the samples also showed that a too thick layer of metal on the top of the pellet (as in infiltration of 15 mm thick pellets) also contributed to poor wetting as adequate contact between alloy and B_4C was lost and there was a net trend for formation of oxidation layers on the metal surfaces.

Figure 4.09: Results of one infiltration run done at 1300℃ in the resistance heated graphite furnace, (A) Non-infiltrated B_4C preform; (B) remnants of the Al-Si alloy on top of preform; (C) thin layer of Al_2O_3; (D) Al_2O_3 plate; (E) and (F) successful infiltrated composites (IV) and (V) respectively with excess Al-Si alloy left on top.

When analysing the causes of non-infiltrating behaviour, major problems arose due to the improper wetting and oxidation of the metal. The lack of wetting is due to the presence of contamination either moisture from the sample or from the slurry coating, or gases adsorbed on the ceramic particle surfaces, and results in Al_2O_3 and aluminium sub-oxide layer that covers liquid Al and native SiO_2 layer that may simply covers Si particles [78]. In general, in such cases the molten metal matrix is blocked from creating the direct contact with the surface of the individual particles [78]. In the spreading process the liquid distributes itself to cover the solid surfaces and there is an important rearrangement stage after the formation of the liquid-solid bonds. Factors like dihedral angle and liquid penetration of the grain boundary between particles affect the process. It is generally found that liquids with low surface tension readily wet most solids, giving a small contact angle, whereas liquids with large values of contact angles as the melts of metals of high surface tension show poor wetting. At molecular level, if cohesion between the atoms or molecules in the liquid is greater than the adhesion between atoms of the liquid and the solid, the

liquid will not show the tendency to wet the solid. Hence, the infiltration of porous solids will not take place in such cases.

There were points where some oxidation of the Al-Si alloy developed during the process. The alloy was prepared in alumina crucibles. Although it was smelted under an inert argon atmosphere, an oxide layer grew on the surface of the smelted alloy. It was also seen forming an interconnected structure which contained pockets of properly smelted alloy. In order to facilitate wetting and initial spreading of the alloy in the following steps, the alloy was cleaned by removing the oxide layer and it was sliced into small pieces and pressed into cylindrical discs as described in section 3.3. Only small oxide particles remained stuck in the alloy bits.

4.3.2 Partial melt infiltration of B_4C preforms

Saw cutting of the melt infiltrated pellets to expose the cross section revealed the presence of infiltration irregularities with non infiltrated volumes of three different types in some of the melt infiltrated pellets: (i) central volumes without infiltration in the middle portion of the pellet, figure 4.10, (ii) volumes at the end face of the pellets centred on the pellet axis in pellets of larger heights, figure 4.11 and (iii) irregularly shaped volumes laid closely to the plan normal to the direction of the uniaxial pressing of the cylindrical pellets, figure 4.12. The unbounded B_4C that filled these volumes were removed to uncover their walls. Such irregularities in infiltration result from changes in the speed of spreading of the alloy along the porosity spaces which may be connected to defects in the pressed pellets or reactions occurring in the volume of the sample during infiltration. Differences in particle packing efficiency during pressing may occur due to unequal loading of the moulds and to internal friction of the hard B_4C particles. Internal flaws due to delamination may appear in the pressed pellets.

Decomposition and pyrolysis of PVA of the binder would produce gases. As escaping of the residual H_2O and pyrolysis gases or removing of gaseous contaminants from the central volume of the pressed pellets may be delayed, to decrease the risk of developing the irregularities of the type shown in figure 4.10 and figure 4.11, the holding time of 15

minutes at 500 ºC in during heating up of the preforms was latter increased to 30 minutes as displayed in figure 3.09.

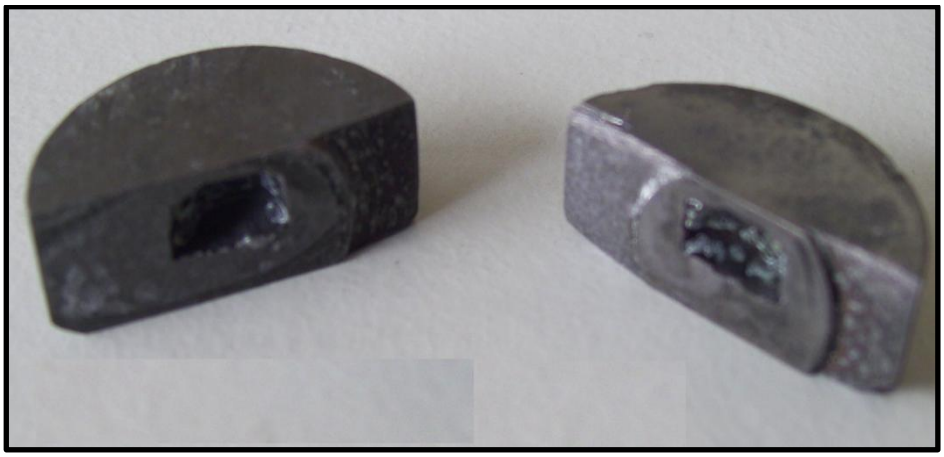

Figure 4.10: Cross sectioned view of composite-III, infiltrated at 1300℃ for 5 minutes with a non-infiltrated volume in the middle region.

The trend for delayed infiltration of the volume at the centre of the end face of cylindrical pellets was early reported in melt infiltration of AlN preforms of with molten Al in vacuum[46]. The infiltration irregularity shown in figure 4.11 comes from insufficient time for complete infiltration at the given temperature, sound melt infiltrated samples would be obtained after longer time at high temperature.

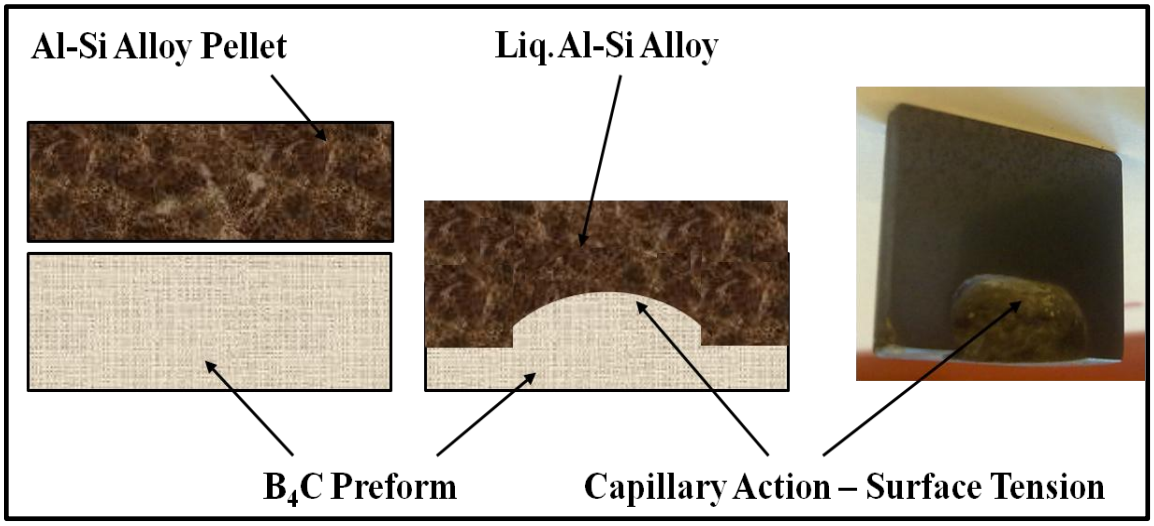

Figure 4.11: Cross sectioned view of the composite-I, infiltrated at 1300º C for 5 minutes with a depression of the liquid Al-Si alloy surface due to slow down of infiltration acted by surface tension forces.

In the temperature range of 1000-1350 ºC liquid Al, as other molten metal has low values of dynamic viscosity of 0.6-0.8 mPa.s which compares to the viscosity of water at room temperature [79]. The viscosity of Al-Si alloy is higher than that of pure aluminium, due to presence of Si in liquid Al. The surface tension of Al-Si is slightly lower than that of pure Al due to the higher melting point of Si than Al. The decreasing of surface tension in the alloy with increasing temperature is similar to pure Al. It is the contact angle of the molten Al on the B_4C surface that must display the most net dependence on temperature and composition of the Al alloy[8].

During the initial preparation of green bodies, the B_4C powder was granulated as described in section 3.1. Binder accumulation and later removal during heating may create pores and cavities by internal differential shrinkage around binder masses. Other lumps of organic contamination of the as supplied powder, namely graphite flakes, or from any other source will also create similar voids in the internal structure of the pellets. At the surfaces of such pores as well as in the planes of internal flaws there is discontinuity of the regular B_4C particle coordination and packing fraction. The concave meniscus of the molten Al-Si alloy disappears; the movement of the melt under the surface tension forces ceases or has local deceleration leaving unfilled volumes being as those seen in figure 4.12.

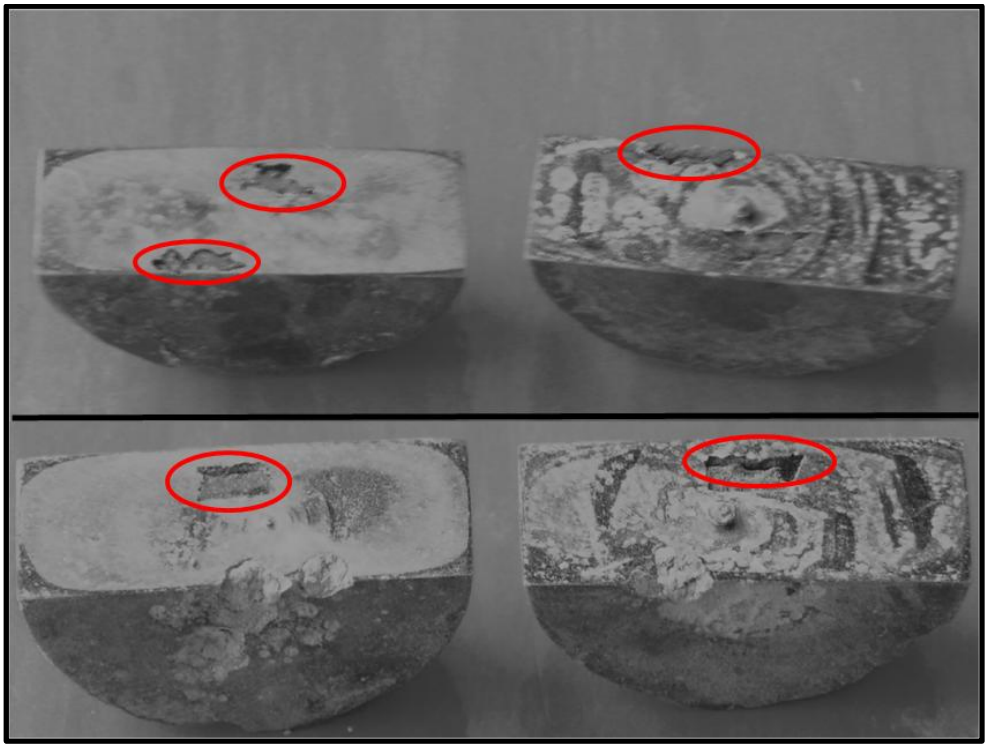

Figure 4.12: Cross sectioned view of two composites with irregularly shaped flaws with non-infiltrated volumes– composite VI (top) & VII (bottom)

4.4. Structural evolution and characterization of the composites

Three fully infiltrated composites of batches II, IV and VIII referred to as A, B, C respectively, were selected for the microstructural characterization in the following sections with the aid of XRD results, SEM/EDS, optical microscopy and determination of mechanical properties of indentation hardness and indentation fracture toughness by Vickers hardness testing. In this section composites A, B and C are analysed for the microstructure, formation of phases and the chemical composition of the crystalline phases. These properties are discussed with graphical representations of the reaction paths in ternary and quaternary phase diagrams. The preparation methods of the composites had been presented in chapter 3.

4.4.1 General characterization of the composites

Composites A, B and C were planned to have the estimated porosity of 50% whereas the actual values of relative density of the composites became 52.9%, 52.9% and 54.1%, respectively, after the uniaxial and isostatic pressing steps. The composition of the alloy, density of preforms and infiltration conditions for the preparation of composites were given before in Tables 4.03 and 4.04.

Composite A was prepared by infiltrating the 47.1% porous B_4C preform with the Al-Si alloy of nominal composition Al-25 wt% Si at 1300 ºC for 5 minutes. The composite appeared dense with smooth faces. It was easy to rub its faces for cleaning of the surfaces before performing any measurements. Composite B was prepared by the applying the same conditions of spontaneous infiltration with the Al-Si alloy of nominal Al-35 wt% Si composition. This silvery-white composite appeared dense and exhibited micropores on top and bottom faces where the excess of smelted alloy accumulated due the excess of about 10% of alloy above the required which was used in this batch. Unlike composite A, hard rubbing of the faces of composite B was needed for removing of the excess of the metals before making the measurements of properties of the composite on its surfaces. By changing the maximum temperature infiltration to 1200ºC with the same 5 minutes infiltration dwell, composite C was produced from a 45.9% porous preform of B_4C with

the twice smelted alloy of nominal Al-25 wt% Si composition. Composite C showed smooth surfaces without any surface flaws or defects.

The graphical representation of the heating schedules used for infiltrating the three composites A, B and C was shown before in figure 3.09. When ground by using silicon carbide grinding paper few minute particles had chipped out (those looked like powder). After grinding, polishing with diamond pastes and ultrasonic cleaning the cross sectioned faces of composite A showed small pores easily identified despite being minute and very shallow. After examination of composite A the dwell time at 500 ºC was increased to 30 minutes to improve the quality of melt infiltrated composites in the following batches. Observation of composites A, B, and C after the infiltration process confirmed that there were no noticeable changes of shape neither expansion nor shrinkage observable at the macroscopic scale. Measurement of the dimensions of pellets of composites A, B, and C confirmed the low increase in the volume of 0.61 %, 0.06 % and 2.04 %, respectively.

4.4.2 XRD and SEM/EDS analysis of the composites

In this section XRD and SEM/EDS results of composites A, B, and C are presented and discussed under separate subheadings. Chemical analysis and microstructural analysis of the composites were made by SEM/EDS. The phase composition of the composites in Al, Si and B_4C phases was plotted in ternary phase diagrams.

In the X-ray diffraction tests, the fractions of the crystalline phases were determined at the top (T), middle (M) and bottom (B) of the infiltration track after cross sectioning the pellets along their axis. All composites were composed of the dual metallic phase with Al and Si and the dual carbide phases, B_4C and SiC. The intensity of major XRD peaks of Al, Si, SiC and B_4C phases were measured at the diffraction angles 2θ between 38.50° - 39.50°, 28° - 29°, 36° and 38°, respectively. The weight fraction of each of these crystalline phases in the composite was calculated by applying the quantitative XRD method with standards previously described in section 3.4. By accounting for the values of density of the crystalline phases the weight fractions were converted to the corresponding volume fractions of the phases present in the composites. Volume fractions of phases are

directly correlated to their area fraction in polished cross-sections and to the dependence of elastic modulus and hardness on the phase composition of the composites [14]. Ternary phases of the B-Si-C and Al-B-C systems were only found in minor or trace amounts in the cross sections of the composites. The mechanically harmful binary Al_4C_3 phase could hardly be detected in the XRD results of the composite A.

Table 4.05: Volume fraction of the three main phases of the composites on different zones of the longitudinal cross sections of the melt infiltrated pellets: top (T), middle (M) and bottom (B).

Zones	Composite A (vol%)			Composite B (vol%)			Composite C (vol%)		
	Al	**Si**	**B_4C**	**Al**	**Si**	**B_4C**	**Al**	**Si**	**B_4C**
Top	59.7	9.4	30.9	55.7	24.2	20.1	56.6	8.9	34.5
Middle	32.7	24.1	43.2	39.4	19.5	41.1	63.1	11.9	25.0
Bottom	48.7	20.8	30.6	42.8	15.1	42.1	50.6	18.1	31.3

In order to determine the reaction path in the Al-Si-B_4C ternary phase system as the evolution of phase composition inside the composites during reactive melt infiltration of the composites table 4.05 was prepared with the results of the quantitative XRD analysis, described in section 3.4, the source of this table 4.05 being given in Annexes A1 to A3. The volume fraction of the forth crystalline phase of the experimental system given in the Annexes A1 to A3, the SiC is not included in table 4.05 because it is present in much lower amounts and the volume fraction of SiC in all the three composites remained inside a narrow range of values between 3.5 vol% to 5.5 vol%. On the following sub sections, the volume fraction of three phases (table 4.05) is discussed with support of XRD spectra. The full collection of the XRD patterns of the A, B and C of Top (T), Middle (M) and Bottom (B) zones are in the Annex B.

4.4.2.1 Composite A

Figure 4.13 shows the XRD patterns of the top, middle and bottom areas of the longitudinal cross section of composite A which can be referred in Annex A1 as XRD

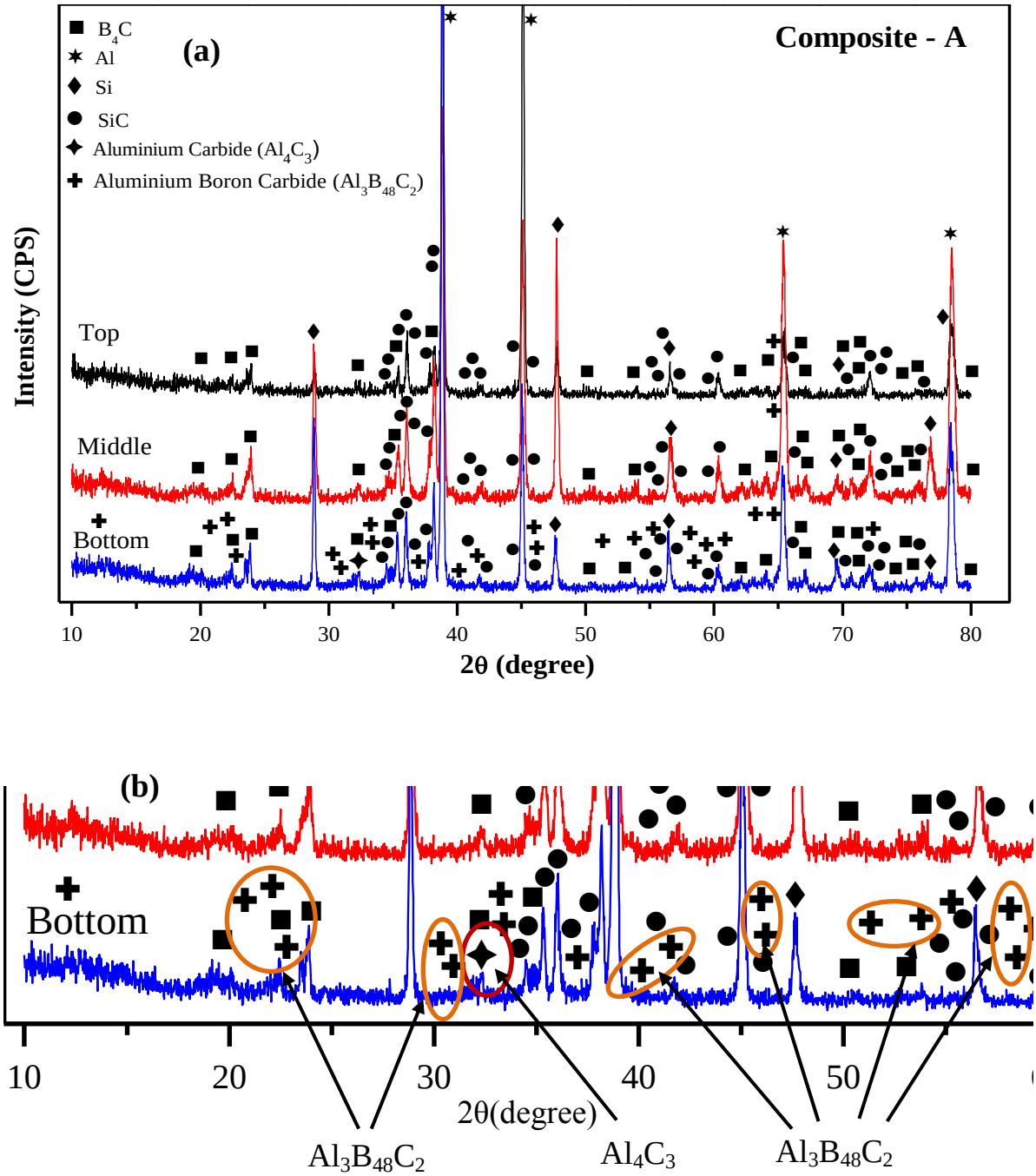

Figure 4.13: XRD patterns of the longitudinal cross section of composite A: a) from top (T), middle (M) and bottom (B) areas; b) Enlarged view of XRD pattern of bottom (B) zone, (✦) Al_4C_3 and traces of (✚) $Al_3B_{48}C_3$ (traces).

result 1. All major phases of the composites namely the Al, Si, B_4C and SiC are observed in the results of figure 4.13. The presence of ternary phases such as $B_{12.97}Si_{0.3}C_2$ and aluminium boron-carbide and of traces of the Al_4C_3 carbide cannot be discharged, but the main XRD peaks of such phases are found overlapping the XRD peaks of the main crystalline phases of the composites.

When comparing the intensity of main XRD peaks of Si and B_4C from the middle and bottom zones they are 3 to 4 times more intense than in the top face, which corresponds to lower concentration of Si and B_4C in the top of the pellet, Al having its maximum relative XRD intensity in the top area. Traces of boron silicon carbide ($B_{12.97}Si_{.03}C_2$) were also noticed on the bottom region (B) of this composite, but they are faint and are not pointed on figure 4.13 (b). Also, wherever the boron carbide is found on the bottom zone, the XRD lines of $B_{12.97}Si_{.03}C_2$ could also be identified. And these kinds of traces were only observed on the bottom (B) area, not on the other two zones (T) and (B). The analysis of SiC content in the three areas indicated that the peak intensity of SiC is high and close to that of B_4C despite the amount of SiC carbide being low, the relative fractions of the phases can only be assigned through the quantitative DRX method with standards.

At cooling state, with constant cooling rate of 50 ºC/min, Si crystallizes out of Al-Si hypereutectic alloy in the inter-particle spaces. The moving Si solidification interface separates the solid Si dendrites with low Al content from the liquid melt of composition increasingly rich in Al, shown in Al-Si phase diagram figure 2.09. At the binary eutectic point 577 ºC Al and Si metallic phases crystallize together the eutectic mixture of phases of the local solidification must have the average composition close to the eutectic point. Depending upon the heating schedule, furnace atmosphere, composition of the alloy constituents and of the B_4C preforms some of the ternary phases of the Al - B - C system may form. Those phases that can be distinguished in the XRD results in figures 4.13 are the $Al_3B_{48}C_2$ or $Al_3B_{12}C_2$ as given by reactions 2.02 and 2.03, respectively. These two phases may also form by the reaction between B_4C and Al_2O_3. Aluminium oxide or sub-oxide was present as a thin oxide coating on the bits of the smelted alloy due to contamination by the residual oxygen in the argon atmosphere of the furnace. However these reactions are not present in relevant levels as these compounds are found in traces only on bottom (b) area of composite A.

The EDS maps in figures 4.14 (a), (b), (c) and (d) give the distributions of the elements Si, Al, B and C in the phases that compose the microstructure of composite A. The metallic phases Si and Al in the microstructure are depicted in orange and green colours, respectively. A thin C coating was applied on the polished surface of the composite to avoid electrical charging in SEM. Because B and C are elements of low atomic number they are detected by the light element EDS detector but cannot be accurately quantified by EDS analysis.

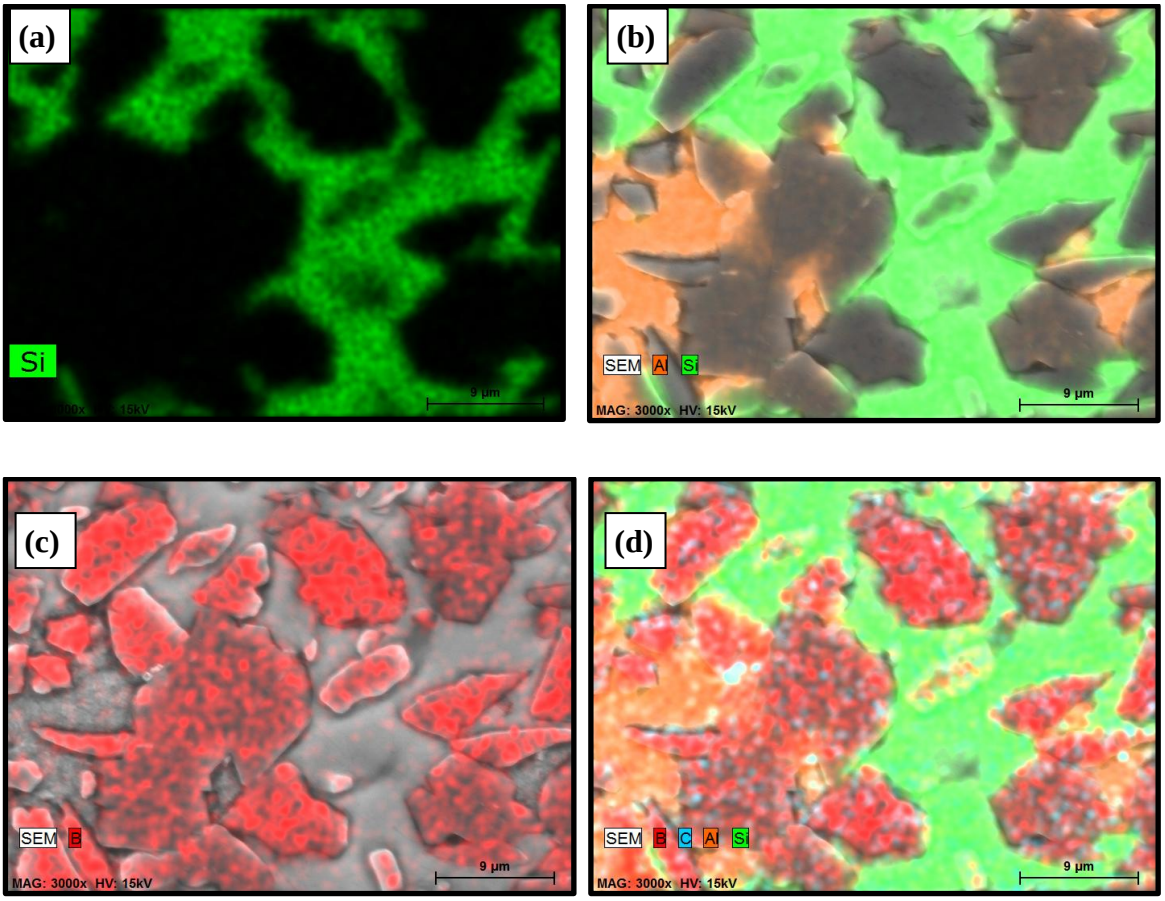

Figure 4.14: EDS maps of the elements of SEM microscopy of bottom zone of composite of A: (a) Si; (b) Al and Si; (c) B and (d) with all four elements Al, Si, B and C.

Figure 4.14 (c) shows the B in B_4C particles of the specimen in red colour and the C in blue stains. Figure 4.14 (d) indicates the joint dispersion of the same elements throughout the same area of analysis. The image of optical microscopy of composite A in figure 4.15 show clusters of the B_4C particles of polished hilltops surrounded the shining metallic phase.

By combining the EDS maps with the SEM image the main phases in the microstructure of the composite A were identified as displayed in figure 4.16. The bright particles with roughed surfaces are Al. The particles of bright contrast and smooth surface are Si. Those of darker contrast and faceted contours are of the B_4C phase.

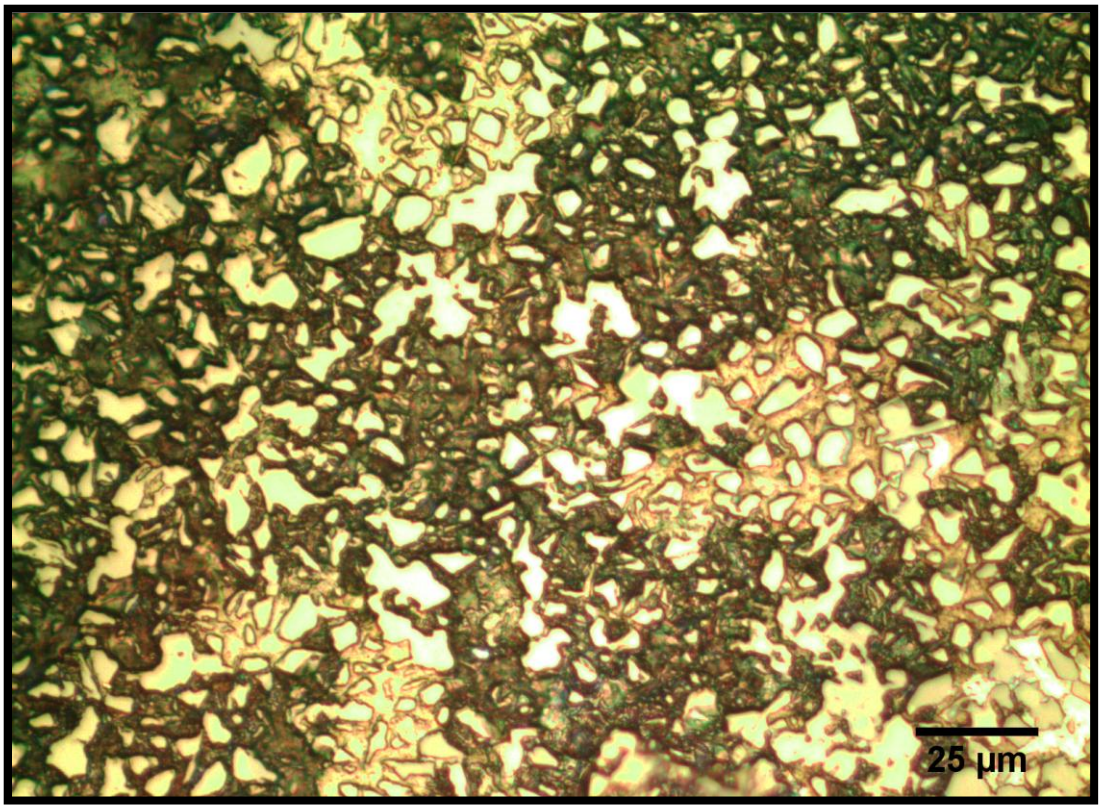

Figure 4.15: Image of optical microscopy of composite A.

Some precipitates of B-Si based phases appear in the Si-rich areas. The Si content inside the Al-rich areas of the solidification eutectic liquid is insufficient to be revealed in the EDS maps.

SEM/EDS analysis was done on all three areas (T, M and B) of the longitudinal cross section of composite A, similar distributions of the elements and crystalline phases as those shown in figures 4.14 and 4.16 having been observed. Corresponding to the results in Annex D1 and table 4.05, the SEM image and EDS analysis of top area revealed that B_4C particles were most often in contact with the Al phase than with Si. The 51R (moissanite) SiC phase has a strong covalent bonding as the boron sub-carbides and provides high hardness to the composites. If the B_4C particles decompose to form the $B_{13}C_2$ sub-carbide, also known as the super hard phase of boron carbide, the hardness would be nearly doubled in relation to the value of B_4C [80]. The presence of the above harder phases is revealed by the abnormally high values of Vickers hardness on the M zone of composite A.

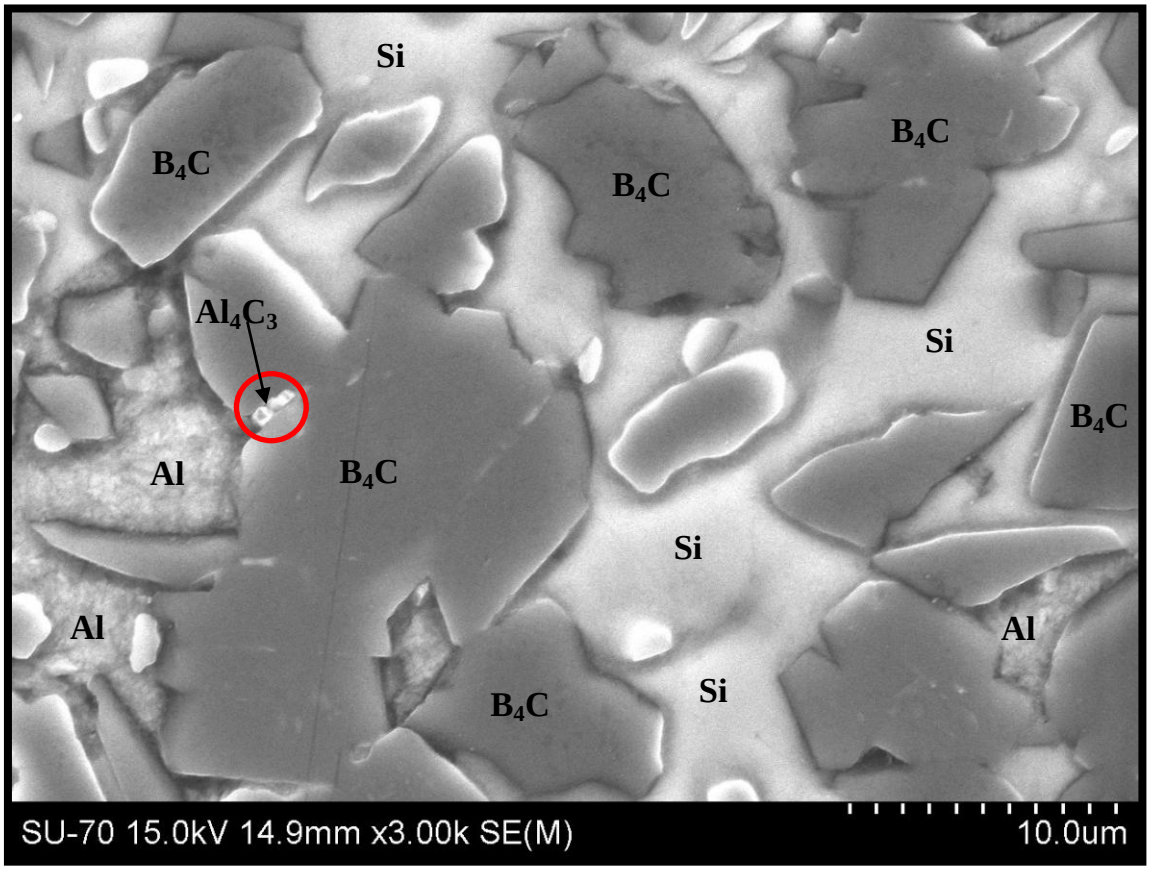

Figure 4.16: EDS map of the elements of SEM microscopy of bottom zone of composite of A.

On the middle (M) area of composite A (Annex, figure D2) the elemental analysis showed that at few points two times less Si was detected than Al and it formed small to medium

sized areas. The B_4C particles were generally distributed throughout the microstructure and SiC and boron carbide being also seen here in agreement with XRD/EDS results (Annex D, figure D2). The EDS analysis showed that at some points there is much high concentration Al in the overall chemical composition of M area which seemingly does not have a sufficiently homogeneous distribution of the elements.

On the bottom (B) area of composite A, B_4C particles are of comparatively large and medium sizes according to the figure 4.16. Metallic Si particles are encroached throughout the B area. At few places of the concentration of Al is negligible which indicates heterogeneity of the distribution of the elements this area too. Particles of B_4C often became isolated at the elevated temperature of reactive melt infiltration; hence the reaction of Si with B_4C and the C (graphite) it bears allowed the formation of new phases as indicated by the XRD results (Annex A1). As per EDS results, it was found in a few places with negligible amounts of Al that the values of the concentration of Si, C and B were close to 3:2:1 ratio respectively. Hence decomposition of B_4C would have contributed to the formation of binary and traces of ternary phases. B and C were seen throughout the (B) area especially where some Al was accumulated. Those conditions could lead to precipitation of the new ternary phase $Al_3B_{48}C_2$. It was also in the (B) area that presence of the fragile Al_4C_3 carbide was noticed as indicated on the figure 4.16. Out of the three composites of the study, only in composite A alone there was a traceable amount of the Al_4C_3 carbide; and confirmed by the EDS/SEM, figures 4.14 and 4.16.

Viala et al reports that when comparing the chemical stability of Al_4C_3 and SiC carbide phases the SiC phase is more stable provided that a certain Si concentration is maintained in the Al-Si molten alloy. In a homogeneous mixture of Si, Al and B_4C under an inert atmosphere the minimum content of 12 wt% Si in the alloy is needed to prevent precipitation of Al_4C_3 [81]. As given by Eq. 2.02 to Eq. 2.04, such decrease of Si in the metallic liquid is caused by the reactions of Si with graphite or with B_4C which primarily yield SiC along the track of the reactive melt in the infiltration of B_4C preforms [76]. Hence, if the Si content in the molten Al-Si alloy becomes lower than such threshold of 12.6 wt% Si previously formed SiC may react back with Al and precipitate the Al_4C_3 phase. However, *Frage et al* have found that the formation of Al_4C_3 could only be inhibited in the Si-Al-B_4C system by adding around 40 wt% Si [76].

4.4.2.2 Reaction path in the Al-Si-B_4C ternary diagram

The evolution of the phase volume fractions from the top (T) to the bottom (B) of the longitudinal cross section of the pellet of composite A as given in table 4.05 is plotted in the Al-Si-B_4C ternary phase diagram in figure 4.17. In which the two nominal proportions of Al-Si alloy involving in these composites were indicated by blue lines and the red line denotes the eutectic limit of 12.6 wt% Si. This figure also includes the corresponding plots for composites B and C which are discussed further below. B_4C is about 31 vol% in (T) and (B) areas of composite A whereas it rises to about 43 vol% in the middle (M) zone of the pellet.

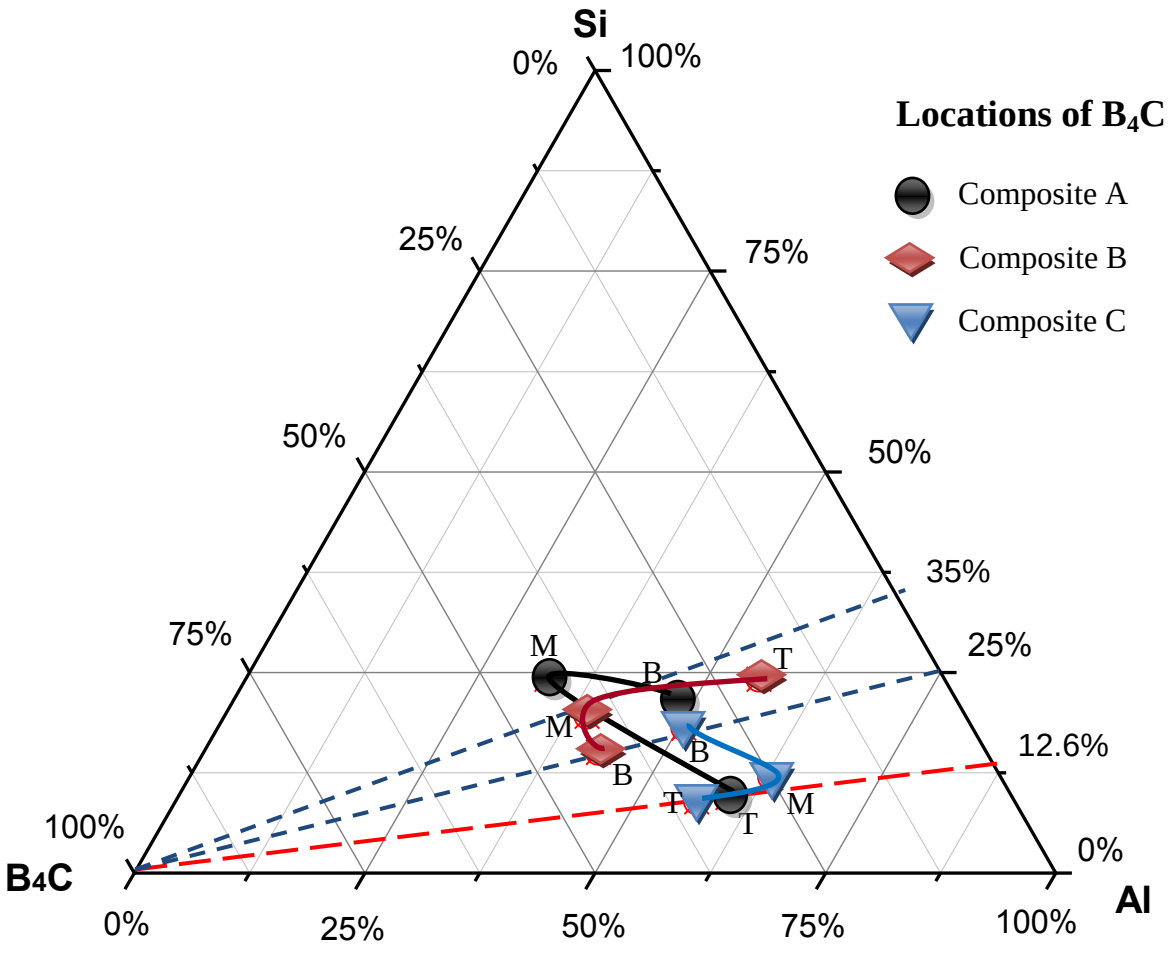

Figure 4.17: Plot of the phase composition in volume fraction in Al-Si-B_4C ternary phase diagram, at (T) top, (M) middle and (B) bottom areas of the longitudinal cross section of composites A ( ), B ( ), and C ( ) .

On the initial area of infiltration the phase volume composition had nearly 2/3 of Al metal whereas the content in metallic Si was only about 9%. The content of metallic Si increased to 1/4 and 1/5 in middle and bottom portions of the composite, respectively. The significant point is that the Al:Si ratio in the alloy taken for this composite was 3:1; hence the content in metallic Si of the alloy that fills the inter-particle spaces in the middle and bottom areas of composite A is comparatively higher than in the original alloy.

4.4.2.3 Composite B

The alloy of nominal content of Al-35 wt% Si was used in the preparation of composite B. In all three positions (T, M and B) of the specimen the phases of Al, Si, SiC and B_4C were found as shown in the XRD spectra in figure 4.18, also referred to in the table in Annex A (table A2 , XRD result 1).

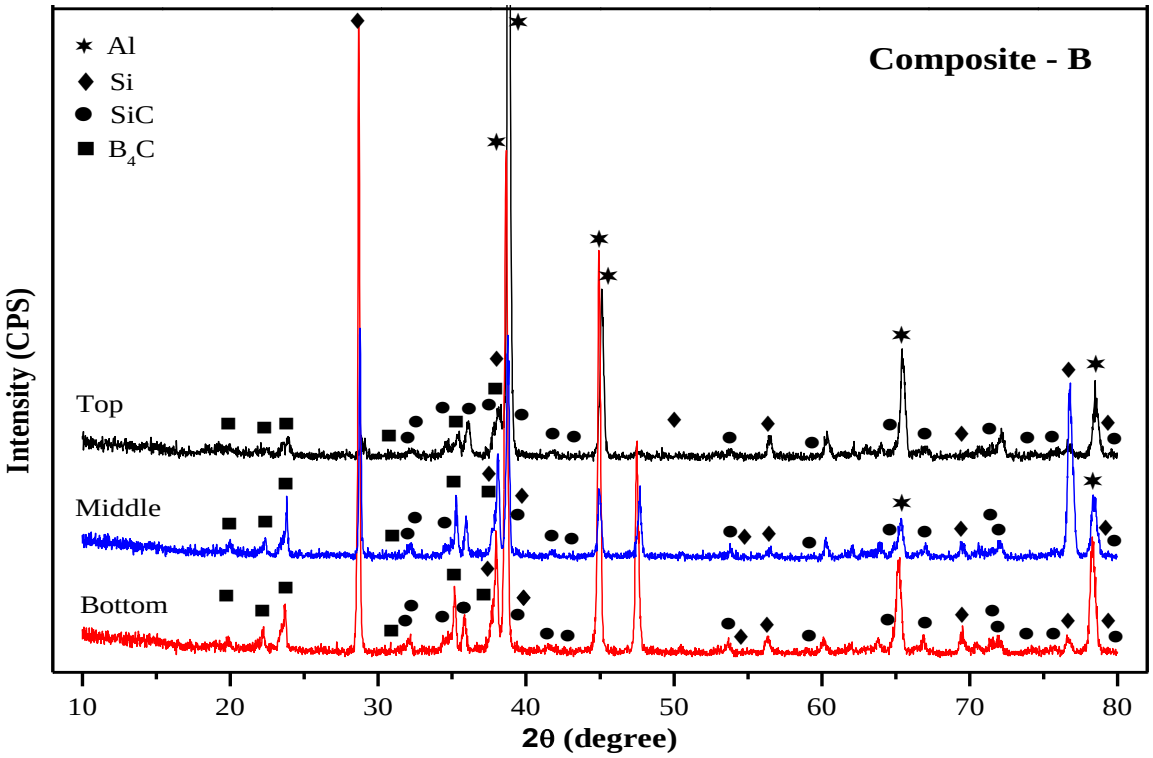

Figure 4.18: XRD spectra of the top, middle and bottom areas of the longitudinal cross section of the pellet of composite B

The intense XRD peak of Si in the (B) side is of about 23 and 9 times the relative intensity of the same peak in (T) and (M) areas. The intensity of the main XRD peak of Al follows the opposite trend, as shown in figure 4.18. Primary peaks of B_4C and SiC of the (M) and (B) areas have similar relative intensities whereas at the top (T) regions they are of low intensity. The formation of SiC is given by Eq. 2.01 and 2.03. The Al-Si alloy used for reactive melt infiltration of composite B has the nominal content of 35 wt% Si, the presence of the fragile Al_4C_3 being less probable in this composite according to the threshold of 12.6 wt% Si set by *Viala et al, [81]*section 4.4.2.1.

The EDS maps in figure 4.19 (a), (b) and (c) give the distribution of the elements Al, Si and B respectively, in the microstructure of composite B. Figure 4.19 (d) combines the

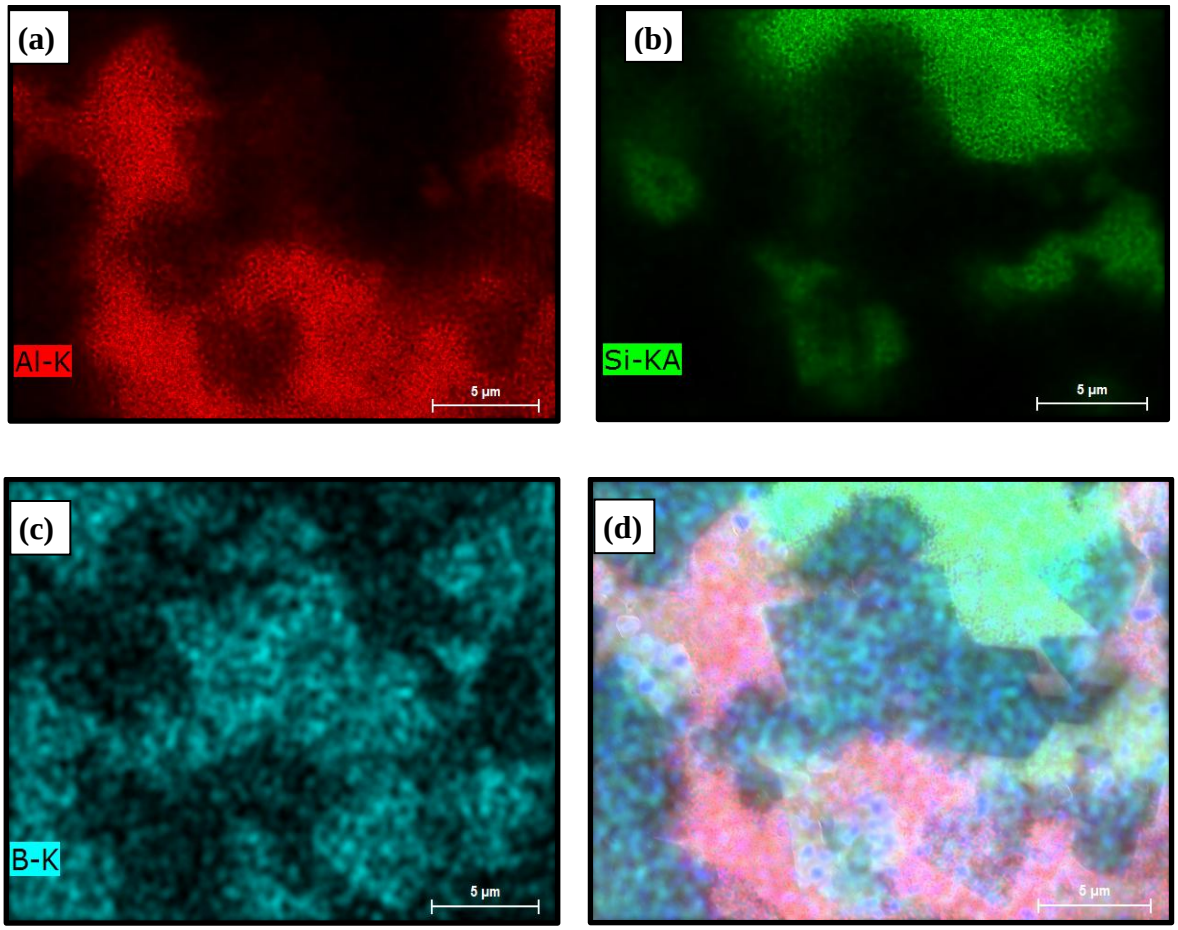

Figure 4.19: SEM microscopy of composite of B with EDS maps of (a) Al; (b) Si, (c) B and (d) the full set of the elements Al, Si, B including C from top (T) area.

EDS maps if the same three elements with the mapping of C. The image of optical microscopy of the same composite B is given in figure 4.20.

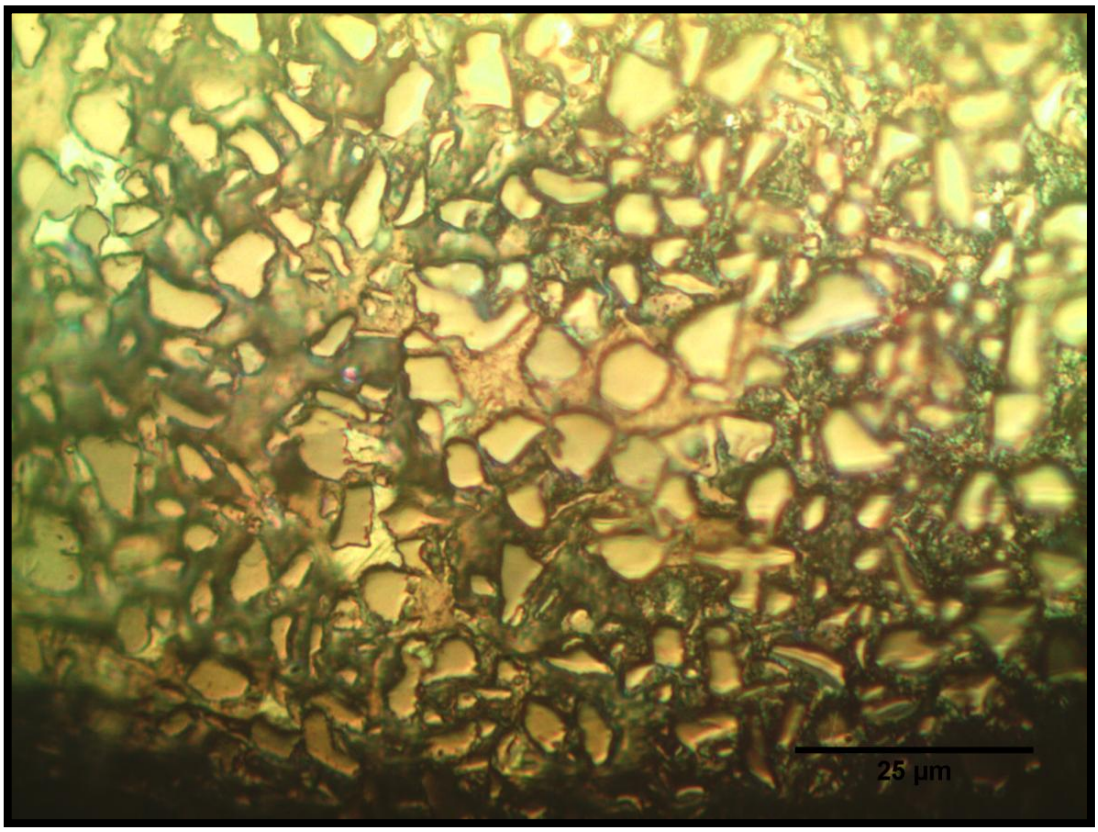

Figure 4.20: Image of optical microscope of a specimen of composite B.

The microstructure of the (T) top zone of composite B is shown in figure 4.21. It corresponds to the same area of the EDS maps in figure 4.19. The crystalline phases are labelled in figure 4.21 in correspondence to the EDS maps and their relative volume fractions determined by XRD given in table 4.05 and Annex A2. The gray scale of contrast, the morphology of the particles and the their distribution closely follow the trends observed in composite A, in figure 4.16 above, the contrast being higher in figure 4.21. The general details for the identification of the phases as given in figure 4.21 are not

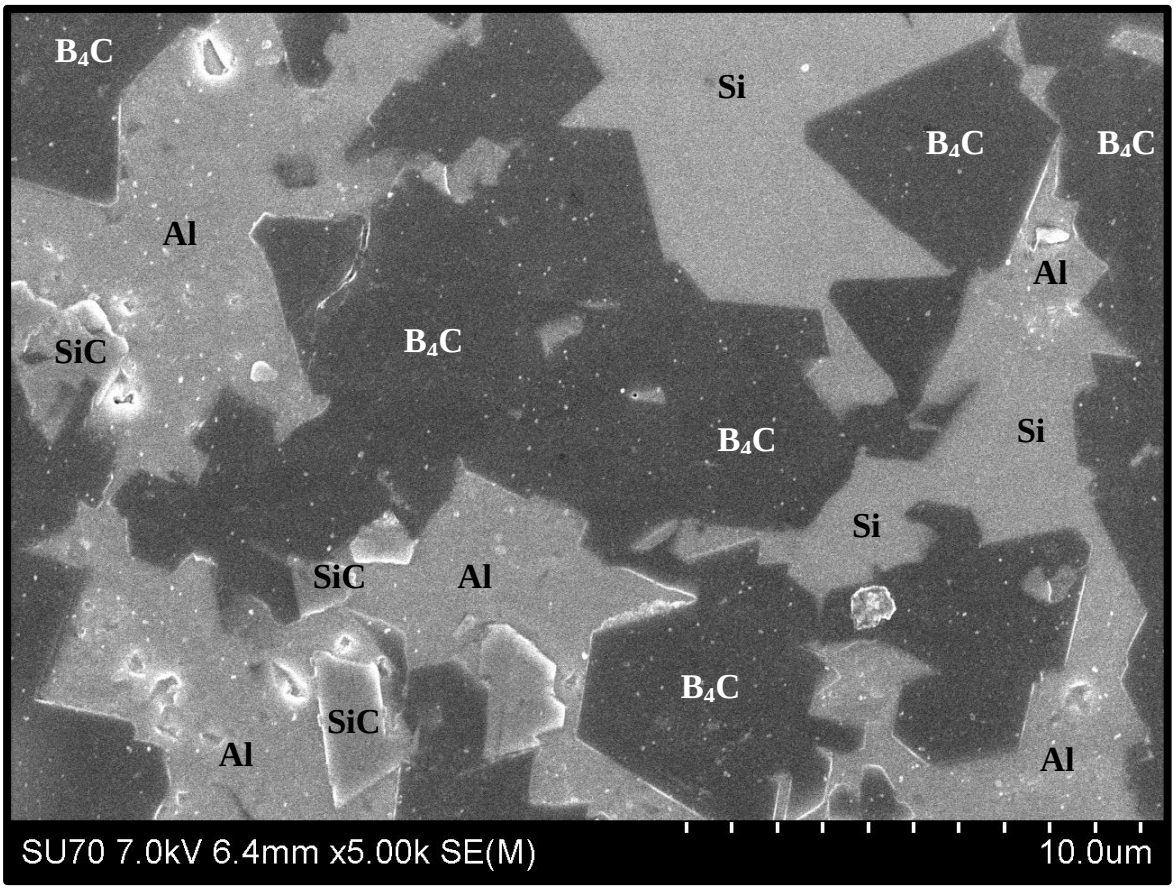

Figure 4.21: SEM image of a specimen of composite B from Top (T) zone. *(Courtesy of MSc Bruno A. Almeida, RNME - Rede Nacional de Microscopia Eletrónica)*

repeated here. Isolated particles tentatively identified as SiC nucleated on surfaces of the B_4C grains are observed in figure 4.21. There is also a widespread distribution of small particles with white contrast in the SEM image of this figure seen as the result of a defective C coating deposited before the SEM/EDS analysis.

In the more general case, the SEM/EDS analysis of composite B revealed a fairly homogeneous distribution of phases in three areas (T, M and B) of the longitudinal cross section of the composite.

When analysing the same top (T) area based on the EDS/SEM spectra given in Annex-D, (figure D3), the EDS indicates a limited of Al content and also a low amount of Si whereas the concentration of B and C elements were comparatively higher. On this top area, B_4C is present as the phase of composition $(B_{10.4}C_{1.6})(BC_2)$. The 15R SiC phase was also observed

along with residual amounts of other phases of the Al-Si-B-C system, in agreement with XRD results in figure 4.19 and observation of SiC and B_4C particles in the microstructure shown in figure 4.21.

In the middle (M) and bottom (B) areas, the concentration of the Si and Al elements given by EDS analysis were nearly equal (Annex D, figure D4 and D5). Small particles of light gray contrast show Al, Si and C. Many particles in this area are constituted by just Si, confirming the XRD results. The formation of 15R SiC was confirmed by EDS. A strong lump of boron carbide was also observed, the result of the reaction of decomposition of B_4C, eq. 2.05 either during the infiltration or at the early stage of synthesis of the B_4C compound.

The data in table 4.05 related to the change of phase composition from the top (T) to bottom (B) area of the cross section of composite B is plotted in the ternary phase diagram of figure 4.17 above. The volumetric fraction of B_4C phase determined in the top (T) area is around 1/2 of the corresponding values at the middle (M) and bottom (B) areas. The opposite holds for the change of Al volume fraction with position; whereas Si has a regular decrease from 25 vol% at the top (T) to 15 vol% at the bottom (B) area of the composite B. Similarly to the composite A, composite B also has the largest Al volumetric fraction of the Al phase at the top. At the top of composite (B) there are mostly metallic phases, the Al (55 vol%) and a fair amount of Si (24 vol%).

4.4.2.4 Composite C

In the XRD results of composite C of figure 4.22 the four major crystalline phases, Al, Si, B_4C and SiC were found as in composites A and B, but none of the previously detected ternary phases could be observed in a significant level in the XRD spectra of composite C. A twice smelted Al-Si alloy with the nominal content of Al-25 wt% Si was used for this infiltration, the actual Al content in the alloy being higher than the nominal value, table 4.03.

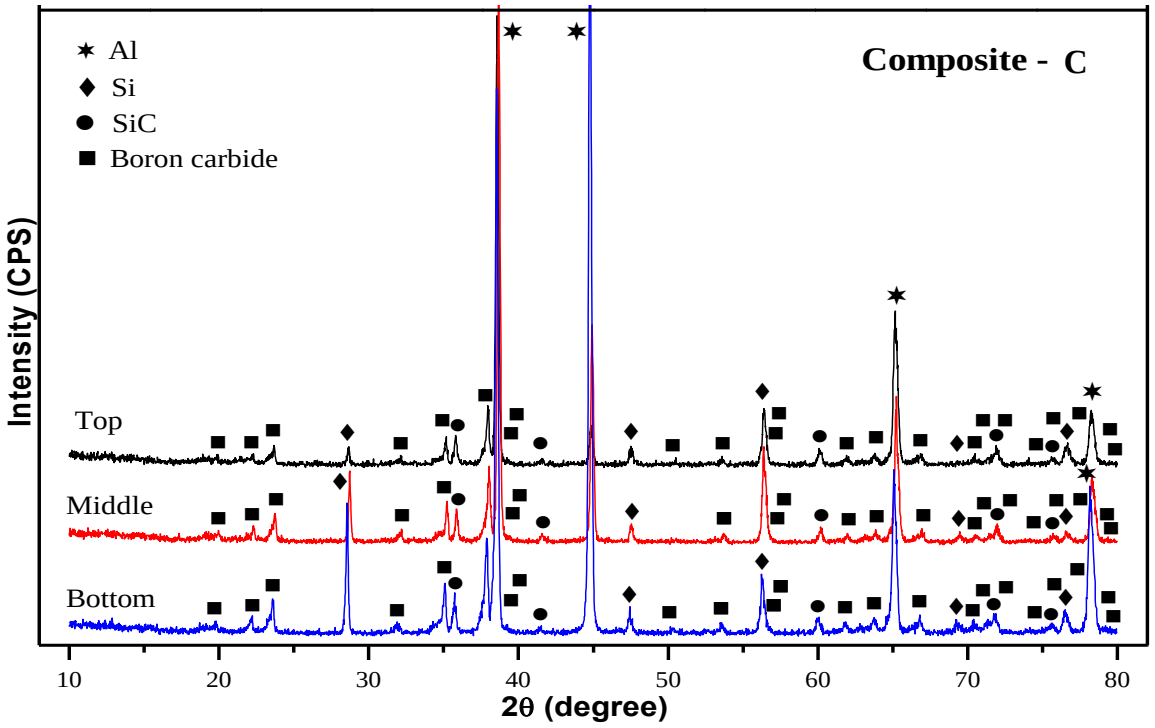

Figure 4.22: XRD patterns of top, middle and bottom areas of the longitudinal cross section of composite C.

The presence of Al dominates the DRX spectra of composite C in all the three areas (T, M and B) shown in figure 4.22 and the details on intensity of the DRX lines for the same phases can be found in the Annex A (table A3 - XRD result 1). Alike the other two composites, the intensity of Si peaks found on the top area are comparatively lower than in the following areas. The main XRD peaks of the B_4C and SiC phases have gradual increments in intensity from (T) to the (B) area. All the three areas have formed the regular 15R SiC phase, and the boron carbide phase is present as $(B_{10.4}C_{1.6})(BC_2)$ which is of stoichiometry close to the chemical formula of the compound B_4C.

The infiltration temperature of 1200 ºC allowed the development of a more regular microstructure where it was hard to find any traces of the Al_4C_3 carbide. The quality of the alloy was also improved by twice smelting and it might have provided more homogenous distribution of the elements in the alloy thus yielding an additional contribute to the regularity of the structure of composite C, noticed by the homogeneous distribution of phases in SEM observation. Both, the low temperature and the homogeneity of the alloy may have prevented the precipitation of the Al_4C_3 carbide phase which is supported by the

work of *Halverson et al*, where Al_4C_3, AlB_{12}, and $AlB_{24}C_4$ begin to form and become favoured at temperatures above 1200 °C during infiltration [8]. As dissolved Si in the alloy reacted with C present as the graphite or from reactions of B_4C forming the SiC the activity of C decreased. As the outcome of this interaction a stable, hard SiC carbide phase of low density was developed instead of Al_4C_3.

The EDS maps in Figure 4.23 (a), (b), (c) give the distribution of the elements Al, Si and B respectively, in the microstructure of composite C. The EDS map in figure 4.23 (d) shows the distribution of the full set of the 4 elements, C included, in the composition of this composite. The image of optical microscopy in given in figure 4.24 corroborates the regularity of the microstructure of composite C.

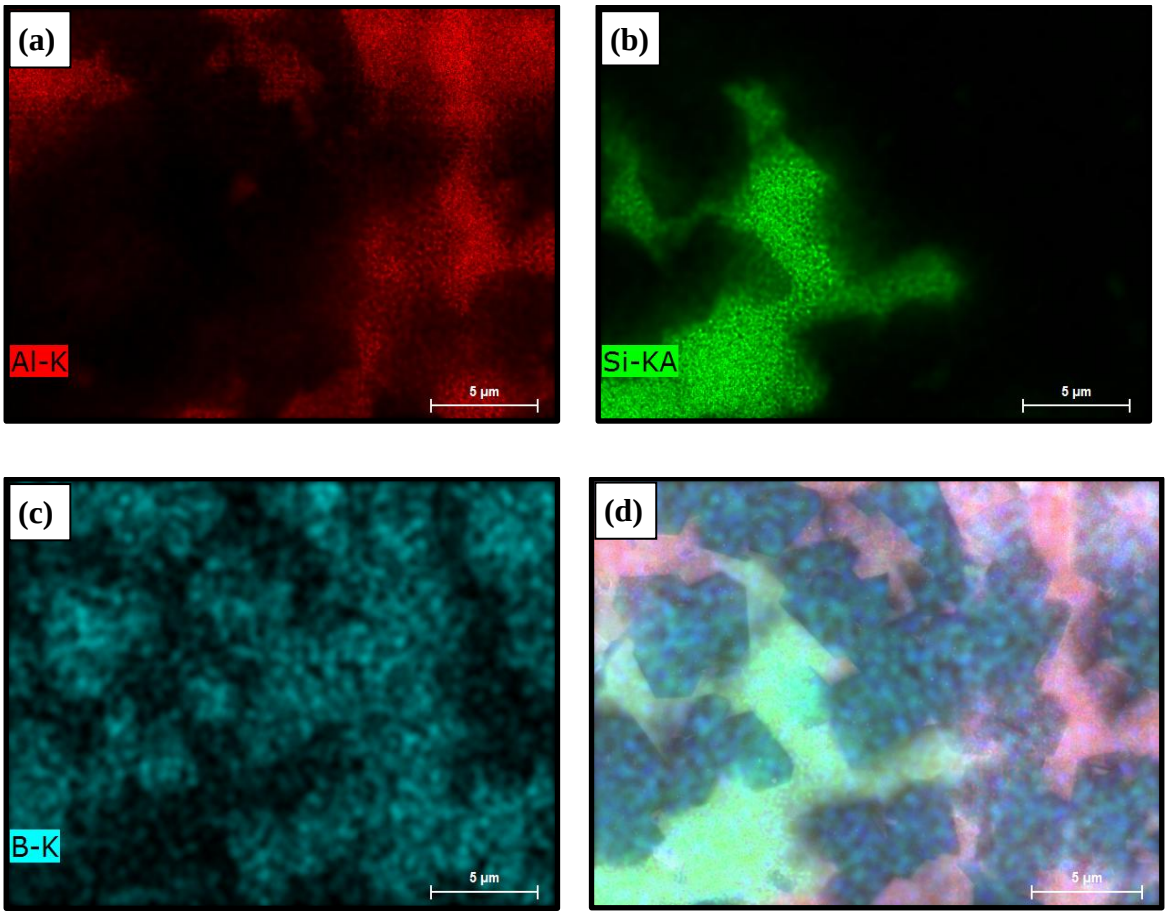

Figure 4.23: EDS maps of the distribution of the elements of composite C done by SEM microscopy: (a) Al, (b) Si, (c) B and (d) all the chemical elements Al, Si, B, including C.

As done before for the composites A and B, the EDS maps in figure 4.23 were combined with the XRD data of main crystalline phases of the composite, figure 4.22, and used to establish the composition of the different phases observed in the SEM image of composite C in figure 4.25. The contrast of the phases seen in figure 4.25, their morphology and distribution follow the same trends as those already described in figure 4.21 and are not repeated here.

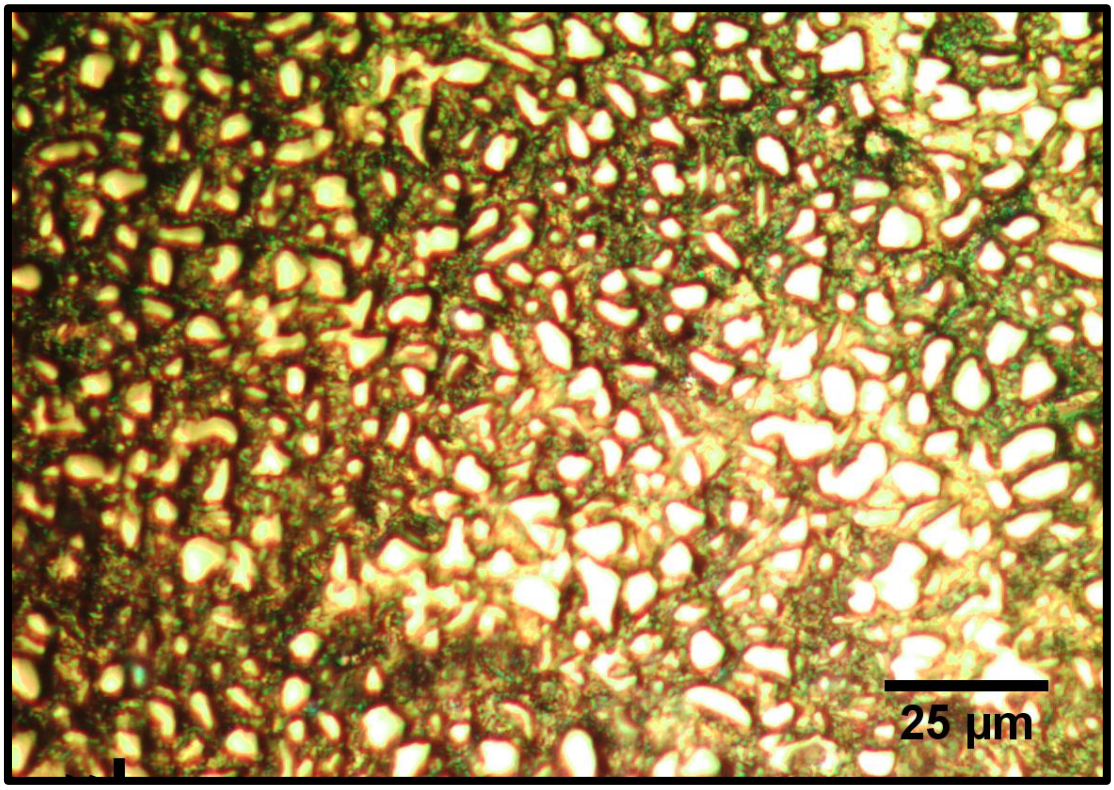

Figure 4.24: Optical microscopy image of composite C.

In more detail, the results of random point counting on the SEM images of figures 4.16, 4.21 and 4.25 yields the following indicative values for the approximate volume fraction of the B_4C phase in composites A, B and C, as 60 vol%, 57 vol% and 72 vol%, respectively. These values of the volume fraction of the B_4C phase are larger than the corresponding values determined by DRX using standards in table 4.05.

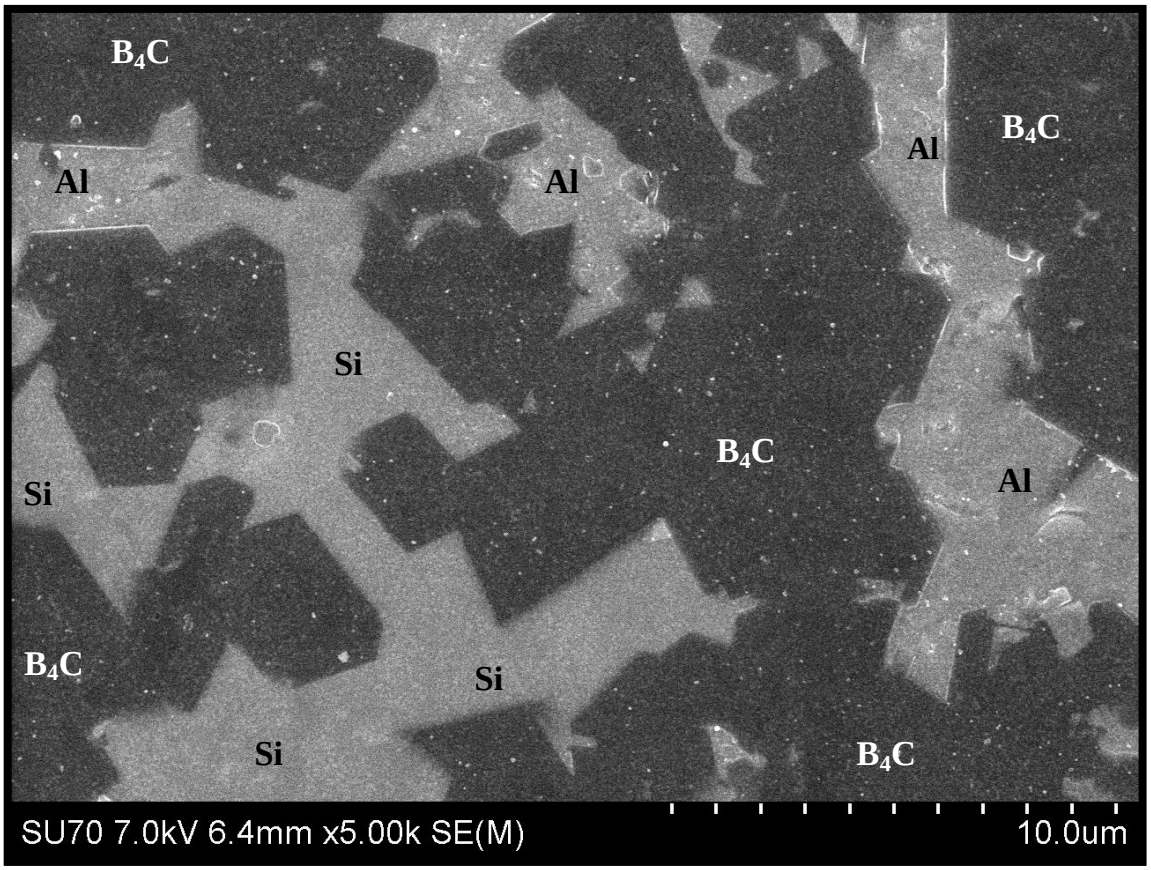

Figure 4.25: SEM image of a specimen of composite C from middle (M) zone. *(Courtesy of MSc Bruno A. Almeida, RNME - Rede Nacional de Microscopia Eletrónica)*

While analysing by EDS/ image the middle area (Annex D – Figure D7) of composite the cross section of the specimen of composite C large concentrations of Al and Si coupled to a lower concentration of B were observed. It must be taken into consideration that boron (B) fraction cannot be quantified by EDS without a large relative error. The EDS analysis showed that in some domains the Si particles occupied around 1.5 times more area than Al phase while in other SEM takes the fraction area of Al phase was 2.5 times greater than that of the metallic Si phase. Boron particles (B_4C phase) are widely dispersed in the middle area of the cross section in a proportion of about 2:1 compared to the area fraction of the Al and Si phases together.

The Al and Si elements also dominate the concentration of the elements in top (T) and bottom (B) areas. The same trends were observed in the Al and Si volume fractions in the XRD results of table 4.05 (Annex A3- XRD 1st result and images in Annex D figures D6, D7 and D8). Due to the comparatively low intensity of the DRX peaks of the B_4C phase in the standards, the volume fraction of B_4C determined by the quantitative XRD methods is seemingly underestimated compared to the area fraction this same phase occupies in the SEM image of the composites.

Based on the volumetric fraction of the phases of composite C in table 4.05, the change in phase composition from the top (T) to the bottom (B) areas of the composite are plotted in the Al-Si–B_4C ternary diagram of figure 4.17, above. The nominal composition of alloy taken for composites A and C was Al-25 wt% Si. A gradual increment of Si is found from the top to bottom areas of composite C. The maximum content of the Al phase is observed at the middle of composite C, whereas the converse trend was observed in composite A. In balance, the relative content of B_4C is lower in middle area, figure 4.17. Due to the accumulation of Al in combination with Si in the middle, the volume fraction of the B_4C was brought down. Hence the reaction of B_4C carbide with the Al-Si alloy was reduced.

4.4.3 Comparison of phase composition of the composites

Based on the prepared standards the volumetric fractions of the individual phases were determined for each composite (A, B and C) at the top (T), middle (M) and bottom (B) areas of the longitudinal cross section and are tabulated in Annex A. The average phase composition of each composite is given in table 4.06 together with the values of density calculated from the density of the phases and the average volumetric fractions of the phases in this table and the measured densities. The same values of the measured density were presented in table 4.04, section 4.3, above. The average volumetric phase fractions of the three composites are also plotted in figure 4.26.

Table 4.06: The processed parameters of composites with its calculated and measured densities and evaluated volumetric phase composition

Indication of Composites (with processed parameters)		**Phase composition of the composites** (vol%)				**Densities of the composites** (g/cm^3)	
		Al	Si	B_4C	SiC	Calculated	Measured
Al-25 wt% Si alloy infiltrated in 10μmB_4C preform at 1300°C - 5mins	**A**	44.6	17.2	33.0	5.2	2.60	2.55
Al-35 wt% Si alloy infiltrated in 10μmB_4C preform at 1300°C - 5mins	**B**	43.9	18.7	32.9	4.4	2.59	2.53
Twice smelted Al-25 wt% Si alloy infiltrated in 10μm B_4C preform at 1200°C - 5mins	**C**	54.9	12.5	29.3	3.3	2.62	2.55

The porosity of the preforms of the composites A, B and C was 47.1%, 47.1% and 45.9%, respectively. Increasing in Si content yields the decrease in density. The presence of metallic Si contributes to higher values of the Young modulus (E) of the Al-Si alloy; the effect of Si on density and E being nearly linear, provided the alloys are prepared in similar conditions [38]. The value of measured density of composite B reflects the effect of increased Si content in the Al-Si alloy of this composite in agreement with the corresponding calculated value of density. Theses composites are dual concerning both the metallic phase (with the Al and Si) and the main carbide phases (the B_4C and SiC). The XRD test discussed in section 4.2 showed that the actual composition of the Si-Al after smelting does not exactly correspond with the nominal values, table 4.03. Besides the difference in the actual composition of the Al-Si alloy, the modifications of the infiltration temperature (from 1300 ºC to 1200 ºC) and smelting times (twice for the alloy of composite C) led to relevant differences in the phase composition of the composites A and C. An analogous conclusion holds when composite B is compared with composite A.

Results in table 4.06 show a slight lower content of SiC in composite B compared to composite A, despite the XRD confirmed the higher Si content of the Al-Si alloy (30 wt% Si) of composite B. In composite C, the content in metallic Si is 12.5 vol% and the formation of SiC became about 3.3 vol%, a lower amount of SiC compared with the two other composites..

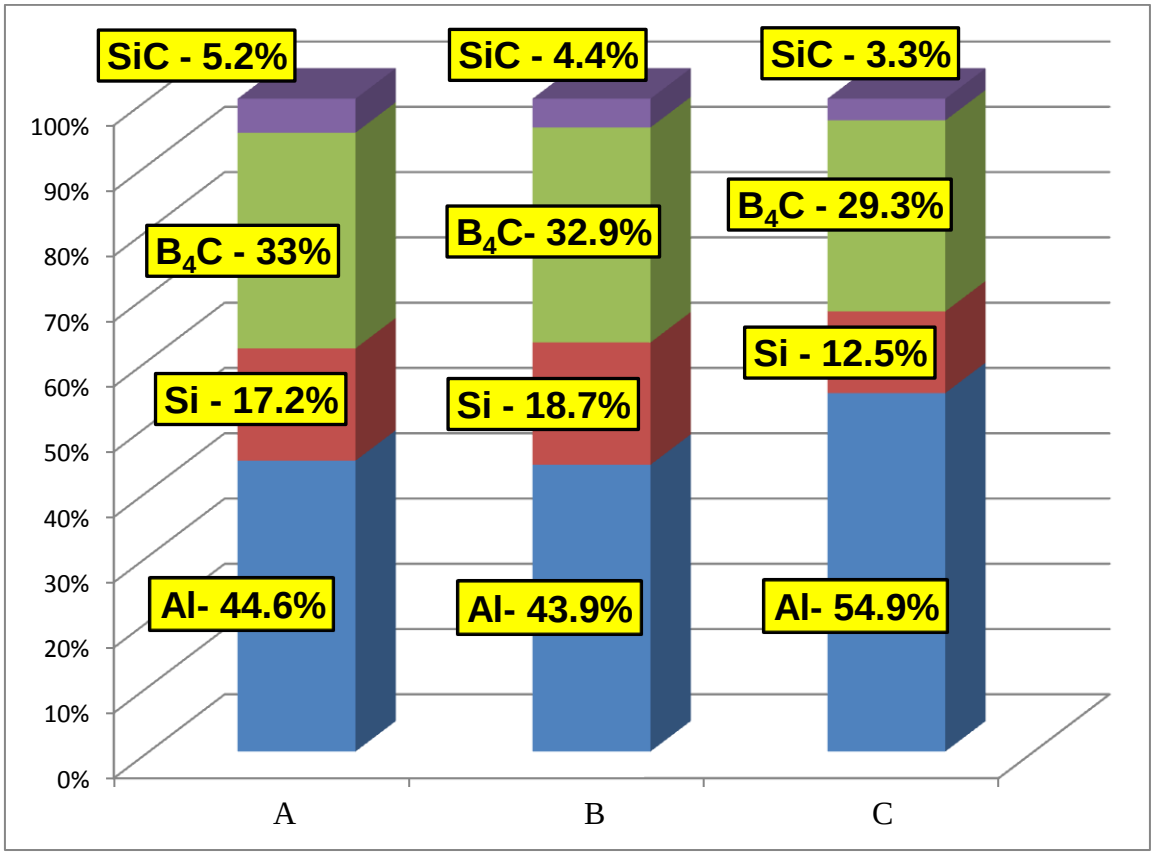

Figure 4.26: Average volumetric phase composition of composites A, B and C

Traces of binary and ternary phases of the Al-B-C ternary were found in the XRD results of composites A and B melt infiltrated at 1300 ºC; but, none of such phases was detected in the composite C. Within the limit of error of the quantitative DRX method applied to determine the fractions of the crystalline phases, such difference in SiC content may be the result either of the lower Si content in the alloy of infiltration of composite C or of less intensive reaction with the B_4C taking into account the difference in infiltration temperature.

The changes in phase volume fractions for all major (four) phases of the composites in the direction of infiltration are displayed given in figure 4.27 (a) and (b). To facilitate reading the graph is divided as two parts, (a) with the phase distribution of Al and B_4C and (b) with the Si and SiC phases.

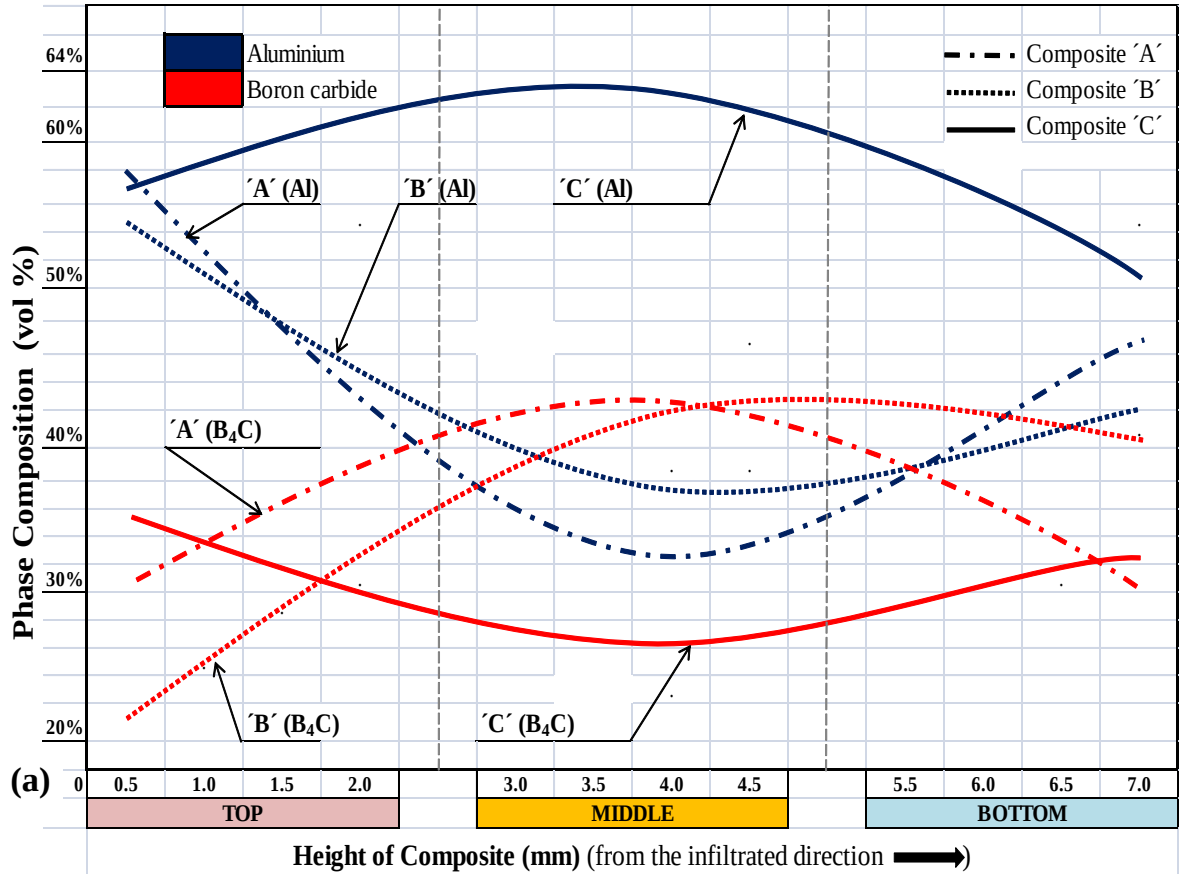

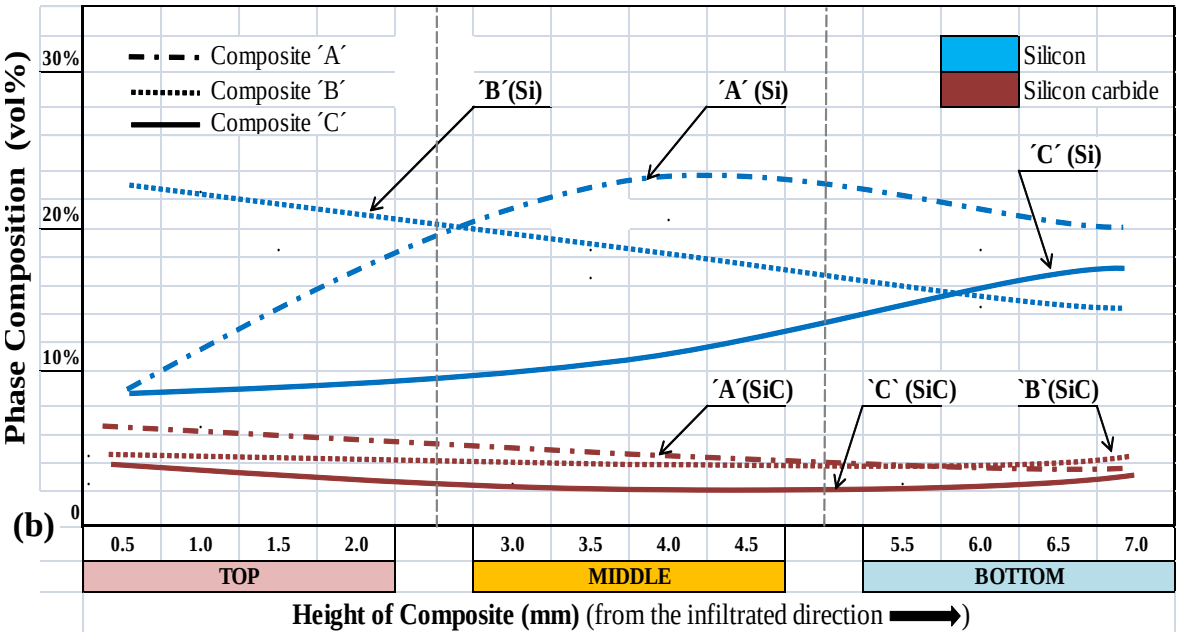

Figure 4.27: Distribution of crystalline phases in top (T), middle (M) and bottom (B) regions of the longitudinal cross sections of composites A, B and C: (a) Al and B_4C; (b) Si and SiC.

The concavity in the curves of concentration of Al in figure 4.27 (a) clearly indicates the reduction of Al phase in the (M) area of composites A and B whereas the inverse is observed for composite C, infiltrated at 1200 ºC. Such changes in the concentration of Al are symmetrical with the trends observed in the curves of concentration of B_4C. A large volume fraction of metallic Al is accumulated in composite C, especially in the (M) area. It is almost the double of the Al volume fractions in the corresponding (M) areas of the other two composites A and B. At the (T) and (B) ends of the composites the values of the Al volume fraction of the three composites are closer together.

As shown in figure 4.27 (b) the concentration of the Si phase of composite C regularly increased from (T) to (B), the opposite trend being observed in composite B. Composite A shows a maximum in Si concentration in the (M) area. Despite the differences in Si content of the Si-Al alloys used for the infiltration and in infiltration temperature, at the lower end (B) the volume fractions of metallic Si in the three composites converge to the same range of values. Within the experimental error of the method used for determination of the phase fractions, the values of SiC concentration found for all three composites A, B and C throughout the (T), (M) and (B) areas are very close to each other, a slight descent from (T) to the end (B) area being observed.

Two times smelted Al-Si alloy was used in composite C which would have provided higher fluidity to the alloy. In general, recycling the Al alloys reduce the fluidity of the alloy during smelting [82]. But, due to the Si added, the twice smelted fresh alloy would display improvement in fluidity from better homogeneity. The infiltration temperature was reduced from 1300 ºC in composites A and B to 1200 ºC in composite C; such drop in temperature would have further diminished effective wetting with the accumulation of some stagnant alloy in the middle of the pellet. The effect would be more visible would the relative density in the middle of the as pressed pellet be lower than the preform average density

4.4.4 Al-Si-C Ternary phase diagrams

The atomic fractions of the elements Al, Si and C present in each of the three composites A, B, and C were calculated from the phase volume fractions given in table 4.06. The mass of each phase of the composite in a fixed volume of reference (1 cm^3) is calculated from the volume fraction and density of the phase. As shown in table 4.07, the mass fraction of the phases were converted into the corresponding atom fractions by accounting for the molecular and atomic weights of the compounds and elements and that Si is present in the metallic Si and in SiC phases and C in SiC and B_4C phases. The calculated values of the atom fractions of Al, Si and C (normalized to unit) in composites A, B and C are given in the three columns on the right of table 4.07.

Table 4.07: Composition of the composites given by the atomic fractions of the Al, Si and C (in at%)

Composites		Al/cm^3	Si/cm^3	C/cm^3	Al	Si	C
		g	g	g	at.%	at.%	at.%
Al-25%Si + B_4C Infiltration at 1300°C - 5mins	**A**	1.203	0.518	0.231	61.6	26.5	11.8
Al-35%Si + B_4C Infiltration at 1300°C - 5mins	**B**	1.186	0.535	0.223	61.0	27.5	11.5
Al-25%Si (Twice fusion) + B_4C Infiltration at 1200°C - 5mins	**C**	1.483	0.366	0.192	72.7	17.9	9.4

The isothermal section at1000 ºC of the Al-Si-C ternary phase diagram [81] is represented in figure 4.28 (a) giving the indication about the liquids of the system at a temperature below the range of infiltration temperatures of this study, 1200 - 1300 ºC. The corresponding isothermal section of the same ternary system at 1497 ºC, above Si melting point (1414 ºC) is given as figure 4.28 (b). The projection of the atomic composition of the composites A, B and C is shown in figure 4.28 (b).

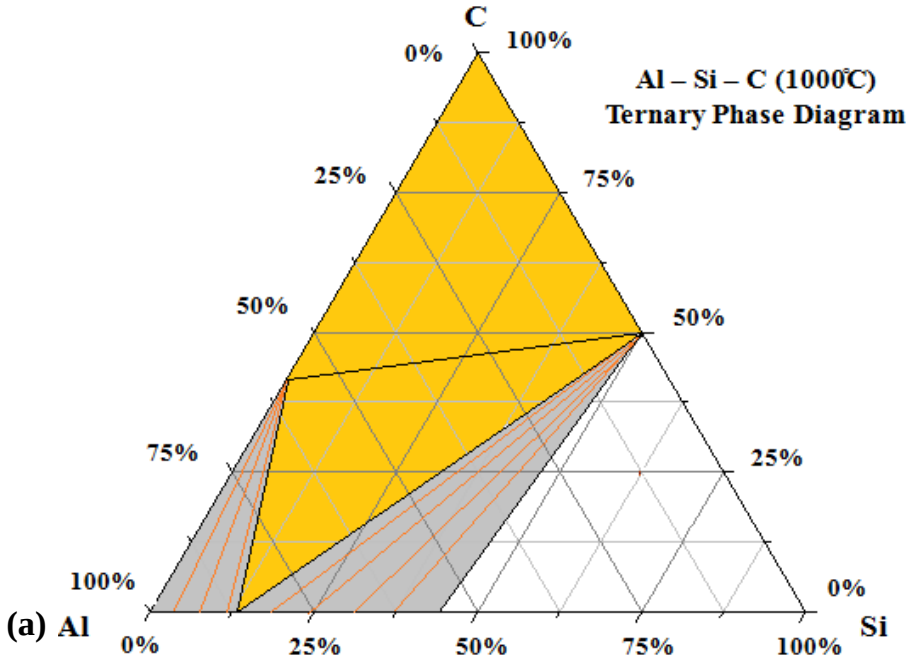

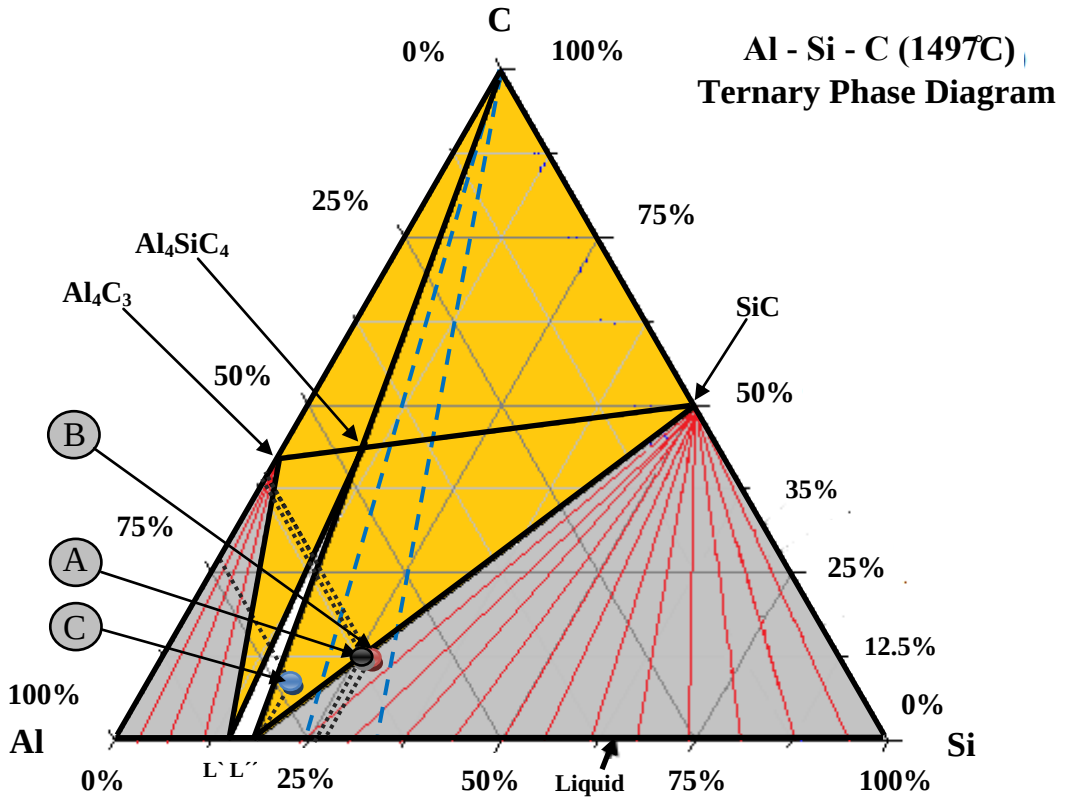

(b)

Figure 4.28: Al-Si-C ternary phase diagram adapted from Viala [81]: (a) Isothermal section at 1000 ºC; (b) Isothermal section at 1497 ºC with projections of the composition of composites A, B and C.

Traces of carbon found in liquids L' and L" of the metallographic study of *Viala et al*, shown in figure 4.28 (b), appeared to be just thin Al_4C_3 tiny particles. The carbon content of about 1 at% was observed in that region of the bulk of the metallic matrix [81].

Composites A and B display almost the same values of the atomic fractions of the elements Al, Si and C in their composition. In composite C, reaction of the alloy and the carbon was comparatively low (9.8 at% of C).

One of the reasons for the differences in table 4.07 and figure 4.28 (b) is, the high temperature enhances the chemical reaction rate which builds up the quick formation of SiC in composites A and B whereas in composite C the infiltration temperature parameter is 100 ºC lower than in the infiltration temperature of the other two composites. In the work of *Hayun et al* the presence of Al increased the solubility of boron in liquid Si. But, by increasing the Al content the activity of boron decreased, yet the solubility of the boron in the melt in equilibrium with B_4C increases [49], hence as a consequence the formation of a less stable phases and occurrence of a partially congruent process.

4.4.5 Al - Si - B -C Quaternary Phase Diagram

Disregarding impurities, the composition of all main phases of the present study are represented in the quaternary phase diagram defined by the elements Al, Si, B and C. Figure 4.29 is a tentative quaternary phase diagram which comprises of four ternary phase diagrams, in which Al-Si-C ternary phases of the isothermal section at 1497 ºC are indicated in blue lines, Si-B-C ternary phases boundaries in the isothermal section at 1480ºC were drawn in red, Al-B-C ternary phases of the isothermal section 1400 ºC were drafted in green lines and the Al-Si-B ternary phase diagram at 1300 ºC is laid on the bottom side of the quaternary one with the black dotted lines. Combinations of these four elements in different proportions render the various metallic, carbide, boride and boron-carbide phases, which will be found in this quaternary phase diagram. Several phases such as SiC, B_4C, $B_{13}C_2$, $B_{12}C_3$, Al_3B_{12}, $Al_3B_{48}C_2$, $Al_3B_{12}C_2$ $B_{13}SiC_2$ $(B_{10.4}C_{1.6})(BC_2)$, liquid Al and Si relevant for the present study are indicated in the figure 4.34. Other possible phases

of potential interest in relation to the future work may also be seen in this quaternary phase diagram.

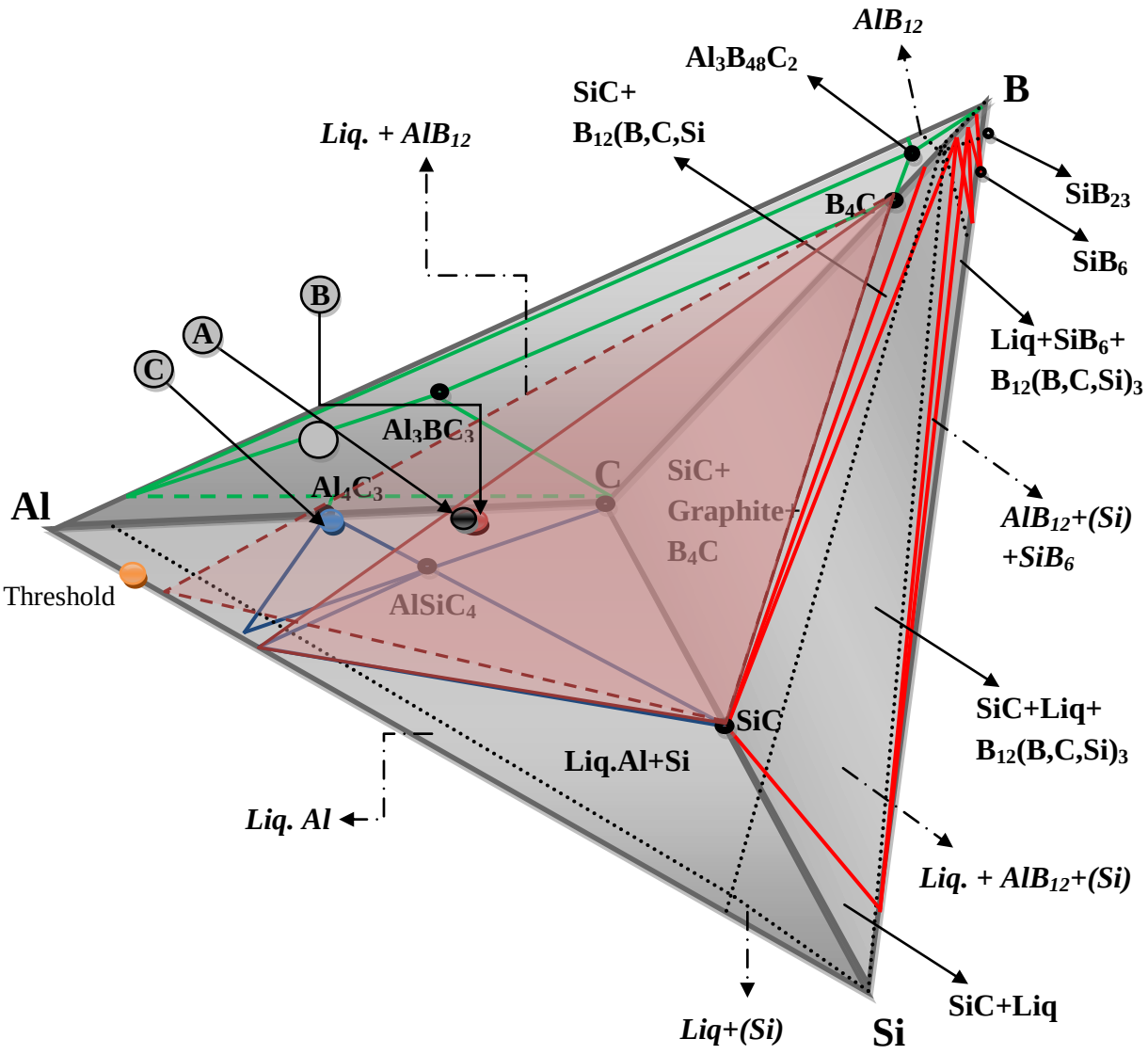

Figure 4.29: Isothermal section of Al - Si - B- C quaternary phase diagram (in at.%) between 1300 ºC -1497 ºC[81], [83-85]. *(Italic lettering with dotted lined arrow marks corresponds to the Al-Si-B ternary phase)*

During the reaction of molten Al with B_4C at elevated temperature some hygroscopic and mechanically weak phases, the Al_4C_3, Al_3BC and Al_3BC_3 may form. The bonding between the boron oxide layer and B_4C can be reduced by allowing the reaction of Al with B_4C and avoiding the Al_4C_3 formation at the interface as much as possible [67]. Between 900 ºC

and 1000 ºC, Al alloys have good contact angles with Si, C and SiC; this transition of temperature would collapse the passive oxide film or hinder the formation of Al_4C_3, or both [86].

Si introduced in the Al molten solution reacts with C precipitating SiC reducing the activity of C to such way that the reactions of formation of Al carbides are either reduced or even stopped [76]. If the boron reaction is slower in the composite due to the lower activity of Si and a high concentration of Al is maintained some of the less stable ternary phases of boron carbide and boron sub-carbides are formed. Hence, the role of Si is important for the composition of phases of composites made of reactive Al-Si melts and B_4C matrixes, and it should not decrease below the threshold of 12.6 wt% Si in the Al-Si alloy [81]. The phase $B_{10.4}C$ polymorph of the boron carbide at the boron-rich edge of the stoichiometry range of this compound is known as a high-boron solid solution of boron carbide. The relevance of this polymorph comes from the large cross section of B for neutrons with application in nuclear technology [12]. At room temperature the hardness of B_4C is only lower to diamond and cubic boron nitride.

The atomic fractions of the four elements Al, Si, B and C in the composite were calculated from the average of the fractions of the phases in table 4.06 by the same method used to establish the values of the atomic fractions in the previous table 4.07. The resulting values as the atomic fractions of the 4 elements are given in table 4.08. The values of C content of composites A and B are close together whereas in composite C it is definitively lower.

Table 4.08: Atomic fractions of the elements Al, Si, B and C in the overall composition of the composites determined from the phase volume fractions (table 4.06)

Composites	Al/cm^3	Si/cm^3	B/cm^3	C/cm^3	Density	Al	Si	B	C
	g	g	g	g	g/cm^3	at.%	at.%	at.%	at.%
A	1.203	0.518	0.652	0.231	2.604	46.2	19.9	25.0	8.9
B	1.186	0.535	0.650	0.223	2.594	45.7	20.6	25.0	8.6
C	1.483	0.366	0.577	0.192	2.618	56.6	14.0	22.0	7.3

The elemental composition of the composites in the quaternary phase diagram of figure 4.29 are coplanar with triangles of phases defined by the corners B_4C-(Al-Si)-SiC the composition of the alloy being found on the Al-Si edge of the 4-D phase diagram in the ratio of the Al/Si elements of table 4.08, the triangles for composites B and C being drawn in figure 4.29 as the triangles in low position (higher Si fraction) and higher position (low Si fraction) respectively. The elemental composition of the composites A, B and C are plotted in the 4-D phase diagram of this figure, the point representing composite A being slightly above the triangle that contains the point representing composite B. As displayed by figure 4.29 the overall composition of composite A is closest to the brittle Al_4C_3 carbide. So far as the Al-Si liquid phase the composite stays to the right of the composition of the threshold point for precipitation of this carbide, as it shown in figure 4.29, the presence of such carbide is not expected based on equilibrium of phases.

As discussed above, section 4.4.3, the Al content as part of alloy is higher in composite C and less Si is found in this composite because the actual concentration of Si in the alloy used for this composite was below the nominal value (table 4.03). Table 4.08 provides clear picture of differences in actual amounts of elements taken in the constitution of the composites by the effect the reactions occurred inside the composites during infiltration. Figure 4.29 gives the graphical representation of those changes in the elemental composition space of the quaternary phase diagram.

4.5. Mechanical properties of the composites

Compacts of B_4C were infiltrated by the Al-Si alloys to provide dual metallic phase dual carbide composites of improved fracture energy. It is known that the hardness and elastic modulus of two phase mixtures of mutually insoluble components increase with the amount of the harder and stiffer phase. The average values of Vickers microhardness (9.8 N) and macrohardness (98 N and 294 N) and indentation fracture toughness K_{IC} of composites A, B and C are given in table 4.09. For comparison calculated values of Vickers hardness are also given in table 4.09 which were calculated by using the rule of mixtures, considering the phase volume fractions given table 4.06 and the following values of the hardness of the phases from the literature, 0.17 GPa, 9 GPa, 28 GPa and 19 GPa for Al, Si, B_4C and SiC, respectively[12, 27, 87].

Table 4.09: Calculated hardness and Young modulus along with the measured values of Vickers microhardness and macrohardness and indentation fracture toughness of composites A, B and C.

Comp-osites	Vickers Hardness (Calculated)	Vickers Hardness (Measured)			Fracture Toughness	Elastic Modulus (Calculated)
		9.8N	98N	294N	98N	
	(GPa)	(GPa)	(GPa)	(GPa)	(MPa . $m^{1/2}$)	(GPa)
A	11.9	8.0 ± 3	5.8 ± 1	4.7 ± 0.2	7.5 ± 0.4	242.0
B	11.8	7.6 ± 2	5.9 ± 1	4.6 ± 0.0	8.3 ± 0.8	239.6
C	10.0	7.2 ± 2	6.4 ± 2	3.7 ± 0.4	7.6 ± 0.4	214.0

Values of the Young modulus (E) of the composites in table 4.09 were also calculated by the use of the same rule of mixtures, taking into account the phase volume fractions given table 4.06 and the following published values of the Young modulus of the phases: 69 GPa, 185 GPa, 470 GPa and 450 GPa for Al, Si, B_4C and SiC, respectively [9, 10, 12, 17, 27, 37, 38, 88]. The Vickers hardness H_V of composites at the given applied loads was

measured as described in section 3.5. The values of E were needed for determining K_{IC} according to the Anstis equation, Eq (3.09).

4.5.1. Microhardness

The distribution of values of Vickers microhardness H_V (9.8 N) along the direction transverse to the axis of the pellet at the top (T), middle (M) and bottom (B) areas of the longitudinal cross sections of the composites are shown figures 4.30 (a) to 4.30 (c). The image of optical microscopy of the microhardness impression of a sampled point of composite B with local value of H_V = 6.7 GPa is shown in figure 4.31. The particles of bright finishing with white/yellow colours and of positive relief in figure 4.31 are B_4C, the darker particles of roughed surfaces are Al and those of golden yellow tones with polished finish and negative relief must be Si. The areas of indenter impressions in microhardness tests with the 9.8 N applied load are small compared to dimensions of the coarse clusters of hard B_4C grains and of the metallic phases in between these clusters. The values of microhardness drastically changed from very high hardness when the Vickers indenter tip landed on grains of the hardest phase, the B_4C, to the lowest values if it landed on places of the soft Al phase. There is a larger scatter in the measured values of H_V (9.8 N) of the composites from point to point as seen in figures 4.30 (a) to 4.30 (c). From 26 to 32 indentations were made on each composite in the determination of microhardness. For the 9.8 N applied load of the microhardness measurements no indentation cracks at the corners or chipping at the edges of the pyramidal shaped impression of indenter on the composites were found, as shown in figure 4.31.

All the three composites show a few odd values in the readings of microhardness. The extreme highest and lowest value of each set of measured microhardness values of the composites were not taken in the calculation of the corresponding average and standard deviation of microhardness and macrohardness given in table 4.09. However, all measured points were considered and are plotted in the graphs of microhardness in figure 4.30.

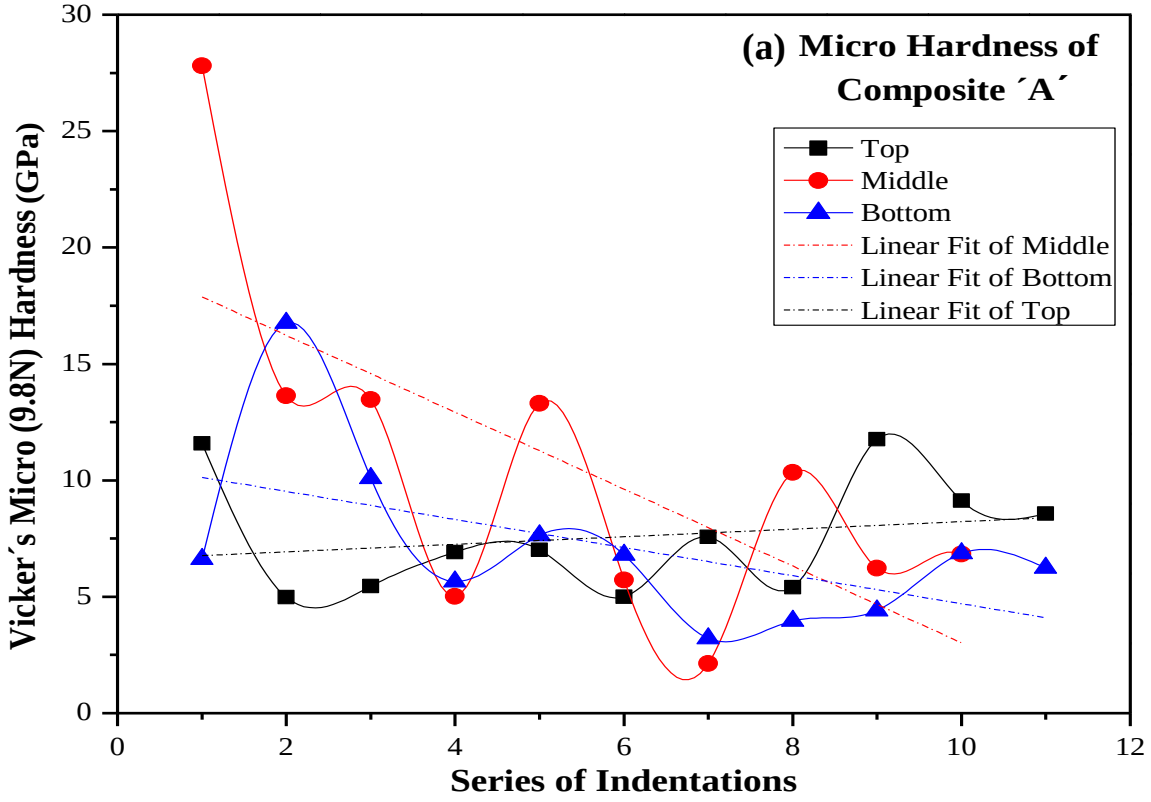
(a) Micro Hardness of Composite ´A´
Top
Middle
Bottom
Linear Fit of Middle
Linear Fit of Bottom
Linear Fit of Top
Vicker´s Micro (9.8N) Hardness (GPa)
Series of Indentations
0
5
10
15
20
25
30
0
2
4
6
8
10
12

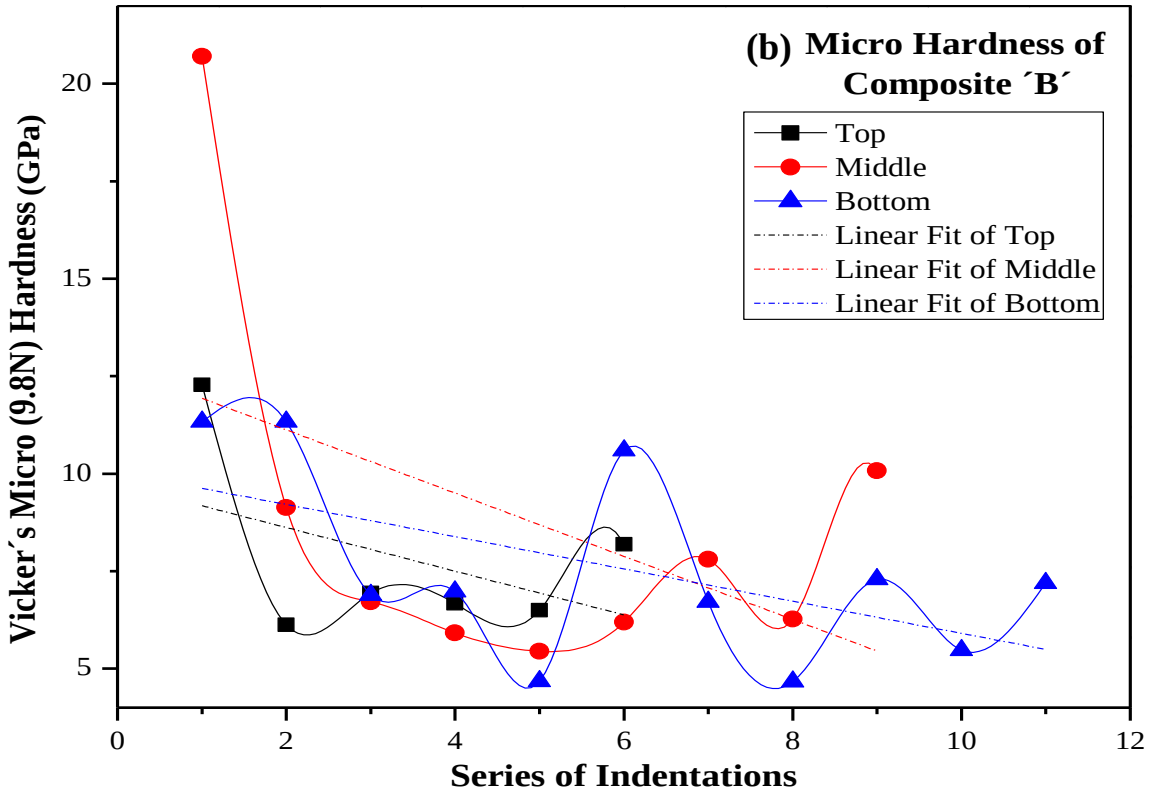
(b) Micro Hardness of Composite ´B´
Top
Middle
Bottom
Linear Fit of Top
Linear Fit of Middle
Linear Fit of Bottom
Vicker´s Micro (9.8N) Hardness (GPa)
Series of Indentations
5
10
15
20
0
2
4
6
8
10
12

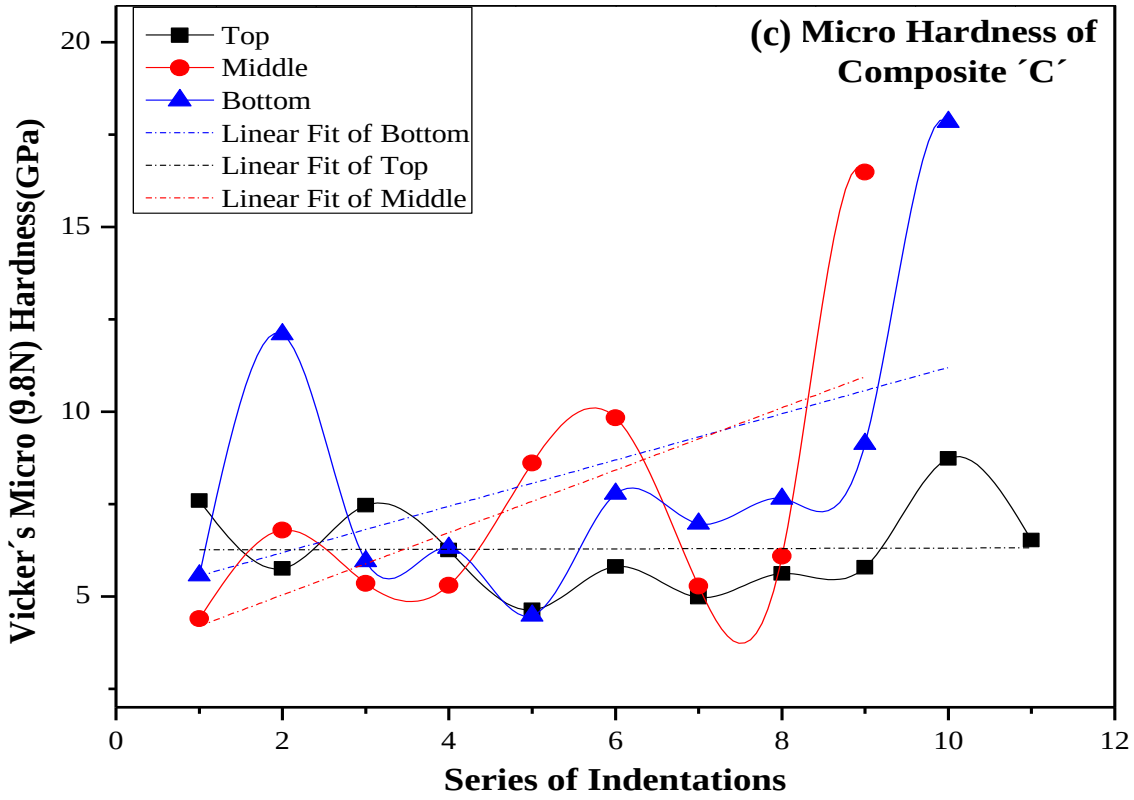

Figure 4.30: Distribution of values of Vickers microhardness H_V (9.8 N) along the direction transverse to the axis of the pellet at the top (T), middle (M) and bottom (B) areas of the longitudinal cross sections of the composites: (a) Composite A, (b) Composite B and (c) Composite C.

The hardness of melt infiltrated composites is strongly affected by the alloy-to-ceramic ratio. The results of microhardness of three composites in table 4.09 are of comparable values, the Si content seemingly displays some effect on the microhardness of these composites.

The average microhardness of composite A is 8.0±3 GPa, table 4.09. The values of microhardness of composite A in figure 4.30 (a), discounting the highest and lowest value in each set, yield the following average values of microhardness for each area 7.6±2 GPa in (T), 9.3±4 GPa in (M) and 7.1±4 GPa in the bottom (B) area. The same analysis yield the following average values of microhardness of each area of composite B in figure 4.30 (b),

7.8±3 GPa in (T), 7.2±2 GPa in (B) and 7.9±2 GPa in the bottom (B) area, while for composite C the following average values of microhardness are calculated from the distributions of points plotted in figure 4.30 (c), 6.3±1 GPa in (T), 8.0±1 GPa in (M) and 7.3±2 GPa in the bottom (B) area of this composite.

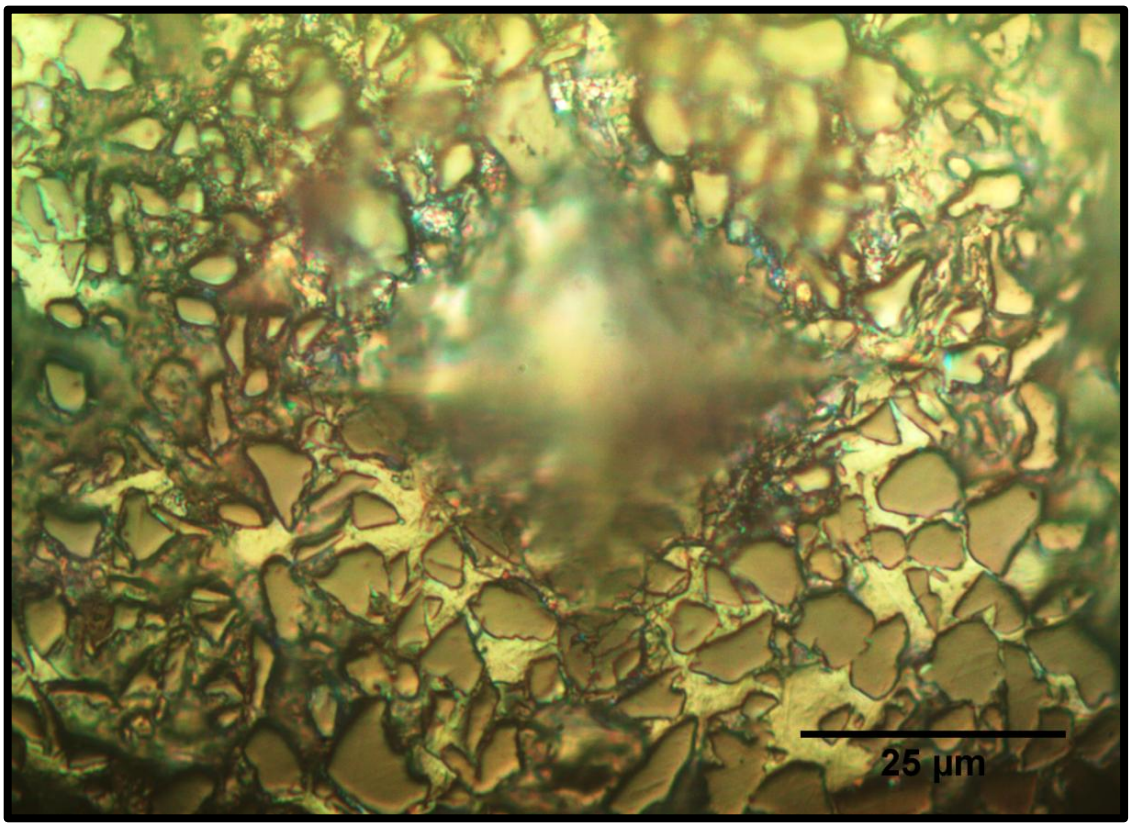

Figure 4.31: Image of optical microscopy of the microhardness indentation impression of a point with H_V = 6.7 GPa, 9.8N applied load on top (T) region of composite B.

The slope of the trend line fitted to the (M) set of microhardness data of composite A in figure 4.30 (a) shows the net effect of the single point of extreme hardness on the left of the composite cross section in the middle area. Similar effects of single points of extreme hardness are observed on the slopes of some trend lines fitted to microhardness data in figures 4.30 (b) and figure 4.30 (c). The microhardness of the measured points of the top (T) and bottom (B) areas of composite A plotted in figure 4.30 (a) are in better balance. The slopes of the corresponding trend lines of (T) and (B) describe some variation of hardness from one side to the other across the longitudinal cross section of this composite. The differences in hardness may come from local differences of relative density in the

preforms or of melt flow and degree of reaction during the RMI stage. Similar fluctuations of slope of the trend lines fitted to microhardness data plotted in figures 4.30 (b) and 4.30 (c) are observed. Accounting for the limited accuracy and large scatter of these measurements no interpretation of the observed changes in slope of microhardness of the plots in figure 4.30 is attempted here.

4.5.2. Macrohardness

Applied loads of 98 N and 294 N were used in the determination of the macrohardness of the RMI composites of this study, the corresponding average values of H_V are given in table 4.09. The image of optical microscopy of a Vickers indenter impression of macrohardness measurement of composite B in figure 4.32 shows that the indenter impressions covers a large area in comparison to the dimensional scale of the main microstructural features of the composite. Adequate area coverage of the microstructure of the ceramic composites by the indenter impression with high enough applied loads is need to rendered the optimal conditions for assessment of hardness and of indentation fracture toughness too. The applied load of 29.4 N was selected by *Wu et al* [1] for the determination of H_V and indentation fracture toughness K_{IC} of similar RMI B_4C composites [89]. Preliminary results of the present study confirmed that the applied load of 98 N was need and better suited for clear depicting of the hardness property of the composites.

General deformation and distortion of the composite structure around the indentation impression is observed near the edges, figure 4.32. The large area coverage of the indenter and high load of macrohardness created different mechanical reactions of the microstructure pressed by the Vickers indenter. Due to the composite structure with metals and ceramics some corners of indentations do not form any linear cracks, the neighbour particles simply break in several directions due to the brittleness of Si and ceramic particles, whereas at other corners (Al) metallic particles dominate and hindered the nucleation of flaws or larger cracks at the site.

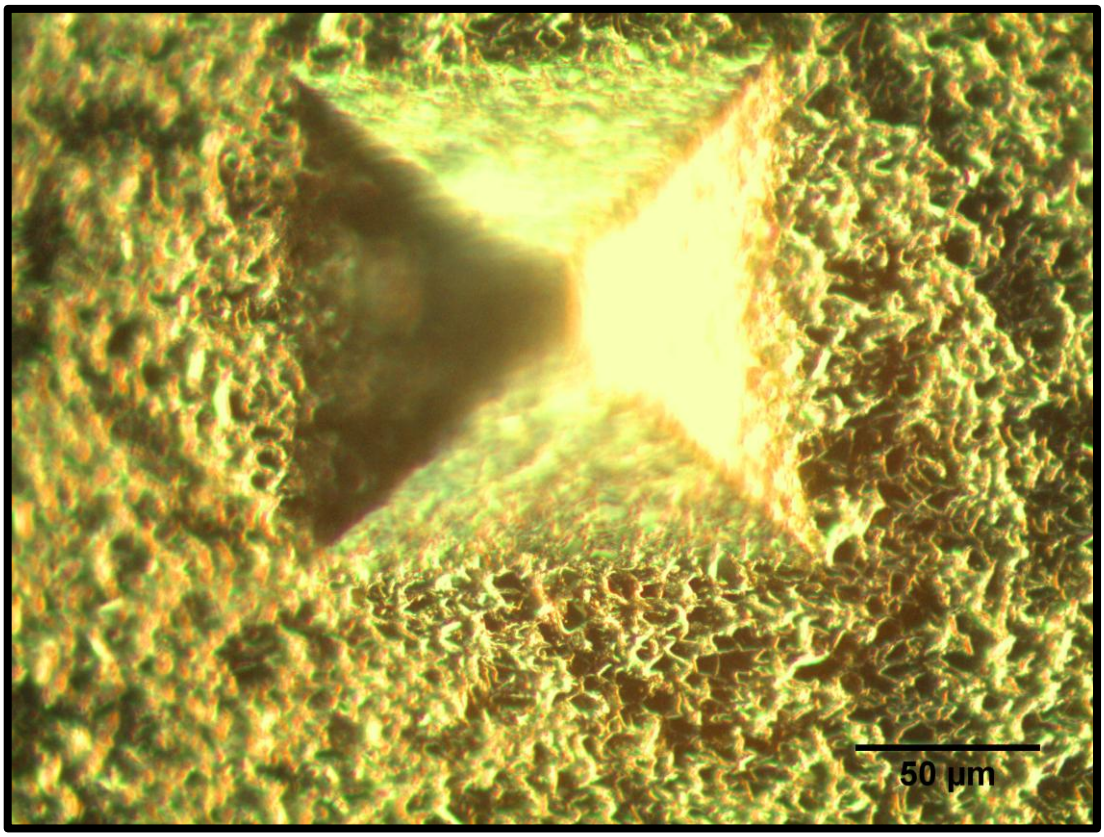

Figure 4.32: Image of optical microscopy of a Vickers indenter impression of macrohardness (98N) measurement of composite C.

There is less scatter in the values of H_V (98 N) macrohardness of the composites in figures 4.33 (a) to 4.33 (c) than in the corresponding values of microhardness. The average of hardness on each area of the cross sections of the composites referenced in figure 4.33 was also calculated.

For comparison with the average values of macrohardness in table 4.09, the values of H_V of composite A for each area shown in distribution of points in figure 4.33 (a) are 5.6±1 GPa in (T), 6.5±1 GPa in (M) and 5.8±1 GPa in the bottom (B) area. The same procedure yield the following average values of macrohardness of each area of composite B in figure 4.33 (b), 6.0±1 GPa in (T), 5.9±1 GPa in (B) and 5.7±2 GPa in the bottom (B) area, while for composite C the following average values of macrohardness are calculated from the distributions of points plotted in figure 4.33 (c), 7.1±2 GPa in (T), 6.2±1 GPa in (B) and 5.9±1 GPa in the bottom (B) area of this composite.

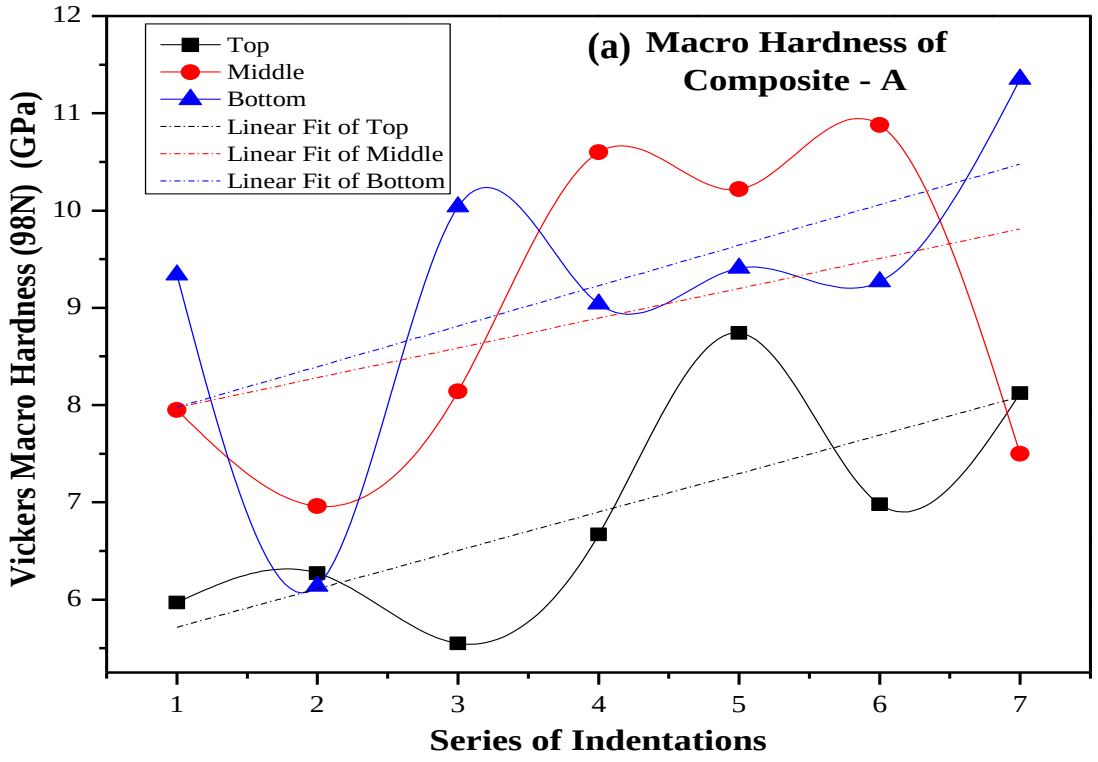
(a) Macro Hardness of Composite - A
Top
Middle
Bottom
Linear Fit of Top
Linear Fit of Middle
Linear Fit of Bottom
Vickers Macro Hardness (98N) (GPa)
Series of Indentations
12
11
10
9
8
7
6
1
2
3
4
5
6
7

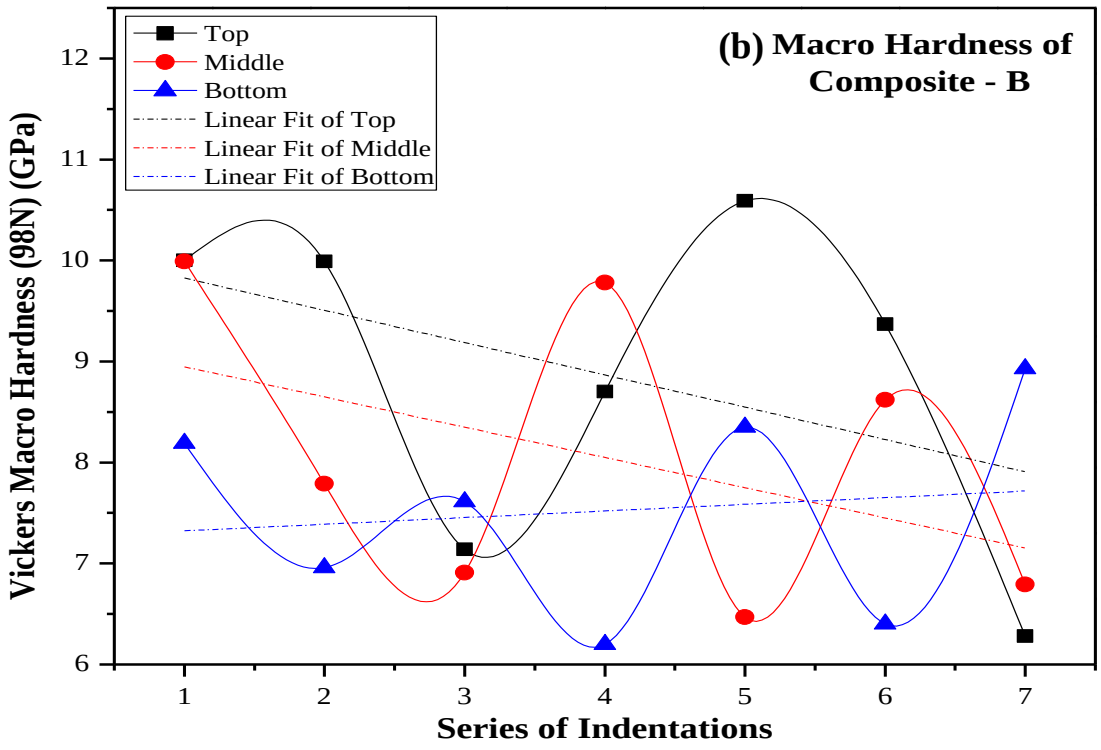
(b) Macro Hardness of Composite - B
Top
Middle
Bottom
Linear Fit of Top
Linear Fit of Middle
Linear Fit of Bottom
Vickers Macro Hardness (98N) (GPa)
Series of Indentations
12
11
10
9
8
7
6
1
2
3
4
5
6
7

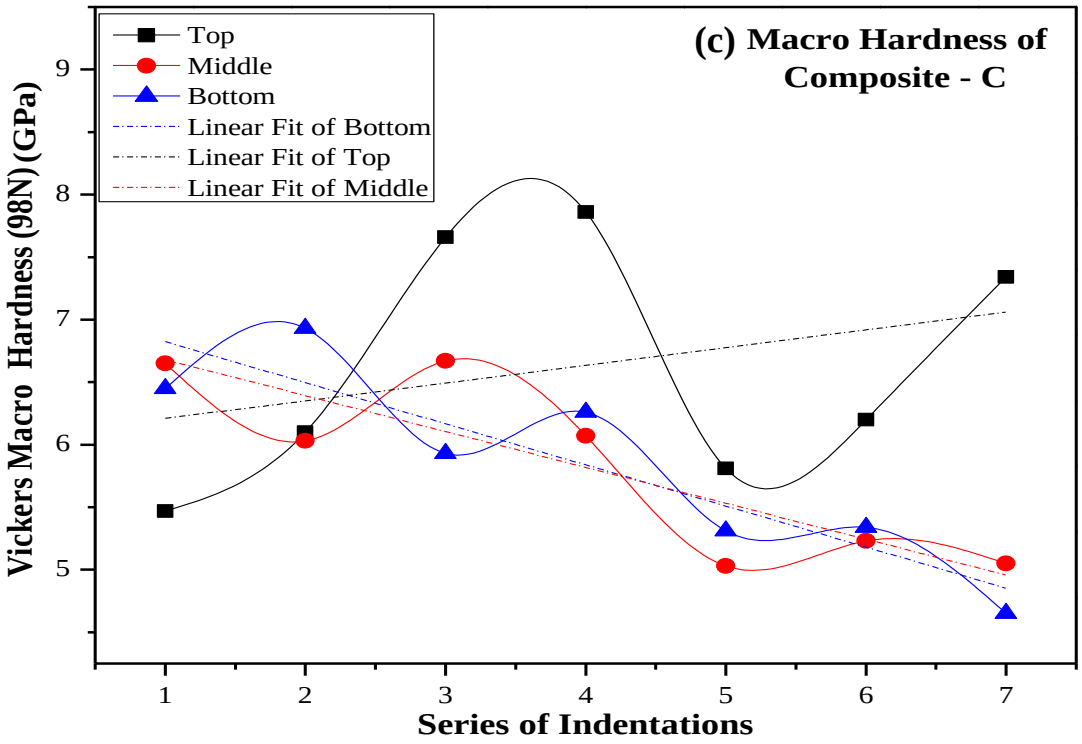

Figure 4.33: Distribution of values of Vickers macrohardness H_V (98 N) along the direction transverse to the axis of the pellet at the top (T), middle (M) and bottom (B) areas of the longitudinal cross sections of the composites: (a) Composite A, (b) Composite B and (c) Composite C.

The mean 98 N macrohardness of composite C is 6.4±2 GPa and it is slightly higher among the three composites. Middle and bottom regions of composite C look quite similar with the harder part in one side (left), the macrohardness gradually decreasing close to the linear trend lines towards the other side, figure 4.33 (c). Similar to the observations in figure 4.30, some variability is observed in the slopes of the trend lines fitted to macrohardness data plotted in figures 4.33 (a) to 4.33 (c) which is seen, as above, as coming from local differences of green density of the preforms or in the RMI kinetics.

The indentation load of 98 N delivered impressions of the pyramidal indenter with some corners with cracks others without cracks. Hence for better understanding of the mechanical behaviour of the composites the indention load was further increased to 294 N. The indentation profile of composite C for the applied load of 294N is shown in figure 4.34. The corners of the indenter impression do not display any cracks nucleated directly

from them due to the brittleness of Si and ceramic phases of the composites and the high applied load. The average values of macrohardness of the three composites for the applied load of 294 N in table 4.09 range from 3.7±0.4 to 4.7±0.2 GPa the highest value being observed in composite A.

Figure 4.35 represents the hardness data in table 4.09 of the set of the three composites at the three levels of applied load 9.8N, 98 N and 294 N. The content of Al metal given in table 4.06 is high for all three composites, nearly 44 vol% to 55 vol%. Hence it is expected that the changes in hardness would be dominated by the Al first and second by B_4C and SiC carbides added together, the total content in ceramic phases varying from 33 vol% to 38 vol%, as most of the composite structure is formed by these three phases.

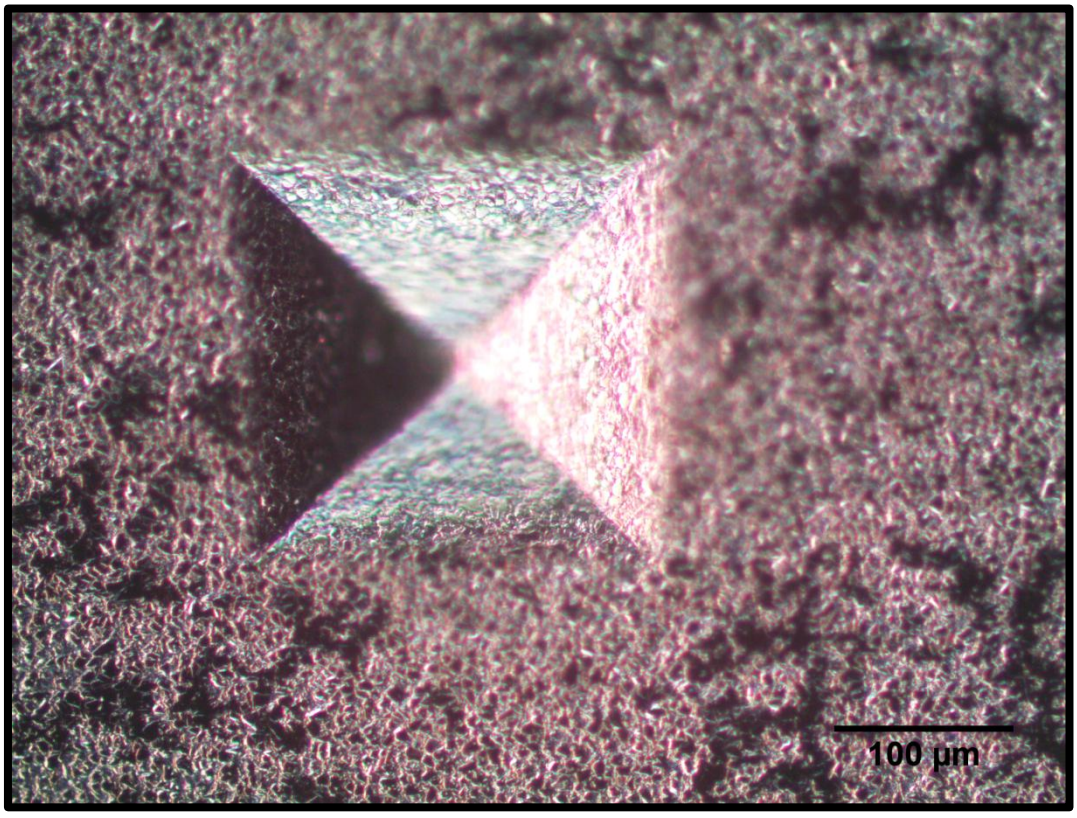

Figure 4.34: Image of optical microscopy of a Vickers indenter impression of macrohardness (294N) measurement of composite C.

The dependence of the values of hardness on the applied loads of the composites in table 4.09 display a strong indentation size effect of this property, the measured values of hardness being almost linearly correlated to the applied load. *Bouchacourt and Thevenot* reported that in B_4C ceramics the hardness values rise exponentially with decreasing applied load. At least an approximately constant value of hardness could be measured with loads at and above 20 N, since such level of loading resulted in larger indentation areas on the microstructure. The residual porosity and the free carbon content had also significant role in determining the hardness of the B_4C [11].

When analysing the mechanical behaviour in the figure 4.35, composite C indicates a trend for lower hardness properties at 9.8 N and 294 N loads whereas it shows a slightly high hardness with the 98N load than other two composites. However, this difference is not large if one accounts for the corresponding values of standard deviation of H_V in table 4.09.

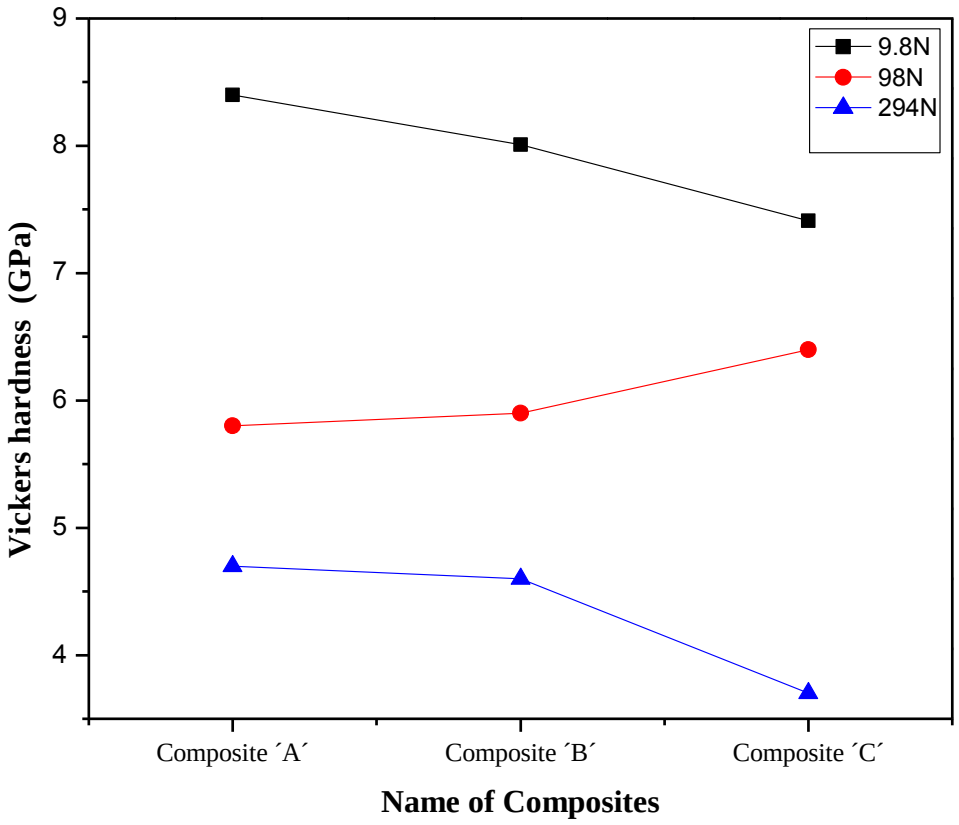

Figure 4.35: A comparison map of micro and macro and hardness of three composites A, B and C at loads 9.8, 98 N and 294 N

For comparison of the values of Vickers hardness of the present study of RMI of the B_4C composites with recently published values of the same property measured on similar RMI B_4C composites, *table 3 in ref.* [1] , prepared with Al-Si alloys of different Si contents, the values of Vickers hardness of each of the composites A, B, C for an applied load of 29.4 N were calculated by linear interpolation using the corresponding dependence of hardness on applied load given by the data in table 4.09. The following values of H_V for a 29,4 N applied load were obtained, 7.3 GPa for composite A, 7.1 GPa for B and 7.1 GPa also for C. The plot of the dependence of (29.4 N) H_V on the Si content of the Al-Si alloy used for reactive melt infiltration of pressed preforms of B_4C in figure 4.36 confirms that both sets of data are closely correlated to the composition in Si of the Al-Si alloy used in the RMI processing of the B_4C based composites. Separate trend lines were drawn from the two sets of published data of hardness of the RMI B_4C composites in figure 4.36, the preforms of as supplied B_4C and preforms with 10 wt% added carbon [1]. The extrapolations of both trend lines towards the composition representing the composites of the present study definitively overlap with the values of H_V of composites A and B.

The correlation in figure 4.36 reflects in indirect way the effect of the Al volume fraction in the structure of the composites as hardness of the softest phase, the Al (0.17 GPa), is 50 times lower than hardness of Si itself. The experimentally determined volume fraction of Al in the composites of the present study was given above in table 4.06, but such quantity is not available in the results published by *Wu et al* [1].

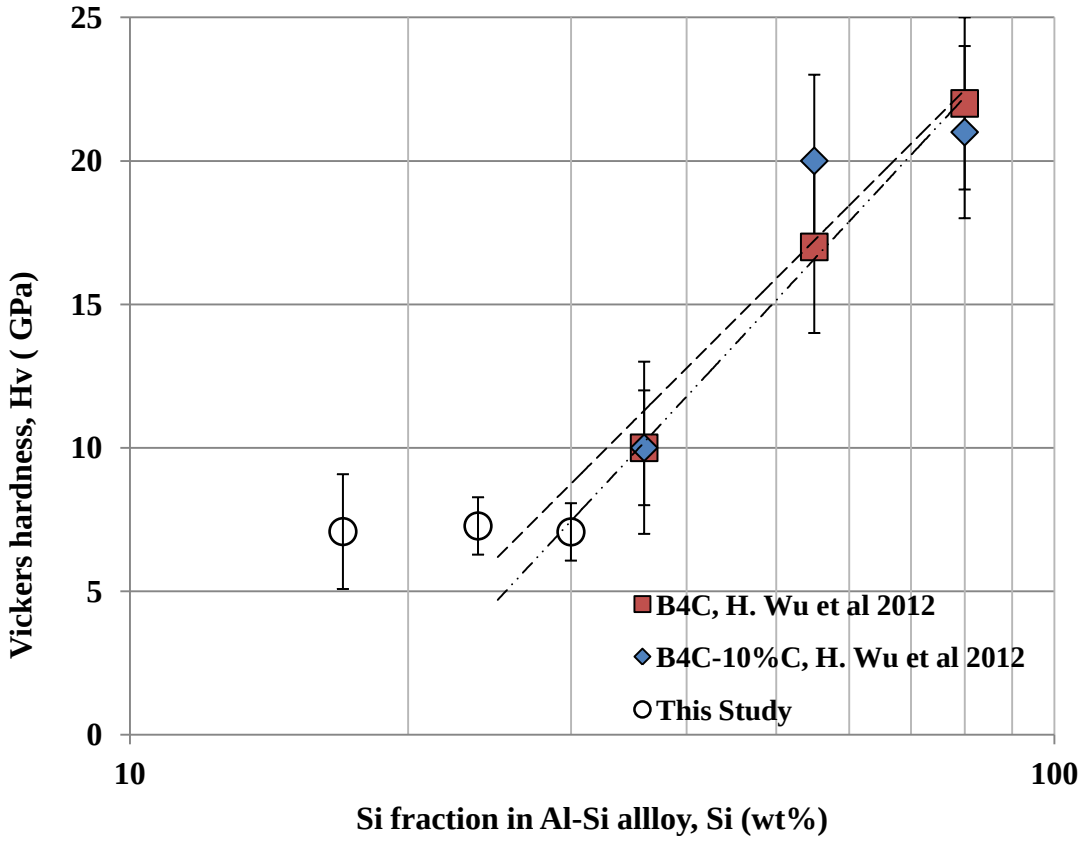

Figure 4.36: Dependence of Vickers hardness the composites on the Si fraction in the Al-Si alloy used for reactive melt infiltration of B_4C preforms, 29.4 N applied load (*Wu et al [1]*).

4.5.3 Indentation fracture toughness

The values of indentation fracture toughness of composites A and C in table 4.09 determined from Vickers indentation at the applied load of 98 N are almost equal accounting for corresponding values of the standard deviation. Composite B has a slightly higher value of K_{IC}. The experimental work was planned under the assumption that in order to obtain a tougher composite the metallic Si content in the RMI composite should be kept to a minimum favouring the maximum volume fraction of the ductile metal Al [1], provided that the Si content would be maintained above the threshold of Si in the Al-Si alloy that inhibits the formation of Al_4C_3 carbide (section 4.4.2). Nevertheless, lowering

the Si content in the alloy would also lead to poor infiltration behaviour. Composite B of higher Si content displays the higher value of K_{IC} in the set of the three composites in table 4.09.

In the process of evaluating K_{IC}, the actual measurement of the crack lengths by optical microscopy was difficult, section 3.5. Only by using indentation loads close to 98 N could the values of K_{IC} be approximately established from indentation fracture results in the present study. Analogous difficulties in determining the values K_{IC} of two MRI B_4C composites prepared with 36 wt% Si alloy from HV_3 (29.4 N) indentation results were recently reported [1]. Whereas in HV_1 no indentation cracks formed due high toughness of the composites, table 4.09, at the highest applied load of 294 N the HV_{30} indentation impressions developed complex damage patterns and no definitive cracks propagating from the indentation corners could ultimately be identified. Differently, with the 98N applied load formation of different types of cracks was witnessed. The maximum extensions of those cracks propagating close to the radial direction defined by the indentation corners were determined with recurs to SEM microscopy and the indentation fracture toughness calculated by using Anstis equation (Eq 3.09). Under such context errors in observation of the crack tips could not be avoided, the values of K_{IC} in table 4.09 must be seen as crude first time estimation of the fracture toughness of these composites with the techniques made available in the laboratory.

The values of Young modulus E of the composites in table 4.09 were calculated by the rule of mixtures. The values of indentation fracture toughness determined by using Anstis equation (Eq 3.09) are dependent on the values taken for E. In a different way, slightly different values of E of the composites would have been obtained if results of the elastic properties Al-Si at the particular Si ratio were taken instead [90]. Microstructural differences in the ceramics often have opposite effects on fracture toughness and strength, such as the observed decrease in strength in parallel with increased toughness with the coarse grains sizes [89]. Mean grain size of B_4C plays a significant role in the fracture toughness of the B_4C ceramics where higher free C content (5 wt%) and low mean grain size (2 μm) reduces fracture toughness. At the same time, the increasing in average grain size up to 10 μm with the same graphite content increased fracture toughness [73]. The

formation of other structures of B_4C resulted in and increased of up to 60% of the fracture toughness; at temperatures above 1200°C hardness is also improved [91].

Details on crack nucleation and propagation from indentation marks of the 98 N indentation test are given in figures 4.37 and 4.38. The radial crack nucleated at the corner of the indentation mark is marked (A) in figure 4.37. Radial cracks formed in the indentation marks of all three composites at 98 N applied load, but rarely in all four corners of the same indentation impression. In the image of a pyramidal profile of Vickers indentation of composite B in figure 4.39 no radial cracks or crack branches were nucleated at the indentation corner, rather instead grain dislodging with matrix microcraking is observed at the indentation edge. A counting was run on the indentation marks of all three composites to estimate the proportion of blunt corners without detectable cracks. Out of all 98 N indentation marks of composite A 22% did not show developed cracks in the corners, the corresponding rates being 15% in composite B and 10% in composite C. Nearly 50% to 60% of the radial cracks of all composites display crack branching in a visible way.

Mark (B) in same figure 4.37 points to cracks normal to surface (as radial cracks) that developed from the edges of the indentation mark. These crack found their path through the white phase (eventually Si). Mark (C) on the right side of the figure indicates the formation of a lateral crack, the round contour of the delaminated chip being delineated on the surface. Such kind of cracks has been observed by SEM at outdistances from the indentation impressions. The corner of the indentation profile to the near right cannot be viewed in figure 4.38 where features of radial and lateral cracks can also be observed.

The Vickers indentation of composite A in figure 4.40 displays the nucleation sites of the radial crack at the indentation corner and of a lateral crack underneath the surface at the indenter-piece interface. It was found that when the maximum contact force of indentation is low, the lateral crack is confined within the shallow surface layer, whereas when the maximum indentation force is higher, the crack tends to nucleate at deep beneath the surface at the indenter-piece interface[92].

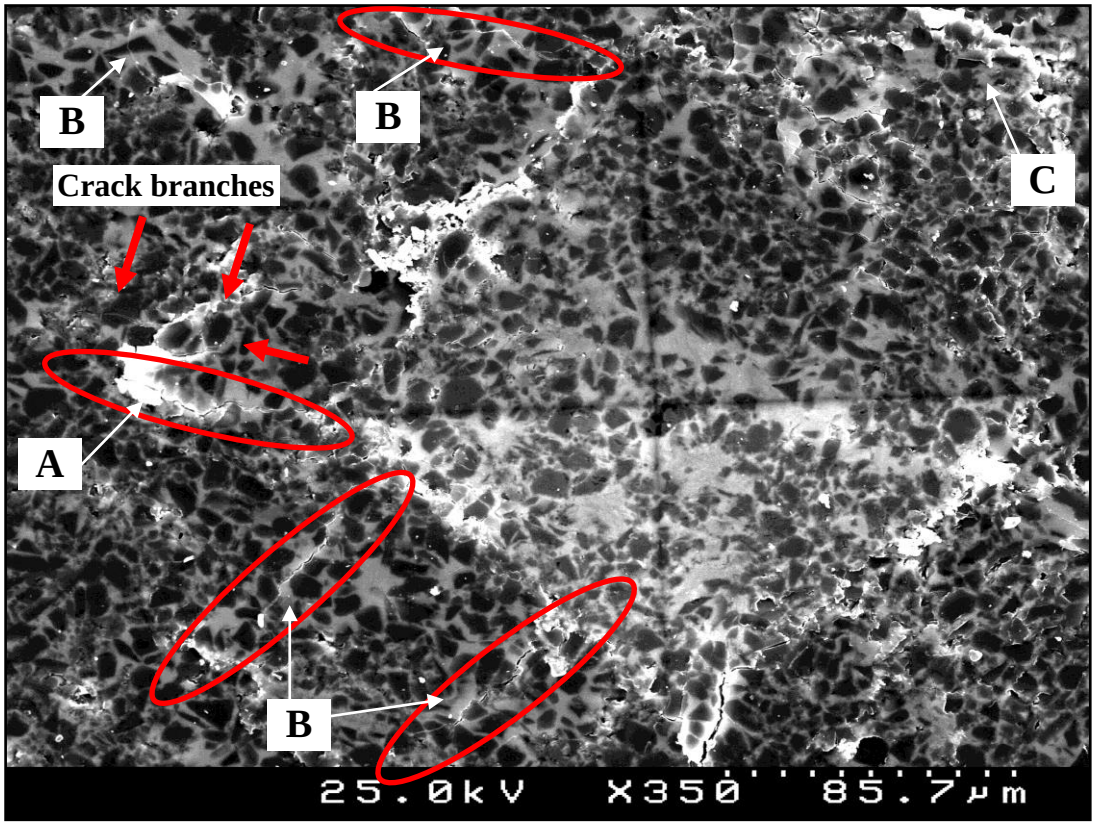

Figure 4.37: SEM image of the pyramidal profile a 98 N Vickers indentation of composite C.

Transgranular fracture and crack bridging are indicated by arrows in the enlarged view of the indentation fracture of composite C in figure 4.38. When analysing figures 4.38 to 4.40 isolated particles of different phases are viewed on the deflected path of the cracks showing cleavage with different aspects according to the crystalline structure of the phases.

Crack deflection increases the fracture toughness of the composites. Figures 4.37 and 4.38 show that small particles (of SiC or B_4C) stopped crack propagation, at the same time others thought to be the Al phase acted as bridges in the crack wake zones. It was often seen that wherever the radial or other cracks branch there are strained bridge ridges nearby, may be due to more abundant Al phase at the place. The usage of more Al would lead to higher energy consumption in fracture. De-bonding at the interface of the phases is seen at few places in figures 4.38 to 4.40. Transgranular fracture of B_4C particles was mostly observed near the indentation corners.

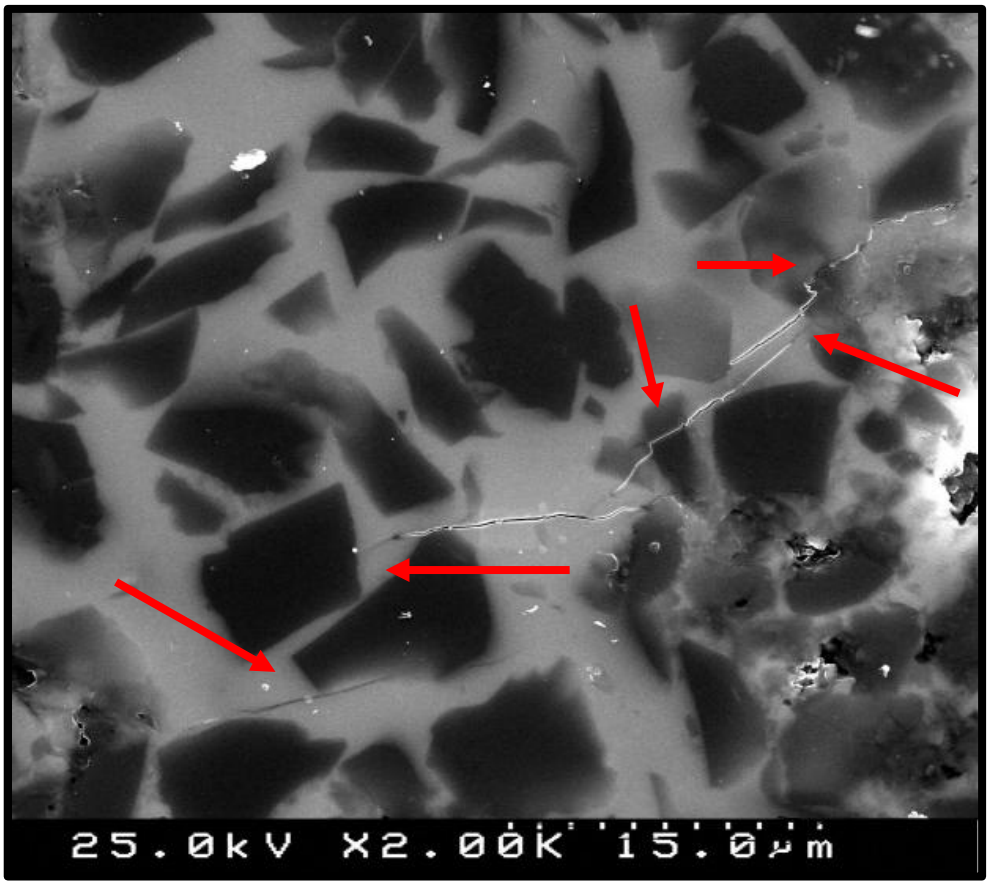

Figure 4.38: SEM enlarged view of indentation fracture cracks of the pyramidal mark of a 98 N Vickers hardness test of composite C (corner of indentation mark to the nearby right, not shown). Lateral cracks, transgranular fracture and crack bridging indicated by arrows.

Though transgranular cleavage of Si and carbides is generally found the intergranular and interphase boundary fracture is rather more extensive than transgranular fracture. But, other mechanisms of mechanical energy dissipation, namely the growth of lateral cracks and the extension of microcracking nearby the corners with no radial cracks, would also add to fracture energy and the effective fracture toughness of the composites.

The ample observation by SEM microscopy confirmed that all the three composites had experienced chipping, pile-up and lateral cracks around the indentations besides the formation of the radial cracks of indentation. Intergranular and transgranular fracture and crack branching were always present along the crack paths.

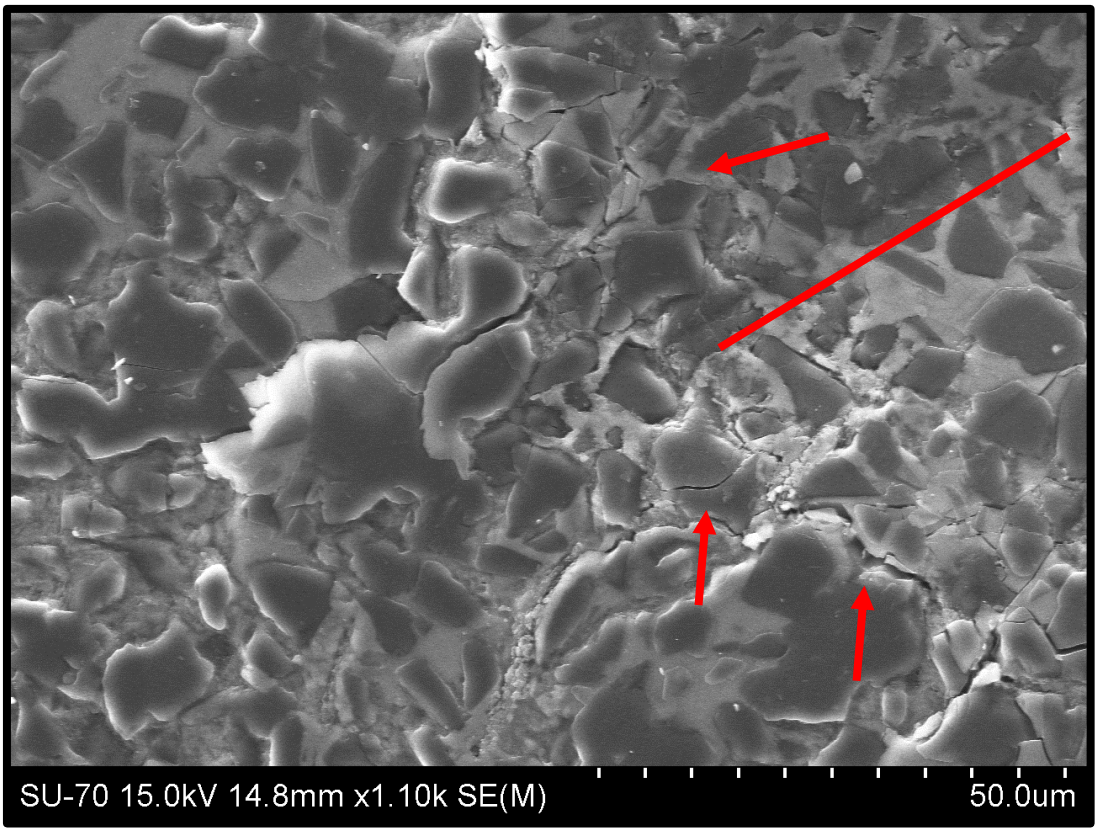

Figure 4.39: SEM image of a pyramidal profile of Vickers indentation of composite B at 98N load no radial cracks or crack branches nucleated at the indentation corner, arrows mark indenter impression diagonal and grain dislodging with matrix microcraking at the indentation edge.

Both transgranular and intergranular fracture modes are seen throughout the composites during the SEM observation of 98 N Vickers macrohardness indentations. In transgranular fracture, crack travels through the crystalline grains of the material. The fracture (cleavage) changes direction from grain to grain due to differences in lattice orientation of the grains. This kind of property is seen in many places where the transgranular fracture cuts straight through the particles. A kind of transgranular fracture is found in the enlarged view of a lateral crack in figure 4.38 which cracks cuts through the particles. In the intergranular fracture cracks have to travel along grain boundaries or interphase boundaries, often contouring the edges of hard particles. This usually occurs where the grain boundaries and interphases are weak or brittle, in the present case the Al/ceramic interface [1].

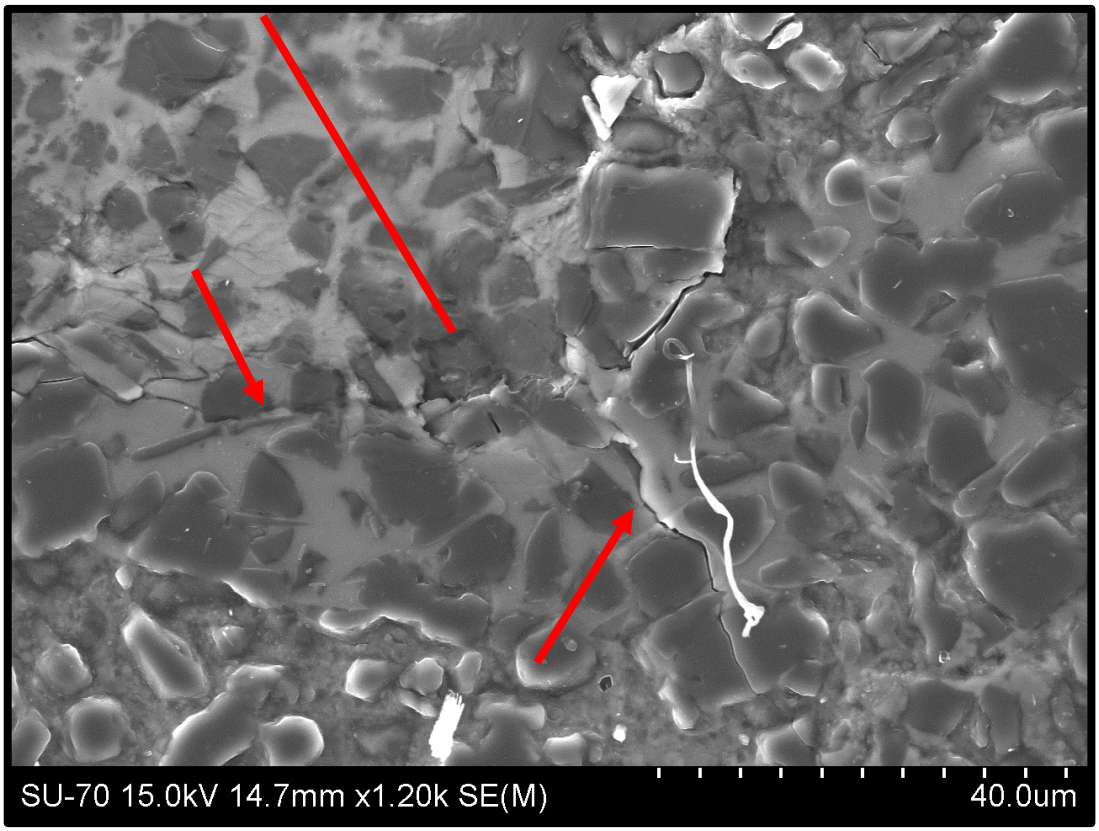

Figure 4.40: SEM image of a pyramidal profile of the Vickers indentation of composite A at 98N load, arrows mark the indentation diagonal, the nucleation of the radial crack at the indentation corner and of a lateral crack at the indenter-piece interface.

Cracks propagate mostly through the metallic phases (white contrast in SEM) and interphase boundaries. The cracks will propagate towards the metallic phases as the metal is in tension and the surrounding ceramic matrix in compression at room temperature [93]. Al can yield and adjust to the fracture strain by plastic deformation contributing to crack bridging. Si included in the metallic phases is known for the fragile fracture at room temperature and presumably is the weakest phase of these composites. If cracks propagate mostly through the Si phase rather than the Al, fracture energy of the composites is lowered. With the opposite effect, for further propagation of the cracks additional stress must be applied to deform the Al bridges and the fracture toughness of the composites is increased.

Recently published values of the 29,4 N indentation fracture toughness of four other RMI B_4C composites, *table 3 in ref*. [1], which were determined by applying Evans equation of indentation fracture [94], are plotted in figure 4.41 as a function of the corresponding Vickers indentation hardness. The values of K_{IC} of composites A, B and C of the present study, determined for the indentation load of 98 N and using Anstis equation Eq 3.09, are also plotted in figure 4.41.

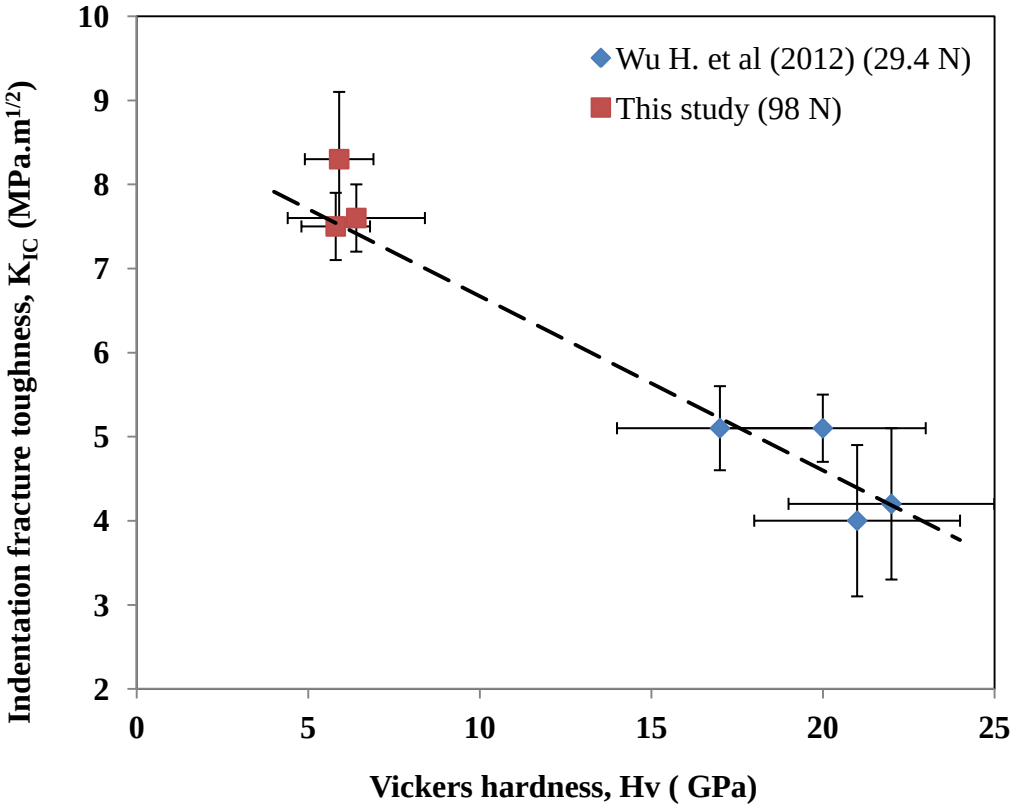

Figure 4.41: Interdependence of indentation fracture toughness on the Vickers hardness of the RMI composites of Al-Si alloy reactive melt infiltrated into B_4C preforms (*Wu et al [1]*).

In spite of the scatter of the K_{IC} points of the published study and of the composites of present study and of the differences in the equations of indentation fracture, raw materials, processing conditions and composition of the Al-Si alloys of both studies, the trend line extracted from the observed increase in K_{IC} with the decrease in H_V in the published values

of *Wu et al* [1], meets the points of the present study when extrapolated to the corresponding range of values of H_V of the composites A to C.

The Si content of the Al-Si alloy used for the reactive melt infiltration of B_4C preforms plays an important role both in setting the hardness as well the fracture toughness of the RMI composites of the B_4C-SiC ceramic matrix. It is beyond the objectives of this study to solve the intricate complexity of the toughening mechanisms active in these composites. Anyhow, as incipiently discussed above in this section, the crack path is not blocked by the presence of Si which has fragile fracture and seemingly is the mechanically weakest phase of the composites. Al does not bind with equally strength to the different phases of the composite [1]. If the Si content increases, there is a more complex network of continuous breaking and bridging points which tend to divert the propagating cracks. At the same time it is anticipated that if the Si content exceeds a certain level the K_{IC} will decrease by further increasing Si content while Si will positively contribute to increase in hardness as shown in figure 4.36.

5.0 CONCLUSIONS

Several batches of the Al-Si alloy were prepared by smelting in a graphite furnace in two nominal concentrations of 25 wt% Si and 35% wt Si. In order to improve the homogeneity of the final alloy twice smelting of two batches was also done. A 10 μm B_4C powder with carbon (graphite) as impurity was used in this study. Porous preforms the 10 μm B_4C with 52-55 % relative density prepared by uniaxial pressing followed by cold isostatic were pressure-less melt infiltrated by hypereutectic Al-Si alloys in argon atmosphere. The analysis of the results of the reactive melt infiltration of as pressed B_4C preforms by the Al-Si hypereutectic alloys leads to the following conclusions:

1) Complete infiltration of B_4C cylindrical preforms of 7.5 mm height was feasible in short cycles of heating at 20 ºC/min with isothermal holds for 5 minutes at the maximum temperature of melt infiltration of 1300 ºC as well of 1200 ºC, but not when maximum temperature is limited to 1100 ºC.

2) During the melt infiltration process a few preforms presented partial infiltration of their volumes or did not infiltrate at all due to poor wetting or oxidation problems related with the presence of oxygen containing gaseous species in the atmosphere of the furnace. Repeated argon flushing of the furnace atmosphere prior to the infiltration runs improved the stability of infiltration.

3) The analysis by a quantitative X-ray diffraction method yielded a concentration of 8 wt% of carbon determined as graphite in the 10 μm B_4C powder. No graphite is detected by XRD in the phase composition of the reactive melt infiltrated composites in the three areas analysed along the longitudinal cross-sections of composites in the downward direction of infiltration, at the top, middle and at the end, near the bottom face of the pellet.

4) Sound composites which were produced from different combinations of the Al-Si alloy and different smelting processes and infiltration conditions possessed measured densities of 2.53-2.55 g/cm^3, corresponding to values of the relative density close to 99%; and they were used in the investigation of the structure and mechanical properties.

5) The considerable amount of residual free carbon in B_4C powder influenced the phase composition as it was converted mostly to SiC which was heterogeneously nucleated on the surfaces of the B_4C particles as revealed by SEM microscopy coupled to EDS mapping of the elements.

6) The volume fraction of the SiC phase was evaluated by XRD analysis with standards as 3.3 vol% to 5.2 vol% in composites made of dual carbide phases of B_4C and SiC and dual metallic phases of Al and Si.

7) Traces of ternary B-Al-C compounds and a minor fraction fragile Al_4C_3 carbide were detected by XRD in the composite that was melt infiltrated at 1300 ºC with the Al-Si alloy of 25 wt% Si nominal composition from single smelting, but these compounds could not be found in the composite produced under equal conditions from the alloy with 35 wt% Si nominal composition, or form a twice smelted alloy of 25 wt % Si nominal composition in a composite melt infiltrated at 1200 ºC maximum temperature.

8) The evaluation of the structural evolution and phase composition of the composites by quantitative XRD analysis with standards and SEM/EDS showed that the Al metallic phase is present in the composites with the highest volume fraction at 44 vol% to 55 vol%, in a balance with the B_4C phase in the range of 29 vol% to 33 vol% and the metallic Si phase in the range of 13 vol% to 19 vol%, the highest Al content in the composites being correlated to the lowest Si concentration of the Al-Si alloy used to prepare the corresponding composite.

9) The projections of the reaction paths in the Al-Si-B_4C ternary phase diagram from top to bottom of the pellets along the infiltration direction show that the volume fraction of B_4C at the middle area can be significantly distinct from the corresponding values at areas close to the top or bottom faces of the composite, the change in the B_4C fraction being primarily balanced by the Al phase.

10) Plotting of the average composition of the composites in Al-Si-B_4C ternary and Al-Si-B-C quaternary phase diagrams indicates that the composition of the two composites from reactive melt infiltration at 1300 ºC is closer to each other than to

that of the composite made of the twice smelted Al-Si and infiltrated temperature at 1200 ºC maximum temperature, all composites displaying Si content in the molten Al-Si alloy above threshold of 12.6 wt% Si needed to inhibit the precipitation of the Al_4C_3 phase.

As for the structural characterization for the investigation of the mechanical behaviour as determined by the Vickers indentation hardness and fracture toughness each composite was divided into the same three zones as above (top, middle and bottom with respect to the infiltration direction). The hardness was evaluated as the microhardness and marcohardness with applied loads of 9.8 N, 98 N and 294 N. The following conclusions were established in the study of the mechanical behaviour of the reactive melt infiltrate B_4C composites:

1) The dependences of the values of H_V of all three composites on the applied loads display a strong indentation size effect of this property, the measured values of hardness being almost linearly correlated to the applied load with a decrease from HV_1 in the rage of 7.2 - 8.0 GPa to HV_{30} at 3.7 - 4.7 GPa.

2) Comparison of the values H_V of the present study, interpolated to 29.4 N load, with recently published values of the same property measured on similar reactive melt infiltrated B_4C composites prepared with Al-Si alloys of different Si contents indicates that both sets of H_V data are generally correlated to the Si content of the Al-Si alloy used for reactive melt infiltration of pressed preforms of B_4C, such correlation reflecting in indirect way the effect of the Al volume fraction in the structure of the composites because it is the softest phase, with $H \approx 0.17$ GPa, 50 times lower than hardness of Si itself.

3) Due to complex structure of these composites some corners of the indentations do not form any linear cracks of the radial type, the neighbour particles simply break in several directions with grain dislodging and microcracking due to the brittleness of Si and ceramic particles, whereas at other corners the plastically deforming (Al) metallic particles dominate and hindered the nucleation of flaws or larger cracks at the site. On the overall, nearly 1/4 of the corners of the indentation marks do not have any radial cracks or crack branching on edges at 98N Load.

4) No measurable indentation cracks formed in the 9.8 N tests due high toughness of the composites, while at the highest applied load of 294 N indentation impressions developed such complex damage patterns that no definitive cracks propagating from the indentation corners could ultimately be identified. In all the three composites, lateral cracks emanating from the indentation sides are very common irrespective of the composites.

5) In the present study, only at the indentation loads of 98 N was possible to find approximate values of toughness of the composites from indentation fracture results, K_{IC} being in the range 7.6 – 8.3 $MPam^{1/2}$ but with large scatter. Analogous difficulties in determining the values K_{IC} of reactive melt infiltrate composites prepared with 36 wt% Si alloy at HV_3 (29.4 N) indentation fracture results were recently reported.

6) It was found, in spite of the scatter of the K_{IC} values, that the high values indentation toughness of K_{IC} of the composites in the present study are correlated to the comparatively low values of Vickers hardness in the same way as observed in similar reactive melt infiltrated B_4C composites prepared with Al-Si alloys of high Si content reported in the literature.

The Si content of the Al-Si alloy plays an important role both in setting the hardness as well the fracture toughness of reactive melt infiltrated composites of the B_4C-SiC ceramic matrix. Along with transgranular and intergranular fracture modes, crack branching of main cracks in sensible level of about 60% of the radial cracks was found. Though transgranular cleavage of Si and carbides is generally found the intergranular and interphase boundary fracture is rather more extensive than transgranular fracture. But, other mechanisms of mechanical energy dissipation, namely growth of lateral cracks, microcracking and bridging by Al ligaments in the crack wake zone would also add to fracture energy and the effective fracture toughness of the composites. When concerning the three composites, the two composites melt infiltrated to 1300 ºC provided similar mechanical performance except in fracture of toughness because of different composition of the alloy used for infiltration. The other composite of melt infiltration at 1200 ºC presents wider variation of the mechanical parameters.

The present study planned under the assumption that in order to obtain a tougher composite the metallic Si content in reactive melt infiltrated composites made from B_4C preforms should be kept to a minimum favouring the maximum volume fraction of tough metallic Al, extended to the low Si and low hardness side the main findings of the recently published similar work on the same type of composites, but here with shorter infiltration time and higher fracture toughness at the expense of lower hardness. From the outcomes of this study and previous published works some suggestions for continuation of the works can be done:

a) In the attempted to avoid the expensive step of pre-sintering of B_4C preforms, optimization of the green density of preforms for reactive melts infiltration is needed as a way to obtain higher hardness of the composites in simultaneous with the minimum safe content of Si in the alloy. Such would imply optimization of the particle size distribution and more efficient forming techniques.

b) Fine pore sizes of the B_4C form the use of powders of finer particle sizes would imply a reduction in the scale of the Si inclusions of the finished composites and large concentration of Al inclusions of smaller sizes bridging the crack wakes, a condition for improved toughness;

c) Faster cooling rates in the final step of the reactive melt infiltration and post-annealing below the eutectic point may lead to refined dendrite sizes and improved ductility of the Al ligaments;

d) The use of wetting dopants in the formulation of the Al-Si alloy may improve the regularity of the infiltration dynamics and decrease sensitivity of the process towards the oxygen contamination in the furnace atmosphere.

BIBLIOGRAPHY

1. Wu, Hongyan, Sengcai Zhang, Mingxia Gao, Dan Zhu, Yi Pan, Yongfeng Liu, Hongge Pan, Filipe J. Oliveira, Joaquim M. Vieira, *Microstructure and mechanical properties of multi-carbides/(Al, Si) composites derived from porous B4C preforms by reactive melt infiltration.* Materials Science and Engineering, 2012. **A 551**: p. 200-208.

2. Thevenot, F., *Boron Carbide A Comprehensive Review.* Journal of the European Ceramic Society, 1990. **6**: p. 205-225.

3. Morosin, B., Kwei G.H., Lawson A.C., Aselage T.L., Emin D., *Neutron powder diffraction refinement of boron carbides Nature of intericosahedral chains.* Journal of Alloys and Compounds, 1995. **226**: p. 121-125.

4. Shibo, L., Guangwu, W., Yong, G., Baosheng, Z., *The Crystal Structure of Boron Carbide.* Journal of Harbin University of Civil Engineering and Architecture, 1998. **31**(4): p. 61-65.

5. Lukas, H.L., *In Constitution of Ternary Alloys* 3. Ed. G.A.E. Petzow, G.1990, Weinheim: VCH. 140-146.

6. Schwetz, K.A., Karduc, P., *Investigations in the boron-carbon system with the aid of electron probe microanalysis.* Journal of The Less-Common Metals, 1991. **175**(1): p. 1-11.

7. Elliott, R.P., *Constitution of Binary Alloys, First Supplement.* 1965, New York: McGraw-Hill.

8. Halverson D.C., Pysik,.A.J., Akzay, I.A., *Processing of Boron Carbide Aluminum Composites.* Journal of American Ceramic Society, 1989. **72**(5): p. 775-780.

9. Frantsevich, I.N., Voronov, F. F., and Bokuta, S.A., *Elastic Constants and Elastic Moduli of Metals and Insulators: Handbook*, ed. I. N. Frantsevich (Naukova Dumka, Kiev, 1982), pp. 60–180.

10. Rey, J. G. M., Ph. Kapsa and J. L. Loubet, *Boron carbide coatings : correlation between mechanical properties and LPCVD parameters values.* Journal de Physique, 1989. **5**(5): p. 311-321.

11. Bouchacourt, M., and Thevenot, F., *The melting of boron carbide and the homogeneity range of the boron carbide phase.* Journal of the Less Common Metals, 1979. **67**: p. 327.

12. Telle, R., Sigl, L.S., and K. Takagi, *Boride based hard materials*. Handbook of Ceramic Hard Materials, ed. R. Reidel. Vol. 2. 2000, Weinheim: Wiley-VCH. p. 802-945.

13. Evans, A.G., Cannon, R.M., *Toughening of Brittle Solids by Martesitic Transformations.* Acta Metall, 1986. **34**: p. 761-800.

14. Larker, H. T., Hermansson, L., Adelborn, J., *Hot isostatic pressing and its applicability to silicon carbide and boron carbide.* Industrial Ceramics 1988. **8**(1): p. 17-20.

15. Kolsky, H. *The role of stress waves in penetration processes*. in Ballistic materials and penetration mechanics. ed. Labile R.C., Elsevier: New York; 1980. p. 185–223.

16. Wilkins, M.L., *Computer simulation of penetration phenomenon,* in Ballistic materials and penetration mechanics. ed. Labile R.C., Elsevier: New York; 1980. p. 225-252.

17. Telle, R., *Structure and Properties of Si-Doped Boron Carbide*. in The Physics and Chemistry of Carbides. Nitrides, and Borides. ed. R. Freer, NATO AS1 SERIES E, Kluwer. Vol. 185. 1990, Dordrecht, The Netherlands. p. 249-258.

18. Litz, L. M., Mercuri, R.A., *Oxidation of Boron Carbide by Air, Water, and Air-Water Mixtures at Elevated Temperatures.* Journal of Electrochemical Society, 1963. **110**(8): p. 921-925.

19. Matje, P., Schwetz, K. A., *Surface oxygen pick-up in submicron SiC and B_4C sintering powders and room temperature*. In Proceedings of the Second International conference: on Ceramic Powder Processing Science,, H. Hausner, Messing, G. L., and Hirano, S., Editor 1989, Deutsche Keramische Gesellschaft: Koln. p. 377-384.

20. Heuberger, M., Telle, R., Petzow, G., *Modification of Ceramic Powders by Ion Beam Treatment.* Powder Metallurgy, 1992. **35**(2): p. 125-132.

21. Lebedev, A. .A., *Heterojunctions and super lattices based on silicon carbide*, in Semiconductor Science and Technology 2006, Institute of Physics Publishing. p. R17–R34.

22. Yamada, K., Mohri, M., *Properties and Applications of Silicon Carbide Ceramics*, in Silicon Carbite Ceramics. S. Somiya, Y. Inomata (Ed.), Ceramic Research and Development in Japan Series, Vol. 1. 1991, Essex: Elsevier Science Pub. Ltd. p. 13-44.

23. Verma, A.R., Krishna, P., *Polymorphism and Polytypism in Crystals.* 1966, John Wiley & Sons Inc.

24. Kordina, O., *Growth and Characterisation of Silicon Carbide Power Device Material*, in *Science and Technology.* Vol. 352 Linköping studies in science and technology: Dissertations, Linköping University, 1994 (140 pages)

25. Heinz K Henisch; R Roy, *Silicon Carbide - 1968*, Proceedings of the International Conference on Silicon Carbide, University Park, Pa., October 20-23, 1968. Materials research bulletin, special issue. Ed. Heinz K. Henisch, R. Roy. Pergamon Press, 1969 (372 pages)

26. Ching, W. Y., Xu, Y. N., P. Rulis, L.Z. Ouyang,, *The Eletronic Structure and Spectroscopic properties of 3C, 2H, 4H, 6H, 15R and 21R polymorphs of SiC.* Materials Science and Engineering A 2006 **422**(1-2): p. 147-156.

27. Schwetz, K.A., *Silicon carbide based hard materials*. Handbook of ceramic hard materials, ed. R. Reidel. Vol. 2. 2000, Weinheim: WILEY-VCH GmpH. p. 683–748

28. Adamsky, R.F., Merz, K. M., *Synthesis and crystallography of the wurtzite form of silicon carbide*. Zeitschrift für Kristallographie 1959. **111**(1-6): p. 350-361.

29. Krishna, P., Marshall, R.C, *Direct transformation from the 2H to the 6H structure in single-crystal silicon carbide.* Journal of Crystal Growth, 1971. **11**(2): p. 147-150.

30. Inomata, Y., Inoue, Z., M. Mitomo, and H. Suzuki, *Relation between the growth temperature and the structure of silicon carbide crystals grown by the sublimation method.* Yogyo-kyokai-Shi, 1968. **76**: p. 313-319.

31. Munch, W. V., *Silicon carbide*, Landolt-Bornstein: Numerical Data and Functional Relationships in Science and Technology, New Series, group III, vol. 17c, M. Schultz, O. Madelung, and H. Weiss, Eds. Berlin, Germany: Springer-Verlag, 1984.

32. Kleykamp, H. and Schumacher, G., *The constitution of the silicon-carbon system.* Reports of the Bunsen Society for Physical Chemistry, 1993. **97**: p. 799-805.

33. Frisch, B., Thiele, W.R., Drumm, R. and Münnich, B., *On the Oxidation Mechanisms of Silicon Carbide in the 300 to 1300°C Temperature Range*,CFI/Ber. Dtsch. Keram. Ges, 1988. **65**: p. 277-284.

34. Shaffer, P.T.B., *SiC Wishkers - Part II*. Ceramic Age, 1966. **82**: p. 42-44.

35. Fickel, A., *SiC Materials*. Refractory Materials - Pocket Manual, ed. G. Routschka1997, Essen: Vulkan Verlag. 74-80.

36. Wu, Hongyan, MingXia Gao, Dan Zhu, Shengcai Zhang, Yi Pan, Hongge Pan, Yongfeng Liu, Filipe J. Oliveira, Joaquim M. Vieira, *SiC whisker reinforced multi-carbides composites prepared from B_4C and pyrolyzed rice husks via reactive infiltration.* Ceramics International, 2012. **38**: p. 3519–3527.

37. Gupta, M.. Ling, S., *Microstructure and mechanical properties of hypo/ hyper-eutectic Al–Si alloys synthesized using a near-net shape forming technique.* Journal of Alloys and Compounds, 1999. **287**: p. 287 - 294.

38. Nikanorov, S.P., Volkov, M.P., V.N. Gurin, Yu.A. Burenkov, L.I. Derkachenko, B.K. Kardashev, L.L. Regel, W.R. Wilcox, *Structural and mechanical properties of Al–Si alloys obtained by fast cooling of a levitated melt.* Materials Science and Engineering, 2005. **A 390** p. 63–69.

39. Richard, M., J.C. Mercier, J. C. and Jacob, S., *Fractography of the Aluminum Casting Alloys.* Fonderie Fondeur d'Aujourd'hui, 1984. **36**: p. 13-19.

40. Warmuzek, M., *Aluminum-Silicon Casting Alloys : Atlas of Microfractographs* 2004, United States of America: ASM International

41. Askeland, D.R., *The Science and Engineering of Materials,* 2d edition, Boston, 1989: PWS-Kent Publishing Co., p. 245-247

42. Lu, S. Z., Hellawell, A., *Modification of Al-Si Alloys: Microstructure, Thermal Analysis and Mechanics.* Journal of Materials, 1995. **47**(2): p. 38 - 40.

43. Davis, J. R., *Aluminum and AluminFum Alloys.* ASM Specialty Handbook:, ed. A.I.H.C. J.R. Davis & Associates1993: ASM International. 784.

44. Stroganov, G.B., V.A. Rotenberg, G.B. Gershman, *Aluminum–Silicon Alloys*. Metallurgiya 1977, Moscow.

45. Hillig, W. B., *Melt infiltration approach to ceramic matrix composites.* Journal of the American Ceramic Society, 1988. **71**(2): p. C-96-C-99.

46. Toy, C. and Scott, W., *Ceramic-Metal composite produced by melt infiltration.* Journal of the American Ceramic Society, 1990. **73**(1): p. 97-101.

47. Chadam, D.H. J., E. Merino, P. Ortoleva, A. Sen, *Reactive Infiltration Instabilities.* Journal of Applied Mathematics, 1986. **36**: p. 207-221.

48. Pan, Y., and Sun, K., *Preparation of TiC/Ni3Al composites by upward melt infiltration.* Journal of Materials Science and Technology, 2000. **16**(4): p. 387-392.

49. Hayun, S., A. Weizmann, H. Dilman, M. P. Dariel, and N. Frage. *Rim region growth and its composition in reaction bonded boron carbide composites with core-rim structure*. in 16th International Symposium on Boron, Borides and Related Materials. IOP Journal of Physics: Conference Series 2009. **176**: 012009

50. Toptan, F., A. Kilicarslan and I. Kerti, *The Effect of Ti Addition on the Properties of Al-B4C Interface: A Microstructural Study*. Materials Science Forum, 2010. **636-637**: p. 192-197.

51. Mortensen, A., Jin, I., *Solidification Processing of Metal Matrix Composites.* International Materials Reviews, 1992. **37**: p. 101-128.

52. Darcy, H.P.G., *Les Fontaines Publiques de la Ville de Dijon, Victor Dalmont, Paris,1856,* in *The Flow of Homogeneous Fluids through Porous Media*, M. Muskat, Editor 1937, McGraw-Hill: New York. p. 653.

53. Carman, P.C., *Capillary rise and capillary movement of moisture in fine sands.* Soil Science, 1941. **52**: p. 1-14.

54. Morrow, N., *Physics and thermodynamics of capillary action in porous media.* Industrial and Engineering Chemistry, 1970. **62**: p. 32–56.

55. Li, J.-G., *Wetting of Ceramic Materials by Liquid Silicon, Aluminium and Metallic Melts Containing Titanium and Other Reactive Elements: A Review*. Ceramics International 1994. **20**: p. 391-412.

56. Young, T., *A Essay on the cohesion of fIuids.* Philosophical Transactions of the Royal Society, 1805. **95**: p. 65-87.

57. D'Souzae, J.I. *Pharmaceutical powder material contains void volume of empty space, distributed within the solid mass in the form of pores, cavities, and cracks of various shapes and sizes.* Mercury Intrusion Porosimetry : A Tool for Pharmaceutical Particle Characterization, 2008. **6**.

58. Gibbs, J.W., *The Collected Works of J. Willard Gibbs*. Thermodynamics. Vol. I. 1928, New Haven: Yale University Press.

59. Batchelor, G. K., *An Introduction to Fluid Dynamics.*1967, New York: Cambridge University Press. 615.

60. Gibbs, J.W., *The Collected Works of J. Willard Gibbs* Thermodynamics. Vol. I. 1928, New Haven: Yale Universlty Press.

61. Dunstan, D., White, L.R., *A Capillary Pressure Method for Measurement of Contact Angles in Powders and Porous Media.* Journal of Colloid and Interface Science, 1986. **111**(1): p. 60-64.

62. Colin, C., Marchal, Y., F. Boland, and F. Delannay, *Stainless steel fibres reinforced aluminium matrix composites processed by squeeze casting: relationship between processing conditions and interface microstructure.* Journal de Physique IV, 1993. **3**: p. 1749-1752.

63. Fukunaga, H., X. Wang, and Y. Aramaki, *Preparation of Intermetallic Compound Matrix Composites By Reaction Squeeze Casting.* Journal of Materials Science Letters, 1990. **9**: p. 23-25.

64. Pastukhov, E.A., V.P. Chentsov, A.V. Kiselev, L.E. Bodrova, A.V. Dolmatov, E.A. Popova, S.A. Petrova, R.G. Zacharov *Wetting of Graphite Surface by the Aluminium Alloys Melts*. 2006. p. 1-178 - 1-181.

65. Li, J.G., Hausner, H., *Wetting and adhesion in liquid silicon/ceramic systems.* Materials Letters, 1992. **14**: p. 329-332.

66. Bergeron, C. G. and Risbud, S.H., *Introduction to Phase Equilibria in Ceramics*. The American Ceramic Society 1984, Ohio.

67. Grytsiv, A. and Rogl, P.,, *Aluminium-Boron-Carbon*. Vol. IV. MSIT Landolt-Börnstein New Series. 2004. **11A1**: p. 29-51.

68. Lim, S.-K., Lukas, H. L., *Thermodynamische Optimierung des Systems B-C-Si und seiner Randsysteme*, in Hochleistungskeramiken - Herstellung, Aufbau, Eigenschaften. ed. G. Petzow, J. Tobolski, and R. Telle, ed., Deutsche Forschungsgemeinschaft 1996, Verlag Chemie, Weinheim: VCH. p. 606-616.

69. Kieffer, R., Gugel, E., Leimer, G., Ettmayer, P., *Investigations on the system boron-carbon-silicon.* Beritch der Deutschen Keramischen Gesellschaft, 1972. **49**(2): p. 44.

70. Werheit, H., Kuhlmann, U., Laux, M., Telle, R., *Solid solutions of silicon in boron-carbide-type crystals.* Journal of Alloys and Compounds 1994. **209**: p. 181.

71. Smith, R.L. and Sandland, G.E., *An Accurate Method of Determining the Hardness of Metals, with Particular Reference to Those of a High Degree of Hardness*. Proceedings of the Institution of Mechanical Engineers. London, IMechE. 1922. **I**: p. 623–641.

72. Anstis, G.R., Chantikul, P., Lawn, B.R., Marshall, D.B., 1981. *A critical evaluation of indentation techniques for measuring fracture toughness. I. Direct crack measurements*. Journal of the American Ceramic Society, 1981. 64 (9): p. 533–538.

73. Schwetz, K.A., Sigl, L. S., and Pfau, L. J. , *Mechanical properties of injection molded B4C-C ceramics*. Journal of Solid State Chemistry 1997. 133 (1): p. 68-76.

74. Telle, R., *Oxidation behavior of B4C-SiC composites with various microstructures Proceedings of 10th International Symposium on Boron, Borides and Related Compounds*, Ed. D. Emin, Aselage, T. L., Switendick, A. C, Morosin, B., and Beekel, C. L, New York. Boron Rich Solids, AIP Conference Proceedings 1991. 231: p. 553-560.

75. Burminskaya, L. N., V.V. Zaboleev-Zotov,, Yu. M. Nikulin, and P. O. Pashkov, *Strength of two-phase aluminum-base mixtures*. Translated from Metallovedenie i Termicheskaya Obrabotka Metallov, 1967. No. 6, p. 27-30.

76. Frage, N., L.Levin, N. Frumin, M. Gelbstein, M.P. Dariel, *Manufacturing B4C–(Al,Si) composite materials by metal alloy infiltration*. Journal of Materials Processing Technology, 2003. 143-144: p. 486–490.

77. Panasyuk, A.D., V.D. Oreshkin., V. R. Maslennikova, *Kinetics of the reactions of boron carbide with liquid aluminium, silicon, nickel and iron*. Translated from Poroshkovaya Metallurgica 1979. Nº 7 (199): p. 79-83.

78. Ribes, H., Dasilva, R., Suery, M. and Bretau, *Effect of interfacial oxide layer in aluminium–silicon carbide particle composites on bond strength and mechanical behavior* Material Science Technology, 1990. **6**: p. 621–628.

79. Assael M.J., K. Kakosimos, Bannish R. M., Brillo J., Egry I., Brooks R., Quested P.N., Mills K.C., Nagashima A., Sato Y., and Wakeham W.A, *Reference Data for the Density and Viscosity of Liquid Aluminium and Liquid Iron*. Journal of Physical and Chemical Reference Data, 2006. 35: p. 285-300.

80. Xie SS, S.L., Guo J, Vasylkiv O, Borodianska H, Xi Z, Krishnan GM, Su H, Tokl AI, *Non-catalytic facile synthesis of superhard phase of boron carbide ($B_{13}C_2$) nanoflakes and nanoparticles.* Journal of Nanoscience and Nanotechnology, 2012. **12**(1): p. 596-603.

81. Viala, J.C, Fortier, P., Bouix, J., *Stable and metastable phase equilibria in the chemical interaction between aluminium and silicon carbide*. Journal Material Science, 1990. **25**(3): p. 1842 -1850.

82. Birru, A.K., Karunakar, D.B., Mahapatra, M.M., *Fluidity of A713 Cast Alloy with and without Scrap Addition using Double Spiral Fluidity Test: A Comparison*. World Academy of Science, Engineering and Technology 2012. **61**: p. 474 – 478.

83. Hayun, S., H. Dilman, M. P. Dariel, and N. Frage *The effect of aluminum on the microstructure and phase composition of boron carbide infiltrated with silicon*. Materials Chemistry and Physics, 2009. **118**: p. 490–495

84. Grytsiv, A., and Rogl, P., *Al-B-C (Aluminium - Boron - Carbon)*. ed. G. Effenberg, Ilyenko, S. . Vol. IV 11A: Light Metal Systems. Part 1. Germany: Springer Materials - The Landolt-Börnstein Database. p. 29–51.

85. Raghavan, V., *Al-B-Si (Aluminum-Boron-Silicon*). Journal of Phase Equilibria and Diffusion 2008. **29**(1): p. 44–45.

86. Kohler, W., Untersuchungen zur Benetzung von Al2O3-und SiC-Kristallen durch Aluminium und Aluminiumlegierungen. Aluminium, 1975. **51**(7): p. 443–447

87. Dowling, N.E., *Mechanical behavior of materials: engineering methods for deformation, fracture, and fatigue* 1993, United States: Prentice-Hall International. 773.

88. Zhao, X. J., Zhang,N., Ru, H. Q., Liang, B., Chen, D.L., *Mechanical properties and toughening mechanisms of silicon carbide nano-particulate reinforced Alon composites.* Materials Science and Engineering, 2012. **A 538**: p. 118– 124.

89. Chen, D., Sixta, M. E., Zhang X. F., De Jonghe, L. C., Ritchie, R. O., *Role of the grain boundary phase elevated temperature strength, toughness fatigue and creep resistance of Silicon carbide sintered with Al, B, and C.* Acta Materialia, 2000. **48**: p. 4599–4608.

90. Sorarù, G.D., and Colombo, P., *Polymer to Ceramic Transformation: Processing of Ceramic Bodies and Thin Films*. in Handbbook of Ceramic Hard Materials, ed. R. Riedel. Vol. 2. 2000, Weinheim: Wiley-VCH Verlag GmbH. 446-478.

91. Telle, D.R., *Boride - eine neue Hartstoffgeneration?* Chemie in unserer Zeit, 1988. **3**: p. 93 - 99.

92. Yonezu, A., Xu, B. X., Chen, X., *Indentation induced lateral crack in ceramics with surface hardening.* Materials Science and Engineering A, 2009. **507**((1-2)): p. 226-235.

93. Rice, R.W., *Mechanisms of Toughening in Ceramic Matrix Composites.* Ceramic Engineering Science Proc, 1981. **2**: p. 661-701.

94. Evans, A. G., *Fracture toughness: The role of indentation techniques*. in: S.W.reiman (Ed.), Fracture Mechanic Applied to Brittle Materials, ASTM STP 678, part 2, American Society for Testing and Materials, Philadelphia, 1979, pp. 112–135.

Annexes

Annex - A

Table A1: Quantification of volumetric phase composition for composite A is derived from XRD patterns and standard data.

Quantification of Volumetric Phase Composition - Composite - A (tested result on cross sectional area)																			
		XRD Test Result - 1 (Oct-Nov2012)				XRD Test Result - 2 (Dec 2012)				XRD Test Result - 3 (Dec 2012)				Average on Zones			
ZONES		Al	Si	B_4C	SiC	Al	Si	B_4C	SiC	Al	Si	B_4C	SiC	Al	Si	B_4C	SiC
TOP	Intensity	1333	103	100	185	1383	220	273	228	1918	595	270	243	1545	306	214	219
	Amount (wt %)	63.7%	4.3%	23.7%	8.3%	51.8%	7.3%	35.4%	5.5%	52.6%	14.9%	27.8%	4.7%	56.0%	8.8%	29.0%	6.2%
MIDDLE	Intensity	1063	435	393	275	793	1213	360	260	943	393	380	285	933	680	378	273
	Amount (wt %)	37.6%	14.4%	42.5%	5.6%	19.3%	40.1%	35.8%	4.9%	35.8%	14.0%	44.0%	6.2%	30.9%	22.8%	40.8%	5.5%
BOTTOM	Intensity	1728	450	295	218	538	475	128	95	1710	543	255	160	1325	489	226	158
	Amount (wt %)	52.4%	12.4%	31.0%	4.3%	34.2%	31.9%	29.8%	4.2%	53.8%	15.6%	27.4%	3.2%	46.8%	20.0%	29.4%	3.9%
Average of individual phases	Intensity	1375	329	263	226	905	636	254	194	1524	510	302	229				
	Amount (wt %)	51.2%	10.4%	32.4%	6.1%	35.1%	26.4%	33.7%	4.8%	47.4%	14.8%	33.1%	4.7%				
Grand average of intensity of phases														1268	492	273	217
Grand average of volumetric phase composition (wt %)														44.6%	17.2%	33.0%	5.2%

Table A2: Quantification of volumetric phase composition for composite B is derived from XRD patterns and standard data.

Quantification of Volumetric Phase Composition - Composite - B (tested result on cross sectional area)																	
		XRD Test Result - 1 (Oct-Nov2012)				XRD Test Result - 2 (Dec 2012)				XRD Test Result - 3 (Dec 2012)				Average on Zones			
ZONES		Al	Si	B_4C	SiC	Al	Si	B_4C	SiC	Al	Si	B_4C	SiC	Al	Si	B_4C	SiC
TOP	Intensity	2813	100	203	153	3028	1533	255	260	4398	3828	378	290	3413	1820	279	234
	Amount (wt %)	63.7%	4.3%	23.7%	8.3%	52.5%	25.4%	18.6%	3.6%	43.1%	39.5%	15.2%	2.2%	53.1%	23.1%	19.2%	4.7%
MIDDLE	Intensity	1853	2310	465	263	1878	698	638	310	1555	1220	548	200	1762	1409	550	258
	Amount (wt %)	37.6%	14.4%	42.5%	5.6%	41.5%	14.3%	40.5%	3.7%	34.4%	27.7%	35.5%	2.4%	37.8%	18.8%	39.5%	3.9%
BOTTOM	Intensity	828	853	395	243	1175	753	618	315	1195	373	460	290	1066	660	491	283
	Amount (wt %)	52.4%	12.4%	31.0%	4.3%	30.8%	19.5%	45.3%	4.3%	39.3%	11.2%	44.2%	5.2%	40.9%	14.4%	40.2%	4.6%
Average of indivutual phases	Intensity	1831	1088	354	220	2027	995	504	295	2383	1807	462	260				
	Amount (wt %)	51.2%	10.4%	32.4%	6.1%	41.6%	19.7%	34.8%	3.9%	38.9%	26.1%	31.6%	3.3%				
Grand average of intensity of phases														2080	1296	440	258
Grand average of volumetric phase composition (wt %)														43.9%	18.7%	32.9%	4.4%
Note : Intensity peaks of Al - 2θ(38°-39.50°), Si 2θ(28° - 29°), B_4C 2θ(37°- 38°), SiC 2θ(35°-36°)																	

Table A3: Quantification of volumetric phase composition for composite C is derived from XRD patterns and standard data.

Quantification of Volumetric Phase Composition - Composite - C (tested result on cross sectional area)																	
		XRD Test Result - 1 (Oct-Nov2012)				XRD Test Result - 2 (Dec 2012)				XRD Test Result - 3 (Dec 2012)				Average on Zones			
ZONES		Al	Si	B_4C	SiC	Al	Si	B_4C	SiC	Al	Si	B_4C	SiC	Al	Si	B_4C	SiC
TOP	Intensity	2968	145	415	220	1745	313	353	258	1583	535	360	250	2099	331	376	243
	Amount (wt %)	64.7%	2.8%	29.6%	2.9%	51.8%	8.3%	35.1%	4.8%	46.3%	14.4%	34.7%	4.5%	54.3%	8.5%	33.1%	4.1%
MIDDLE	Intensity	3805	488	520	288	5558	2745	603	240	4450	175	490	283	4604	1136	538	270
	Amount (wt %)	62.0%	7.0%	28.1%	2.9%	54.1%	25.4%	19.1%	1.4%	68.8%	2.4%	26.0%	2.8%	61.6%	11.6%	24.4%	2.4%
BOTTOM	Intensity	3598	883	653	358	2438	503	485	303	1353	1013	238	160	2463	800	459	274
	Amount (wt %)	53.7%	11.9%	31.2%	3.2%	52.5%	9.7%	33.9%	4.0%	40.4%	30.7%	25.7%	3.2%	48.8%	17.4%	30.3%	3.5%
Average of indivutual phases	Intensity	3457	505	529	289	3247	1187	480	267	2462	574	363	231				
	Amount (wt %)	60.1%	7.2%	29.6%	3.0%	52.8%	14.5%	29.3%	3.4%	51.8%	15.8%	28.8%	3.5%				
Grand average of intensity of phases														3055	756	457	262
Grand average of volumetric phase composition (wt %)														54.9%	12.5%	29.3%	3.3%
Note : Intensity peaks of Al - 2θ(38°-39.50°), Si 2θ(28° - 29°), B_4C 2θ(37°- 38°), SiC 2θ(35°-36°)																	

Annex – B

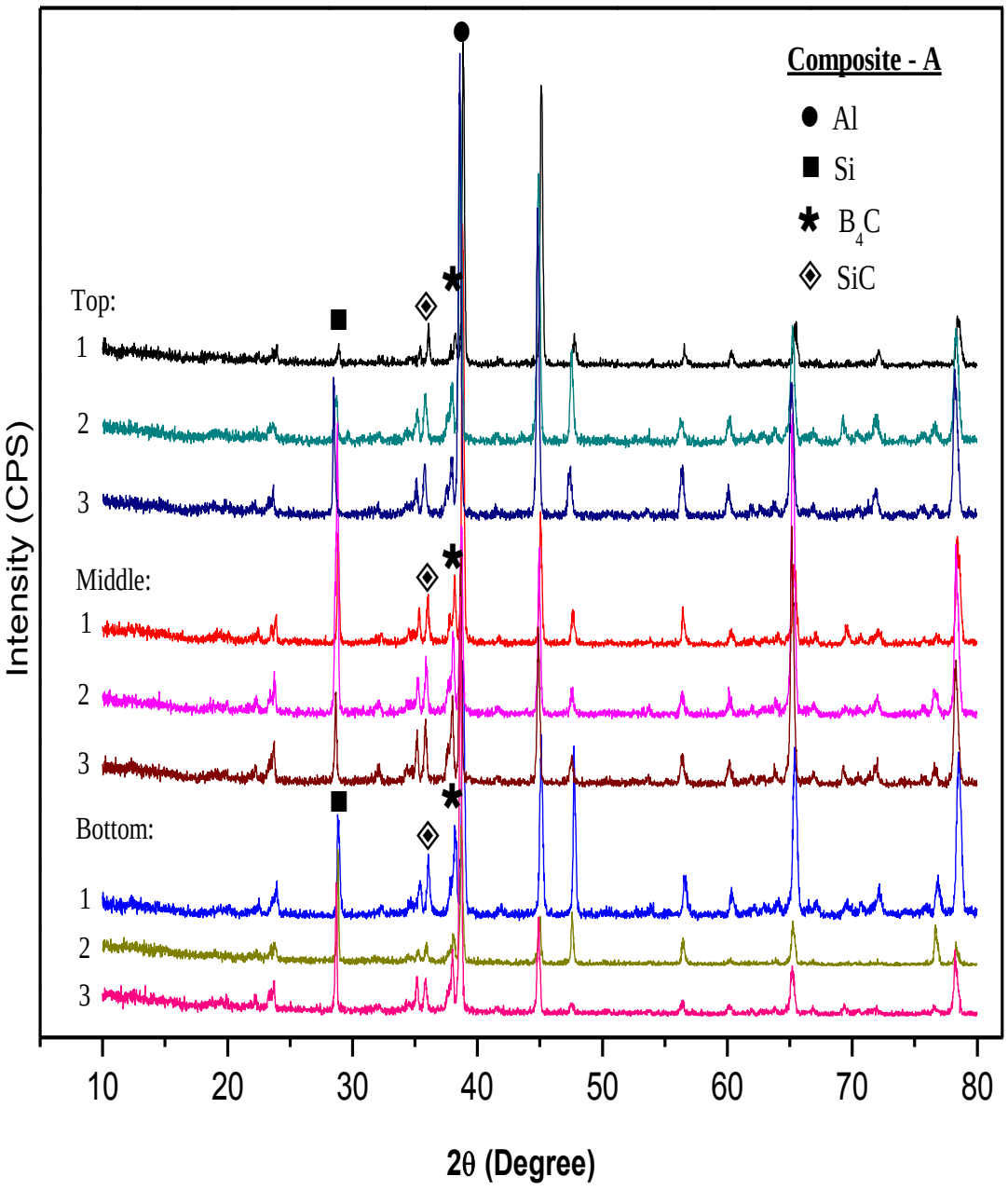

Figure B1: XRD patterns on the longitudinal cross section of composite A from top (T), middle (M) and bottom (B) areas after three tests on each region.

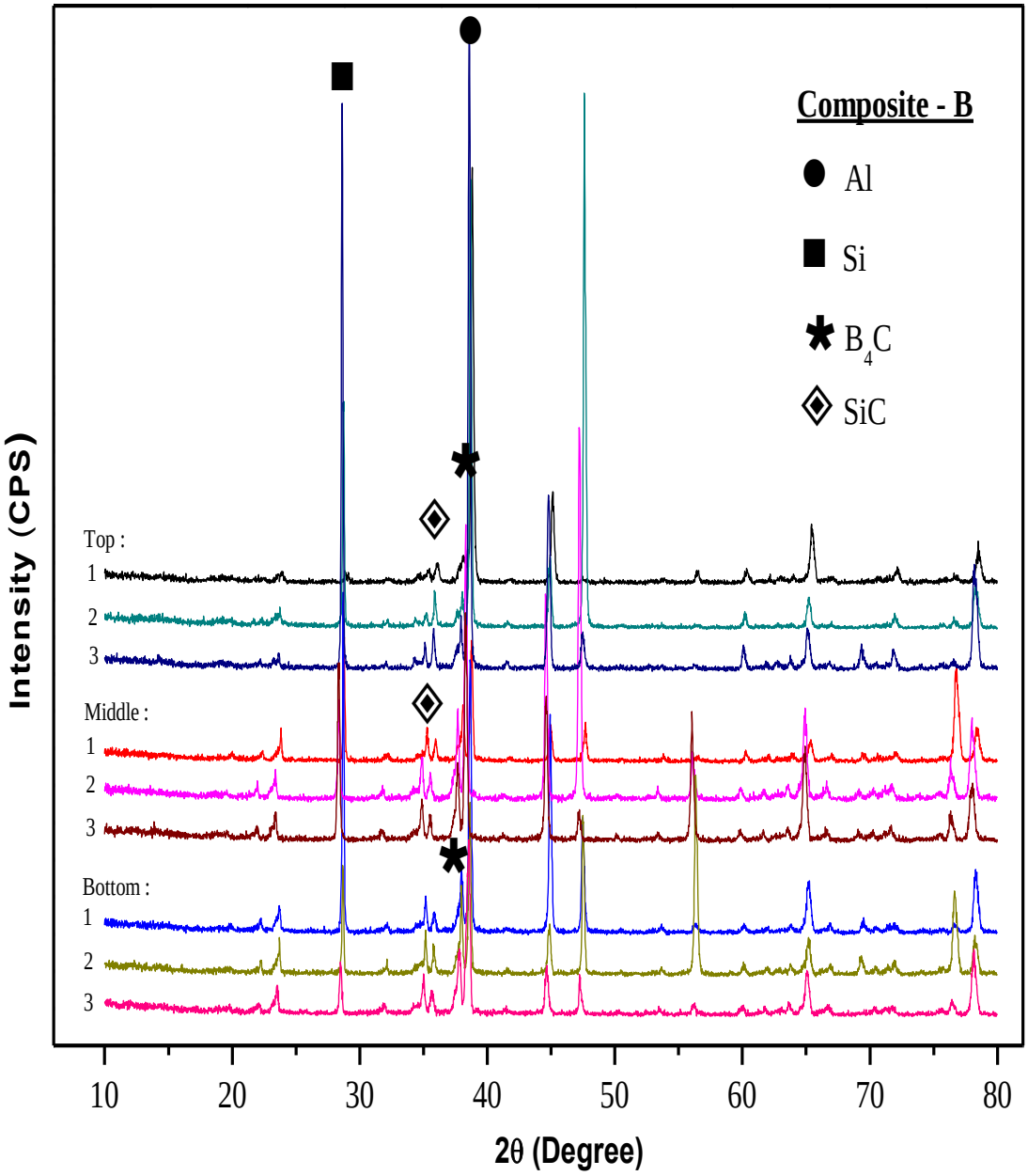

Figure B2: XRD patterns on the longitudinal cross section of composite B from top (T), middle (M) and bottom (B) areas after three tests on each region.

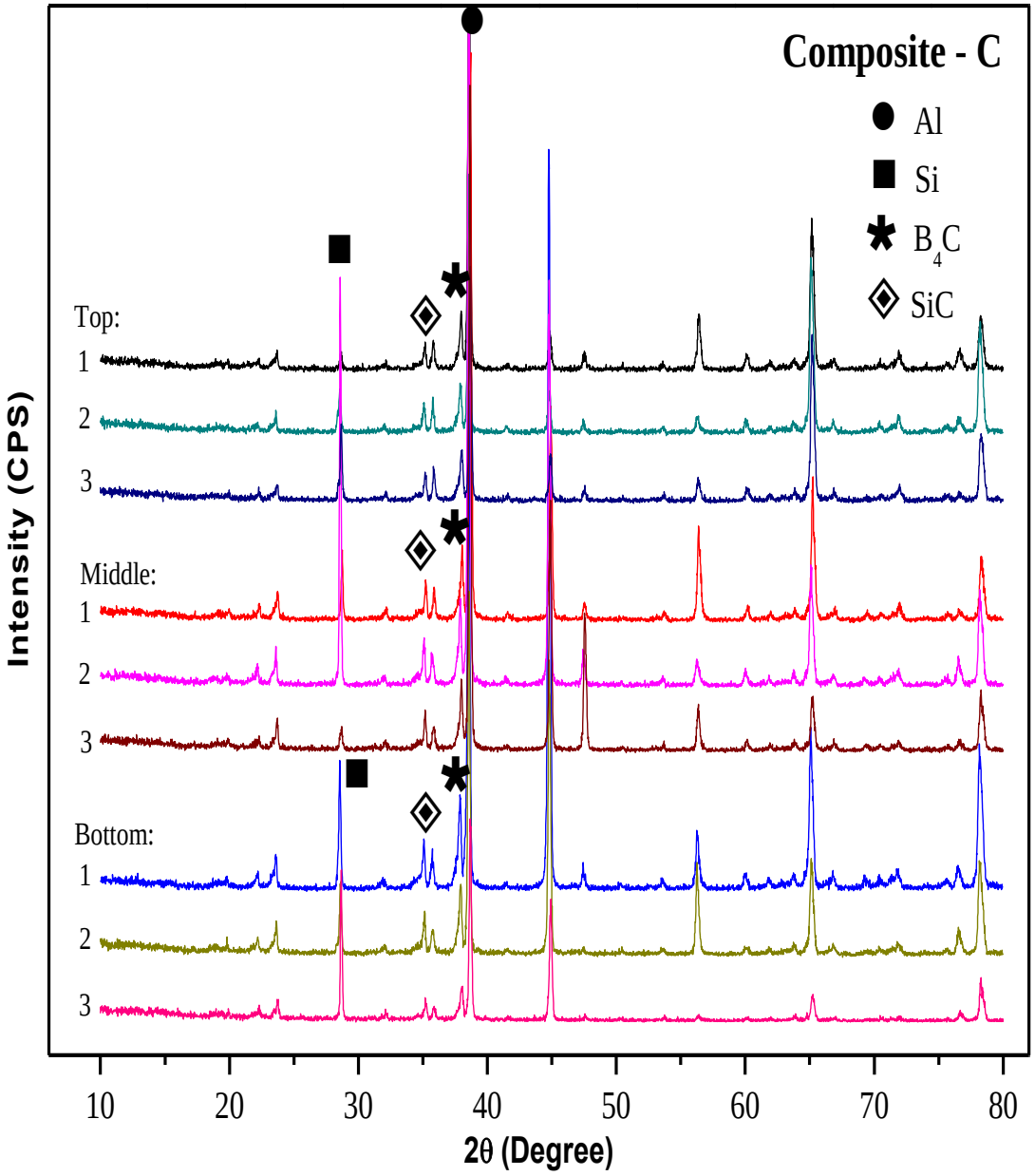

Figure B3: XRD patterns on the longitudinal cross section of composite C from top (T), middle (M) and bottom (B) areas after three tests on each region.

Annex – C

Table C1: Status of composite I and II (A) - on each stage of preparation.

Observation and Calculation Sheet

Description		COMPOSITE - I			Powder Density		2.52 g/cm^3		Porosity assumed 50%		COMPOSITE - II / A			Powder Density	2.52 g/cm^3		Porosity assumed 50%	
		Dia meter	Length	Area	Volume	Mass	Density	Actual densification	Porosity		Dia meter	Length	Area	Volume	Mass	Density	Actual densification	Porosity
		(mm)	(mm)	(mm^2)	(cm^3)	(g)	(g/cm^3)	(%)	(%)		(mm)	(mm)	(mm^2)	(cm^3)	(g)	(g/cm^3)	(%)	(%)
Powder	Nominal values (B_4C+4 wt% PVA)	20.0	15.0	314.16	4.7124	5,9346+0,2374	1.2600				20.0	7.5	314.16	2.3550	2,9673+0,1186	1.2600		
	Actual taken					5.9800									3.0220			
Compacted Preform	Uniaxial	20.0	15.7	314.16	4.9166	6.0530	1.2311	48.85	51.15		20.0	7.2	314.16	2.2462	2.9736	1.3238	52.53	47.47
	Isostati	19.6	15.5	301.72	4.6766	5.9859	1.2800	50.79	49.21		19.6	7.0	301.72	2.1120	2.9168	1.3810	54.80	45.20
Composite	Conventional method	19.6	15.2	300.49	4.5674	10.5518	2.3102	-	-		19.7	7.0	304.81	2.1336	5.3786	2.5209	-	-
	Archemidies method				4.2241	6.3277	**2.4980**	-	-					2.1066	3.2720	**2.5532**	-	-

Density of the alloy (Al + 25 wt% Si)	2.60 g/cm^3	Density of the alloy (Al + 25 wt% Si)	2.60 g/cm^3
Volume of the alloy	2.35 cm^3	Volume of the alloy	0.97 cm^3
Mass of the alloy Req. for Infiltration (102%)	6.10 g	Mass of the alloy Req. for Infiltration	2.53 g
Mass of the alloy used for Infiltration	6.15 g	Mass of the alloy used for Infiltration	2.52 g
Excess material used	0.77 %	Excess material used	-0.46 %
Volume of the Liquid = Mass dry - Mass Immersed	4.22 g	Volume of the Liquid = Mass dry - Mass Immersed	2.11 g
Density (Archemidies) = Mass dry /Volume of the liquid	**2.50 g /cm^3**	Density (Archemidies) = Mass dry /Volume of the liquid	**2.55 g /cm^3**

Note: Powder used B_4C 1200 Mesh

Table C2: Status of composite III and IV (B) - on each stage of preparation.

Observation and Calculation Sheet

Description		COMPOSITE - III			Powder Density	2.52 g/cm^3		Porosity assumed 50%		COMPOSITE - IV / B			Powder Density	2.52 g/cm^3		Porosity assumed 50%	
		Dia meter	Length	Area	Volume	Mass	Density	Actual densification	Porosity	Dia meter	Length	Area	Volume	Mass	Density	Actual densification	Porosity
		(mm)	(mm)	(mm^2)	(cm^3)	(g)	(g/cm^3)	(%)	(%)	(mm)	(mm)	(mm^2)	(cm^3)	(g)	(g/cm^3)	(%)	(%)
Powder	Nominal vlaues (B_4C+4 wt% PVA)	20.0	7.5	314.16	2.3550	2,9673+0,1186	1.2600			20.0	7.5	314.16	2.3550	2,9673+0,1186	1.2600		
	Actual taken					3.0746								3.0800			
Compacted Preform	Uniaxial	20.0	7.3	314.16	2.2777	3.0203	1.3261	52.62	47.38	20.0	7.2	314.16	2.2619	3.0718	1.3580	53.89	46.11
	Isostati	19.7	7.2	304.81	2.1885	2.984	1.3635	54.11	45.89	19.5	7.1	299.87	2.1291	2.9596	1.3901	55.16	44.84
Composite	Conventional method	19.7	7.3	303.26	2.1986	4.9000	2.2287	88.44	11.56	19.6	7.1	300.88	2.1376	5.3908	2.5219	-	-
	Archemidies method				2.0100	2.8900	**2.4378**	96.74	3.26				2.1303	3.2605	**2.5305**	-	-

Density of the alloy (Al + 25 wt% Si)	2.60 g/cm^3
Volume of the alloy	1.02 cm^3
Mass of the alloy Req. for Infiltration (102%)	2.67 g
Mass of the alloy used for Infiltration	2.70 g
Excess material used	1.08 %
Volume of the Liquid = Mass dry - Mass Immersed	2.01 g
Density (Archemidies) = Mass dry /Volume of the liquid	**2.44 g /cm^3**

Density of the alloy (Al + 35 wt% Si)	2.56 g/cm^3
Volume of the alloy	0.95 cm^3
Mass of the alloy Req. for Infiltration	2.45 g
Mass of the alloy used for Infiltration	2.52 g
Excess material used	2.71 %
Volume of the Liquid = Mass dry - Mass Immersed	2.13 g
Density (Archemidies) = Mass dry /Volume of the liquid	**2.53 g /cm^3**

Table C3: Status of composite V and VI - on each stage of preparation.

Observation and Calculation Sheet

Description		COMPOSITE -V			Powder Density	2.52 g/cm^3		Porosity assumed 50%	
		Dia meter	Length	Area	Volume	Mass	Density	Actual densification	Porosity
		(mm)	(mm)	(mm^2)	(cm^3)	(g)	(g/cm^3)	(%)	(%)
Powder	Nominal vlaues (B_4C+4 wt% PVA)	20.0	7.5	314.16	2.3562	2,9673+0,1186	1.2600		
	Actual taken					3.0640			
Compacted Preform	Uniaxial	20.0	7.4	314.16	2.3091	3.0306	1.3125	52.08	47.92
	Isostatic	19.5	7.2	298.95	2.1495	3.0002	1.3958	55.39	44.61
Composite	Conventional method	19.6	7.3	300.71	2.2025	5.5212	2.5068	-	-
	Archemidies method	19.6	7.3	300.71	2.2050	3.3162	**2.5039**	-	-

Density of the alloy (Al + 35 wt% Si)	2.58 g/cm^3
Volume of the alloy	0.96 cm^3
Mass of the alloy Req. for Infiltration (102%)	2.46 g
Mass of the alloy used for Infiltration	2.75 g
Excess material used	11.62 %
Volume of the Liquid = Mass dry - Mass Immersed	2.21 g
Density (Archemidies) = Mass dry /Volume of the liquid	**2.50 g /cm^3**

COMPOSITE - VI	Powder Density	2.52 g/cm^3		Porosity assumed 50%	
Dia meter	Length	Area	Volume	Mass	Density	Actual densification	Porosity
(mm)	(mm)	(mm^2)	(cm^3)	(g)	(g/cm^3)	(%)	(%)
20.0	7.5	314.16	2.3550	2,9673+0,1186	1.2600		
				3.0900			
20.0	7.1	314.16	2.2400	3.0369	1.3558	53.80	46.20
19.4	7.1	295.29	2.0859	3.0070	1.4416	57.21	42.79
19.5	7.1	299.13	2.1200	5.3244	2.5115	-	-
		0.00	2.1177	3.2067	**2.5142**	-	-

Density of the twice smelted alloy (Al + 25 wt% Si)	2.63 g/cm^3
Volume of the alloy	0.89 cm^3
Mass of the alloy Req. for Infiltration	2.33 g
Mass of the alloy used for Infiltration	2.55 g
Excess material used	9.57 %
Volume of the Liquid = Mass dry - Mass Immersed	2.12 g
Density (Archemidies) = Mass dry /Volume of the liquid	**2.51 g /cm^3**

Table C4: Status of composite VII and VIII (C) - on each stage of preparation.

Observation and Calculation Sheet

Description		COMPOSITE -VII			Powder Density	2.52 g/cm^3		Porosity assumed 50%		COMPOSITE - VIII / C			Powder Density	2.52 g/cm^3		Porosity assumed 50%	
		Dia meter	Length	Area	Volume	Mass	Density	Actual densification	Porosity	Dia meter	Length	Area	Volume	Mass	Density	Actual densification	Porosity
		(mm)	(mm)	(mm^2)	(cm^3)	(g)	(g/cm^3)	(%)	(%)	(mm)	(mm)	(mm^2)	(cm^3)	(g)	(g/cm^3)	(%)	(%)
Powder	Nominal vlaues (B_4C+4 wt% PVA)	20.0	7.5	314.16	2.3562	2,9673+0,1186	1.2600			20.0	7.5	314.16	2.3550	2,9673+0,1186	1.2600		
	Actual taken					3.0639								3.0490			
Compacted Preform	Uniaxial	20.0	7.2	314.16	2.2462	3.0041	1.3374	53.07	46.93	20.0	7.1	314.16	2.2305	2.9908	1.3408	53.21	46.79
	Isostatic	19.3	7.0	293.46	2.0432	2.9685	1.4528	57.65	42.35	19.4	7.0	294.68	2.0598	2.9550	1.4346	56.93	43.07
Composite	Conventional method	19.5	7.1	297.66	2.0993	5.2181	2.4856	-	-	19.5	7.1	297.42	2.1028	5.3727	2.5550	-	-
	Archemidies method			0.00	2.0762	3.1419	**2.5133**	-	-			0.00	2.1116	3.2611	**2.5544**	-	-

Density of the twice smelted alloy (Al + 25 wt% Si)	2.61 g/cm^3
Volume of the alloy	0.87 cm^3
Mass of the alloy Req. for Infiltration (102%)	2.26 g
Mass of the alloy used for Infiltration	2.32 g
Excess material used	2.62 %
Volume of the Liquid = Mass dry - Mass Immersed	2.08 g
Density (Archemidies) = Mass dry /Volume of the liquid	**2.51 g /cm^3**

Density of the twice smelted alloy (Al + 25 wt% Si)	2.61 g/cm^3
Volume of the alloy	0.89 cm^3
Mass of the alloy Req. for Infiltration	2.31 g
Mass of the alloy used for Infiltration	2.55 g
Excess material used	10.24 %
Volume of the Liquid = Mass dry - Mass Immersed	2.11 g
Density (Archemidies) = Mass dry /Volume of the liquid	**2.55** g /cm^3

Annex – D

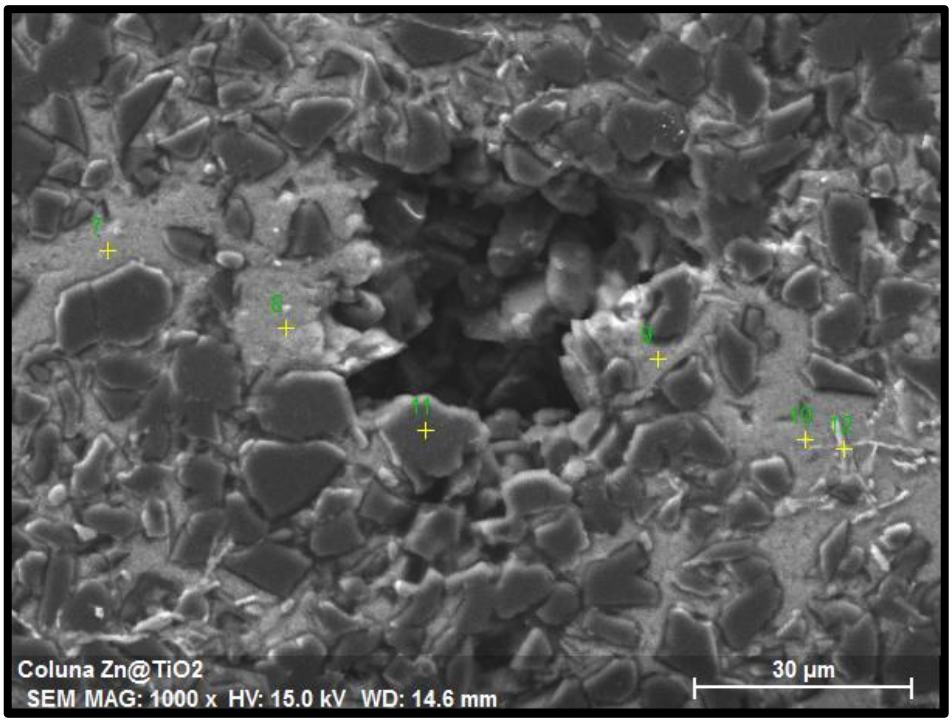

Figure D1: EDS image of SEM microscopy - Top zone - Composite A

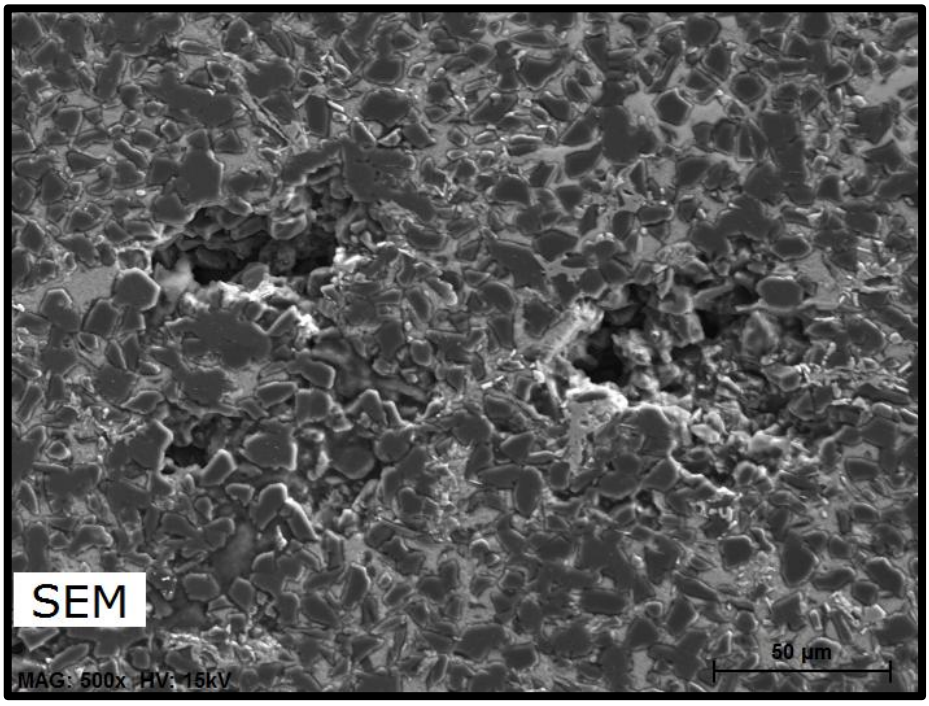

Figure D2: EDS image of SEM microscopy - middle zone - Composite A

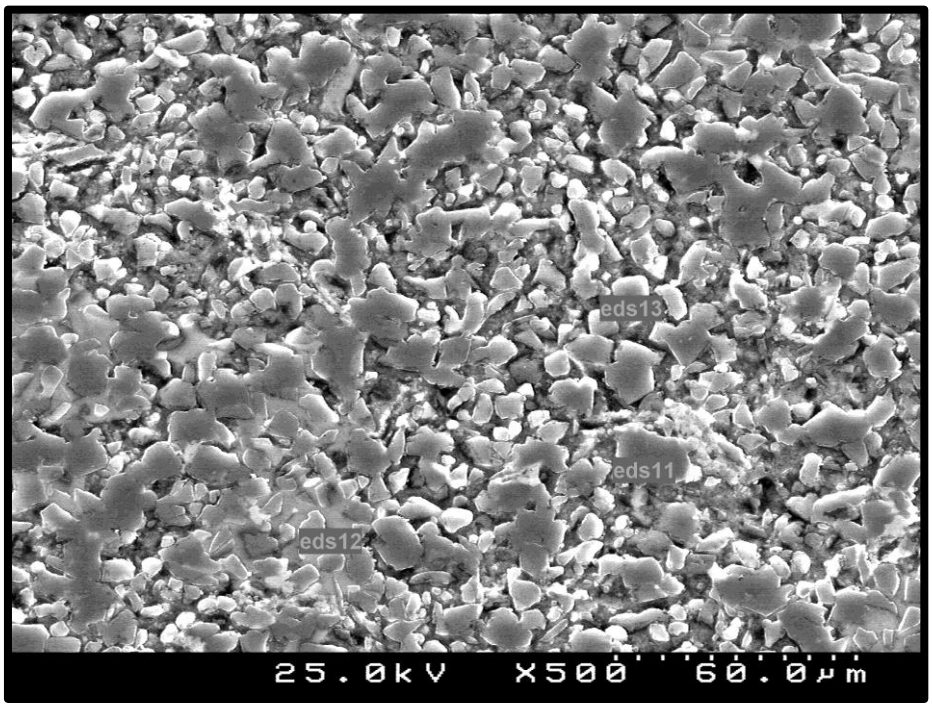

Figure D3: EDS image of SEM microscopy - Top zone – Composite B

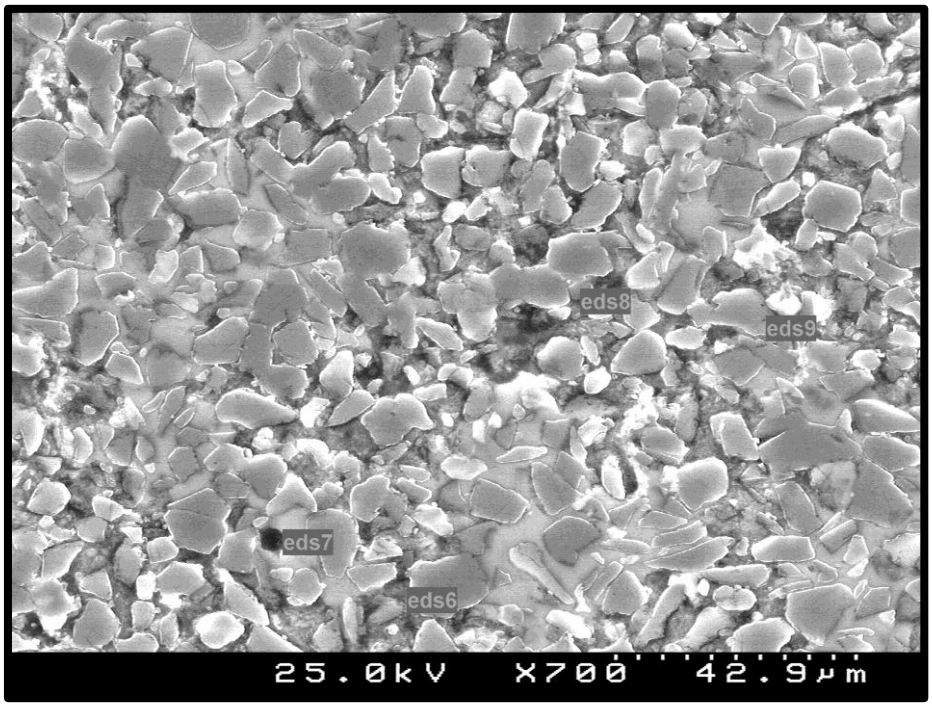

Figure D4: EDS image of SEM microscopy - Middle zone – Composite B

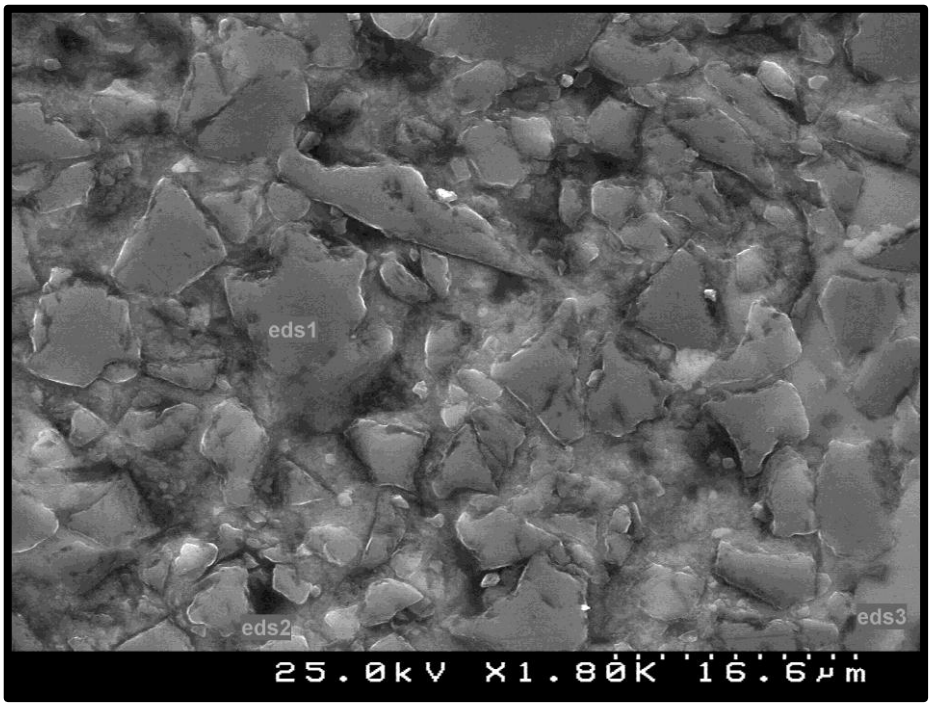

Figure D5: EDS image of SEM microscopy - Bottom zone – Composite B

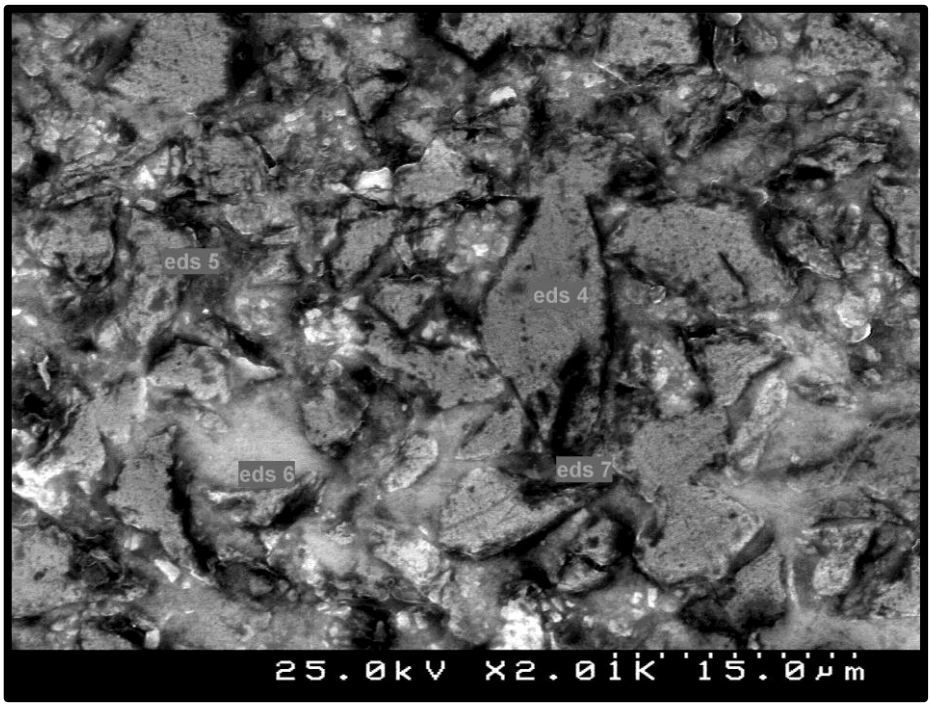

Figure D6: EDS image of SEM microscopy - Top zone – Composite C

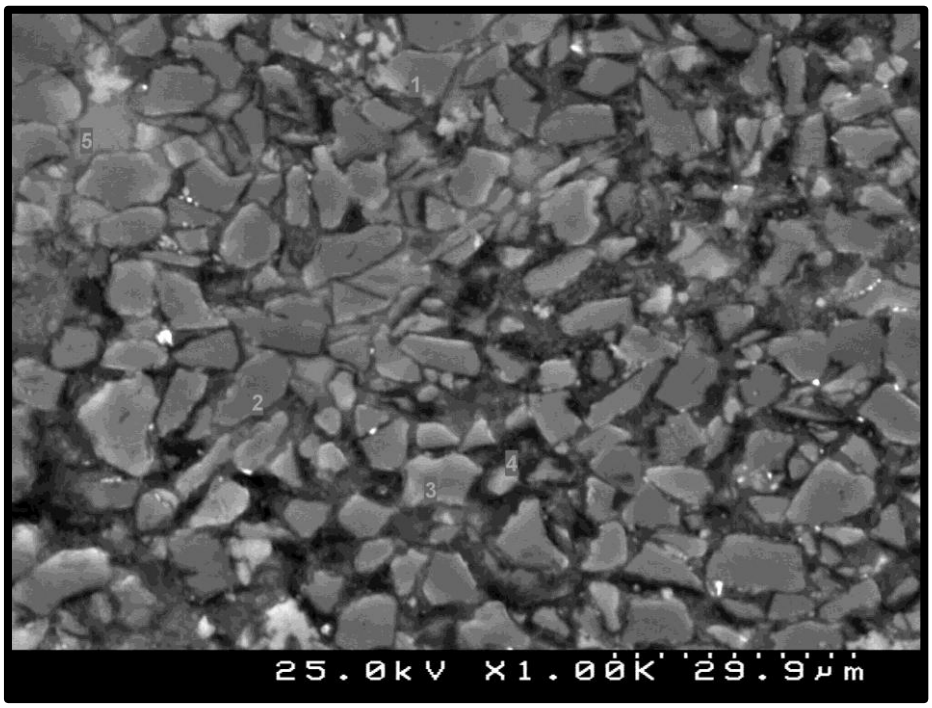

Figure D7: EDS image of SEM microscopy - Middle zone – Composite C

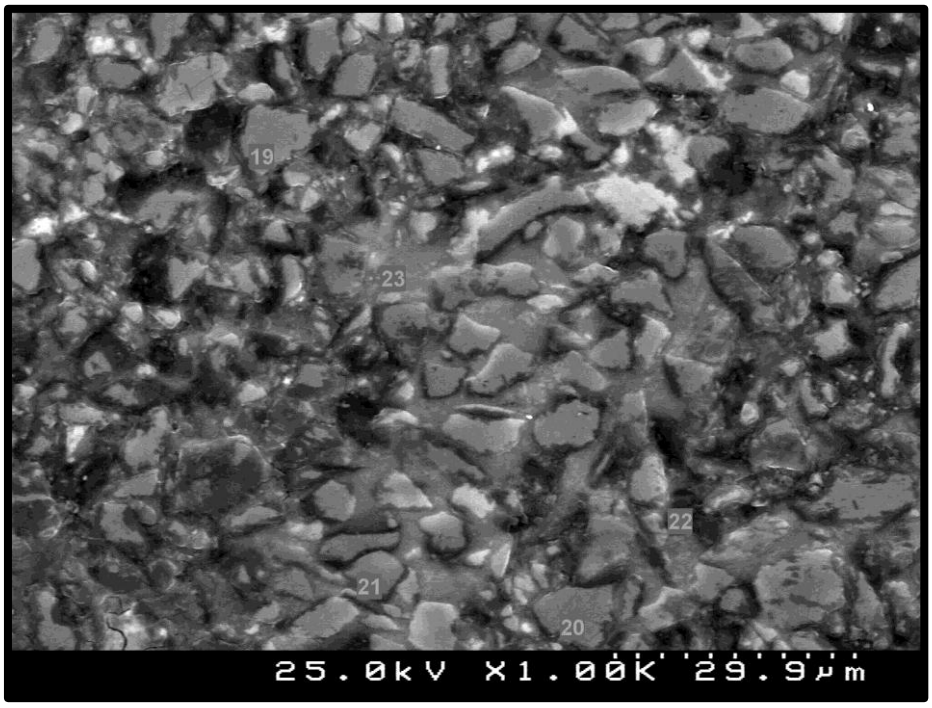

Figure D8: EDS image of SEM microscopy – Bottom zone – Composite C